Numerical and Experimental Investigations of Darrieus Wind Turbine Start-up and Operation

DU, LONGHUAN

Numerical and Experimental Investigations of Darrieus Wind Turbine Start-up and Operation

Longhuan Du

Submitted to Durham University for the degree of

Doctor of Philosophy

School of Engineering and Computing Sciences

2015

Abstract

The performance of small, H-Darrieus vertical axis wind turbines has been investigated numerically and experimentally with particular attention paid to turbine performance at low tip speed ratios (low Reynolds number) and to turbine self-starting. Comprehensive wind tunnel measurements have been performed to provide accurate aerofoil data at low Reynolds numbers and high angles of attack; a unique requirement for vertical axis wind turbine (VAWT) starting studies. Two-dimensional CFD models and blade element momentum (BEM) models were created and assessed to provide new insight into turbine performance for different wind conditions and into different turbine geometries in order to guide the design of the experimental investigation.

The experimental and numerical studies have demonstrated that design parameters including turbine solidity, blade profile, blade pitch angle and blade surface roughness have strong influences on turbine performance and turbine self-starting capability. Although other authors have conducted numerical studies of the effect of these parameters, this work represents the first experimental validation for turbine performance at low tip speed ratios. In contrast to some previous studies it is shown that there is no advantage to be gained from the use of cambered blades and that symmetrical blades set at small negative incidence provide the best design solution. It is also shown that increasing the turbine's solidity can significantly improve self-starting capability and that for a given solidity, increasing the rotor radius with a corresponding increase of blade chord improves performance further. However, these starting performance gains are achieved at the expense of a small loss of peak power output.

In addition, bio-inspired blades with tubercle leading edges are demonstrated to be able to significantly improve the turbine self-starting capability by introducing a more gradual stall characteristic. These results are the only reported measurements of the effect of tubercle leading edges on vertical axis wind turbines.

Finally, a novel, real-time on-board pressure measurement system was developed and employed to examine the instantaneous blade pressure distribution and its variation when the turbine is rotating. The complex flow physics including dynamic stall, laminar separation and flow curvature were successfully recorded and provide unique, unsteady data to increase our knowledge and understanding of the transient aerodynamics of the H-Darrieus wind turbine.

The experimental results were also compared with the available CFD and BEM predictions. It is demonstrated that BEM based approaches are highly sensitive to the quality of the aerofoil data that is provided as input to the model.

This thesis provides validation of previous work on the question of whether H-Darrieus wind turbines can start without external assistance and in the light of this research a set of revised design rules are proposed to achieve self-starting turbines.

Declaration

This thesis is based on the work carried out by Longhuan Du under the supervision of Professor Robert Dominy, Dr Grant Ingram and Dr Arganthaël Berson as a part of the Energy group, School of Engineering and Computing Sciences, Durham University. No part of this thesis has been submitted elsewhere for any other degree or qualification and all research included in this thesis is the author's own work unless referenced otherwise.

Acknowledgement

The success of this thesis would not have been possible without the support and guidance of my supervisors: Professor Robert Dominy, Dr Grant Ingram and Dr Arganthaël Berson. Their advice, suggestions and expertise have helped to shape this thesis. My sincere thanks go to them all.

I would like to express the deepest appreciation and thanks to Mr Peter Baxendale at Durham University for helping to build and setup the on-board pressure measurement system.

I am indebted to the technical staff in the School of Engineering and Computing Sciences. Special thanks are due to: Collin Wintrip, Gary Parker and Simon Apps for their assistance in the wind tunnel setup; Phillip Duffy for his excellent work on aerofoil rapid prototyping; Ian Garrett for his assistance in the installation of motor and clutch. This research work would have been less fruitful without their contributions.

Many people helped me during my three-year study: Dr David Sims-Williams, Dr Richard Williams, Dr Michael Hilfer and Dr Nick Cresswell. I am extremely grateful for their help.

The final thank you belongs to my parents and fiancée for their continuing support over these years. I would certainly not be here today were it not for them.

Content

List of Figures

List of Tables

Nomenclature

English symbols

Symbol	Definition
$\dot{a}$	Upwind induction factor/axial interference factor
$\dot{a}'$	Downwind induction factor/axial interference factor
A	Frontal area of turbine at rotation plane
A_0	Streamtube frontal area at upstream
A_1	Streamtube frontal area at wake/downstream
A_a	Amplitude
A_c	Aerofoil cross section area
c	Blade chord length
C_l	Lift coefficient, $C_l = F_l/(0.5\rho V^2 c)$
C_{lc}	Corrected lift coefficient
C_{lu}	Uncorrected lift coefficient
$C_{l_{dyn}}$	Lift coefficient under dynamic stall effect
ΔC_l	Residual correction to lift coefficient
C_d	Drag coefficient, $C_d = F_d/(0.5\rho V^2 c)$
C_{dc}	Corrected drag coefficient
C_{du}	Uncorrected drag coefficient
$C_{d_{dyn}}$	Drag coefficient under dynamic stall effect
ΔC_d	Residual correction to drag coefficient
C_n	Normal force coefficient
C_t	Tangential force coefficient
C_K	Thrust force coefficient
C_{Ka}	Aerofoil thrust force coefficient, $C_{Ka} = K/(0.5\rho V^2 c)$
C_{Na}	Slope of normal force coefficient
C_{nf}	Normal force component from curvature effect
C_p	Power coefficient
C_{PP}	Pressure coefficient
C_T	Torque coefficient
d	Minimum distance between calculation point and vortex filament
D	Turbine diameter
f	Frequency
f'	Separation location
F_l	Lift force
F_d	Drag force
F_n	Normal force component

Symbol	Definition
F_t	Tangential force component
F_{loss}	Tip loss factor
h	Blade length/Blade height
$\mathrm{h_0}$	Non-dimensionalized plunge amplitude
$\mathrm{h(t)}$	Plunge motion
H	Tunnel height
I_s	Turbine system moment of inertia including blades
I_{rig}	Turbine system moment of inertia without blades
I_{arm}	Moment of inertia of turbine support arm
I_t	Moment of inertia of turbine centre shaft
I_c	Moment of inertia of turbine circle plate
J	Inertia
K	Thrust force
K_{ave}	Averaged thrust force
k	Reduced frequency
l	Length of vortex filament
$\dot{m}$	Mass flow rate
m	Blade mass
M	Mach number
n	Number of blades
$N_{\Delta\theta}$	Number of streamtubes
O	Calculation point
P	Power
P_B	Power extracted by blades
P_∞	Power in the free-stream
q_c	Corrected dynamic pressure
q_u	Uncorrected dynamic pressure
R	Turbine radius
R_s	System resistance
S	Blade span
s	Second
St	Strouhal number
S_a	Surface roughness arithmetic mean height
S_p	Surface roughness maximum peak height
S_q	Surface roughness root mean squared height
S_v	Surface roughness maximum valley depth
S_z	Surface roughness maximum height
t	Physical time

Symbol	Definition
t_c	Aerofoil thickness
T	Torque
T_B	Torque generated by blades
T_{res}	Turbine system resistance
T_{ave}	Averaged torque
V	Upstream wind speed
V_a	Induced velocity at upwind
V_a'	Induced velocity at downwind
V_b	Blade velocity
V_R	Apparent wind speed/Relative wind speed at upwind
V_R'	Apparent wind speed/Relative wind speed at downwind
V_w	Wake velocity at upwind
V_w'	Wake velocity at downwind

Greek symbols

Symbol	Definition
α	Angle of attack/Incidence angle
α_c	Corrected incidence angle
α_u	Uncorrected incidence angle
$\Delta\alpha$	Residual correction to incidence angle
α_0	Zero-lift angle of attack
α_1	Angle of attack without pitch angle
$\dot{\alpha}$	Incidence difference between previous and current time step
α_s	Static aerofoil stall angle
α_{ss}	Incidence angle at which the lift slope leaves the linear regime
α_{ref}	Effective angle of attack under dynamic stall effect
α_{pitch}	Pitch component of Darrieus incidence angle
α_{plunge}	Plunge component of Darrieus incidence angle
β	Pitch angle
θ	Azimuth angle
θ_m	Mean angle of attack
θ_0	Pitch amplitude
$\theta(t)$	Pitch motion
λ	Tip speed ratio
σ	Turbine solidity

Symbol	Definition
ρ	Fluid density
ζ	Wavelength
ξ	Angular acceleration/deceleration
ω	Rotational speed
μ	Fluid dynamic viscosity
γ	Prandtl-Glauert factor, $\gamma = \sqrt{1 - M^2}$
γ_0	Nominal angle of attack
ε_s	Solid blockage
ε_w	Wake blockage
ε_{sep}	Blockage from flow separation
Ω	Separation blockage factor
φ	Phase angle between pitch and plunge
δt	Time step
Γ	Circulation of vortex filament
Γ_b	Bound vortex strength
$\emptyset$	Streamtube expansion angle
Φ_p	Phase angle for plunge motion
Φ_θ	Phase angle for pitch motion

Acronyms

Acronym	Definition
VAWTs	Vertical Axis Wind Turbines
HAWTs	Horizontal Axis Wind Turbines
BEM	Blade Element Momentum
CFD	Computational Fluid Dynamics
Re	Reynolds Number
RPM	Revolutions Per Minute
AR	Aspect Ratio
VTM	Vorticity Transport Model
PIV	Particle Image Velocimetry
DMST	Double Multiple Stream Tube
TGS	Turbulence Generation System
FSO	Full Scale Operation
CNC	Computer Numerical Control
CCD	Charge Coupled Device

Chapter 1

Introduction

As the world economy continues to grow, energy demand is likely to increase even if enormous endeavours are made to increase the efficiency of energy use [1]. The urgent need to meet this increasing demand and to reduce greenhouse gas emissions is being met, at least in part, by the development of wind turbines, both onshore and offshore. Nevertheless, as pointed out by Leventhall [2], the development of large-scale onshore wind power can result in wind turbines close to habitation leading to the possibility of noise problems. In this scenario, in addition to the development of offshore wind farms the quest for clean energy is now focused on the local decentralised production of electric power, spread across a wide area, so as to complement the big electric power plants which are located in just a few specific, strategic locations.

One of the most promising local production sources of clean electricity, within the built environment of industrial and residential areas, is small-scale wind turbines. Although these small-scale wind turbines usually have a low power rating, they can help to save power costs, improve a building's energy efficiency [3] and make a significant contribution to the future electricity generation mix [4]. However, winds in the urban area are usually low speed and unsteady with high levels of turbulence for significant proportions of the time, resulting in air flows characterised by rapid changes in speed and direction. Under these circumstances, Vertical Axis Wind Turbines (VAWTs) have been highlighted (e.g. [5, 6]) as more appropriate for urban applications than the more commonly adopted Horizontal Axis Wind Turbines (HAWTs) thanks to several distinct advantages such as insensitivity to wind direction, ease of maintenance, simple blade shape, low cost and low noise.

Since VAWTs are usually reported to suffer from low efficiency compared with their counterpart HAWTs, the most challenging aspect of employing these small machines is to make them self-starting and more efficient in the complex low-wind urban environment. Turbine self-starting capability is defined as the turbine's ability to reach its optimal power-extraction operation condition without any external force and the 'start-up period' is the period that the turbine takes to reach that condition from rest [7]. In the complex low-wind urban environment, the performance of VAWTs is often limited and unsatisfactory as they might fail to accelerate to the point that power can be extracted. Nevertheless if external power sources are required to start-up the

turbine, it brings extra complexity and is detrimental to the public image of the device even though the amount of energy consumed during the turbine start-up period may be low [8].

In this thesis, the emphasis is put on one of the most widely studied VAWT configurations: the H-Darrieus wind turbine. Research studies focus on turbine self-starting capability and overall performance. Although the configuration of the H-Darrieus wind turbine is simple, the aerodynamics is complex since the blades will experience all possible angles of attack during the start-up period. The study of turbine starting behaviour is relatively limited and the literature provides conflicting data and conclusions. Kentfield [9] and Baker [10] identified the presence of a negative torque band between tip speed ratio (λ) ranges from 0.5 to 2 depending on the blade geometry, which prevents self-starting. However recent studies conducted by Hill et al. [11] and Dominy et al. [12] demonstrated the capability of unassisted self-starting of a three-bladed H-Darrieus turbine at low Reynolds numbers. The comprehensive literature review conducted by Worasinchai [7] illustrated that turbine configurations having a high solidity ($\sigma = {}^{nc}/_{R}$) with three blades are reported to be self-starting and this is consistent with Mays and Musgrove's [13] study that longer chord blades (higher solidity, higher Reynolds number) have positive effects on turbine performance. Therefore, the turbine's self-starting behaviour is a key study component in this study and a major objective is to present clear guidelines to answer the question of how to design an H-Darrieus wind turbine that can self-start.

Considerable improvements in understanding and predicting VAWT performance including the critical start-up period can be achieved through the use of BEM (Blade Element Momentum) and CFD (Computational Fluid Dynamics) models. However, since the above two methods have their own advantages and disadvantages (detailed in Chapter 2), both methods were applied in this study to investigate three-bladed H-Darrieus turbine performance. The numerical results demonstrate conclusively the capability of a three-bladed H-Darrieus wind turbine to self-start if appropriate design parameters are adopted including: turbine solidity ($\sigma = {}^{nc}/_{R}$), blade profile and blade pitch angle. These numerical results are used to provide guidance to the experimental design in this study. In turn the experimental measurements validate the simulation results and conclusions and further demonstrate that blade surface roughness also plays a key role in turbine performance. Furthermore, bio-inspired blades with tubercle leading edges are also experimentally tested in this thesis demonstrating considerable improvements in turbine performance especially during the self-starting period.

Besides the experimental measurements of turbine self-starting behaviour and power output, a brand new technique using the on-board pressure measurement is also employed in this study to examine the instantaneous blade pressure distribution and its variation when the turbine is rotating. The blade dynamic stall, laminar separation bubble and flow curvature are clearly recorded by the on-board pressure measurement system. To the authors' knowledge, this is the first time that this kind of time-accurate technique has been used to study VAWTs.

This thesis advances the state of the art of understanding of the operation of the H-Darrieus wind turbine and examines various design parameters that may influence turbine performance using both numerical and experimental methods. It provides comprehensive and convincing guidance for designing an H-Darrieus wind turbine that can self-start. The main purposes of this thesis are summarised as follow:

I. Provide a comprehensive dataset for studying the performance of typical, small-scale Darrieus wind turbine blades, which mainly operate at relatively low Reynolds numbers and experience extreme angles of attack particularly during turbine start-up period.
II. Model and investigate the performance of three-bladed H-Darrieus wind turbines under different wind and geometrical conditions using both CFD and BEM methods.
III. Experimentally investigate the effects of various design parameters on the three-bladed H-Darrieus wind turbine self-starting behaviour and power output.
IV. Present the preferred turbine design parameters with respect to the small-scale H-Darrieus wind turbine achieving self-starting capability and good overall performance.
V. Provide better understanding about the flow around the turbine blades and the associated aerodynamics based on instantaneous on-board pressure measurements.
VI. Propose and test a new bio-inspired blade geometry which can enhance turbine self-starting capability and over-all performance.

The thesis is structured into the following seven chapters:

Chapter 1 – Introduction

This chapter

Chapter 2 – Literature review

Literature relevant to this study of H-Darrieus wind turbines is reviewed including: turbine self-starting behaviour, turbine design parameters, turbine blade aerodynamic dataset and different numerical models.

Chapter 3 – Computational Fluid Dynamics (CFD) model description and validation

The 2-D aerofoil/blade model and the 2-D H-Darrieus wind turbine model are created in this chapter. Both models are validated by comparing the predicted results with those measured by experiments.

Chapter 4 – Computational Fluid Dynamics (CFD) study results

Aerofoil/blade static lift and drag forces are predicted by the validated 2-D CFD model in this chapter to examine the capability of CFD models in predicting blade performance in the deep-stall region. The validated 2-D H-Darrieus machine model is then used to examine the effects of different design parameters on the turbine performance especially at low tip speed ratios. The simulation results are used to guide the design of experimental tests.

Chapter 5 – Blade Element Momentum (BEM) based approaches in this study

A BEM based model, the Start-Up model, is used in this chapter to examine the turbine dynamic start-up process which cannot be predicted by the CFD model. Simulation results are used to guide the design of experimental tests. Moreover, another BEM based model, the double multiple streamtube model (DMST) is built to investigate the sensitivity of the BEM based model to the quality of the input aerodynamic dataset. Based on the DMST sensitivity study, a bio-inspired blade with tubercle leading edge is also proposed and tested experimentally in this thesis.

Chapter 6 – Experimental methods

This chapter describes all the experimental facilities and techniques employed in this thesis. Data post-processing methods and results uncertainties are also detailed.

Chapter 7 – Experimental results

Comprehensive aerofoil/blade static wind tunnel measurements at low Reynolds numbers are presented in this chapter. The associated flow behaviour is also examined and illustrated.

The effects of various design parameters on the H-Darrieus wind turbine performance are investigated and the results are presented.

The instantaneous pressure measurement obtained by using an on-board pressure measurement system is also presented in this chapter.

Chapter 8 – Bio-inspired blades with tubercle leading edges

The bio-inspired blades with tubercle leading edges are studied in this chapter. Both BEM results and experimental results are presented here.

Chapter 9 – Conclusion

Conclusions and recommendations for future work are presented in this chapter. Significant and original contributions from this thesis are also outlined.

Kinematics of the H-Darrieus VAWT

Although the complicated rotor aerodynamics makes the H-Darrieus turbine difficult to analyse, a simplified kinematic approach in 2-D will help to clarify its behaviour and identify the governing parameters. The aerodynamics are dependent on the kinematics and in turn the kinematics of the turbine also influence the flow physics as well as determining the performance efficiency. Therefore, the theory that defines the parameters involved in the geometry of motion and their interrelationship with respect to the blade forces must be understood. Discussions are made in terms of Reynolds number, apparent wind, incidence angle, tip speed ratio, torque and power.

The Reynolds number influences the performance of turbine blades and is defined based on apparent wind speed (V_R) in this thesis as shown in Equation 1.1:

$$Re = \frac{c\rho V_R}{\mu} \qquad \text{Equation 1.1}$$

where ρ is air density, c is the blade chord length and μ is air dynamic viscosity.

Equation 1.2 defines tip speed ratio (λ):

$$\lambda = \frac{V_b}{V} = \frac{\omega R}{V} \qquad \text{Equation 1.2}$$

where V is free stream wind speed, V_b is blade velocity, ω is turbine rotational velocity and R is turbine radius.

As the turbine rotates the blades experience a large and rapid change in angle of attack (α). The α changes with the blade's azimuth angle (θ) and also with the λ as the blade travels around a cycle. During a single revolution the blades may operate in both stalled and unstalled conditions, and encounter their own wakes and the wakes of other blades and the shaft. A schematic diagram is presented in Figure 1.1 in order to

illustrate the velocity and force vector acting on the blades of a VAWT rotating at a constant rotational velocity (ω). The vector addition of upstream wind (V) and the blade velocity (V_b) establishes a relative resultant flow velocity (V_R) which is seen by the blades.

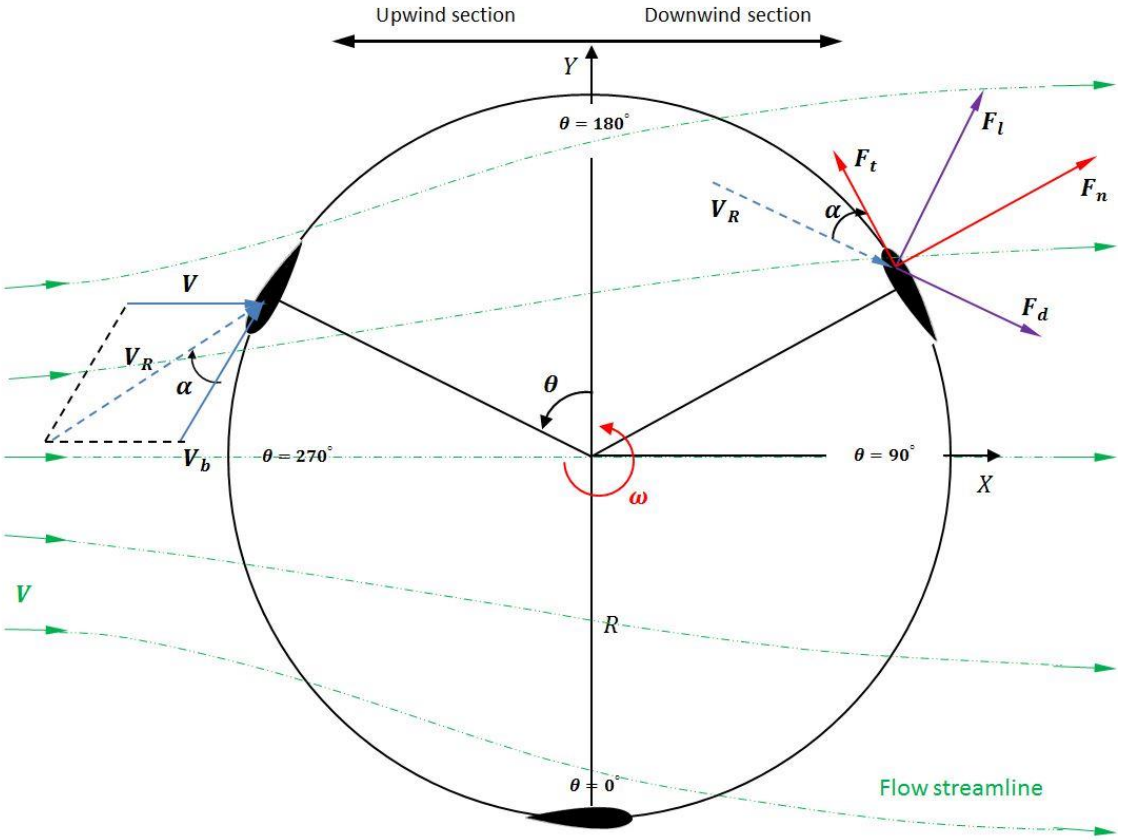

Figure 1.1 Schematic drawing of velocity and force vector for the H-Darrieus wind turbine at certain rotational speed with definition of the upwind and downwind parts of the rotation

Ignoring the rotor effects on the incoming upstream flow and assuming the induction factor to be zero, the instantaneous resultant wind speed (V_R) and angle of attack (α) that the blade experiences can be calculated from the Equation 1.3 and Equation 1.4 respectively:

$$V_R = V \times \sqrt{\lambda^2 - 2\lambda cos\theta + 1} \qquad \text{Equation 1.3}$$

$$\alpha = tan^{-1}\frac{sin\theta}{\lambda - cos\theta} \qquad \text{Equation 1.4}$$

Figure 1.2 (a) shows that the variations of the resultant wind is periodic and has a maximum value at the azimuth angle of 180° when the blade moves windward and a minimum value at 0° when the blade moves away from the incoming flow. At $\lambda = 1$,

the resultant speed becomes zero at an azimuth angle of 0°. With regard to incidence angle, it can be seen (Figure 1.2 (b)) that the incidence variation is large and strongly dependent on the tip speed ratio. The resultant variation in α represents a skewed sinusoid, the amplitude and skewness of which reduces with the increase of λ. For $\lambda < 1$, the change of α roughly follows a cotangent curve while for λ beyond the unity tip speed ratio, the variation follows a sine-like curve but it is not perfectly sinusoidal suggesting that the motion can be decomposed into plunge and pitch components [14].

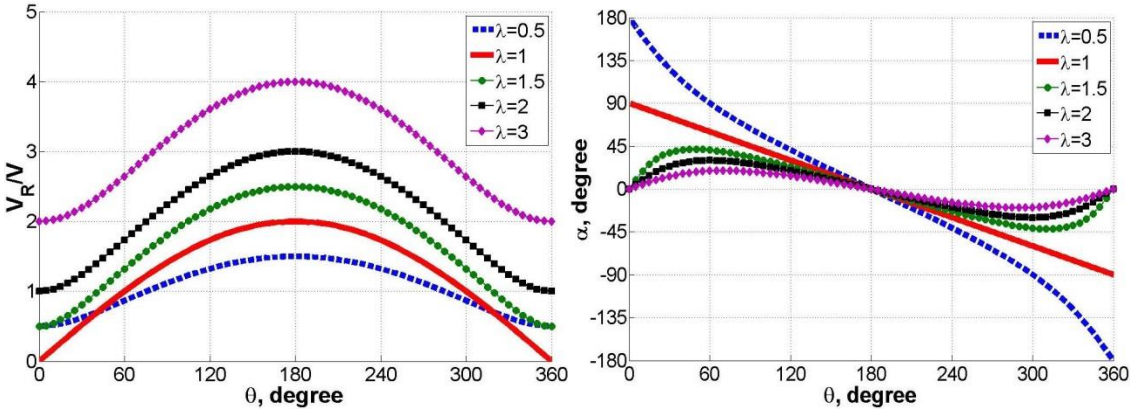

(a) (b)

Figure 1.2 (a) Calculation of ratio of resultant wind speed to free stream and (b) angle of attack variation against azimuth angle

According to Worasinchai et al.'s study [14], this non-pure sine-like curve is due to the translational speed that the aerofoil experiences when moving along its rotational path, which results in the aerofoil apparently experiencing a plunge movement making the Darrieus blades operate with a combined pitch and plunge motion. The pitch and plunge component can be decomposed and calculated based on Equation 1.5 and Equation 1.6. An example of combined pitch and plunge motion is presented in Figure 1.3

$$\alpha_{pitch} = tan^{-1}(\frac{sin\theta}{\lambda}) \qquad \text{Equation 1.5}$$

$$\alpha_{plunge} = tan^{-1}(\frac{sin\theta cos\theta}{\lambda^2 - \lambda cos\theta + sin^2\theta}) \qquad \text{Equation 1.6}$$

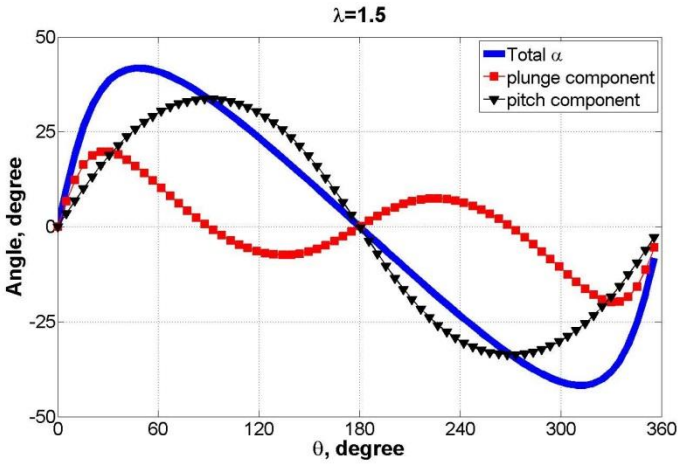

Figure 1.3 Example of combined pitch and plunge motion of H-Darrieus turbine

As the blades rotate the flow incidence on the blades causes the generation of aerodynamic forces of lift (F_l) and drag (F_d), which vary with the change in the blade's azimuth position and with λ. The blade generated aerodynamic forces are usually resolved into the normal force component (F_n) which is important in structural consideration and the tangential force component (F_t). F_t acts at a radius, R, creating a torque, T (Equation 1.7), about the rotation axis which actually causes the turbine to rotate and produce power (P). From the sign convention in Figure 1.1, the blade's normal and tangential force can be inferred and defined in Equation 1.8 and Equation 1.9 respectively:

$$T = F_t R \qquad \text{Equation 1.7}$$

$$F_n = F_l cos\alpha + F_d sin\alpha \qquad \text{Equation 1.8}$$

$$F_t = F_l sin\alpha - F_d cos\alpha \qquad \text{Equation 1.9}$$

The contribution of the aerodynamic moment to torque, which depends on the chord-wise mounting position of the blade, is usually ignored as it is small and has opposing effects in the upwind and downwind parts of the rotation. In terms of turbine efficiency, it is usually expressed as power coefficient (C_p, shown in Equation 1.10), which determines how much power the VAWT can extract from the available power in the free stream by the ratio of the blade power (P_B) across the swept frontal area of the VAWT to the wind power (P_∞). For an H-Darrieus VAWT, the swept frontal area is $A = Rh$, where h is the blade's length.

$$C_p = \frac{P_B}{P_\infty} \qquad \text{Equation 1.10}$$

where for an n bladed machine

$$P_B = n\omega \int_0^{2\pi} T(\theta) d\theta \qquad \text{Equation 1.11}$$

From the above simplified kinematic description of H-Darrieus VAWTs, some important observations can be revealed:

1. As the resultant speed that is experienced by the blades varies throughout the rotation (Figure 1.2 (a)), so does the blade Reynolds number. To allow a simple comparison between different VAWTs, it is common to use the resultant speed based Reynolds number (defined in Equation 1.1) rather than the upstream wind speed based Reynolds number.
2. From the turbine performance point of view, F_n has no contribution and is beyond the scope of the investigation presented in this thesis. Nevertheless, it should be observed that except at very small λ the F_n is usually much larger than F_t. Therefore both forces must be considered during the design stage.
3. A detailed study from the kinematics of the turbine reveals that although the Darrieus turbine is categorised as a lift-driven machine, the turbine operates as a 'combined lift- and drag-driven machine' at $\lambda < 1$, and only when the $\lambda > 1$ does the turbine begin to change its mode to a pure 'lift-driven' machine.
4. At high tip speed ratios, according to Equation 1.9 the tangential resolution of the lift and drag forces shows that the blade is very sensitive to the drag force contribution, for example when $\lambda > 2$ the maximum α is lower than 30°. As a result, it is usually the case that a drop of drag would yield a lager improvement in the torque than the same amount of increase in lift. However, since the drag also contributes to the torque at $\lambda < 1$, a low drag aerofoil may not be absolutely better than a relatively large drag aerofoil considering the turbine self-starting capability.

The kinematics of the Darrieus turbine have been explained in the simple analysis above. One simplification that is made is that the rotor effect on the freestream wind is not considered. The rotor presence in the freestream affects the actual wind velocity seen by the blades, especially for the downstream part of the rotation where the flow velocity may be significantly lower than the upstream due to the energy extraction of the upwind part of the rotation. Meanwhile due to the vortex shedding from the blades in the upwind and turbulent wake from the shaft, the resultant angle of attack might be different to that predicted in the simplified analysis above making the machine performance vary significantly relative to predicted results.

Chapter 2

Literature review

Due to the inherent advantages Vertical Axis Wind Turbines (VAWTs) have over Horizontal Axis Wind Turbines (HAWTs), VAWTs have attracted increasing research interest. This chapter reviews the literature pertaining to the study of VAWTs in this thesis. The main topics surveyed are different types of wind turbines, the advantages and disadvantages of VAWTs, H-Darrieus wind turbine self-starting behaviour, H-Darrieus wind turbine design considerations, analytical models and CFD models. It also explains the motivation behind this research and shows its technical and social significance.

2.1 Different types of wind turbines

Wind turbines can be broadly classified into drag-type and lift-type machines. Lift-type wind turbines are again broadly classified into HAWTs and VAWTs. The most common example is the modern three-bladed HAWT shown in Figure 2.1(a), which generates torque, T, through aerodynamic lift that is generated by the blades, implying that their blades generally travel at a velocity of many times the wind speed. The designation horizontal axis means that the axis of rotation lies parallel to the incoming wind vector, V. Due to its high power coefficient compared to VAWTs, this configuration nowadays dominates in the field of large-scale wind power generation both on land and in the sea. Nevertheless, the disadvantages of HAWTs include the requirement of a yaw mechanism to turn the rotor towards the wind, poor performance in urban environment where the flow is highly unsteady and difficult maintenance. Other iconic examples of HAWTs are the traditional Dutch windmill and the American-style wind pump shown in Figure 2.1(b) and Figure 2.1(c), respectively.

With respect to the Vertical Axis Wind Turbine, which is the main focus of this research, the rotor rotates perpendicular to the direction of the wind instead of parallel. This allows the device to capture energy from every wind direction. The performance of the wind turbine is the main concern in the design stage. It is argued that vertical axis wind turbines could play a significant part in the provision of power supplies. The Sandia National Laboratories of the Department of Energy in the USA, the National Research Council of Canada, and Reading University in the UK performed the first large-scale research on VAWTs in the late 1970s and 1980s [15-20].

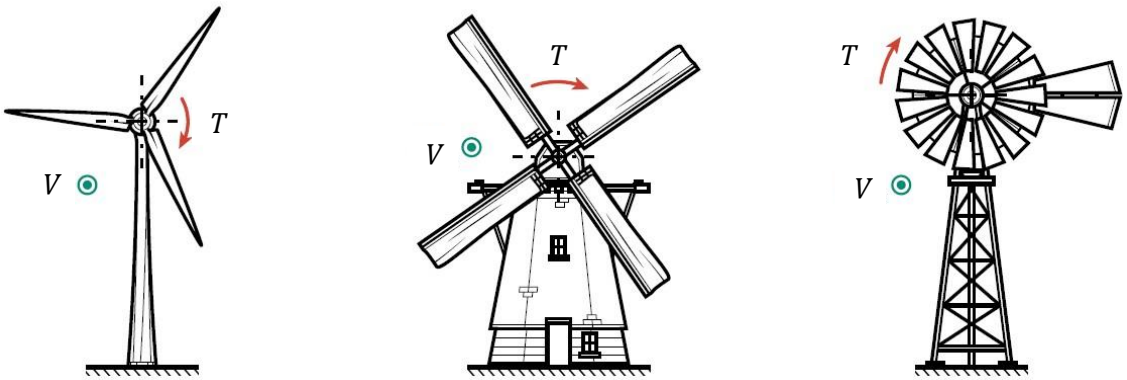

(a) Morden HAWT (b) Dutch windmill (c) Wind pump

Figure 2.1 Typical horizontal axis wind turbine configurations [8]

The most well-known lift-driven VAWT is the Darrieus machine, which is named after the French aeronautical engineer Georges Jean Marie Darrieus (1888-1979) who patented the design in 1931 (as shown in Figure 2.2 (a) and (b)). This wind turbine consists of a set of vertically orientated aerofoils connected to a rotating shaft, and is characterised by its C-shape or H-shape rotor blades. It is normally built with two or three blades and previous experimental measurements have demonstrated that the lift-driven Darrieus machine can produce a maximum power coefficient of around **0.4** [15, 16], which is much higher than that obtained from the drag-driven Savonius VAWT (power coefficient of about **0.3** [21, 22]) shown in Figure 2.2 (c). Previous studies claimed that the Darrieus machine typically develops little or no torque at low speed and is inherently non-self-starting [9, 10], which indicate motors are required to 'speed it up' making the machine inefficient and unsuitable for stand-alone operation. However, recent studies [11, 12] demonstrated conclusively the capability of three-bladed H-Darrieus turbines to self-start based on a careful aerofoil selection.

Due to the conflicting data and conclusions in the literature with regard to the self-starting capability of the Darrieus turbine, this thesis focuses on the aerodynamics and performance of the three-bladed H-Darrieus VAWTs. Numerical and experimental tests were carried out in order to reveal the flow structures of the turbine during the start-up period and examine the design parameters that affect the turbine's self-starting capability. The key objective and motivation of this thesis is to provide a clear answer to the questions of under what conditions the H-Darrieus wind turbine can self-start and how to design an H-Darrieus wind turbine that will self-start.

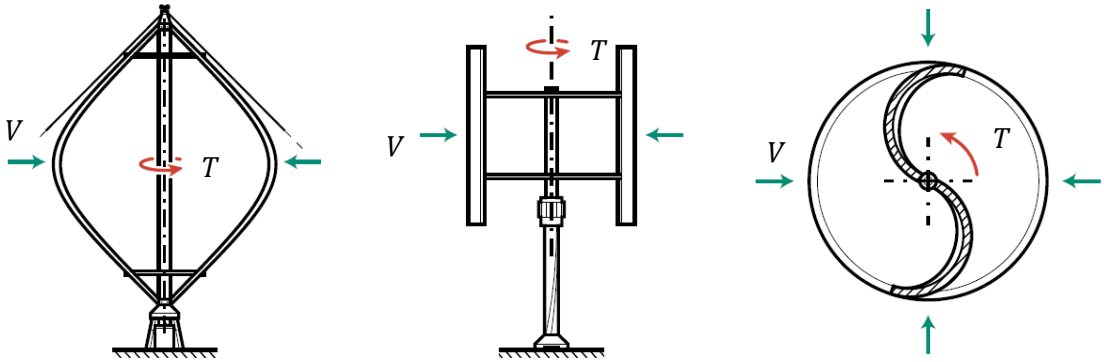

(a) C-type Darrieus (b) H-type Darrieus (c) Savonius

Figure 2.2 (a) and (b) Lift-driven Darrieus wind turbine and (c) Drag-driven Savonius VAWT [8]

2.2 Advantages and disadvantages of VAWTs compared to HAWTs

It has not been proven beyond doubt that HAWTs are better than VAWTs in terms of maximum performance when compared on an equal scale. However, with the inherent advantages the VAWTs have over the HAWTs, the VAWTs have attracted increasing research interests in recent times. The advantages of the three-bladed H-Darrieus VAWT over the more established HAWT, especially when used in the built environments, are as follows:

- VAWTs do not need a complex yaw mechanism since they rotate in a plane parallel to the wind direction and the blades are attached to the rotor at equally spaced angles of 120° for the three-bladed machines. Therefore VAWTs are insensitive to wind direction whereas the vertical plane of the conventional upwind HAWT's blades must be perpendicular to the wind stream direction. Consequently, there is no loss of performance due to turning the turbine towards the wind or misalignment of the turbine axis with the wind direction. Yawing is a problem especially with large horizontal turbines which have high inertia, and in the built environment where the wind direction changes suddenly (uneven terrain or eddying around buildings) and the yawing mechanism is often unable to track changes quickly enough.
- VAWTs are well suited to drive a vertical transmission shaft to ground level so the heavy transmission system, gear box, generator and control box could easily be situated at or below ground level allowing easy installation, operation and maintenance. Meanwhile, sound insulation can also easily be provided to

minimise mechanical nose nuisance in the surrounding area. In contrast, the HAWT's drive system is mounted on a column tower high above the ground.

- Optimal blades for VAWTs are fairly simple in design, being an aerofoil of constant shape along its span without twist or taper. This simple design makes the blades relatively easy to manufacture by extrusion, pultrusion or fabrication [23]. Optimal blades for HAWTs, on the other hand, are twisted and tapered from the root to the blade tips (since the speed of a blade element will differ according to the distance from the hub) in order to achieve better performance. These complex blades, which are usually of many meters in length, results in manufacturing and transportation that is far more complicated and expensive.
- Aerodynamic noise from the VAWTs is lower due to lower tip speed ratio for optimal operation. HAWTs achieve their maximum power at relatively higher λ and produce loud noise. As wind turbine numbers increase, noise is emerging as one of the main objections to onshore wind turbines/farms and so this point may be important although it could be argued that HAWTs could be designed to operate efficiently at lower λ with reduced noise levels.
- VAWTs achieve better performance in complex urban wind environment [24] where the wind is low speed and unsteady with high levels of turbulence for significant proportions of the time. By comparison, HAWTs suffer from a power decrease in skewed flow [24]. This makes the VAWTs suitable in areas where tall devices are prohibited by planning permission and law [25].
- Recent studies [26, 27] show that VAWTs can be installed much closer to each other compared to horizontal-axis turbines, so that the power density per square meter could be considerably higher than for the configurations used presently. This could lead to smaller wind farm arrays and reassessment of VAWTs.
- VAWTs are normally designed in such a way that centrifugal loads are balanced. However, for HAWTs the bending moments at the roots of the blades due to their own weight may be high when the blades are near horizontal.

VAWTs also present some disadvantages when compared to HAWTs:

- The flow around the VAWT is highly unsteady due to the changes of azimuth angle and angle of attack. The turbine blades will experience all possible angles of attack during operation and this presents a complex aerodynamics problem which is not fully understood.
- VAWTs are usually constructed and placed close to ground level resulting in them being less accessible to higher wind speeds that occur at higher altitude.

Therefore for the same rotor size (swept area) and weight, the power output of VAWTs is less than that of comparable HAWTs.

- Torque and power generated by VAWTs fluctuate in a cyclic manner during each revolution as the blades move in and out of the wind and the aerodynamic force on the blades varies with the azimuth angle. This cyclic blade loading could lead to blade fatigue [28] and resonance issues which should be considered in the design stage. However, it is argued that the generation of a pulse each time the blade of a HAWT passes its tower also presents a big issue.
- Straight VAWT blades are subjected to a bending moment due to centripetal acceleration, which presents a serious problem especially for small turbines [23].
- Darrieus VAWTs may fail to self-start even under no-load conditions, depending on the characteristics of the aerofoils used, the upstream wind speed and turbine solidity. HAWTs are inherently self-starting under no-load conditions.

2.3 The H-Darrieus turbine critical self-starting behaviour

Self-starting needs to be defined carefully. A Darrieus turbine, although it is able to produce a small amount of forward torque when stationary, creates a net torque per revolution which drops below zero under certain circumstances over a range of λ from about 0.5 to 2 depending on blade geometry. This region of negative net torque is described as the 'dead band' by Baker [10]. According to his study, a turbine with this characteristic may just start but will not generally accelerate through the 'dead band' to its optimum working speed only if the wind suddenly drops while the rotor inertia maintains its rotational speed can the tip speed ratio reach a value that is sufficient to drive the machine to working speed.

A review of previous research into the operation of vertical-axis turbines reveals inconsistency in the use of terminology and in particular the definition of self-starting. Ebert and Wood [29] define the starting process as having been completed when significant power extraction commences, whereas Kirke [23] adopts a similar definition in which a turbine is considered to be self-starting only if it can accelerate from rest to the point where it starts to produce useful output. In both cases, the definition of terms 'significant power' and 'useful output' are themselves imprecise. Others (e.g. Lunt [30]) adopt a more specific definition by which a turbine is deemed to have started if the rotor has accelerated from rest to a steady speed that exceeds the wind speed arguing that for this to occur significant lift must be produced during the rotational cycle.

Although more precise, this definition also has its limitations. In particular, there is evidence that reaching the point at which the blades begin to produce lift over a significant part of a revolution does not guarantee that the machine will to continue to accelerate. In this thesis, the turbine is deemed to be self-starting only if the machine is able to reach its optimal power-extraction operation condition from rest without any external force. Meanwhile the 'start-up period' is the period that the turbine takes to self-start.

According to Worasinchai's review [31] of Darrieus turbines, most previous experimental tests were conducted in terms of peak power-extraction performance. Very few investigations focused upon the turbine self-starting behaviour. To the best of the authors' knowledge, there exist only three experimental studies that provide starting behaviour in a time-varying format: tests performed by Chua [32], Hill el al. [11] and Dumitrescu et al. [33]. Table 2.1 summaries the parameters used for these studies.

Configuration	Chua	Hill et al.	Dumitrescu et al.
Number of blades	3	3	3
Aerofoil	NACA0015	NACA0018	NACA0018
Chord length (m)	0.07	0.083	0.08
Blade pan (m)	0.5	0.6	0.3
Turbine radius (m)	0.25	0.375	0.25
Solidity	0.84	0.664	0.96
Inertia ($kg.m^2$)	0.015	0.018	N/A
Aspect ratio	7.143	7.229	3.75
Wind speed (m/s)	~5	6	11.7
Self-start or not	Yes	Yes	Yes

Table 2.1 Summary of parameters for Darrieus self-starting behaviour studies in the literature

In Chua's test [32], a set of three fans was employed to provide an airflow to the turbine. The shaft of the unloaded rotor was fitted with reflective tape which, together with a tachometer, was used to measure the turbine rotational speed. It is observed from his measurement (Figure 2.3(a)) that the rotor had a relatively high initial acceleration rate for approximately 30 s. After that the increase of rotor speed fell to a steady rate. The rotor continued spinning at this steady rate until about 160 s when the turbine experienced another high speed acceleration to its final tip speed ratio of 3.2 after around 200 s. The torque curve as shown in Figure 2.3(b) is consistent with the observation for turbine acceleration. At the beginning the torque coefficient is relatively large indicating a fast increase of turbine speed. However only a very small

net toque is generated by the blades for the tip speed ratio range from 0.5 to 1.5, which is consistent with the slower pace of acceleration. Beyond $\lambda = 1.5$ the torque increases quickly resulting in fast turbine acceleration starting at around $150\,\mathrm{s}$ as shown in Figure 2.3(a).

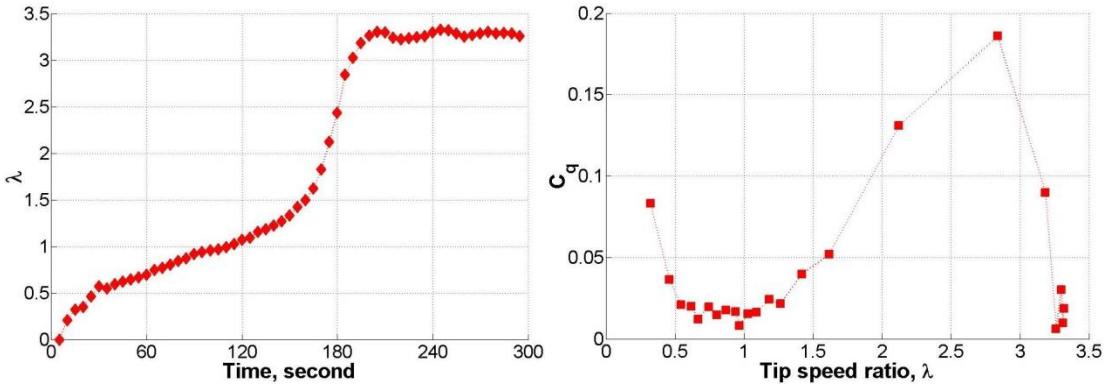

(a) rotor speed (b) torque coefficient

Figure 2.3 H-Darrieus wind turbine performance from Chua's test [32]. (a) Tip speed ratio against time (b) Torque coefficient against tip speed ratio.

Turbine starting behaviour was further investigated by Hill et al. [11]. In their experimental tests, a three-bladed H-Darrieus machine equipped with NACA0018 was tested in a $2\,\mathrm{m}^2$ wind tunnel. The turbine rotor was held stationary until the wind tunnel's speed had stabilized at its predetermined value. The release of the rotor triggered the start of the data capture process. Each trial began from a random starting position and it was found the angular position had no discernible effect on behaviour, which is consistent with Dominy et al.'s study [12] that a three-bladed rotor will self-start irrespective of its starting position. Their wind tunnel testing of this three-blade turbine with no load demonstrated a repeatable starting characteristic thus confirming that, contrary to much of the available literature, a Darrieus turbine using symmetrical aerofoils can reliably self-start in a steady airflow.

There are four main processes taking place during the start-up period according to Hill el al. [11] (Figure 2.4). The first stage is an approximately linear acceleration from rest, followed by a plateau stage where the increase of turbine rotational speed becomes very slow. When the tip speed ratio gradually increases to about 1.5 the rotor then accelerates rapidly to its maximum speed of $\lambda \approx 3$ and enters its steady operating stage. It is observed that Hill et al.'s test is in good qualitative agreement with Chua's tests.

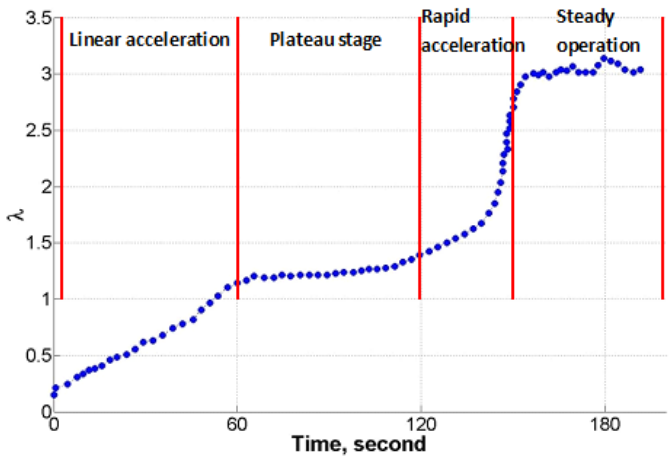

Figure 2.4 Measured H-Darrieus turbine starting behaviour from Hill et al [11].

More recently, Dumitrescu et al. [33] also examined the performance of an H-Darrieus wind turbine including the critical starting period. The turbine rotor comprised of two vertically arranged stages. A total of six blades, three in each stage, formed the basic configuration of the rotor. Each stage contained three straight blades arranged symmetrically at 120 degree-angle. The rotor stages were separated by circular endplates where each blade was hinged. The blades could be arranged at $0, 3, 6,$ or 9 degrees setting (pitch) angles.

According to their measurement (Figure 2.5), the two-stage H-Darrieus turbine with 3° blade pitch experiences a small linear acceleration from rest which is followed by a higher acceleration and finally reaches a constant rotational velocity of 650 RPM. Although the entire curve looks similar to that measured by Hill et al. [11] and the author claims that the turbine has self-starting capabilities, a detailed examination found this two-stage turbine only reaches a tip speed ratio of approximately 1.4.

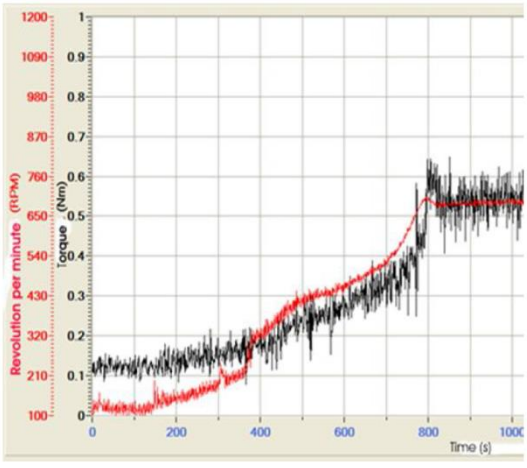

Figure 2.5 Measured H-Darrieus turbine starting behaviour from Dumitrescu et al [33]

All in all, the literature review demonstrates that there are only a limited number of studies and few data available with respect to turbine self-starting behaviour. The complex aerodynamics and flow structures experienced by the turbine blades are not fully understood during the start-up period. Therefore studies presented in this thesis will shed some light on the problem in order to provide better understanding of the turbine.

2.4 Darrieus turbine design considerations

In order to anticipate the performance of Darrieus wind turbines, many design parameters that influence the turbine should be thoroughly understood. However this is not an easy and straight forward process since one variable usually has more than one effect on performance. For example, increasing the blade chord length c will increase the c/R ratio which has an effect on the turbine solidity σ. Meanwhile the flow curvature and blade Reynolds number will also be modified. This section reviews the current state of understanding of the main design considerations that will influence turbine performance based on experimental studies and numerical simulations from the literature.

2.4.1 Turbine solidity

Solidity has a strong influence on turbine performance affecting C_p variation with λ and the maximum efficiency. The solidity of an H-Darrieus wind turbine is a measure of ratio of blade area to turbine swept area and is defined in Equation 2.1 (it is noted that there is another definition of $\sigma = \frac{nc}{2R}$, which appears to be less common in the literature and will not be used in this thesis).

$$\sigma = \frac{nc}{R} \qquad \text{Equation 2.1}$$

Templin [17] seems to be the first author in the literature to investigate VAWT solidity. He developed a computational programme (single stream tube model) to test the theoretical effects of blade solidity as a geometric variable within a range of $\sigma = 0.05$ to 0.5 inclusive. Moreover Mays and Holmes [34] also employed a momentum model to study the effects of high solidity on the performance of vertical axis windmills. The above two study results were compiled and compared by Kirke [23] as shown in Figure 2.6. Increasing the solidity will result in greater blockage of the flow, causing a change in the incoming flow velocities and blade angles of attack. Higher blockage

results in lower angles of attack in the upstream half of the rotor which means that the λ at which the blades no longer stall decreases to a lower value. This tends to move the peak power coefficient to lower λ, but the continued drop in angle of attack as λ increases means that the aerodynamic torque generated is less than that for a lower solidity rotor at high λ. Moreover, the efficiency of high solidity machines drops away quickly either side of the optimum λ while the $C_p - \lambda$ curve is flatter for low solidity machines.

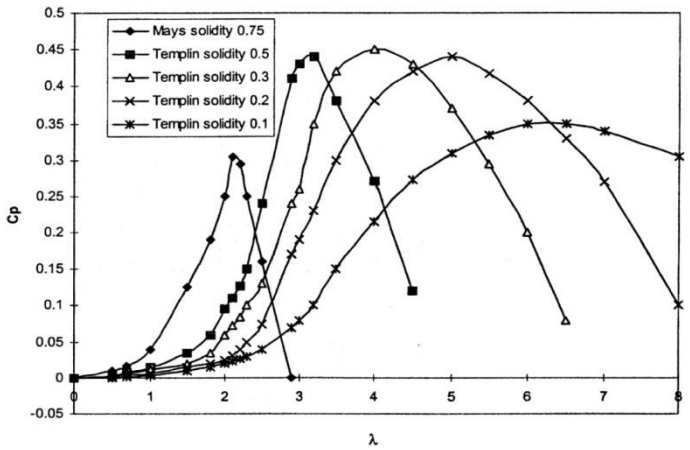

Figure 2.6 Curve for VAWTs under different solidities from Kirke's study[23]

One way to alter solidity is to change the number of blades (n) keeping the c and R constant, and in doing so the curvature and blade Reynolds number remain the same between cases. Consul el al. [35] used a two-dimensional CFD model to numerically simulate two-bladed and four-bladed VAWTs using a NACA0015 profile. The corresponding solidity was $\sigma = 0.019$ and $\sigma = 0.038$. From their study, as shown in Figure 2.7, the maximum power coefficient increased from 0.43 to 0.53 as a result of the increase in the number of blades from two to four. Meanwhile the entire performance curve of the higher solidity machine is shifted to the left hence attaining the maximum power coefficient at $\lambda = 4$ while the smaller solidity machine attained maximum power coefficient at $\lambda = 6$. Consul et al. [35] state the turbine power output is proportional to the thrust that the turbine exerts on the flow. The larger the thrust the larger the flow impedance and hence the lower flow velocity and energy flux through the turbine, which also influences the variation of blade angle of attack.

The four-bladed turbine is found to present a larger impedance, resulting in a reduction in streamwise velocity between the lower and higher solidity configurations of between 14% and 26% depending on the tip speed ratio [35]. The effect of impedance on C_p depends on λ. At high λ, an increase in solidity leads to higher impedance,

resulting in a decrease in power as α is low and a higher impedance reduces it further, leading to reduced lift and torque. Lift is further reduced by the reduction in the flow velocity from the increased impedance. At low λ, increasing solidity increases the VAWT power, as a low solidity device may experience significant stall at low λ, whilst a higher solidity turbine may not due to decreased streamwise velocity. Consul et al.'s study and assertions are consistent with previous experimental [36, 37] and computational studies [38].

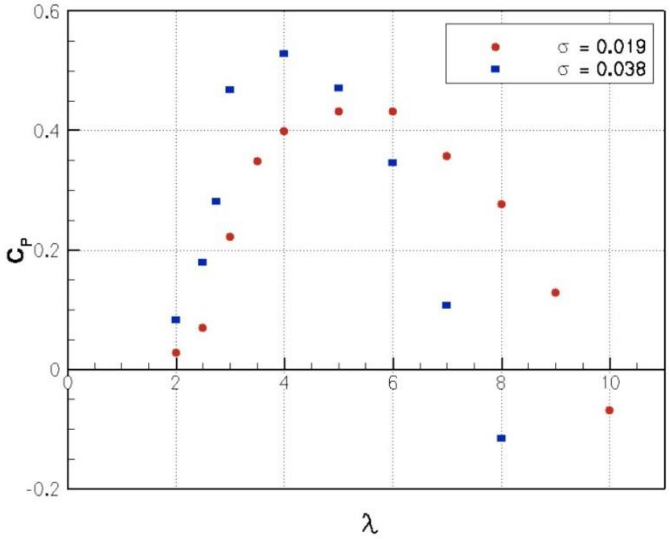

Figure 2.7 Curve for two- and four-bladed turbine from Consul et al.[35]

More recently, Howell et al. [39] pointed out the importance of solidity in determining the rotational velocity at which the turbine reaches its maximum performance coefficient and they conducted an experimental study on the performance of small two- and three-bladed H-Darrieus wind turbines. They demonstrated experimentally that the two-bladed VAWT attained a higher C_p at a higher tip speed ratio, while the three-bladed VAWT attained lower C_p at a lower tip speed ratio. Furthermore Castelli et al. [40] also studied the effect of blade number on a straight-bladed vertical-axis Darrieus Wind Turbine. Three-, four- and five-bladed H-Darrieus turbines with NACA0015 profiles were compared in a 2-D CFD model. As shown in Figure 2.8, the results illustrate that the peak power coefficient lowers with the increase of rotor solidity which means that a larger number of blades allows attainment of maximum power coefficient for lower angular speeds, but is penalized as far as efficiency is concerned.

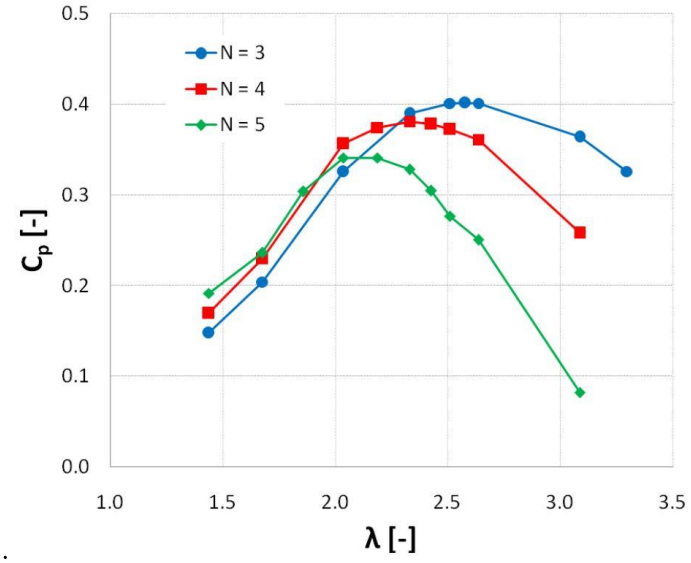

Figure 2.8 Curve for three-, four- and five-bladed turbine from Castelli et al.[40]

Although low solidity turbines enjoy a relatively large power output for a large range of λ as can be seen in Figure 2.6 ($C_p - \lambda$ curve is flatter) making it less sensitive to sudden changes in wind speed, the associated low power produced at low tip speed ratios is always a problem for stand-alone application (self-starting required) which is the main concern of this thesis. Although it was pointed out by Kirke [23] that a load disengaging device could be employed in order to avoid any resistance from the generator, too low solidity means the blade would not be effective in generating an unsteady force and this small force is not sufficient to bring the turbine from the 'dead band' back to the region that it could generate force again [31]. It is argued that the advantage of a turbine with higher peak C_p will be cancelled out if the turbine cannot self-start (or requires external power to start-up) in built environments under complex wind conditions.

Musgrove and Mays [41], Mays and Holmes [34] and Simhan [42] had suggested increasing VAWT solidity in order to produce a relatively large starting torque. In Musgrove and Mays' study [41] a VAWT with $\sigma = 0.6$ and aspect ratio $AR = 4$ demonstrated significant torque throughout the 'dead band' region, unlike an earlier turbine with $\sigma = 0.17$ and high blade AR. The improved self-starting ability of the later turbine was ascribed to 'increased solidity and reduced aspect ratio'. Although later corrected by Kirke [23] in that low AR actually reduces starting torque, the increase of solidity improved turbine self-starting capability. Furthermore Mays and Holmes' study [34] also claimed that a 'useful starting torque' was generated for turbines with high solidity.

Both Simhan [42] and Kirke and Lazauskas [43] performed studies by increasing c so as to increase σ based on theoretical analysis. The results suggested that increasing c increases the non-dimensional starting torque coefficient because the blade Reynolds number is increased leading to better blade performance and blade area is increased, resulting in more aerodynamic force generated on a stationary blade.

From the above literature review of turbine solidity, it is observed that most studies about the effect of solidity on turbine performance (e.g. [35-37, 40, 44, 45]) are concerned only with the turbine peak power output, and hence the measurements and simulations are only conducted at relatively larger tip speed ratios (typically $\lambda > 2$). Limited analytical studies indicate that a turbine with higher solidity can produce more power (torque) at small λ, which is beneficial to turbine self-starting capability. Furthermore, although Simhan [42] and Kirke and Lazauskas [43] noted that increasing c will result in more force being generated, system inertia is also increased with bigger blades. Therefore, whether increasing c can really improve turbine self-starting behaviour and reduce self-starting time needs to be further tested by experiments.

In order to fill the gaps in our knowledge, H-Darrieus wind turbine performance under different solidities is examined numerically and experimentally in this thesis. Studies focus on turbine behaviour at low tip speed ratios and how the solidities affect turbine self-starting capabilities. Moreover, for a given turbine solidity the way in which different combinations of blade chord length (c) and rotor radius (R) influence turbine self-starting capability and overall performance are also investigated.

2.4.2 Number of blades

As noted by Kirke [23], the power produced by a wind turbine depends primarily on wind velocity and the swept area, not on the blade area. Therefore a single blade machine is, in theory, potentially as efficient as turbines with two or three blades, in terms of the percentage of kinetic energy extracted and converted to shaft power. In principle a single blade turbine could be built with a counterweight in order to balance the mass of the single blade, but this counterweight would generate parasitic drag. Moreover the forward torque cannot be produced by the only blade at the majority of azimuth angles, resulting in the turbine fail to self-start.

Three blades offer some advantages for VAWTs: cyclic variation in both torque and the magnitude and the direction of the net force on the rotor due to the combined effects of lift and drag on all blades are very much reduced with three blades [23]. The aerodynamic forces on two blades, 180° apart, will act in approximately the same

direction on both blades, leading to potential problems with resonant vibrations in the tower (for example as reported by Storer [46]), while those from three blades, 120° apart, will tend to produce an almost steady force analogous to three phase electrical power [23].

The number of blades, from an overall design point of view, is not a variable that only concerns the solidity, it also has a strong influence on the variation in loading on the turbine structure. Varying loads are an inherent part of VAWT operation due to the unsteady aerodynamics, and fatigue was a serious issue with early VAWTs [47] which should be considered in the design stage. According to the studies performed by Consul et al. [35] and McIntosh et al. [48], the variation of torque is shown to be significantly reduced with three or four blades rather than two.

With regard to turbine self-starting capability, the one-bladed turbine cannot produce forward torque during a large part in each revolution and therefore becomes very difficult to self-start. Two-bladed turbines have the potential to self-start but that self-starting capability does not extend to all possible starting positions which could prove to be problematic for commercial turbines (Dominy et al. [12]). Finally a three-bladed turbine is reported to be self-starting [11, 12] irrespective of its starting position with careful rotor and blade design [23]. Therefore, based on the above literature review concerning the number of blades used on H-Darrieus wind turbines, a three-bladed design is employed in all numerical and experimental studies in this thesis.

2.4.3 Blade profiles and aerodynamic data

2.4.3.1 Blade profiles

In the early studies of Darrieus turbines, symmetrical NACA00xx profiles in particular NACA0012, NACA0015 and NACA0018 were widely used. These profiles were well understood and data were available covering a wide range of conditions, which makes aerodynamic design and theoretical prediction easier. Nevertheless, it was later realised that these aerofoils, which were developed for aviation, might not be the best for VAWT application [49]. It has been suggested that a specially designed blade, such as a laminar flow aerofoil, a cambered profile or increased thickness profiles could improve turbine performance. However, in most cases, the studies were not thorough enough to draw a firm conclusion.

Migliore and Fritschen [49] examined ten different aerofoils and their effects on the aerodynamic performance of Darrieus turbines. They found that the use of NACA6-series blades can produce a broader and flatter power curve whilst the peak power

coefficient is comparable to the use of NACA00xx series. Their calculations showed that energy yield can be increased by 17% for turbines with $\sigma = 0.07$ to 27% for turbine with $\sigma = 0.21$ if a NACA 63_2-015 was used. However, their study was focused on a Darrieus rotor at high Reynold number and higher tip speed ratios. Their finding has little relevance to small turbines under real field conditions.

A set of aerofoils was developed by Sandia researchers [50, 51] with the objective of maintaining a laminar boundary layer over as much of their length as possible, known as natural laminar flow (NLF) aerofoils. This series consists of three sections: SAND0015/47, SAND0018/50, and SAND0021/50. The designation is similar to the NACA00xx that were used as a reference for the design of the SAND00xx/xx. A number added after a slash indicates an aerofoil portion that supports laminar flow. The aerofoil geometries were presented in Berg's study [50] as shown in Figure 2.9.

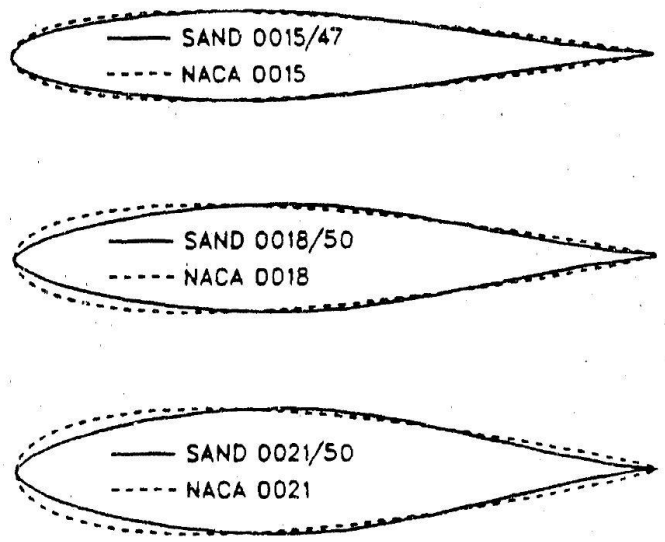

Figure 2.9 SAND 00xx/xx and NACA00xx profiles [50]

The analysis performed by Klimas et al. [51] for VAWTs showed the NLF aerofoil SAND0015/47 produce lower peak efficiency due to its earlier stall characteristic. Moreover, the study conducted by Masson et al. [52] demonstrated that for the $17m$ Sandia VAWT machine, the SAND0015/47 could only improve the performance slightly at high tip speed ratios compared with the NACA0015 baseline. The static lift and drag data showed the SAND0015/47 to be superior at low α but earlier stall resulted in better performance from the NACA0015 at moderate to high α.

Normally it is assumed that symmetrical aerofoils should be used for wind machines. Since cambered sections are not designed to operate at negative incidence, (relative wind approaching the convex side of the aerofoil), any gain made by a cambered blade

with a favourable angle of wind attack on the upstream pass would be lost on its downstream pass because of the unfavourable incidence angle. One of the first studies on the effect of blade camber was conducted by Healy [53] using multiple streamtube models. Healy concluded that the closer the cambered aerofoil is to symmetry the better its power output. Meanwhile with the same model, Healy also claimed that thicker blades performed better than thinner aerofoils at low turbine Reynolds numbers due to the thicker aerofoil's resistance to stall [53]. However, in contrast to Healy's conclusion, Kirke [23] showed that a cambered S120 aerofoil gave a higher maximum power output with much improved turbine self-starting performance by using a multiple streamtube model. Kirke also suggested that cambered aerofoils such as those used on model aircraft may perform better than traditional symmetric aerofoils, the performance of which was known to suffer at low Reynolds numbers. In addition Kirke and Lazauskas [43] also predicted that a turbine with cambered NACA4415 blades of $0.32\,\mathrm{m}$ chord should easily self-start in a $10\,\mathrm{m/s}$ wind, unlike the symmetrical NACA0015 blades with a negative net torque range ('dead band') as shown in Figure 2.10. More recent studies including [54, 55] also feature analysis on cambered aerofoils suggesting they improve the turbine performance.

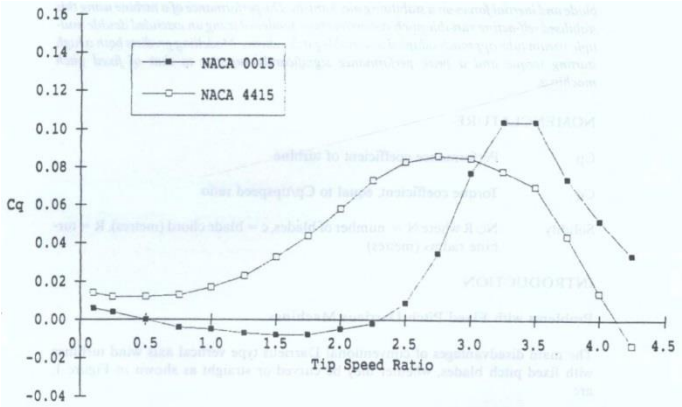

Figure 2.10 Camber influence on turbine performance, by Kirke and Lazauskas [43]

Keeping a symmetrical profile but increasing the blade thickness has also been proposed since a thicker blade profile may be more beneficial to the VAWT structural engineer trying to create a blade with good bending resistance, which would make it possible to have longer blade spans and/or higher rotational speeds. Angell et al. [56] have shown that sections up to approximately 21% thickness may be used with no loss in performance. Islam et al. [54], Healy [53] and Kirke and Lazauskas [43] also state the potential advantages of thicker aerofoils including improved starting performance and lower noise. More recently McIntosh [48] used a 2-D VTM (Vorticity Transport Model)

code to estimate the potential change in the power coefficient for a 3-bladed rotor with different symmetrical NACA00xx blade profiles. McIntosh concluded that the thinner profiles have a higher peak power coefficient at higher λ while the thicker profiles have a broader peak with relatively lower value as shown in Figure 2.11. Furthermore at low λ thicker profiles generate much more power than thinner ones, which is beneficial to a turbine designed to achieve self-starting.

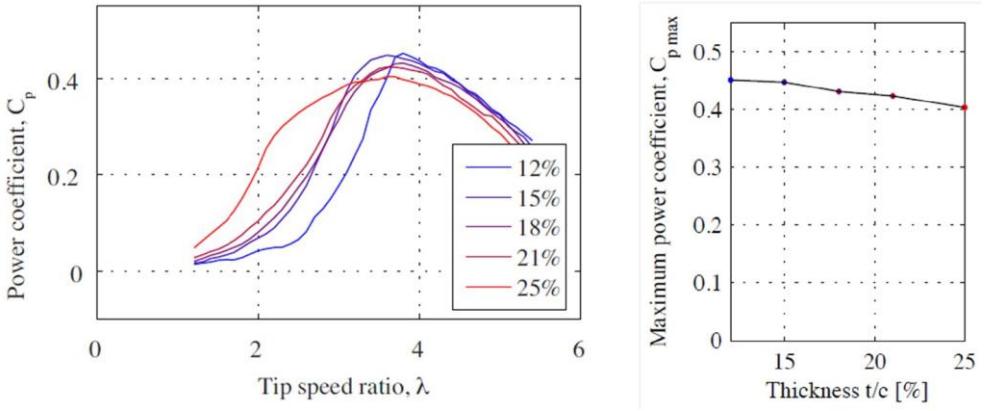

Figure 2.11 Power coefficient for symmetrical NACA aerofoils with different thickness computed by using a 2-D VTM model from McIntosh's study [48]

More recently, Claessens [57] proposed a new aerofoil designated as DU06W200 to comply with the Delft aerofoil designation system. This new aerofoil is designed specifically for VAWT application having 20% thickness with 0.8% camber. The NACA0018 section which is commonly used on Darrieus turbines was compared as a reference as can be seen in Figure 2.12. The DU06W200 demonstrates a 5% increase of peak power output compared with the NACA0018. Moreover the whole curve is shifted left which indicates that the new proposed aerofoil could generate more torque (power) at low tip speed ratios, increasing the turbine's self-starting capability.

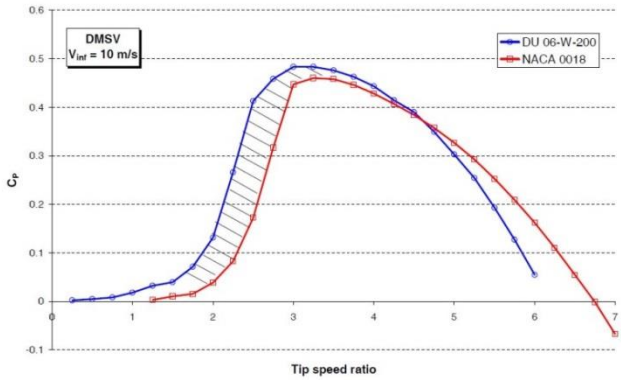

Figure 2.12 Turbine power coefficient with DU06W200 profile compared with NACA0018 profile [57]

According to the above literature review of blade profile for the H-Darrieus wind turbine application, the widely used symmetric NACA0018 and NACA0021 blades are chosen to be the reference blades for numerical and experimental investigations performed in this thesis. The cambered aerofoil NACA4415 and newly proposed DU06-W-200 are also tested and compared with those reference blades. Focus is placed on examining the H-Darrieus wind turbine performance at low tip speed ratios and the turbine self-starting capability with different blade profiles, which were not fully studied and presented in the literature.

2.4.3.2 Aerofoil aerodynamic dataset for small-scale wind turbines

Due to the characteristic of the H-Darrieus wind turbine, the blades will experience all possible angles of attack (0°~180° for symmetric aerofoil and 0°~360° for nonsymmetric aerofoil) during the turbine start-up period. In addition, Darrieus turbines are usually comparatively small and therefore they experience lower Reynolds numbers (~10^5) than most other wind turbines and aerospace applications (~10^6). It is well known that the aerodynamic performance of the blades at low Reynolds numbers differs significantly from that at high Reynolds numbers (e.g. [58-60]). A review of aerofoil tests in the literature is conducted in this section and special attention is paid to low Reynolds numbers and high angles of attack test conditions.

One of the most extensive and reliable sources of low-speed aerofoil performance data is that provided by Selig and his colleagues at UIUC Applied Aerodynamics Group [61]. They had measured 34 aerofoils at low Reynolds numbers comparable to those experienced by Darrieus turbines. Most of these aerofoils are intended primarily for model aircraft. Nevertheless, the incidence angle range for all their measurements was limited between -10° and 25°. Aerofoil performance at post-stall and deep stall was not available therefore these data are not suitable for studying the small scale Darrieus turbine.

The most complete available dataset was published by Sheldahl and Klimas [62] who studied seven symmetrical aerofoils at angles of attack up to 180° and whose data has provided the foundation for many VAWT performance studies (e.g. [63-65]). However, their actual measurements were conducted at three Reynolds numbers of 360,000, 500,000 and 700,000. Data for lower Reynolds number was extrapolated by using the computer code PROFILE [62]. Recent researches [11, 64] have raised questions over the reliability of this dataset especially that extrapolated at low Reynolds numbers.

Timmer [66] performed full incidence angle tests with aerofoils of DU96-W-180 and DU97-W-300 sections at the Reynolds number of 700,000. Based on his measurement, they concluded that different aerofoils exhibit different characteristics even when fully stalled and a thicker aerofoil often generates higher lift. Furthermore there are some other full incidence range tests on the NACA0012 profile at Reynolds numbers over 1,000,000 [67], on NACA0018-64 at Reynolds number of 300,000 [68], and on NACA4415 at Reynolds numbers ranging from 250,000 to 1,000,000 [69]. All these measurements were conducted at relatively high Reynolds numbers which are not appropriate for study on a small-scale Darrieus turbine especially during its starting period.

More recently, Worasinchai et al. [31, 70] performed a series of measurements over the full incidence range and at relatively low Reynolds numbers. They also studied the wind tunnel wall effects on the measured data and concluded that wind tunnel testing must be performed either in half-open test sections or in closed sections with low blockage ratios since at deep stall incidence the tunnel wall has a significant influence on the flow structure around the aerofoil [70]. Furthermore, an aerofoil 'second-stall' behaviour was also recorded by Worasinchai at angle of attack ranges from approximately 40° to 56° depending on aerofoil geometry. A summary of aerofoils measured by Worasinchai et al. is presented in Table 2.2.

Aerofoil	**Incidence range**	**Reynolds number**
NACA0012	0°~360°	62,000 ; 86,000 ; 148,000
SG6043	0°~360°	64,000 ; 90,000
SD7062	0°~360°	65,000 ; 151,000
DU06W200	0°~360°	67,000 ; 91,000 ; 151,000
S1223	0°~360°	62,000 ; 83,000 ; 133,000
S1223B	0°~360°	62,400 ; 84,400 ; 134,100

Table 2.2 Aerofoils measured in Worasinchai's study [31, 70]

The literature reviewed in this section clearly illustrates that although a large number of wind tunnel datasets are available, only limited data are suitable for investigating the small scale Darrieus wind turbine over the full 0°~360° incidence and at low Reynolds numbers. Therefore, full range aerofoil static wind tunnel measurements are performed in this study in order to provide a complete and convincing data source for analytical study of H-Darrieus wind turbines. Furthermore, the wind tunnel wall effect on the measured data and the aerofoil

'second-stall' behaviour observed in the literature are also examined and explained in detail in this thesis.

2.4.4 Curvature effects

As shown by Migliore et al. [71], the aerodynamic characteristics of an aerofoil differ for curvilinear and rectilinear flow. A symmetrical aerofoil moving in a curved path has the same aerodynamic characteristics as a cambered aerofoil moving in a rectilinear flow field with a virtual angle of incidence as shown in Figure 2.13. Migliore et al. [71] illustrated that the flow curvature effects become more pronounced at large c/R ratio. As an example, at $\lambda = 6$, and with $c/R = 0.26$ the difference between leading and trailing edges was close to 12° while for $c/R = 0.11$ the difference is approximately 5°. The potential blade performance might be modified due to the curvature effects and it should be considered when translating 2-D aerofoil data for VAWT modelling purposes.

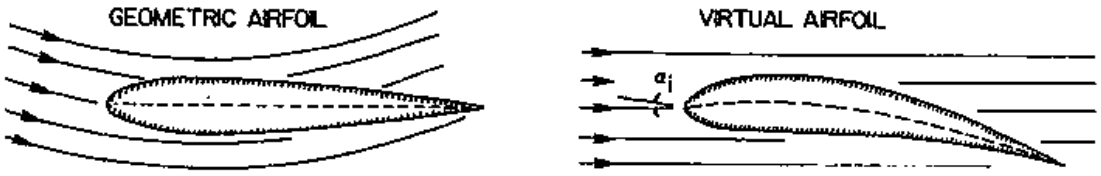

Figure 2.13 Curvature effects for symmetric blades move in a curvilinear flow [71]

Due to the orientation of the virtual camber, an addition to the normal force acts toward the centre of rotation. Therefore normal force is increased in the upstream pass and decreased in the downstream pass. Sharpe's analysis [72] provides an expression for the contribution to normal force as:

$$C_{nf} = 0.25\left(\frac{dC_l}{d\alpha}\right)\frac{c}{R}\lambda \qquad \text{Equation 2.2}$$

It is noted that despite curvature effects, early theoretical models [73-75] still produce reasonably good results without taking the curvature into consideration. This might be because the effects of flow curvature only become significant at high λ as it is pointed out by Soraghan et al. [76]. Nevertheless recent studies conducted by Goude [77] clearly demonstrate that analytical models with curvature correction can predict the turbine performance that better matches experiments.

From this review of curvature effects, it has been found that the curvature is an important factor which should be considered in modelling VAWTs. Therefore a correction method is incorporated into the BEM model developed in this thesis. The

results demonstrate that the curvature has a significant effect on predicting turbine performance at high tip speed ratios which is consistent with Soraghan et al.'s study [76]. Moreover, experimental measurements are performed in this study to further study the flow curvature effect.

2.4.5 Surface roughness

A turbine's blade surface roughness will be expected to increase during its lifetime through erosion or contamination, potentially affecting the machine's performance. The effects of the blade surface roughness need to be quantified and understood since contamination by some kind of atmospheric particles would be hard to avoid over the long lifetime of the VAWT.

Howell et al. [39] experimentally tested the influence of blade surface roughness on the turbine power output. Blades with a rough surface were manufactured by using high-density foam, which results in the largest scales of roughness were approximately **0.5 mm** in height (measured by a roughness feeler gauge). The blades were later smoothed by using fine-grade glass paper leading to scales of roughness estimated to be about **0.05 mm** (an order of magnitude lower than the previous case). Their measurements (shown in Figure 2.14) illustrate that at low wind speeds the turbine with the rougher surface increases performance significantly. It is hypothesised that this is due to the rougher surface undergoing a laminar to turbulent boundary layer transition much earlier, and so being more inclined to stay attached resulting in a lower drag on the aerofoil [39]. In contrast, the turbine performance was decreased considerably with the rough surface blades at high wind speeds which might be due to the increased skin drag [39]. However, Howell et al.'s measurements were only performed at relatively high λ; data at turbine start-up period was not available.

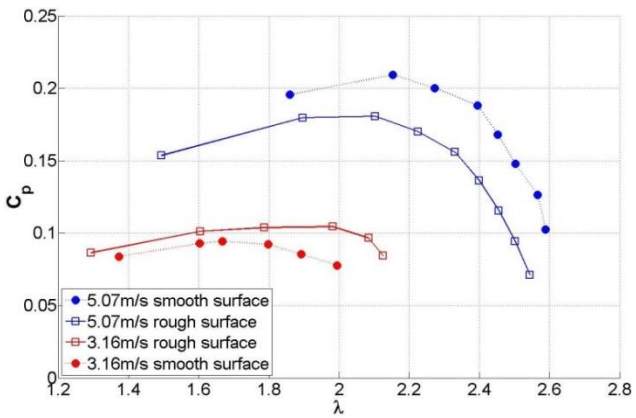

Figure 2.14 Turbine power output at different wind speed for smooth and rough blade surfaces from Howell et al.'s study [39]

Tests conducted by Ashwill [78] in Sandia laboratories shows a noticeable effect when the blades became contaminated with 'bug reside'. The 34m VAWT rotated at a fixed speed while the upstream wind speed was modified in order to examine the influence at different λ. Ashwill's study demonstrates that the 'dirty blades' underperformed the clean blades by up to 7% for wind speed lower than $V < 11\,\mathrm{m/s}$ and the percentage effects were worse for very low wind (high λ). The 'dirty blades' then outperformed the clean blades by a significant amount at higher wind speeds (low λ). Ashwill [78] stated that the rough surfaces act as tiny vortex generators, tripping the boundary layer into turbulent flow and helping the flow remain attached to the aerofoil surface for longer which results in improved performance at low λ where stall becomes significant.

The literature review of blade surface roughness effects on H-Darrieus wind turbine performance reveals that investigations are very limited especially for the blade roughness effect on turbine self-starting capability. Therefore, experimental tests are performed during this study using turbine blades with different surface finishes (different surface roughness). Blades surface roughness is measured using a 3-D profiler machine in order to provide quantified information for future comparison. Focus is put on examining the influence of roughness on turbine self-starting capability as well as overall performance.

2.4.6 Reynolds number effects

Approaches utilising aerofoils designed for aviation use have limited potential for studying small-scale VAWTs since the aerofoil data are usually measured at very high Reynolds numbers ($\sim 10^6$). As pointed out by Edwards [79] for a small-scale VAWT of $1.2\,\mathrm{kW}$ rated power, the maximum blade Reynolds number is less than $400{,}000$. Although for the purpose of wind tunnel measurements in this study, the Reynolds number is based on blade chord, the relative velocity and the effective Reynolds number the blades seen are not constant in the cyclic motion at each tip speed ratio. The extreme scenario is when the blades move towards the upstream wind at a tip speed ratio of one and the blade Reynolds number will decrease to zero. The Reynolds effects are not only limited to the extraction efficiency with which energy in the wind is converted to power but also on the lifespan of the machine.

Selig and McGranahan [80] tested six aerofoils at relatively low Reynolds numbers ranging from $100{,}000$ to $500{,}000$. They found aerofoils at lower Reynolds numbers show reduced lift and higher drag. Moreover, on some of the aerofoils the laminar

separation at low angles does not reattach to the aerofoil surface whilst at moderate Re it does. How this behaviour may affect a VAWT blade has yet to be addressed. Jones and William [81] examined the characteristics of NACA0012 at a wide range of Reynolds numbers illustrating that the airfoil lift will increase with the increase of Reynolds number, which is also confirmed by Gregory and O'Reilly [82]. Aerofoil data at low Reynolds numbers were also reported by Sheldah and Klimas [62] but show big discrepancies with other measurements (e.g. [83, 84]) demonstrating the difficulty of testing aerofoils at low Reynolds numbers. With limited experimental aerodynamic data at low Reynolds numbers, numerical studies were carried out in order to predict VAWT performance including self-starting capability. One of the earliest studies was performed by Templin [17] with NACA blade data at the Reynolds number of 300,000 showing the Darrieus turbine could self-start. Although this Reynolds number may be a realistic value for large turbines in a strong wind, it is not suitable for studying small turbines, especially during the start-up period. Therefore Templin's calculation simply establishes that the turbine can only self-start under some conditions.

Tests about the Reynolds number effects on the turbine power output were investigated numerically and experimentally at the Sandia laboratory [15]. The turbine rotation speed was kept constant while the free steam velocity was varied. The measurements (shown in Figure 2.15) demonstrated that the Reynolds number has very limited effects at low tip speed ratios but the peak power coefficient and power coefficient at high λ increase with the increase in Reynolds number and also decrease in power coefficient with decrease in Re. Recent studies conducted by Danao et al. [85] showed similar results.

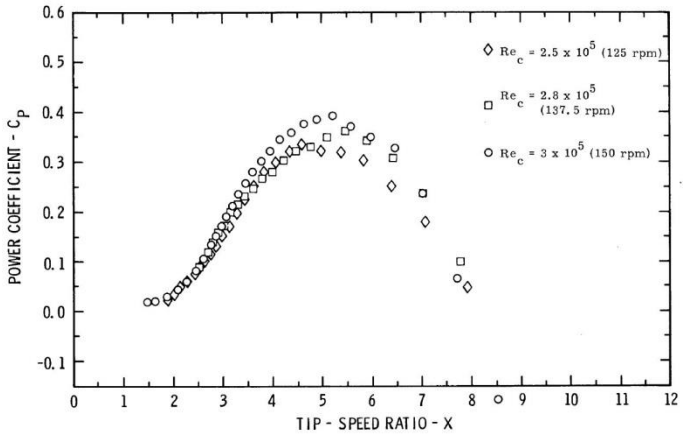

Figure 2.15 The influence of varying Reynolds number on VAWT performance [15]

In this thesis, the blade Reynolds number is modified by changing the upstream wind speed. The Reynolds number effect on turbine performance is examined numerically and experimentally. The limited studies performed in the literature only related to the Reynolds effect on turbine performance at high λ, therefore this thesis aims to reveal the Reynolds influence on H-Darrieus wind turbine self-starting period.

2.4.7 Pitch control strategy

The disadvantages of VAWTs stem from the fact that there is cyclical variation in the angle of attack on the aerofoils as the rotor rotates. As a result, optimal loading cannot be sustained for all azimuth angles, leading to inherently low aerodynamic efficiency. This is further exacerbated as the blades depart from their optimal lift to drag ratio at most azimuth angles. Additionally, pulsating lift causes significant ripples in the torque and power generated. The ability to pitch the blades as they move around the path of rotation would address these disadvantages to some extent by sustaining optimal angles of attack for most azimuth angles as the blades rotate [86]. The definition of blade pitch (β) in this study is shown in Figure 2.16. Blade nose out is negative pitch ($-\beta$) and nose in is positive pitch (β).

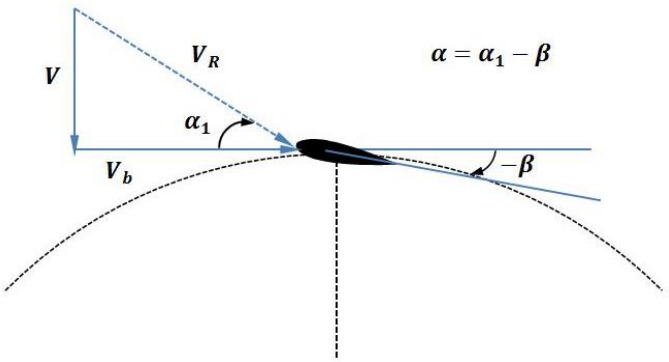

Figure 2.16 Definition of pitch angle in this thesis

2.4.7.1 Active pitch control

Active pitching would improve turbine control. Many of the significant improvements in wind turbine performance (especially HAWTs) over the past three decades have been due to the move towards pitch control. Pitch regulation has not only improved energy capture, but achieved secondary objectives with the most important being the ability to alleviate transient structural loads [87]. It is acknowledged that active pitch control can significantly increase torque generation at low λ and improve turbine self-starting capability. The study performed by Grylls et al. [88] using a simple sinusoidal

pitch variation demonstrated experimentally that a large pitch amplitude produces good performance at low λ but poor performance at high λ, while small pitch amplitude produces poor performance at low λ but good performance at high λ. Relatively simple force pitch mechanisms used in Grylls et al.'s study were unable to adjust pitch amplitude in response to changes in λ and could not achieve the required combination of high starting torque with high efficiency at high λ. More recently, Soraghan et al. [76] used a Double Multiple Streamtube model to simulate an H-Darrieus wind turbine under a sinusoidal pitch and the results are shown in Figure 2.17. Soraghan et al.'s results illustrate that the pitch regime is successful in increasing the peak aerodynamic performance. However, this comes at the cost of reducing efficiency at high and low λ [76]. Despite the practical difficulties involved in achieving optimum pitch control, theoretical studies (e.g. [89-92]) were performed in the literature to calculate the optimal pitch strategy as a function of azimuth angle and tip speed ratio.

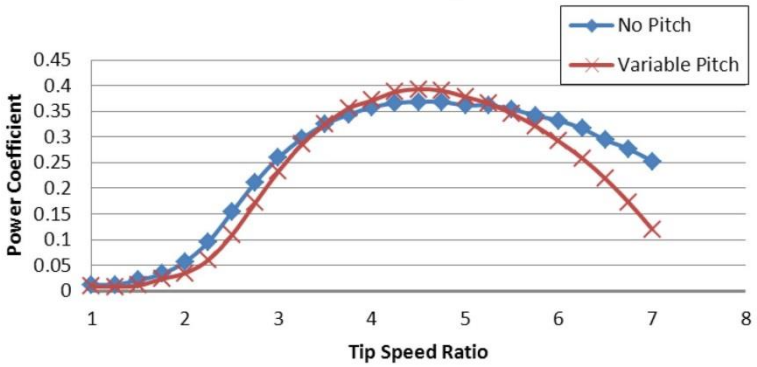

Figure 2.17 Turbine performance under sinusoidal pitch control compared to no pitch from Soraghan et al.'s study [76]

2.4.7.2 Fixed pitch angle

The problems of dynamic stall on a VAWT could be completely avoided if the blades could have their pitch varied with azimuth to achieve the optimal angle of attack around the whole revolution. Varying the pitch would however, be extremely mechanically challenging in practise. Variable pitching has been considered in the past for VAWTs as shown in the previous section, but active pitch mechanisms were regularly dismissed as too complicated in the context of relatively small turbines, which is the main concern in this thesis. Therefore another relatively easy way to improve turbine performance is to have a pre-set, non-zero fixed pitch angle. With a negative pitch angle as shown in Figure 2.16, the angle of attack in the upstream half of the rotor will be reduced but increased in the downstream half of the rotor. Therefore

fixing a pitch angle in this way can be thought of as a translation of the angle of attack curve up or down by exactly the pre-set pitch angle.

This pre-set negative pitch angle would have some effects on the blades as noted by Pearson [93]:

- The blade dynamic stall would be delayed since the angles of attack are reduced in the upstream half of the rotor. This would lead to the blade producing torque for a greater portion of the revolution. Since the lift force produced as the blade approaches the most upstream location acts increasingly in the direction of rotation, maintaining attached flow in this region could result in a significant increase in torque output.
- In the downstream half of the rotor the onset of blade dynamic stall would be earlier since the angles of attack are increased. This leads to a decrease of torque produced in the downstream part.

Klimas and Worstell [94] experimentally studied the effects of blade pre-set pitch on curved-blade Darrieus VAWT performance and the results are shown in Figure 2.18. For scenarios of $\beta = -2$ and $\beta = -4$, it clearly shows an improved turbine performance at low λ and peak power coefficient. Moreover for negative pitch angle of $\beta = -7$, the turbine performance over the entire working range is significantly decreased. Klimas and Worstell's study clearly illustrates that only a slightly pitched blade (negative pitch) could improve turbine performance. Too large negative pitch angles or positive pitch angles will decrease the turbine's overall performance. However Klimas and Worstell's study was performed at relatively high λ, data for turbine performance during the start-up period is not available.

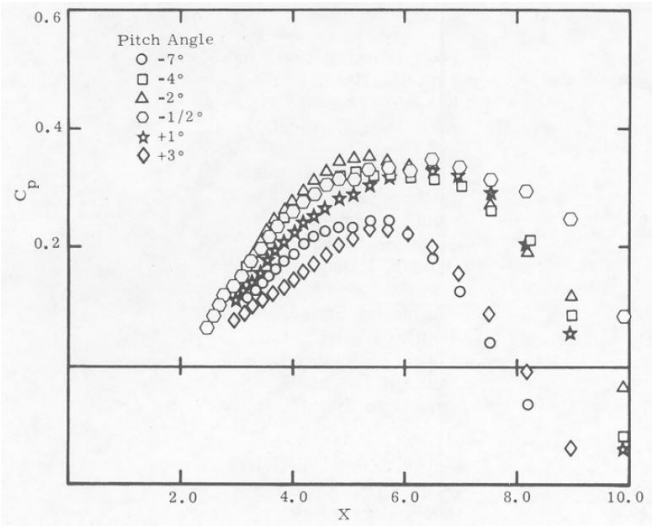

Figure 2.18 Turbine power coefficient under different fixed pitch angle [94]

From this literature review it is concluded that the blade pitch angle plays a significant role in turbine performance. Previous studies focused on the turbine power output at high tip speed ratios under different blade pitch angles, therefore this study aims to investigate the pitch strategy effect on H-Darrieus wind turbine performance at low tip speed ratios including turbine self-starting capability. Considering the complexity of active pitch mechanisms, a fixed pitch control strategy is adopted for the experimental tests conducted in this thesis. Meanwhile, numerical studies are performed under the same testing conditions in order to compare with the experimental results.

2.4.8 Dynamic stall

As shown in Figure 1.3, VAWT blades experience a skewed sinusoidal change in angle of attack far beyond the static stall angle during rotation, which results in the blades dynamic stall. Dynamic stall is an important flow phenomenon that significantly affects the performance of VAWTs. It comprises of the initiation of flow separation from the blade's surface, full separation of the boundary layer, detachment, shedding of vortices and reattachment of the flow to the aerofoil surface. Dynamic stall models (e.g. [16, 95-97]) were developed in order to improve the performance prediction derived from static aerofoil datasets. Leishman [98] found that the dynamic loads can exceed the static values by up to 100%.

Above a certain critical angle of attack (depends on the aerofoil profile) the flow will separate from the aerofoil surface resulting in dynamic stall associated with a loss of lift and a large increase in drag. For an aerofoil undergoing a rapid increase in α, the onset of stall will be delayed to incidences above the critical angle of attack resulting in a higher peak lift value. Conversely, beyond stall a rapid decrease of α will lead to a delayed reattachment of flow. The overall effect is a hysteresis in the aerofoil aerodynamic force that differs significantly from the behaviour under the static situation. For the inherently unsteady VAWT blade aerodynamics, the effects of dynamic stall must be correctly assessed in order for performance to be successfully evaluated.

McCroskey et al. [99] and Car et al. [100] were among the first to study the dynamic stall of aerofoils. McCroskey et al. employed hot films and hot wires to examine the flow. The influence of dynamic stall on pitching moments, flow fields separation, flow reattachment and aerofoil force generation were studied. Car et al. applied a smoke visualisation method to study the effects of dynamic stall and they found that dynamic

stall is dependent on a large number of factors including flow speed, Reynolds number, pitching rate and aerofoil profile.

More recently, Ferreira et al. [101] used a single bladed rotor to investigate the influence of dynamic stall on VAWTs. The Detached Eddy Simulation (DES) and Large Eddy Simulation (LES) models both predicted that during dynamic stall the blades would experience highly unsteady loading which appears to agree with the high frequency load measurements performed by Tsang et al. [102] for a range of dynamic stall conditions. Wang et al. [103] used CFD to model dynamic stall and found that the flow reversal on the suction surface produced a highly unstable region of flow near the blade, which resulted in the generation of a number of small vortices on the blade surface. They stated that it was these small vortices advecting over the blade that were responsible for the unsteadiness observed in the blade loads. Fujisawa and Shibuya [104] used a small model in a water tank to examine the streamlines by using a dye injection technique. Moreover, they performed Particle Image Velocimetry (PIV) to analyse the flow during dynamic stall around a VAWT blade at $\lambda = 2$. Fujisawa and Shibuya's study illustrated the shedding of intense vortices during dynamic stall, and these vortices were seen to advect through the blade to volume such that they are likely to interact with the blade in the downstream half of the rotor (shown in Figure 2.19).

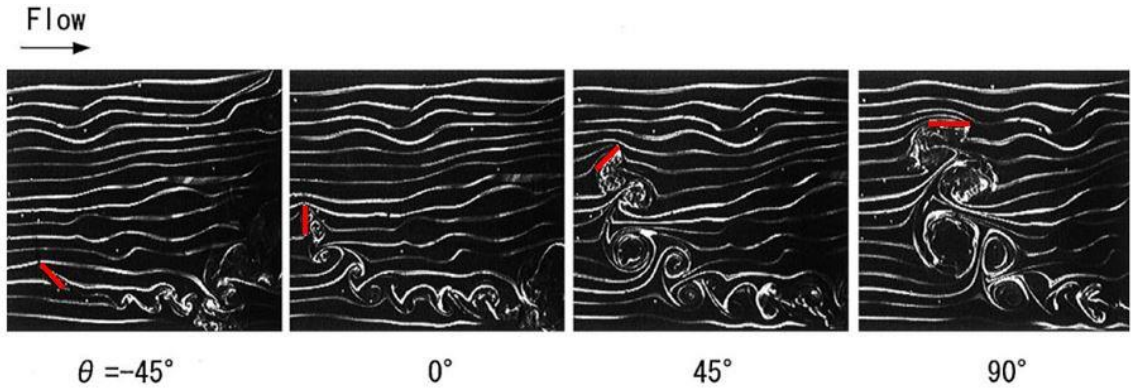

Figure 2.19 Flow visualization of dynamic stall on a VAWT [104]. Blades are indicated by red line.

All of the above studies have contributed to the understanding of the dynamic stall phenomenon and the dynamic stall process is characterised by the following sequence of events as it is pointed out by Leishman [98] and shown in Figure 2.20:

STAGE 1: The boundary layer is thin without flow reversal at very low incidence angles. However, shortly after the incidence exceeds the critical angle of attack a layer of reversed flow develops at the aerofoil trailing edge. With the further increase of

incidence angle, the flow in the boundary layer starts to reverse at the surface towards the aerofoil leading edge.

STAGE 2: The lift coefficient increased further when the incidence passed the static stall angle with the flow reversal having considerably moved to the leading edge. Larger eddies start to form and full flow reversal moves from the trailing edge to the leading edge. When the flow reversal reaches the leading edge, a strong leading edge vortex is formed. The centre of pressure is shifted to the aft of the blade causing an abrupt change in the pitching moment coefficient, which is typically described as moment stall.

STAGE 2-3: The vortex continues to roll-up and grows as it is convected toward the rear of the aerofoil. It is this large, intense vortex that maintains flow curvature over the aerofoil and prevents lift stall. As the vortex moves towards the trailing edge, the flow curvature starts to reduce and the lift coefficient starts to drop.

STAGE 3-4: Once the leading edge vortex has been shed into the wake, the aerofoil can no longer produce the flow curvature required for lift generation. This results in an abrupt drop in the lift coefficient. The flow over the aerofoil is fully separated after this point as seen in full static stall, therefore the aerodynamic force coefficients tend towards their static values. Small vortices continue to form and be shed from the leading and trailing edge leading to further unsteadiness in the blade loading.

STAGE 5: As the blade pitches down, the onset of flow reattachment is initiated. Although there is delay in reattachment due to interaction with the shed vortices, the subsequent reattachment of the flow fields to the aerofoil surface occurs when the incidence is low enough. The reattachment point moves toward the trailing edge at a rate below the freestream velocity, eventually resulting in a recovery of the aerodynamic forces at static value.

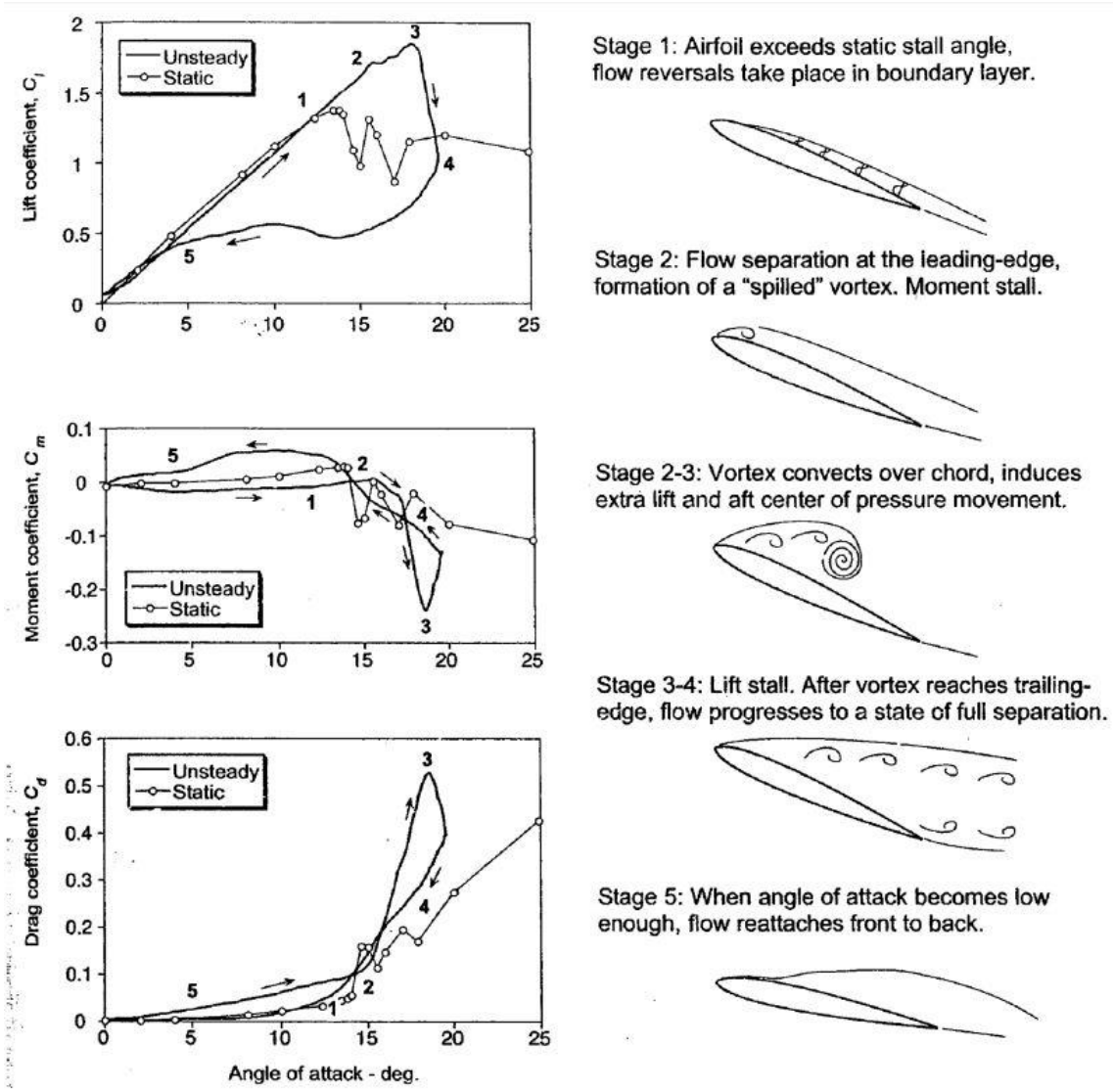

Figure 2.20 The stages of dynamic stall and reattachment [98]

In order to relate the period of transit of flow structure over the blade to the period of oscillation, a non-dimensional reduced frequency (k) needs to be defined:

$$k = \frac{\omega c}{2V} = \frac{c}{D}\lambda \qquad \text{Equation 2.3}$$

Equation 2.3 clearly indicates that the level of unsteadiness at a specific tip speed ratio is dependent on the rotor radius ($D = 2R$), which can also be regarded as the solidity ($\sigma = {}^{nc}/_{R}$) if the blade number is fixed.

In this thesis, the blade dynamic stall phenomenon is investigated experimentally. The instantaneous changing pressure around the rotating blade is measured directly for the first time in order to shed some light on this complicated problem. CFD models are also used to examine vortex shedding during dynamic stall and how these vortices

affect turbine performance. Finally a semi-empirical dynamic stall model, the Leishman-Beddoes model, is incorporated in the BEM model developed in this thesis and all the static values are calculated from the wind tunnel measurements performed in this study.

2.5 VAWT modelling

In the following subsections, a review of the literature for mathematical modelling of the VAWT is detailed. A sequence of the evolution of the various models applied to VAWT research is made while pointing out their deficiencies and improvements. Different momentum models, also known as Blade Element Momentum (BEM) models, are based on calculation of flow velocity through a turbine by equating the streamwise aerodynamic force on the blades with the rate of change of momentum of air (which is equal to the overall change in velocity times the mass flow rate). Bernoulli's equation is applied in each streamtube and the force is equal to the average pressure difference across the rotor. However, as noted by Paraschivoiu [105], the main drawback of these BEM based models is that they become invalid for high tip speed ratios and also for high rotor solidity because the momentum equations in these particular cases are inadequate. Over the past decades, different approaches were also proposed to predict turbine performance including the vortex model and cascade model. These models, which have their own advantages and disadvantages, will also be discussed briefly in the following subsections.

2.5.1 Single Streamtube model

The first attempt at using momentum theory to study VAWT was made by Templin [17]. He proposed the most simple prediction method for calculation of the performance characteristics of a Darrieus type VAWT, which is called the Single Streamtube model. Here the induced velocity (rotor axial flow velocity) is assumed to be constant throughout the disc and is obtained by equating the streamwise drag with the change in axial momentum. Figure 2.21(a) presents an example of the simple single stream tube including the turbine represented as an actuator disc (Figure 2.21(b)) within which the momentum equation is solved.

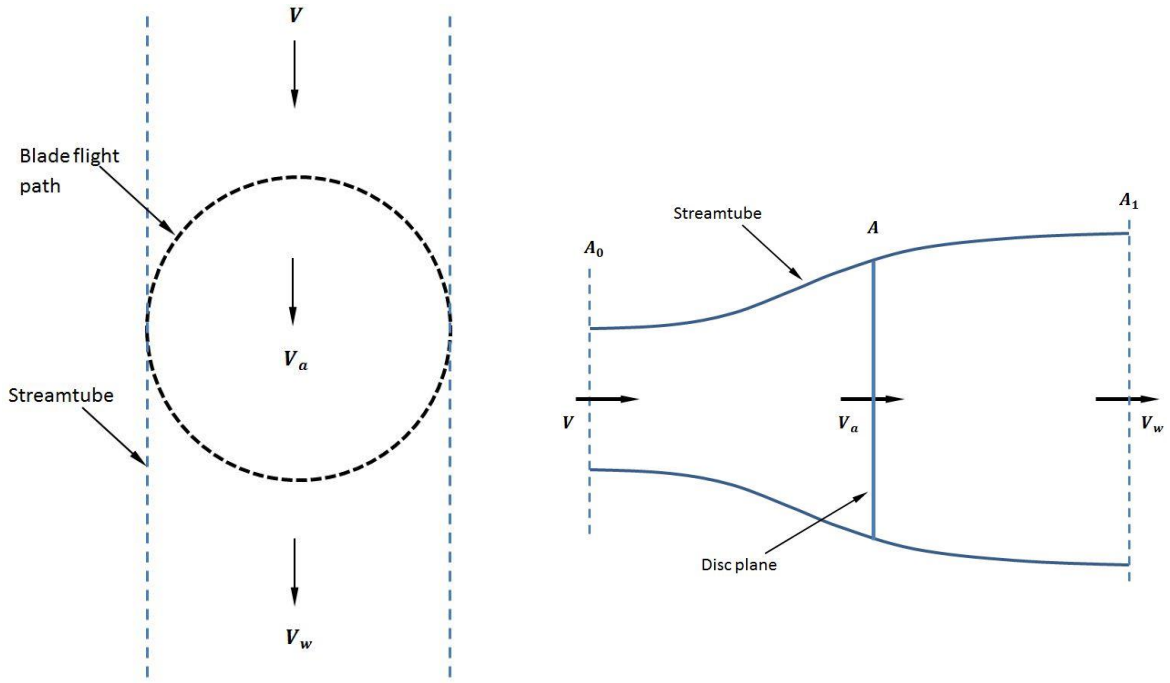

Figure 2.21 Schematic of single streamtube model (a) and actuator disc theory (b)

In this model, the effect of the aerofoil stalling on the performance characteristics is taken into account. The effects of geometric variables such as turbine solidity and blade height have been included in the analysis. The effect of the zero-lift-drag coefficient on the performance characteristics has also been included.

Applying the conservation of linear momentum to the control volume enclosing the whole system, it is possible to find the net force on the contents of the control volume:

$$K = \dot{m}(V - V_w) \qquad \text{Equation 2.4}$$

where $\dot{m}$ is the mass flow rate and V_w is the downstream velocity.

Since no work is done on either side of the turbine rotor, thus the Bernoulli function can be used in the two control volumes on either side of the actuator disk and the net force can also be expressed by

$$K = \frac{1}{2}\rho A(V^2 - V_w^2) \qquad \text{Equation 2.5}$$

If one defines an axial interference factor, $\dot{a}$, as the fractional decrease in wind velocity between the free stream and the rotor plane, then

$$\dot{a} = \frac{V - V_a}{V} \qquad \text{Equation 2.6}$$

$$V_a = V(1 - \dot{a}) \quad \text{Equation 2.7}$$

$$V_w = V(1 - 2\dot{a}) \quad \text{Equation 2.8}$$

Combining the above equations, the power generated by the turbine can be calculated as:

$$P = \frac{1}{2}\rho A V^3 4\dot{a}(1 - \dot{a})^2 \quad \text{Equation 2.9}$$

$$C_p = \frac{P}{P_\infty} = \frac{\frac{1}{2}\rho A V^3 4a(1 - a)^2}{\frac{1}{2}\rho A V^3} = 4\dot{a}(1 - \dot{a})^2 \quad \text{Equation 2.10}$$

When solved for the maximum power coefficient, this yields the Betz limit, stating that $C_{Pmax} = \frac{16}{27} = 0.593$.

This model can predict the overall performance of a lightly loaded wind turbine but it always predicts higher power than the experimental results. It does not consider the wind velocity variation across the rotor which increases with the increase of turbine solidity and tip speed ratio. Furthermore, this model is based on the following assumptions:

- Homogenous, incompressible, steady state fluid flow throughout the streamtube domain
- No frictional drag from the blades and the streamtube boundary
- An infinite number of blades and blade length
- Uniform thrust over the disk or rotor area irrespective of angle of attack
- Non-rotating wake behind the rotor
- The pressure across the disc is constant so there is no change in velocity across the disc
- The static pressure far upstream and far downstream of the rotor is equal to the undisturbed ambient static pressure

2.5.2 Multiple Streamtube model

The limitations of the Single Streamtube model were improved by Strickland [16] through the implementation of the Multiple Streamtube model which extended the model boundary, resulting in the division of the flow through the domain into many independent streamtubes as shown in Figure 2.22. In this model, the induced velocity is found by equating blade elemental forces (lift and drag) and the change in the

momentum along each streamtube. By taking the wind shear effect into consideration, this model predicts the overall performance to be closer to the experimental measurements showing improvements over the Single Streamtube model.

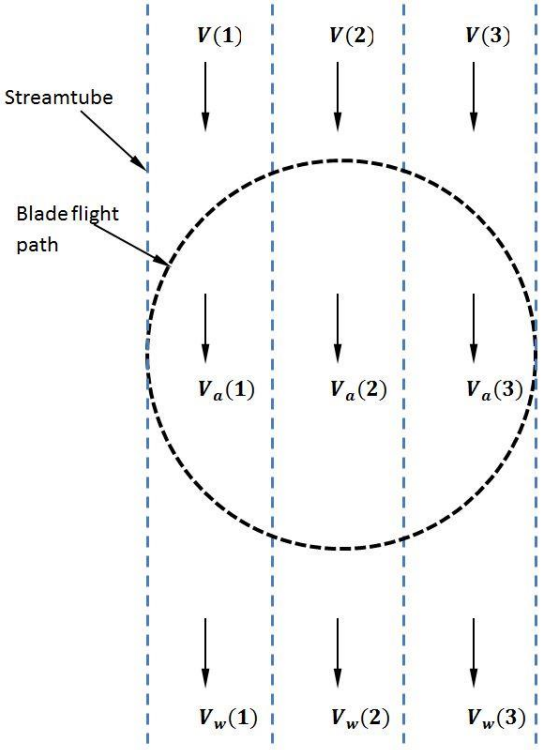

Figure 2.22 Schematic Multiple Streamtube model

Muraca et al. [106] proposed another theory based on the Multiple Streamtube model including the effects of aerofoil geometry, support struts, blade aspect ratio, turbine solidity and blade interference. Moreover, the flow curvature influence was evaluated by treating the blades as flat plates. According to Muraca et al.'s study the curvature effect on turbine performance characteristics is insignificant for low solidity turbines, which is consistent with Migliore et al.'s study [71].

Sharpe [107] incorporated the effect of the Reynolds number into the theoretical calculation in his BEM model which is similar to that of Strickland [16]. An improved version of the Multiple Streamtube model was presented by Read and Sharpe [108] by taking the expansion of the streamtube into consideration. It is strictly applicable to low solidity lightly loaded wind turbines with a large aspect ratio. Although their model can predict the instantaneous aerodynamic blade forces and the induced velocities better than predictions made by the conventional Multiple Streamtube model, the prediction of the overall power coefficient is always lower than experimental measures.

2.5.3 Double Multiple Streamtube model (DMST)

Paraschivoiu [75] developed the Double Multiple Streamtube model, to correct the deficiency encountered with the Multiple Streamtube model mentioned above. The model incorporated the differences in the upwind and downwind sections rotation through the division of each streamtube further into two halves of upwind and downwind respectively as shown in Figure 2.23(a). Calculation is done separately for the upstream and downstream half cycles of the turbine. The induced velocity at each level of the rotor (upstream and downstream) is obtained using the principle of two actuator discs in tandem (Figure 2.23(b)). With an additional disc at the downwind section signifying a secondary induction factor, the turbine interacts with the wind twice so the predictions are more accurate compared with the Multiple Streamtube. For the downstream half-cycle, the induced velocity and wake velocity is represented by:

$$\dot{a}' = \frac{V_w - V_a'}{V_w} \qquad \text{Equation 2.11}$$

$$V_a' = V_w(1 - \dot{a}') \qquad \text{Equation 2.12}$$

$$V_w' = V_w(1 - 2\dot{a}') \qquad \text{Equation 2.13}$$

where $\dot{a}'$ is the interference factor in the downwind zone

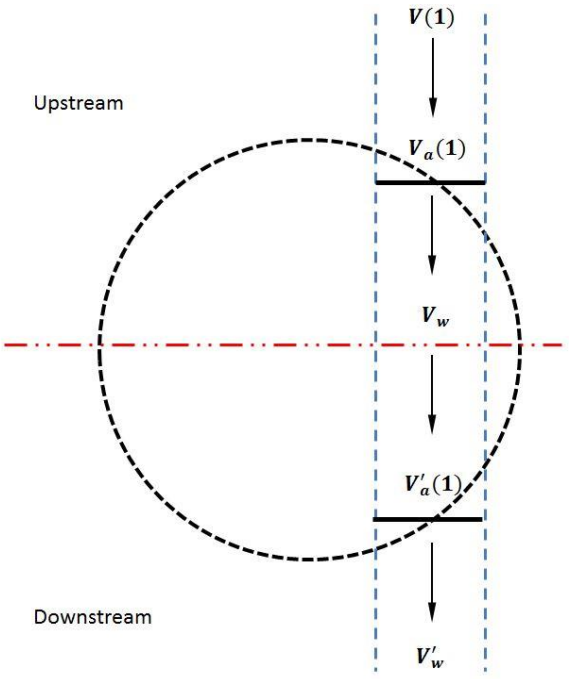

(a)

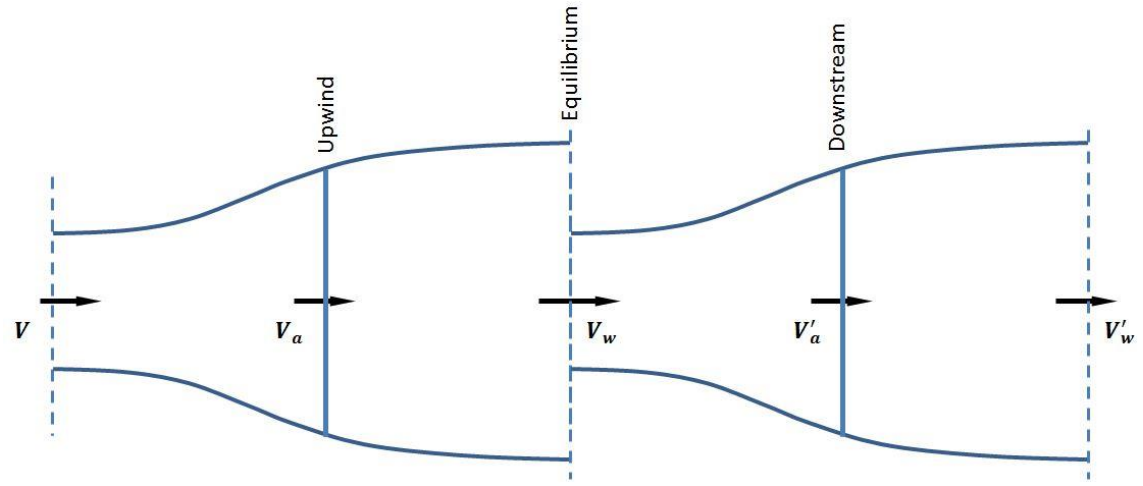

(b)

Figure 2.23 Schematic of double multiple streamtube model (a) and two actuator discs in tandem (b)

The study performed by Paraschivoiu et al. [109] demonstrated the significant influence of secondary effects including the blade geometry, rotating tower and the presence of struts, especially at high tip speed ratios (up to 27% discrepancy for torque at particular azimuth angles). They considered the variation of the induced velocity as a function of the azimuth angle that gives a more accurate calculation of the aerodynamic loads. Later, Paraschivoiu and Delclaux [73] improved this DMST model by considering the induced velocity variation as a function of the azimuth angle for each streamtube.

Although the DMST provides better correlation between the calculated and experimental results, this model over-predicts power output for a high solidity turbine and there appears to be a convergence problem especially in the downstream side and at the higher tip speed ratios [110].

2.5.4 Vortex model

Vortex models are basically potential flow models based on the calculation of the velocity field about the turbine through the influence of vorticity in the wake of the blades. Bound vortex filaments (sometimes called a lifting line) are used to represent the rotor blade, and the vortex strengths are calculated using relative flow velocity, angle of attack and aerofoil aerodynamic datasets. Moreover, regular shedding of span wise vortices from the trailing edge also affects the strength of the bound vortex.

The 2-D vortex model was first proposed by Larsen [111] for predicting the performance of a cyclogyro windmill. However in his model the stall effect is neglected

due to the assumption of a small angle of attack. Fanucci and Walters [112] also presented a 2-D vortex model to study the straight-bladed VAWT but eliminating the stall effect. Earlier studies (e.g.[111-114]) using vortex models were all based on similar principles and assumptions that:

- The model only considers small angles of attack so could not be used to analyse the stall effect
- Only slightly loaded turbines are considered
- 3-D problems cannot be solved very well by using 2-D models

Strickland et al. [115] presented an extension of the vortex model which included the capability of modelling 3-D effects, free wake and dynamic stall phenomenon. Even with this improved model, their calculation could not accurately predict the real performance of VAWT as the results deviated from experimental results especially at higher solidity due to the inability of the vortex model to accurately predict the stalling characteristics around a VAWT blade. Strickland et al. [116] then made improvements based on the previous model by incorporating the dynamic stall, pitching circulation and added mass effect. However, the correlation of the value predicted by the latest model and the experimental measurements seem to be reasonable only in some cases.

Cardona [117] later incorporated the effect of flow curvature as suggested by Migliore et al. [71] into Strickland et al.'s model [115] and found an improved correlation with the calculated and experimental results for overall power coefficient. More recently, Scheurich et al. [118] employed Brown's vortex transport model (VTM) [119] to simulate the aerodynamic performance and wake dynamics of a VAWT. The results from their simulation compared well with those of the experimental data of similar VAWT.

The main disadvantage of the vortex model is that it takes much more computation time than the BEM model. Moreover, vortex models still rely on significant simplifications. For example potential flow is assumed in the wake and the effect of viscosity in the blade aerodynamics is included through empirical force coefficients [120].

2.5.5 Cascade model

The cascade model has been widely used to describe turbomachinery, but was first applied to VAWTs by Hirsch and Mandal [121]. Here, the blades of a turbine are lined up in a plane surface termed the cascade with the blade interspace equal to the turbine's circumferential distance divided by the number of blades as shown in Figure 2.24.

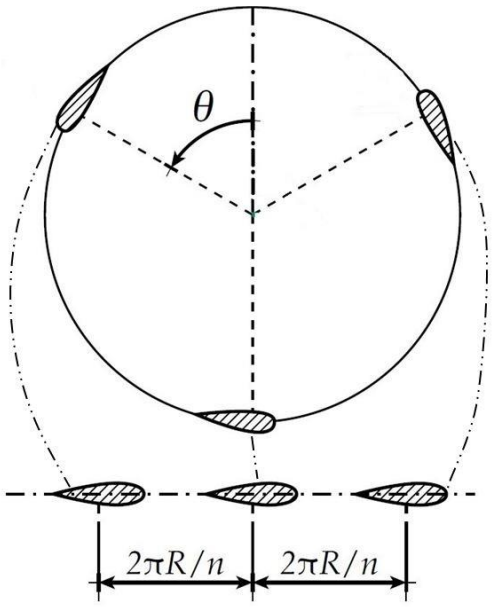

Figure 2.24 Cascade model where the blades are placed equidistantly in the cascade [8]

In this model, each blade's aerodynamic characteristics, including Reynolds number and local angle of attack, are obtained independently for the upwind and downwind halves of the rotor just like the Double Multiple Streamtube theory (see Figure 2.23). After determination of the local relative flow velocity and the angle of attack, the VAWT is developed into a cascade configuration that is shown in Figure 2.24. The flow condition for all blades is assumed to equal that of the centre reference blade. This process is continued for one complete revolution of the reference blade with a step of $d\theta$. Empirical variables are used to determine the induced velocity [121].

The effects of the local Reynolds number variation at different azimuth angles and finite aspect ratio can be incorporated. Furthermore, dynamic stall and flow curvature effects were taken into account by Mandal and Burton [122] in order to improve the analytical capability of this model.

According to limited studies performed in the literature, the cascade model does not have any convergence problem and can predict the overall values of both low and high solidity turbines reasonably well. However, predictions are based on empirically determined parameters [110].

2.5.6 Summary

Due to the resurgence of interest in VAWTs, numerous universities and research institutions have carried out extensive research activities and developed several designs based on different aerodynamic computational models. The challenge is to determine

the apparent wind speeds, angle of attack, induced velocities, etc. at each azimuth location. This inevitably needs to incorporate all the aerodynamic effects discussed in the previous section. These aerodynamic computational models are crucial for deducing optimum design parameters and also for predicting the performance before a VAWT is fabricated.

At present the most widely used models are the Double Multiple Streamtube mode, free-Vortex model and the Cascade model [110]. Since all these models are based on different assumptions and require accurate aerofoil aerodynamic data at appropriate Reynolds numbers (which are scarce as discussed in the previous section), it has been found that each of these three models has its own strengths and weaknesses. Because the aerodynamics of a VAWT is so complex, these models are seen to suffer from their inability to accurately simulate complicated problems. Furthermore, the above traditional computational models are unable to provide insight into the flow physics around the rotor and the wake despite the huge effort that has been made. Also these models only dwell upon considerations of energy extraction, and are unable to display the turbine dynamic self-starting behaviour. However, with all the above shortcomings, the BEM model is still favoured by many researchers due to its low computational cost compared with other methods such as CFD.

From the above literature review of variable mathematical models, it is found that all these different models have a common point: they require high quality aerofoil aerodynamic data as the model input. However, as mentioned above, the database for aerofoils operating at full incidence angles and at low Reynolds numbers is very limited. Another unanswered question is how sensitive these models are to the accuracy of different aerodynamic databases. Since there is no similar research available in the literature, the DMST model is developed in this thesis in order to investigate the effect of database accuracy on the prediction of turbine performance. In addition, an advanced BEM model, called the Start-Up model proposed by Worasinchai [31], is also developed and employed in this thesis so as to display turbine self-starting behaviour.

2.6 CFD methods and recent studies

The benefits of CFD are not limited to its application in the evaluation and optimisation of turbine performance, but it can also be used to visualise the flow structure around a virtual prototype turbine that provides insight into design parameters and performance which may not be possible with other methods (such as BEM). Various desired test conditions including different aerofoils, wind speed, solidity,

etc. can be altered easily making the model very flexible. Furthermore, CFD also has the capability to calculate aerodynamic forces on blades so it does not rely on an external database for further analysis which can be seen as a major advantage over the momentum models, vortex models and cascade models reviewed earlier.

The following subsections provide a review of some CFD validation tests and studies applied to VAWTs.

2.6.1 CFD model validation and turbulence model selection

Howell et al. [39] employed both 2-D and 3-D CFD models to study the effects of solidity effect on turbine performance. The simulation data was compared with their experimental measures at the University of Sheffield's low speed wind tunnel using a three-bladed VAWT with NACA0022 blade. Although the study provided an insight into the understanding of turbine performance in relation to the tested parameters, the turbulence model ($\mathrm{k-\epsilon\ RNG}$) significantly over-predicted the power coefficient in the 2-D model while under-predicting the performance in the 3-D model. Castelli et al. [123, 124] used an enhanced wall treatment $\mathrm{k-\epsilon}$ realisable turbulence model in their 2-D CFD and the results were compared with the experimental measurements in Bovisa's low turbulence wind tunnel with three-blade VAWT using the NACA0021 profile [123]. Although the comparison of the computed results with experimental data showed that the prediction obtained using this turbulence model successfully replicated the shape of the experimental curve in terms of the power coefficient, it still significantly over-predicted the performance.

Edwards et al. [6] implemented a thorough verification and validation campaign in their study, which is treated as the first proper and complete validation of a VAWT CFD model [125]. By narrowing down a list of turbulence models and comparing the simulation results with the experimental measurements of a pitching aerofoil performed by Lee and Gerontakos [126], Edwards et al. stated that the low-Reynolds $\mathrm{SST\ k-\omega}$ model predicted the force best, showing the closest results to experimental measurements. Moreover, the flow fields predicted by the $\mathrm{SST\ k-\omega}$ model successfully captured the development and shedding of the dynamic stall vortex that was illustrated in the experiment.

Edwards et al. [6] claimed that the $\mathrm{SST\ k-\omega}$ turbulence model is the better turbulence model and satisfactorily predicts not only the forces acting on the pitching aerofoil but also the physics of the flow that accompanies it. They employed the $\mathrm{SST\ k-\omega}$ turbulence model to simulate a three-bladed VAWT with NACA0022 profile

and compared it with their experimental results. In terms of power output, the 2-D CFD model's recurrent over-prediction of turbine performance was thought to be due to the 3-D effects and losses at the tip not being considered as explained by Edwards et al.[6]. With regard to CFD flow field validation with PIV, the CFD prediction showed a similar pattern of the roll-up and shedding of pairs of stall vortices (shown in Figure 2.25). However, for the upwind section the stalling process in the simulation lagged behind the PIV by an approximately 10° difference in angular position [6] (Figure 2.25(1)). For the downwind section the CFD demonstrated a good match with the experiment although CFD showed a delay in flow reattachment (Figure 2.25(2)). Both stalling and reattachment delays in the CFD are likely to be due to the inability of the $\mathrm{SST\,k-\omega}$ turbulence model to accurately model the flows within the transitional low Reynolds numbers region. Overall, the $\mathrm{SST\,k-\omega}$ turbulence model provides satisfactory results and has been applied by many authors (e.g. [127-129])

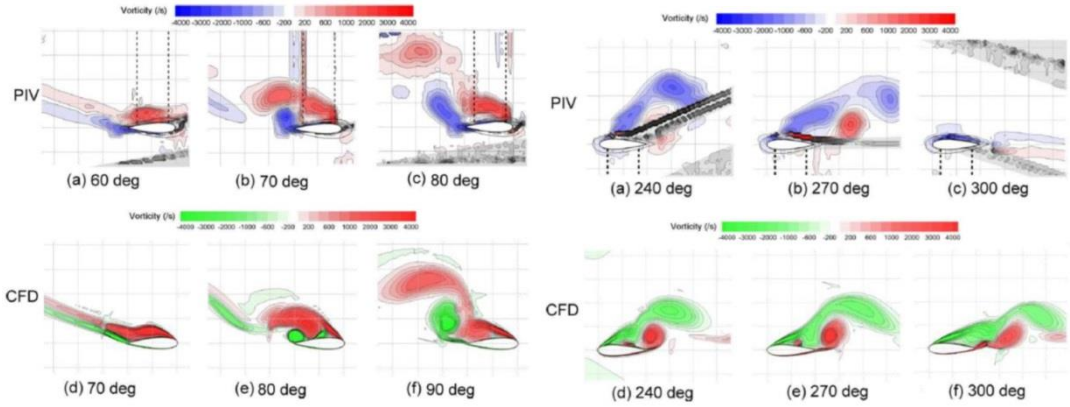

(1) Upwind section (2) Downwind section

Figure 2.25 Flow field validation by turbulence model, adopted from [6]

More recently, Danao et al. [130] investigated the VAWT by using the Transitional SST turbulence model due to its better ability to model transition Reynolds numbers. The study shows the Transitional SST model calculated $C_p - \lambda$ values closer to experiments compared to the $\mathrm{SST\,k-\omega}$ model. Meanwhile, the formation and shedding of the dynamic stall vortex at 70° as shown in Figure 2.26 was properly captured by the Transitional SST model without delay. In contrast, the $\mathrm{SST\,k-\omega}$ model still predicted the vortex to be on the blade surface at this azimuth angle.

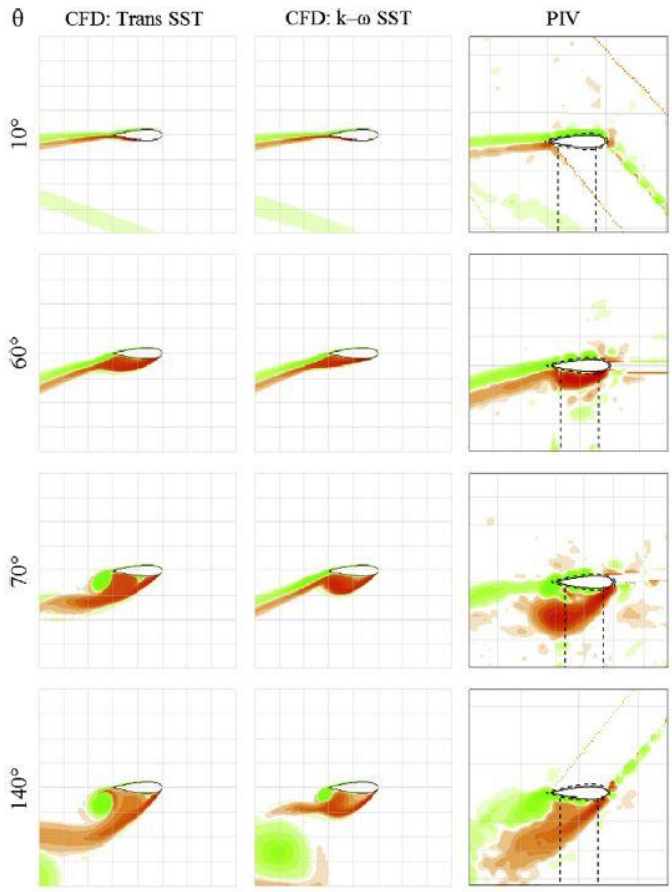

Figure 2.26 Flow field validation by Transitional SST model, adopted from [130]

2.6.2 Recent CFD studies

In order to improve the performance of the VAWT, Mohamed [44] carried out a study using a 2-D CFD model with 20 different aerofoils (symmetric and nonsymmetric) in order to maximize the output torque coefficient and the output power coefficient. Based on Mohamed' study, the S-1045 aerofoil showed an increase of the power output coefficient by 26.83% compared to the symmetric NACA0018 aerofoil presenting the most promising choice for wind energy generation. However, the poor grid resolution, especially on the trailing and leading edges, and the compromisingly low node density on the aerofoil surface cast doubt on the reliability of the results.

Castelli et al. [123] proposed a new performance prediction model based on CFD. A rectangular outer zone was created to define the whole domain with a circular inner zone containing all blades. A sliding mesh was created between the rectangular outer zone and the circular inner zone. Moreover, a rotor sub-grid was built in order to allow a precise dimensional control of the grid elements in the area close to the rotor blades. According to their study, the maximum torque values are generated during the upwind

revolution of the turbine and for azimuth positions where rotor blades are experiencing very high relative angles of attack, even beyond the stall limit. Although the average rotor power is low, the instantaneous power coefficient locally exceeds the Betz's limit for almost 40° of rotor revolution reaching a maximum value of 0.664 as shown in Figure 2.27. The authors hypothesize that this phenomenon is probably due to a sudden pressure coefficient drop concerning the whole rotor disc and the surrounding flow region which violates the assumptions of Rankine-Froude actuator disc theory.

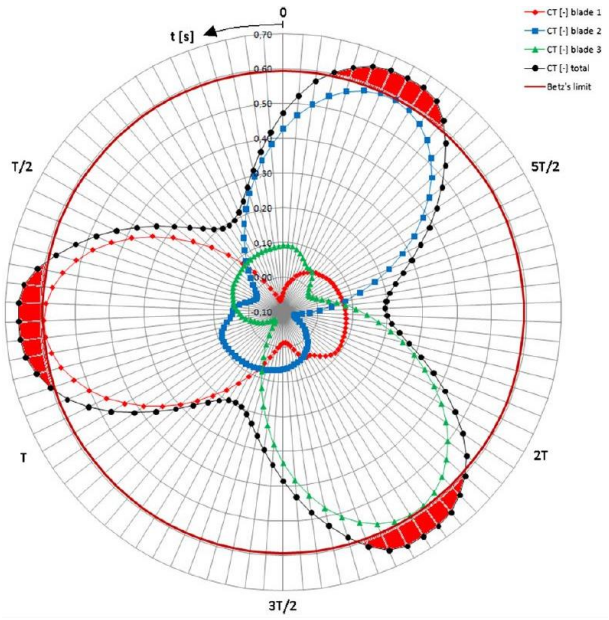

Figure 2.27 Instantaneous power coefficient as a function of time for three rotor blades [123]

Rossetti and Pavesi [64] employed both 2-D and 3-D CFD models to study the performance of an H-Darrieus wind turbine. The 2-D analysis highlighted the presence of a complex pattern of vortex, which interacted with the blades and strongly modified the overall performance. The 3-D study illustrated the great importance of 3-D effects for small tip speed ratios. When compared to 2-D results, the vortex intensity inside the rotor was significantly reduced. This is ascribed to the instability of vortices which were subjects to secondary flows along the turbine axis. The local incidence angle was reduced near the blade tip and the stall was avoided. Due to both the reduction of vortex intensity and the reduced incidence near the blade tip, turbine mean torque is expected to increase. Rossetti and Pavesi [64] also claimed that the increase in the local tip speed ratio near the tip section (larger than the tip speed ratio for the main part of the blade) appears to have positive effects on the start-up characteristics.

Danao et al. [130] applied a 2-D model to investigate the influence of unsteady wind on the performance and aerodynamics of a VAWT. The amplitude and frequency of the fluctuating wind were studied as shown in Figure 2.28. In this periodically fluctuating wind condition, overall performance was slightly improved if the following were satisfied:

- The mean tip speed ratio was just above that of the steady performance maximum
- The amplitude of the fluctuation was smaller than **10%**
- The frequency of the fluctuation was higher than **1 Hz**

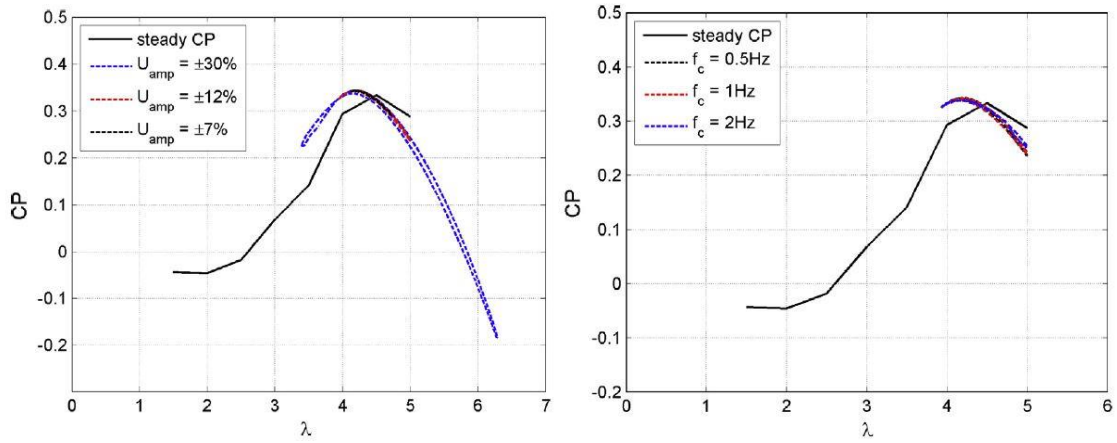

(a) (b)

Figure 2.28 Study on effect of varying wind amplitude (a) and frequency (b), adopted from [130]

Danao et al. [130] concluded that turbines operate at a mean λ that is lower than the λ for the peak performance coefficient causing them to run in the λ band with deep stall and vortex shedding. With large fluctuation in the wind speed the turbines operate in λ conditions that are drag dominated, thus reducing performance. Furthermore, under realistic conditions, higher frequencies of fluctuation marginally improve the performance of the VAWT.

Amet et al. [127] employed a 2-D CFD model to simulate the dynamic stall of a Darrieus wind turbine. The simulation closely matched the experimental measurements [131]. The lift and drag coefficients of the computed results for one revolution at $\lambda = 2$ illustrate a similar trend with a discrepancy of over-prediction of the experimental results as shown in Figure 2.29.

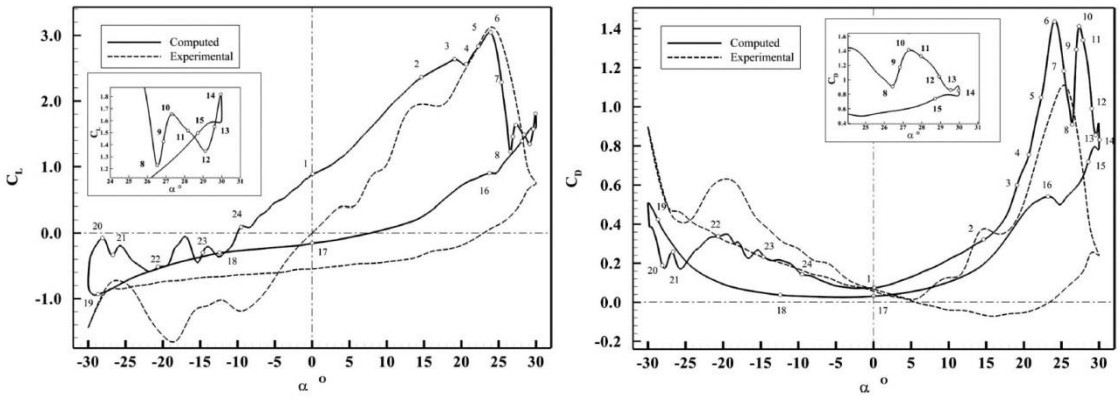

(a) (b)

Figure 2.29 Lift coefficient for one revolution at (a) and drag coefficient for one revolution at (b), [127]

Untaroiu et al. [132] used both 2-D and 3-D CFD models to investigate the self-starting capability of a wind tunnel scale VAWT. Their simulation results were compared with Hill et al.'s [11] experimental measurements [11]. The 2-D model over-predicted the final peak rotational speed by 12% while the 3-D model under-predicted it yielding an error of approximately 15%. This is consistent with the observations of Howell et al. [39]. But both 2-D and 3-D models predicted start-up 10 times faster than the experimental measurements. The CFD models failed to predict the initial velocity plateau ('dead band') resulting in the turbine accelerating approximately linearly to the peak rotational speed. The authors claimed the discrepancies between simulation and experiment are due to the inability of the $k-\epsilon$ turbulence model to accurately model the blade's near wall and flow transition on the blade surface. Moreover, Untaroiu et al. [132] claimed that regardless of which turbulence model is chosen, it can be asserted that little is gained by switching to a three dimensional approach due to a poorer mesh quality and excessive computational time. Although tip vortices may be illustrated with a 3-D model, they impact most turbines only modestly unless the height to width ratio is significantly less than 1.

Table 2.3 is created here to summarise typical recent CFD studies reviewed in this thesis.

Authors	Year	Turbulence model	Dimension	Topics
Howell et al. [39]	2010	$k-\epsilon$ RNG	2-D and 3-D	Solidity; Blade surface roughness; 3-D effects;
Castelli et al. [123]	2011	$k-\epsilon$ realisable	2-D	Aerodynamic force; Power coefficient
Edwards et al. [6]	2012	$k-\epsilon$ RNG S − A SST $k-\omega$ SST $k-\omega$ *LR*	2-D	Turbulence model validation; Flow structure examination (PIV)
Danao et al. [130]	2014	SST $k-\omega$ Transition SST	2-D	Unsteady wind effects
Mohamed [44]	2012	$k-\epsilon$ realisable	2-D	Blade shape effects
Rossetti and Pavesi [64]	2013	SAS	2-D and 3-D	3-D effects; Tip loss; Flow around the blades
Amet et al. [127]	2009	$k-\omega$	2-D	Flow structure; Wake interaction; Blade force
Untaroiu et al. [132]	2011	$k-\epsilon$	2-D and 3-D	Self-starting behaviour

Table 2.3 Summary of recent CFD studies in the literature

2.6.3 Summary

In this thesis, a 2-D CFD model is built to study the H-Darrieus wind turbine since the literature demonstrates that the 2-D model is able to reveal the most important factors that might influence turbine performance and much of the associated flow physics. The conventional model validation procedure adopted in the literature is employed to justify the choice and accuracy of the chosen turbulence model for the present CFD studies. Turbine performance and flow structure under different design parameters are investigated and special attention is paid to turbine performance at low tip speed ratios.

The CFD results also guide the design of experimental measurements performed in this study.

2.7 Conclusion

There are many design parameters that can be adjusted to change the performance of a VAWT. An outline of these variables and their impact on the rotor aerodynamics has been presented. Since a single parameter can affect turbine performance in different ways, the designer must be able to make appropriate choices of individual parameters so the end product can meet the customer's expectations.

Despite the significant number of studies conducted over the past a few decades, some fundamental aspects of VAWT performance are still not thoroughly understood

and it is only in recent years that publications on fundamental design aspects such as solidity and aerofoil profile have been published. Many performance aspects that have been investigated using mathematical models are not capable of yielding a full understanding of the flow physics. Recently, researchers have begun to take more enlightened approaches to study the flow physics aided by the continued use and development of CFD and the improvement of experimental capabilities such as Particle image velocimetry (PIV). Researchers are beginning to gain a better understanding of the influence of fundamental design parameters on the VAWT performance. However, good experimental data illustrating the performance trends associated with design parameters is still scarce and very limited work has been performed regarding turbine performance at low tip speed ratios and its self-starting capability, which is critical for small-scale VAWTs working in the built environment.

This thesis is intended to fill the gaps in the literature. Turbine performance including self-starting behaviour under various design parameters is examined experimentally and numerically. The complex flow structure around the turbine blades is also investigated and design guidelines are presented.

Chapter 3

Computational Fluid Dynamics (CFD) model description and validation

With the development of advanced CFD codes, VAWT studies can now be conducted more easily and accurately under various wind and geometry conditions. Unlike blade element momentum (BEM) based methods which usually suffer from the absence of complete and accurate aerofoil aerodynamic datasets covering the full incidence range and at appropriate low Reynolds numbers, CFD provides an alternative method to predict turbine performance with any blade geometry thanks to the inherent ability of the code to determine the aerodynamic forces through the integration of the Navier-Stokes equations in the neighbourhood of the turbine blade. Moreover CFD is able to visualize the structure of the flow field and provide better understanding of the associated aerodynamics. Nevertheless, the CFD has its disadvantages for this application:

- The turbine blades experience extreme incidence angles (far beyond stall angle) at low tip speed ratios (λ), and CFD simulations at these deep stall angles are questionable [103, 133, 134]
- It is time consuming to perform time-accurate CFD even for 2-dimensional tests [123]

A 2-D aerofoil model was initially built in this study to examine the CFD prediction of aerofoil static aerodynamic forces both at low incidence angles and deep stall angles at relatively low Reynolds numbers.

A 2-D H-Darrieus wind turbine model was then created in order to study turbine performance including the critical turbine self-starting capability under various blade profiles, wind speed, rotor radius, etc. The process involved in the development and selection of the 2-D VAWT turbulence model in this study is outlined in this chapter. A detailed description of the model features such as the boundary conditions including the inlet and outlet, the mesh around the blade and also the rotating and stationary domains is presented. Furthermore, parametric studies of time step size, the node density (mesh density) around the blade and domain side wall distance are also presented.

3.1 2-D aerofoil studies

3.1.1 Model description

In order to examine the CFD prediction of aerofoil performance at both low incidence angles and deep stall angles at low Reynolds numbers that will be experienced by small-scale VAWT blades, a 2-D aerofoil model was first created. Figure 3.1 presents the computational domain with the NACA0012 aerofoil.

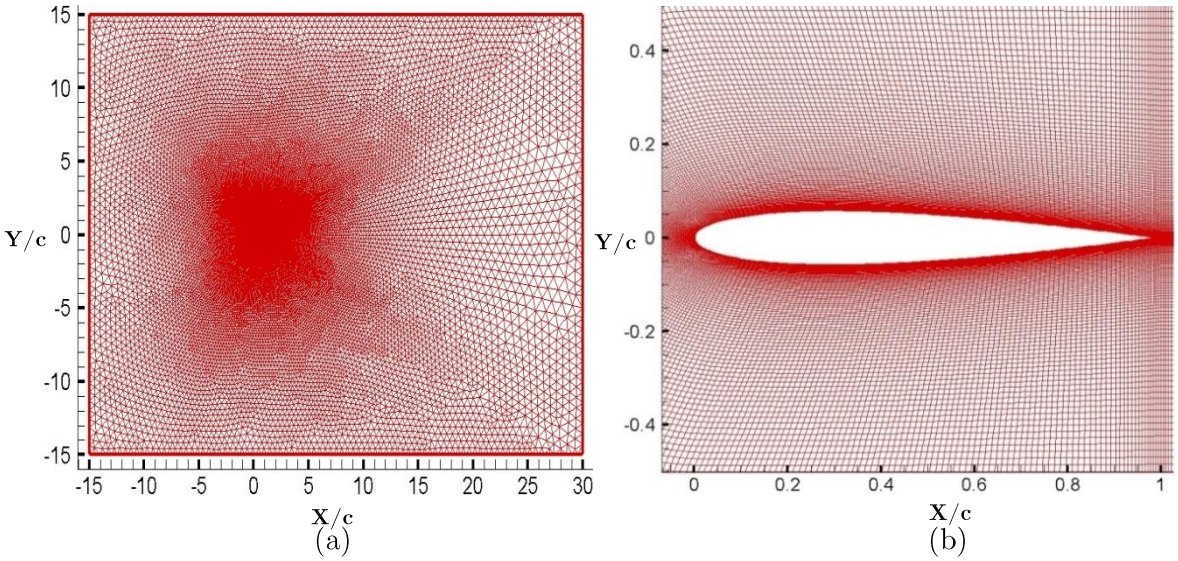

Figure 3.1 Computational domain (a) and enlarged view (b)

A hybrid mesh was employed in this model by applying an unstructured mesh (triangular elements) for the far field and a structured mesh (quadrilateral elements) around the aerofoil so as to provide more accurate predictions for the flow near the aerofoil boundary layer. The aerofoil surface had 250 nodes which were properly clustered at the leading and trailing edge where high gradients in the pressure and flow were expected. The first cell spacing on the aerofoil surface was less than $0.001c$ in the direction normal to the surface. In order to ensure sufficient boundary layer modelling, a growth rate of 1.1 was applied to the mesh inflation giving approximately 30 layers within the boundary layer. For the far field domain, a growth ratio of 1.2 was applied. The far field domain was extended 15 chord lengths upstream, above and below the blade in order to eliminate the effects of wall proximity. It was also extended 30 chords length downstream so as to make the pressure outlet as close to a uniform atmospheric pressure as possible.

The Reynolds number considered in the following validation studies was $Re = 20{,}000$ based on chord length. Since the Reynolds number was relatively low and

to make a valid comparison with the studies in the literature directly, a laminar model was adopted for all validation tests although it was claimed by Lian and Shyy [135] that the laminar flow simulation might not have the resolution to solve the flow structure for Reynolds numbers in this range. The full Navier-Stokes equations were solved with a pressure based scheme called SIMPLE (Semi-Implicit Method for Pressure-Linked Equations) [136, 137]. A 2nd-order interpolation scheme for pressure was used and a 1st-order implicit time integration was chosen for the temporal discretization with a minimum convergence criterion for each time step set to residual of 10^{-6}. Each simulation was run until the averaged force coefficient showed a deviation less than 1% from that in the previous cycle. Parameters and schemes are summarised in Table 3.1 below:

Software	Fluent 14.0
Number of cells	$\approx 114{,}000$
Number of surface nodes	250
Model	Laminar
Solution scheme	SIMPLE
Pressure interpolation	Second Order Upwind
Temporal discretization	First Order Implicit
Residual	$< 10^{-6}$
Domain length	$45c$
Domain width	$30c$

Table 3.1 Simulation parameters and schemes for 2D aerofoil model validation tests

3.1.2 Validation tests

For the 2-D aerofoil model validation, several tests were conducted based on flapping wing kinematics since the blade motion of a VAWT could be decomposed as a combined pitch and plunge motion (flapping wing) in one revolution based on Worasinchai et al.'s study [14]. The results were compared with the available data from the literature. The NACA0012 aerofoil with a chord length of $100\,\mathrm{mm}$ was used throughout all the validation tests based on the experimental models used in the literature. Aerofoil plunge motion and pitch motion are defined in Equation 3.1 and Equation 3.2 respectively as follow:

$$h(t)/c = h_0 \sin(2\pi f t + \Phi_p) \qquad \text{Equation 3.1}$$

$$\theta(t) = \theta_m + \theta_0 sin(2\pi ft + \Phi_\theta) \quad \text{Equation 3.2}$$

where h_0 is the plunge amplitude non-dimensionalized by chord length c, $\theta(t)$ depicts the pitching motion of amplitude θ_0 and frequency of f. Moreover t denotes the physical time and θ_m denotes the mean angle of attack. The phase angle between pitch and plunge is defined as $\varphi = \emptyset_\theta - \emptyset_p$. For plunge motion h_0 is defined as positive upwards and for pitch motion θ_0 is defined as positive clockwise.

Furthermore, two non-dimensional parameters are introduced in the literature: one is the reduced frequency in Equation 3.3 based on Anderson et al. [138]:

$$k = 2\pi fc/2V \quad \text{Equation 3.3}$$

the other is the Strouhal number in Equation 3.4 based on Anderson et al. [138]:

$$St = 2fch_0/V \quad \text{Equation 3.4}$$

3.1.2.1 Validation of lift and drag coefficient histories

Three validation tests were performed for this 2-D model in present study. For the first validation the aerofoil underwent pure plunge motion. The reduced frequency,k, was 3.93 and the non-dimensional amplitude, h_0, was 0.0125. An implicit scheme with 80 time steps per flapping cycle was chosen to solve the problem. The results from the present study were compared with the results from Lian and Shyy [135] and Young and Lai [139]. In Lian and Shyy's study, a laminar model of an implicit scheme with 100 time steps per flapping cycle was employed while in Young and Lai's study, an explicit scheme with 16,860 time steps per flapping cycle was applied. The Figure 3.2 shows the histories of lift and drag coefficient.

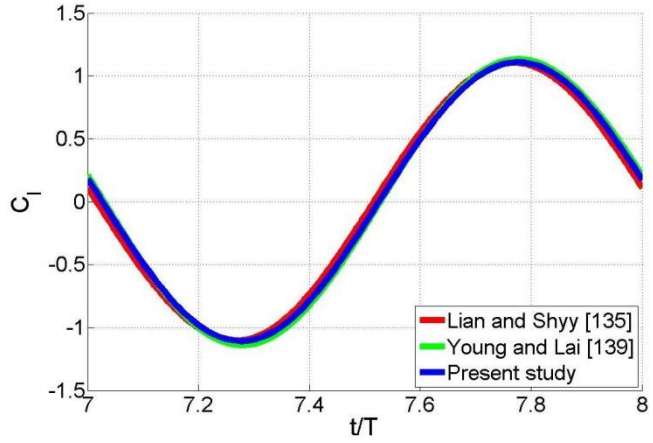

(a)

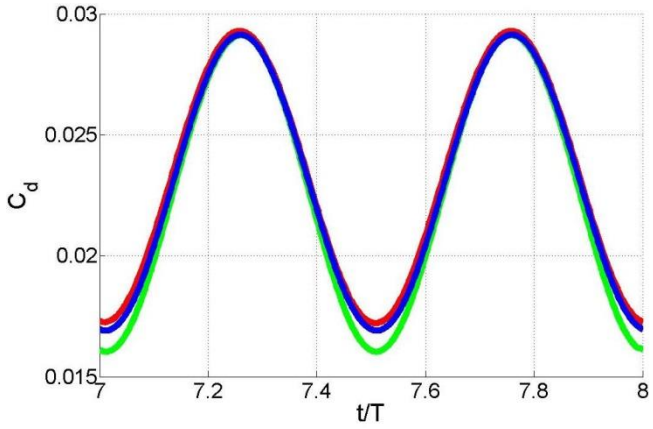

(b)

Figure 3.2 Validation test of (a) lift and (b) drag coefficient for aerofoil under pure plunge motion at $Re = 20{,}000,\ k = 3.93,\ h_0 = 0.0125$ and $St = 0.03$

As it can be seen the drag varies at twice the frequency of lift. Both lift and drag coefficient show good agreement with the results from literature except some discrepancies in the trough of the drag. The time averaged drag coefficient from present study is 1.1% lower than Lian and Shyy's result and 1.9% higher than that of Young and Lai. At this amplitude and reduced frequency, both pressure and viscous forces contribute to the drag and the aerofoil is referred as drag-producing [140].

3.1.2.2 Validation of wake structure

Lai and Platzer [140] studied the wake structure of the NACA0012 experimentally by releasing non-intrusive dye in a water tunnel at the Reynolds number of 20,000 based on chord length. The corresponding numerical simulations were performed by Young and Lai [139] and Lian and Shyy [135]. In this study the particle tracking method was

employed in order to illustrate the streakline. One of Lai and Platzer's study cases was chosen here as $k = 3.93$ and $h_0 = 0.05$. Figure 3.3 shows the results.

It can be seen that the aerofoil wake structure from present study shows qualitative agreement with experimental results and other simulation results from the literature. Both experiment and simulations show a reversed Karman Vortex Street, indicating a momentum surplus in the wake compared to the upstream and a thrust is generated as a consequence.

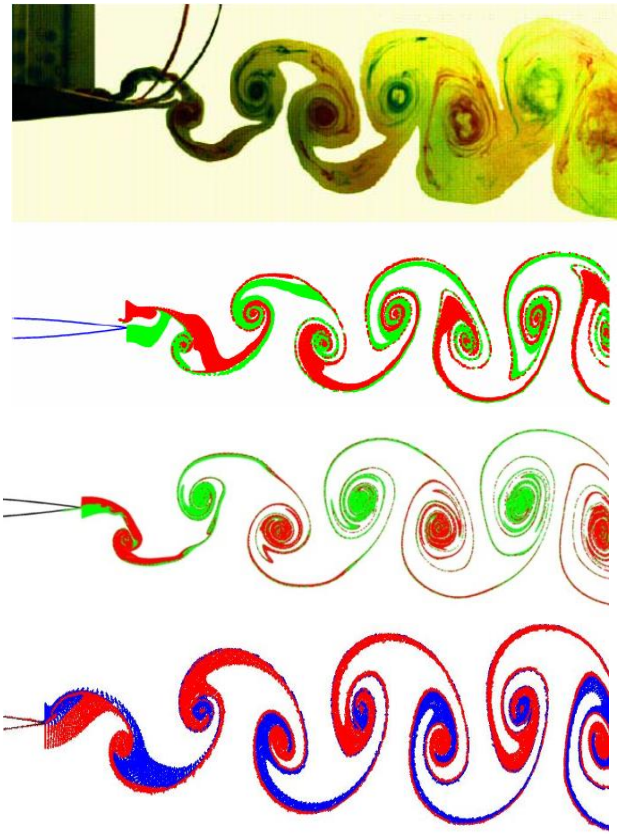

Figure 3.3 Validation test of wake structure for aerofoil under pure plunge at $Re = 20{,}000$

3.1.2.3 Validation of thrust coefficient

The third validation tested in present study was for the NACA0012 aerofoil under combined pitch and plunge motion. The non-dimensional plunge amplitude was $h_0 = 0.75$ and the nominal angle of attack (γ_0) was 15° ($\gamma_0 = -\theta_0 + tan^{-1}2kh_0$). Meanwhile, the phase angle between aerofoil pitch motion and plunge motion was $\varphi = 75^\circ$ (pitch leading). The mean thrust coefficients at different Strouhal numbers were compared with the experimental measurements performed by Anderson et al. [138]

in a water tunnel and numerical simulations conducted by Lian and Shyy [135] and Young and Lai [139].

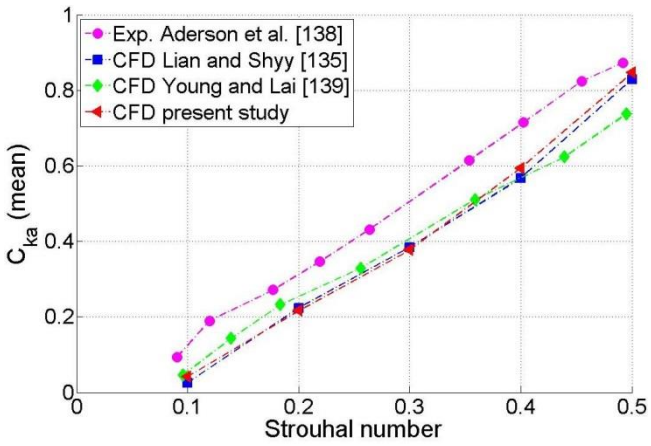

Figure 3.4 Validation test of aerofoil thrust coefficient as a function of Strouhal number at $Re = 20{,}000$.

As shown in Figure 3.4, the results from this study match closely to that of Lian and Shyy [135]. However there are some discrepancies between the results from current study and that of Young and Lai [139], especially at high Strouhal number. For $St = 0.5$, this study shows a mean thrust coefficient 17% higher than that from Young and Lai. Moreover, all the numerical simulations under-predict the mean thrust coefficient when compared with the experimental results. This under-prediction might result from the incapability of CFD code to accurate predict the aerofoil performance in the stall region.

In conclusion, all the above three validation tests demonstrate that the 2-D aerofoil model created in this study is able to provide valid and accurate results for future studies.

3.2 2-D H-Darrieus wind turbine study

3.2.1 Model description

A two-dimensional CFD model was used to represent the VAWT (H-Darrieus type) since the literature [6, 39, 85, 127] demonstrated that a 2-D CFD model was able to reveal the most important factors that might influence the turbine performance and much of the associated flow physics. 3-D effects including the blade tip loss and blade-support arm junction might be significant but were considered to be of secondary importance in this particular study. Two dimensional VAWT models were essentially VAWTs with infinite aspect ratio blades (no tip loss). The effect of blade aspect ratio

(AR) came in the form of shifting the C_p curve upwards and to the right as AR increases [48], but the general shape was maintained. According to Untaroiu et al.'s assertion [132] that although the 3-D effects like tip vortices might be illustrated by a 3-D model, they impacted most turbines only modestly unless AR ratio was significantly less than 1. Regardless of which turbulence model was chosen, little was gained by switching to a three dimensional approach due to a poorer mesh quality and immense computational time requirements [132]. Therefore the 3-D models were not considered in present study.

A sliding interface boundary condition was defined between an inner circular rotating domain that contained the rotor and a stationary rectangular outer domain, which ensured that both mass and momentum were conserved during the simulation (see Figure 3.5). Two symmetry boundary conditions were employed for the two side walls while a velocity inlet and a pressure outlet are used for the test section inlet and outlet, respectively. The rotation of the inner domain relative to the outer domain is prescribed within the solver that implements the algorithm for the sliding mesh technique. Care was taken such that the mesh on both sides of the interface had approximately the same characteristic mesh cell size in order to avoid excessive numerical diffusion and obtain faster convergence [141]. Based on the parametric studies detailed in the following sections, the near blade and the entire mesh surrounding blades including the extent of the boundaries were defined.

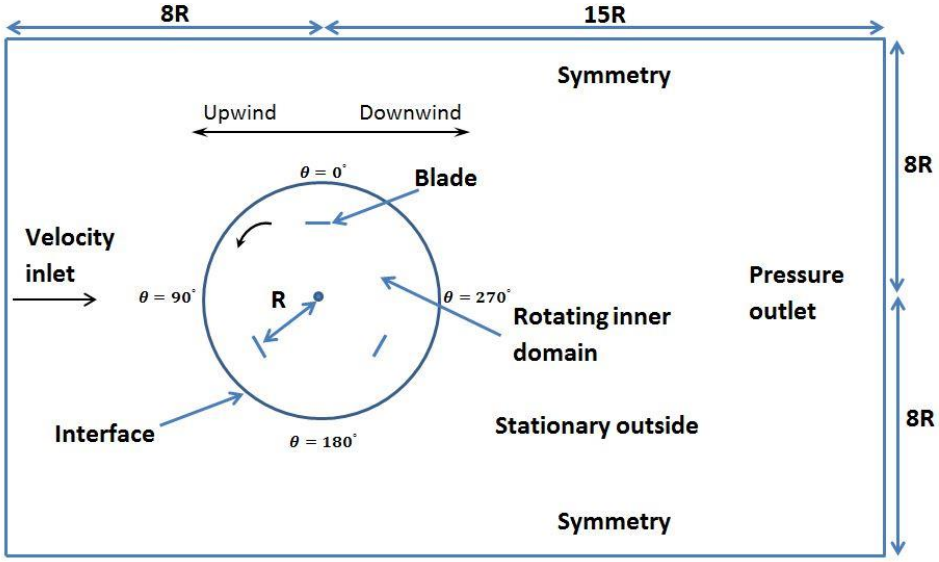

Figure 3.5 Schematic drawing of the 2-D CFD simulation domain and mesh strategy

A 2nd-order interpolation scheme for pressure was used along with a 2nd-order upwind discretization scheme for other parameters. The gradients required for the

discretization of the convective and diffusive fluxes were computed using the Green-Gauss Node Based approach. A 1st-order implicit time integration was chosen for the temporal discretization with a minimum convergence criterion for each time step set to a residual of 10^{-6}. Each simulation was run until the current averaged torque coefficient showed a deviation of less than 1% compared with that of the previous revolution (examples are shown in Figure 3.6). This reqiured 6~18 revolutions depending on the λ and a maximum CPU time of about 110 hours for a 4-processor, 3 GHz computer. A parameter summary table for the setting up of the 2-D H-Darrieus wind turbine in this study is provided in Table 3.2.

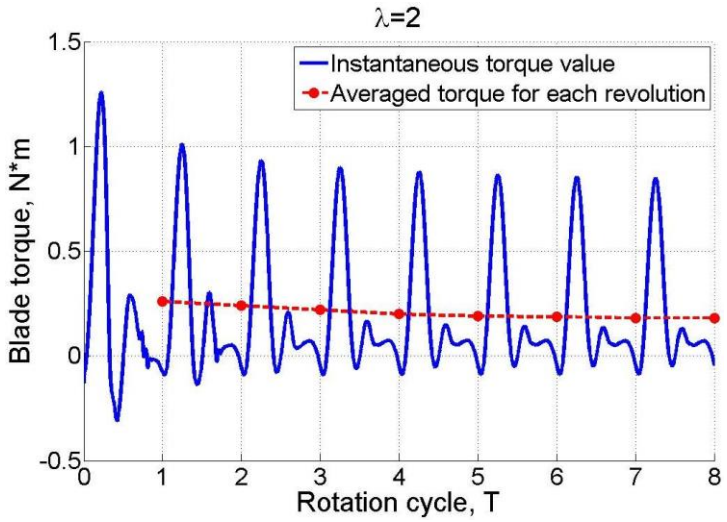

(a)

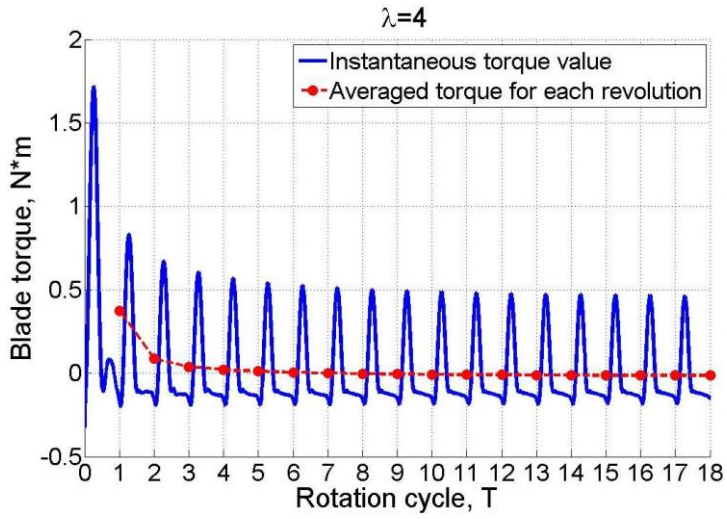

(b)

Figure 3.6 Torque ripple of one blade for $\lambda = 2$ (a) and $\lambda = 4$ (b). The averaged torque value for the last revolution cycle shows less than 1% deviation compared with the previous averaged value

Software	Fluent 14.0
Number of cells	Maximum 250,000
Number of surface node	250
Model	Transition SST
Solution scheme	SIMPLE
Pressure interpolation	Second Order Upwind
Spatial discretization	Second Order Upwind
Temporal discretization	First Order Implicit
Time step	$\delta t = 0.36^{\circ}$

Table 3.2 Summary of parameters for setting up the 2-D CFD H-Darrieus wind turbine

3.2.2 Parametric studies

The parametric studies were performed in this section in order to enable an appropriate choice of model features. It includes a mesh density study, a downwind boundary location study and a time step size study. The parametric studies were conducted at both low and high tip speed ratios to ensure each parameter chosen in this study can produce accurate results for the whole tip speed ratio range.

3.2.2.1 Mesh independency study

Node density is considered to be very important since it dictates the coarseness and fineness of the mesh so can affect the accuracy of the aerodynamic forces generated on the blade surface. To reduce errors caused by a poor mesh quality, a comprehensive study was conducted in which a range of node densities was tested.

Each blade surface was meshed by a structured mesh with approximately 200, 250 or 300 nodes and the mesh was properly clustered in the leading and trailing edge where high gradients in pressure and flow were expected. A node density study was performed to determine the appropriate number of surface nodes. Figure 3.7(a). illustrates that at $\lambda = 1$ all the node points attained maximum torque at approximately $\theta = 60^{\circ}$ with negligible difference seen between the two larger densities (250 and 300), whereas for the 200 nodes density the peak torque is predicted lower than the other two cases. For the turbine downwind region, the torque curve for the two larger node densities match each other closely with some small discrepancies predicted by the 200 nodes. The results and trend at $\lambda = 3.2$ (Figure 3.7 (b)) for the three node densities are similar with that at $\lambda = 1$.

Comparing the effects of node density based on the average torque attained, the 200 node density attained $T_{ave} = 0.007\ N \cdot m$ at $\lambda = 1$ followed by 250 node density with a $T_{ave} = 0.011\ N \cdot m$ and 300 node density with a $T_{ave} = 0.012\ N \cdot m$. Meanwhile at $\lambda = 3.2$, the corresponding averaged torque for 200, 250 or 300 nodes density is $0.0527\ N \cdot m$, $0.0545\ N \cdot m$ and $0.0551\ N \cdot m$, respectively. The results clearly illustrate that the tests for larger node densities (250 and 300 nodes) show no significant difference. Therefore the blade surface was meshed with 250 nodes in this study.

An unstructured mesh instead of the usual C-grid was used for the remaining inner circular domain (see Figure 3.8 (a) and (b)) because the wake is not fixed on a specific path relative to the blade but rather varying greatly in direction especially at low tip speed ratio. Moreover, it is much easier to create an unstructured mesh than a C-grid.

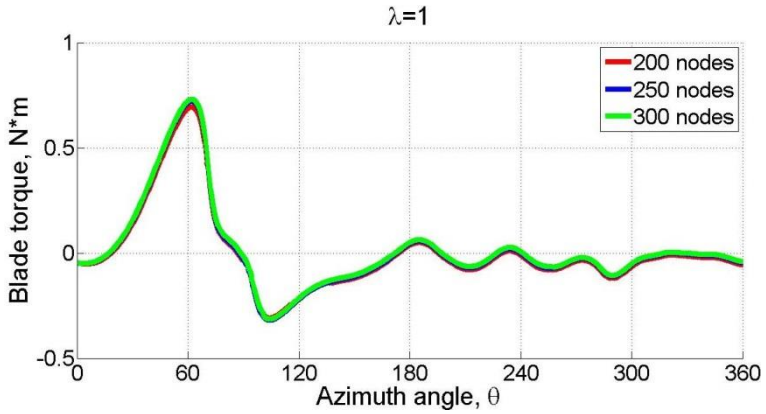

(a)

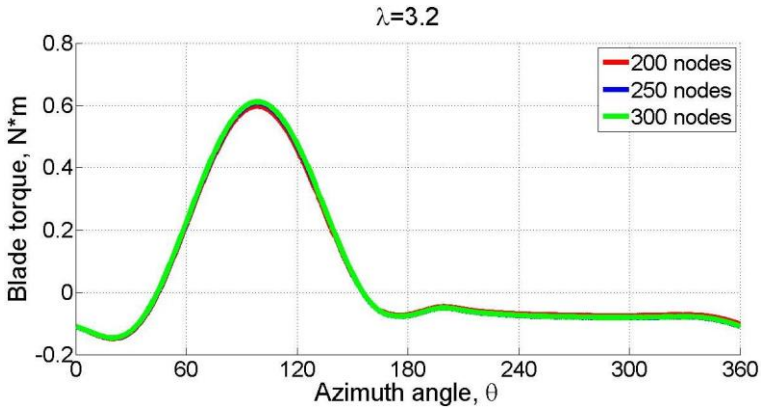

(b)

Figure 3.7 Node density study at $\lambda = 1$ (a) and $\lambda = 3.2$ (b)

The first cell height was less than $0.001c$ in order to ensure a y^+value lower than 1, which is the limit of the turbulence model that was chosen for the following simulations [141]. In order to ensure sufficient boundary layer modelling, a growth rate of 1.1 was applied to the mesh inflation around the blade giving approximately 30 layers within the boundary layer (Figure 3.8 (a)). For the remaining domain of inner circular and

outside far field, a growth rate of 1.2 was used (see Figure 3.8 (b) and (c)). A smoothing algorithm in the meshing software was used to reduce the angle skewness of the cells such that the maximum was observed to be less than 0.7.

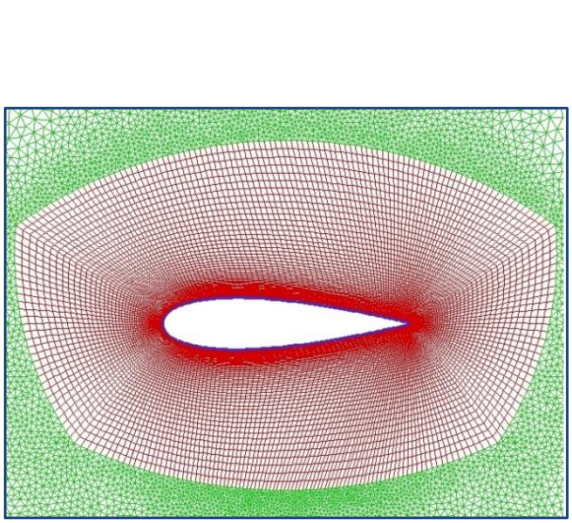

(a)

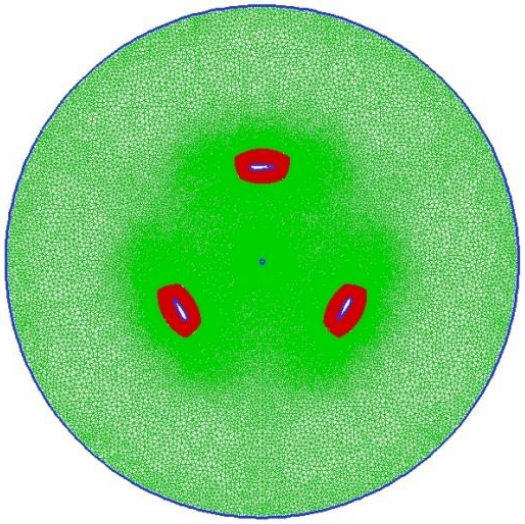

(b)

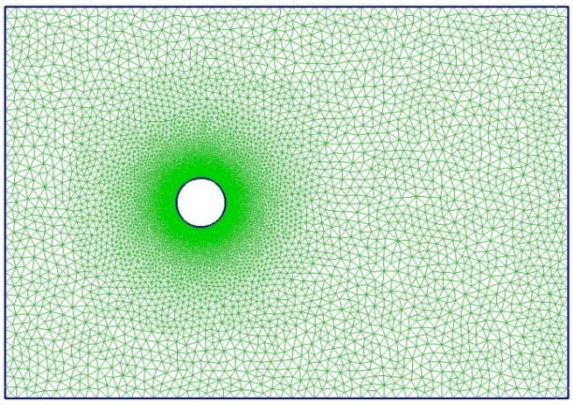

(c)

Figure 3.8 Mesh images of the model: (a) near blade structured mesh, (b) unstructured inner rotating domain, (c) unstructured outer domain.

Mesh quality is summarised in Table 3.3.

Blade surface y^+	< 1
Cell skewness	< 0.7
Growth rate around blades	1.1
Growth rate for the farfield	1.2
Number of layers at the blade boundary	~30

Table 3.3 Mesh quality summary table

3.2.2.2 Boundary location examination

An outlet distance study was conducted to investigate the effects of wake development on the performance of the H-Darrieus wind turbine. The distance between the pressure outlet and the centre of the turbine (shown in Figure 3.5) was set to be $10R$, $15R$ and $20R$ (R is based on the largest rotor diameter investigated in present study). The turbine power coefficient against tip speed ratio curve is plotted in Figure 3.9. As can be seen that the results of $15R$ matches closely to that of $20R$. In contrast, the $10R$ case under-predicts the turbine peak power output at $\lambda = 2$ by approximately 5%. Moreover, power coefficients from $10R$ case at high λ are also slightly lower than other two cases investigated here.

To reduce computation time without compromising the accuracy of the simulation, the downwind pressure outlet was set to be $15R$. Meanwhile the velocity inlet was placed $8R$ upwind and a total width of $16R$ for the two symmetry side walls was determined. (see Figure 3.5).

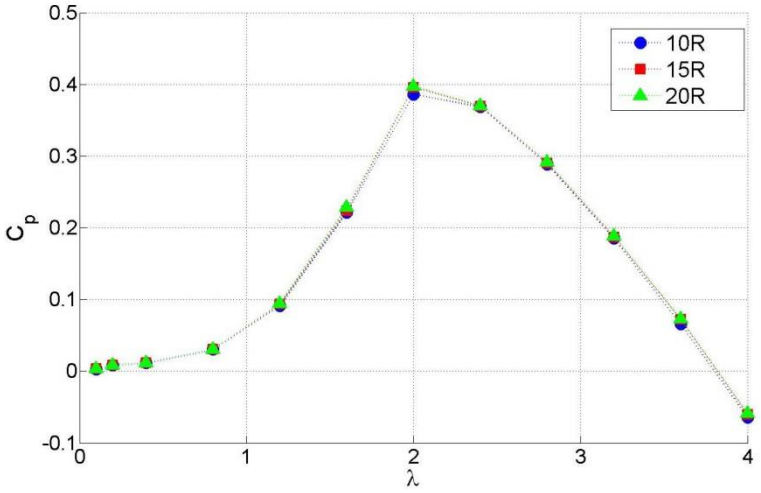

Figure 3.9 Pressure outlet location study for the 2-D model

3.2.2.3 Time step independence study

Sufficient temporal resolution is necessary to ensure proper unsteady time dependent simulation of the VAWT. Since the turbine rotates about an axis the choice of different time step sizes are equivalent to specific rotational displacements along the azimuth. In this study the temporal discretization was achieved by imposing a physical time step equal to the lapse of time the rotor takes to make a certain degree rotation. Three different degree equivalent time step sizes were tested. The lowest tested δt was equal to a $\delta t = 0.18^{\circ}$ and was multiplied by factors of 2 and 4 in order to get $\delta t = 0.36^{\circ}$ and $\delta t = 0.72^{\circ}$. The corresponding number of time steps for one revolution were $2{,}000$,

1,000 and 500, respectively. The time step independence studies were conducted at low tip speed ratio of $\lambda = 1.6$ and high tip speed ratio of $\lambda = 3.2$ in order to provide more representative results.

Figure 3.10 presents the plot of torque against azimuth angle for three different time steps. At $\lambda = 1.6$ a negligible variation is seen when $\theta < 120^{\circ}$ for all the three time step sizes investigated in present study. The maximum torque was predicted at approximately $\theta = 82^{\circ}$ and the stalling characteristics of the blade is captured at all values of δt. Between $\theta = 120^{\circ}$ and $\theta = 180^{\circ}$, $\delta t = 0.72^{\circ}$ shows the most deviation but the peaks and troughs are still in synchronise with the other two δt cases. For the downwind region $180^{\circ} < \theta < 360^{\circ}$, $\delta t = 0.36^{\circ}$ follow the same trend of $\delta t = 0.18^{\circ}$ with a small difference predicted around $\theta = 250^{\circ}$. However $\delta t = 0.72^{\circ}$ under-predicts the torque for the majority of the azimuth angle at the downwind region compared with the other two cases. With regard to the averaged torque, the corresponding results for $\delta t = 0.18^{\circ}$, $\delta t = 0.36^{\circ}$ and $\delta t = 0.72^{\circ}$ are 0.0126, 0.0128 and 0.0121, respectively.

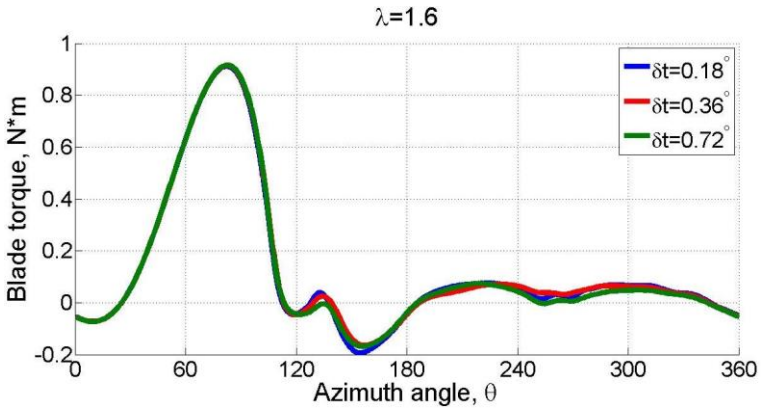

(a)

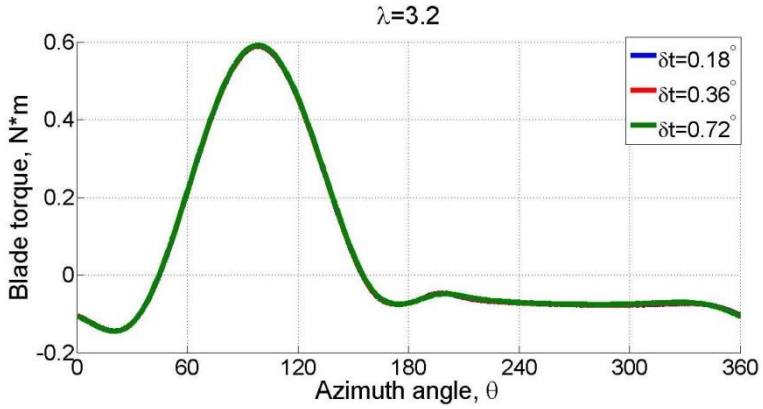

(b)

Figure 3.10 Time step size study at $\lambda = 1.6$ (a) and $\lambda = 3.2$ (b)

For $\lambda = 3.2$, all three time step sizes match each other closely as show in Figure 3.10 (b). There is very little variation between the three cases with the only noticeable difference in the torque ripples from $\theta = 220^{\circ}$ to $\theta = 340^{\circ}$ that $\delta t = 0.72^{\circ}$ slightly under-predict the blade negative torque. Since sufficient time resolution was required for accurate simulations in this study, without increasing computational time unnecessarily and as well as avoiding convergence problems with the use of lower time step, $\delta t = 0.36^{\circ}$ were chosen and adapted for all the modelling runs in this study.

3.2.3 2-D model validation and turbulence model selection

In order to validate the CFD model developed in present study, the results were compared with experimental measurements from Castelli et al. [123]. The blade connection position was set at $0.5c$ according to the experiment. The validation was not considered exact, since the CFD model was 2-D, while the actual problem was 3-D. Nevertheless, a good 2-D CFD model will provide substantial insight into the factors driving the performance of the VAWT and a key element of present work is to obtain the trend of turbine power coefficient (C_p) against tip speed ratio (λ).

Several turbulence models were employed in the literature to numerically investigate the turbine performance. Some typical studies are listed in Table 3.4:

Author(s)	Dimension	Turbulence model
Howell et al. [39]	2-D and 3-D	$\mathrm{k}-\epsilon$ RNG
Castelli et al. [123, 124]	2-D	Enhanced wall treatment $\mathrm{k}-\epsilon$ Realisable
Untaroiu et al. [132]	2-D and 3-D	Scalable wall effects $\mathrm{k}-\epsilon$ Standard
Amet et al. [127]	2-D	$\mathrm{k}-\omega$ TURBFLOW
Edwards et al. [6]	2-D	low-Reynolds SST $\mathrm{k}-\omega$
Danao et al. [130]	2-D	Transition SST

Table 3.4 Typical turbulence model employed in the literature

Based on the literature, three candidate turbulence models were selected to compare with the experimental measurements in the validation tests: the Enhanced wall treatment $\mathrm{k}-\epsilon$ Realisable turbulence model, the low-Reynolds SST $\mathrm{k}-\omega$ turbulence model and the Transition SST turbulence model. The parameters used for setting up

the turbulence model are summarised in Table 3.5 and the results are illustrated in Figure 3.11.

Intermittency	1
Turbulent kinetic energy (m^2/s^2)	1
Turbulent dissipation rate (m^2/s^3)	1
Specific dissipation rate $1/s$	1

Table 3.5 Turbulence model parameter

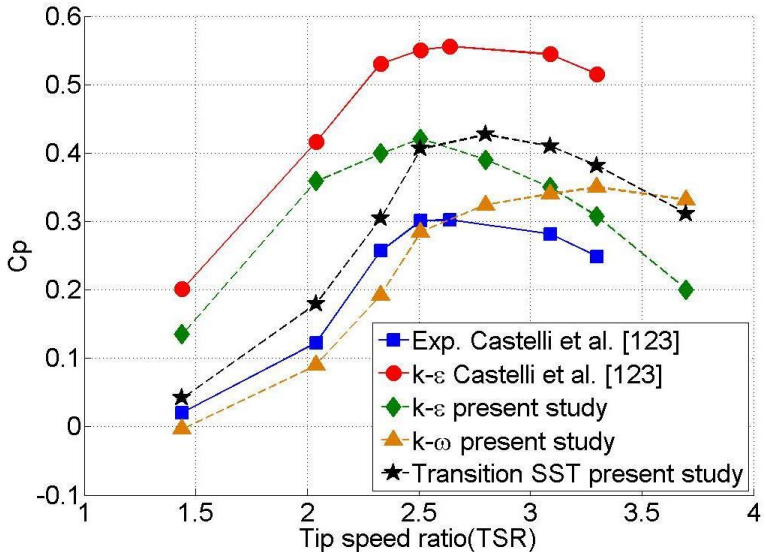

Figure 3.11 Validation tests and turbulence model selection

The power coefficient (C_p) at a range of tip speed ratios was examined by using the above turbulence models. As can be seen in Figure 3.11, the $k-\epsilon$ turbulence model significantly over predicts the power coefficient for the whole range tip speed ratio, with a maximum $C_p = 0.41$ predicted at $\lambda = 2.5$. In contrast, the SST $k-\omega$ turbulence model in present study under-predicts the C_p when $\lambda < 2.8$. This indicates a significant error since the 2-D model does not take any 3-D effect into consideration which would result in an over-prediction of turbine performance as observed in the literature. Moreover the SST $k-\omega$ predicts a peak $C_p = 0.35$ around $\lambda = 3.3$ while the experimental measurements indicate a peak value around 2.8. With regard to Transition SST turbulence model, the simulation over-predicts the C_p starting from $\lambda = 1.4$ all the way up to $\lambda = 3.3$, which is consistent with the literature. Meanwhile the Transition SST model predicts a maximum C_p of 0.43 at $\lambda = 2.8$ which follows the same trend as observed in the experimental results, where the maximum C_p lies between $\lambda = 2.6$ and $\lambda = 3.1$. Furthermore the Transition SST model results from this

study provide a closer match to the experiment than does Castelli et al.'s CFD simulation [123] with a $k-\varepsilon$ turbulence model.

In conclusion, according to the validation tests the general performance trend of the turbine predicted by the Transition SST turbulence model matches well with the experimental data and it has been selected as the better model in this study.

Chapter 4

Computational Fluid Dynamics (CFD) study results

4.1 2-D aerofoil study results

4.1.1 Static aerodynamic force

The validated 2-D aerofoil model was employed to examine the static aerodynamic forces predicted by CFD. The aerofoil profile used was the NACA0018 section since the thick symmetric NACA series was widely used in VAWT studies and shows reasonably good turbine performance. The results were compared with the experimental measurements conducted by Gerakopulos et al. [83] and Timmer et al. [84] at a similar Reynolds number of $150{,}000$. The transition SST turbulence model was applied in this study as it has better capability of predicting laminar-to-turbulent flow behaviour at this low Reynolds number [141]. The y^+ value was kept below 1 in order to meet the requirement of the Transition SST turbulence model. The upstream turbulence intensity in the CFD model was 0.3% based on Gerakopulos et al.'s [83] experiment. The temporal discretization was achieved by imposing a fixed physical time step of 1×10^{-4} s. A 2nd-order interpolation scheme for pressure was used along with a 2nd-order upwind discretization scheme for other parameters. Parameters are summarised in Table 4.1.

Software	Fluent 14.0
Turbulence model	Transition SST
Turbulence intensity	0.3%
Solution scheme	SIMPLE
Pressure interpolation	Second Order Upwind
Temporal discretization	First Order Implicit
Residual	$< 10^{-6}$
Aerofoil surface y^+	< 1
Domain length	$45c$
Domain width	$30c$

Table 4.1 Simulation parameters and schemes for 2-D static aerodynamic prediction

Figure 4.1 and Figure 4.2 show the results. The CFD prediction of lift coefficient matches closely with both sets of experimental measurements at low incidence angles $\alpha < 6^{\circ}$, showing a linear increase of lift coefficient with the increase of angle of attack. However for $6^{\circ} < \alpha < 16^{\circ}$ the CFD results under-predict the lift force and demonstrate a delayed aerofoil stall at $\alpha = 16^{\circ}$. In contrast the corresponding stall angle measured by Gerakopulos et al. [83] and Timmer et al. [84] is 12° and 14° respectively. For the post-stall prediction, CFD illustrates a rapid lift increase predicted between the incidence angles of $\alpha = 16^{\circ}$ and $\alpha = 30^{\circ}$ while the experimental measurements from Timmer et al. [84] shows a gradual increase of lift force. The CFD model over-predicts the lift coefficient at post-stall angles demonstrating inaccurate predictions using the Transition SST turbulence model at deep stall angles.

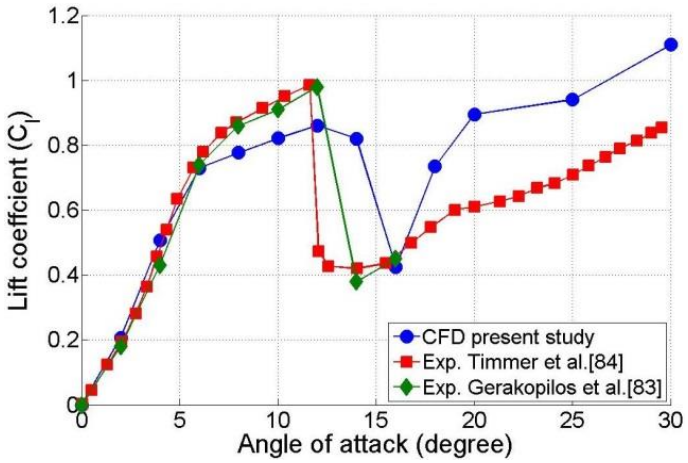

Figure 4.1 CFD lift coefficient compared with experimental measurements. NACA0018, $Re \approx 150{,}000$.

In terms of drag coefficient shown in Figure 4.2, the CFD results are in close agreement with Timmer et al.'s [84] measurements at $\alpha < 12^{\circ}$. The CFD predicts a rapid C_d increase after the aerofoil stalls, which is consistent with the experimental trend, but starts at a higher incidence angle of $\alpha = 16^{\circ}$. Although Timmer et al. [84] did not measure the aerodynamic force at deep stall angles, the unusually large value ($C_d > 3$) for drag coefficient calculated at $\alpha = 90^{\circ}$ by CFD indicates an over-prediction and inaccuracy of C_d.

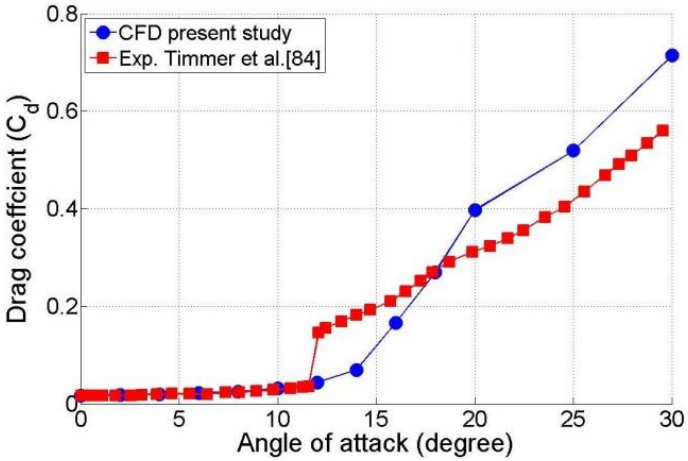

Figure 4.2 CFD drag coefficient compared with experimental measurements. NACA0018, $Re \approx 150{,}000$.

4.1.2 Aerofoil surface pressure coefficient

At the tested Reynolds number of $Re = 150{,}000$, the laminar boundary layer on the aerofoil upper surface undergoes laminar-to-turbulent transition, which results in flow reattachment closing the recirculating flow into a laminar separation bubble. The Transition SST turbulence model employed in the present CFD successfully captured this laminar separation bubble.

Figure 4.3 illustrates the aerofoil surface pressure coefficient before stall and at the stall angle of $\alpha = 16^{\circ}$. A constant pressure region followed by sudden surface pressure recovery signifies the presence of a separation bubble on the aerofoil surface when $\alpha < 16^{\circ}$. Increasing the angle of incidence causes the separation bubble to move upstream and to reduce in length, which is qualitatively consistent with the study performed by Gerakopulos et al. [83]. When the aerofoil stalls at 16° (Figure 4.3 (d)), the bubble bursts resulting in a full leading-edge stall characterised by a sudden and significant reduction in the suction pressure peak (up to 60% reduction) and lift coefficient.

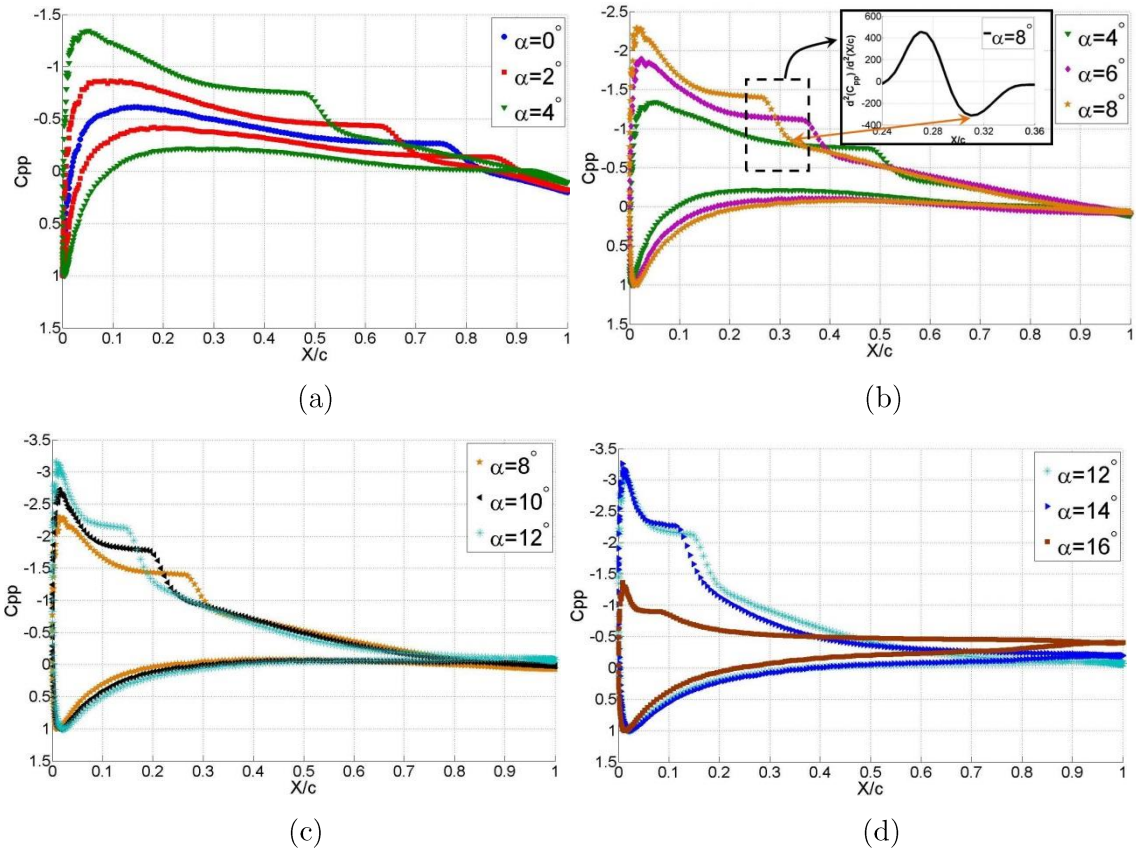

Figure 4.3 Aerofoil surface pressure coefficient predicted by CFD by using Transition SST turbulence model. $Re = 150{,}000$

In order to compare the CFD results of bubble separation and reattachment location with those measured by Gerakopulos et al. [83], the same methodology of location as that used by Gerakopulos et al. was applied in this study. The separation location was estimated as the intersection of (i) a linear fit to the surface pressure recovery region following the suction peak and (ii) a linear fit to the nearly constant surface pressure region within the laminar separation bubble region. To estimate the reattachment location, a shape-reserving polynomial fit to the discrete surface pressure distribution in the regions of constant surface pressure and subsequent rapid surface pressure recovery was used. The reattachment location can be identified as the location downstream of the separation point where a rapid decrease in the rate of surface pressure recovery is observed as proposed by O'Meara and Muelle [142]. Therefore in accordance with this approach the reattachment location was estimated as the location of the local minimum in the second derivative of the shape preserving polynomial fit (an example is provided in Figure 4.3 (b) at $\alpha = 8^{\circ}$). In order to further validate this method, the skin friction coefficient was examined and the separation/reattachment locations indicated by skin friction coefficients match with those calculated by using above methods.

Figure 4.4 clearly demonstrates that the CFD is able to predict the separation and reattachment location of the laminar bubble on the aerofoil surface accurately. Figure 4.4 further illustrates the advancing of the bubble towards the leading edge and the reduction of bubble length with the increase of angle of attack. Moreover, Figure 4.4 shows two distinct regions for both the separation curve (S) and reattachment curve (R), which will be referred to as Region I and Region II. Region I is associated with a nearly linear reduction of S (or R) from $\alpha = 0^{\circ}$ to $\alpha = 6^{\circ}$, whereas Region II is associated with a more gradual linear reduction of S (or R) from $\alpha = 8^{\circ}$ to the stall angle. According to Gerakopulos et al.'s study [83] this rate of change in separation and reattachment locations with the angle of attack is linked to the slope change of lift curve as can be seen in Figure 4.1(b).

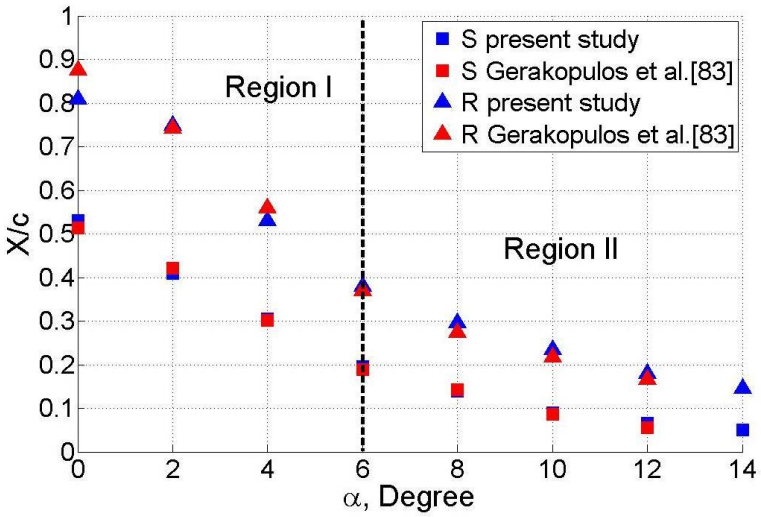

Figure 4.4 Laminar separation bubble separation and reattachment locations against the incidence angle predicted by CFD in this study compared with the experimental measurements [83] at $Re = 150{,}000$. S is separation location. R is reattachment location.

4.1.3 Conclusion

Based on the 2-D static aerofoil aerodynamic study performed in this study, the following conclusions can be drawn:

- The 2-D CFD with Transition SST model is able to provide a reasonably good prediction for aerofoil lift and drag coefficients at low incidence angles (below stall angle). The predicted results demonstrated a sudden aerofoil stall behaviour characterised by a sudden decrease of lift force and sudden increase of drag, which

is in agreement with the experimental trend. Nevertheless, The CFD significantly over-predicts the aerodynamic lift and drag at deep stall angles.

- The Transition SST model successfully captured the laminar separation bubble formed at the aerofoil surface at low Reynolds numbers. The locations of bubble separation and reattachment closely match those measured by experiment [83]. The burst of the laminar separation bubble which is responsible for the aerofoil stall is also successfully captured by CFD but at a delayed incidence angle.
- By comparing the static lift coefficients predicted by CFD with those experimental measurements, the CFD results also shows two distinct lift slope regions. These two regions are linked to the rate of advancement of bubble separation and reattachment locations.

4.2 2-D H-Darrieus wind turbine study results

Several H-Darrieus wind turbine design parameters that were discussed in Chapter 2 were investigated in this section by using the validated 2-D H-Darrieus wind turbine model. The examined parameters include: turbine solidity, blade profile, blade pitch angle and Reynold number. Focus will be put on turbine performance at low tip speed ratios under different geometric conditions. Turbine self-starting capability will also be examined and discussed.

4.2.1 Turbines under different solidities

Among the many factors that influence turbine aerodynamic behaviour, solidity (defined as $\sigma = {}^{nc}/_{R}$) plays an important role since it has a strong influence on turbine performance affecting C_p variation against λ. The solidity also determines the rotational velocity at which the turbine reaches its maximum performance coefficient. Solidity can be modified by changing the number of blades (n), blade chord length (c) and rotor radius (R). In this study the rotor radius (R) was changed while keeping the blade chord length (c) and number of blades (n) constant in order to modify the σ. The widely used NACA symmetric aerofoil profile with large thickness, the NACA0018, was initially adopted. Four different solidities were investigated and Figure 4.5 shows the results.

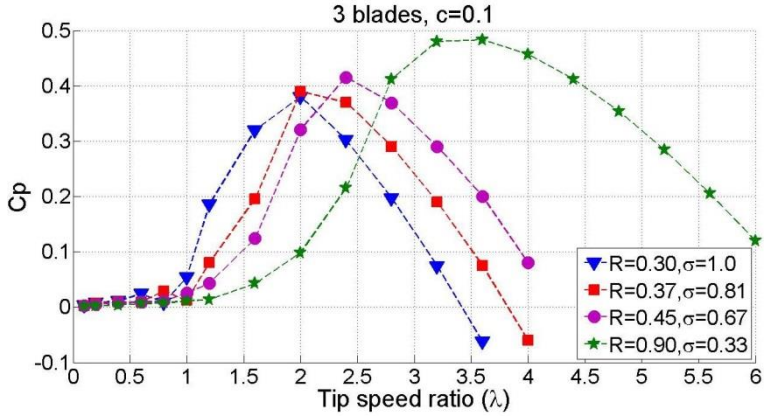

(a)

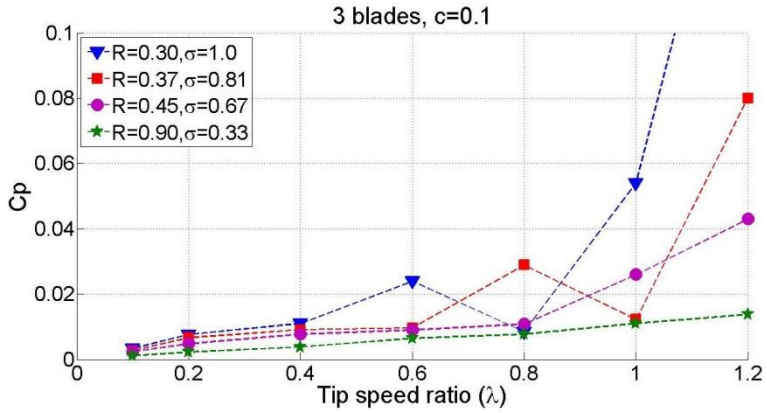

(b)

Figure 4.5 (a) Solidity effects on turbine performance with NACA0018 blades and (b) enlarged view. Radius R and chord length c are in meters. Upstream wind speed $V = 6\ m/s$.

By increasing the solidity from 0.33 to 1.0, the corresponding peak C_p decreases from about 0.49 to 0.39. However, the turbine's maximum power is achieved at a lower tip speed ratio. The maximum C_p occurs at $\lambda \approx 2$ for $\sigma = 1.0$ while the maximum C_p occurs at $\lambda \approx 3.3$ for $\sigma = 0.33$ as shown in Figure 4.5 (a). The influence of solidity on turbine performance found in this study is consistent with previous studies (e.g.[40, 143]).

The enlarged view (Figure 4.5 (b)) indicates that all four different solidities examined in this study demonstrate a turbine self-starting capability since the predicted C_p is always positive at low tip speed ratios (ignoring any system resistance). Larger solidity shows a slightly larger power coefficient at low λ indicating that the turbine with larger solidity is more efficient at low λ. Nevertheless, the enlarged view also shows that for the two scenarios with large solidity of $\sigma = 1$ and $\sigma = 0.81$, a sudden decrease of C_p is observed at $\lambda = 0.6$ and $\lambda = 0.8$, respectively. A detailed study

of the flow structure was conducted in order to shed some light on the reason for this sudden fluctuation. As it can be seen in Figure 4.6, the vorticity magnitude is plotted at azimuth angle $\theta = 0^{\circ}$ at $\lambda = 0.8$ for the turbines under the above four different solidities. At $\sigma = 1$ and $\sigma = 0.81$, the turbine experiences strong mutual aerodynamic interactions between the wakes generated by the blades (Figure 4.6 (a) and Figure 4.6 (b)). According to the study performed by Mohamed [144], the strong wake effect will cause significant deterioration of the turbine's overall performance, which explains the sudden decrease of C_p at certain tip speed ratios shown in Figure 4.5 (b). With the increase of rotor radius (decrease of turbine solidity), the distance between two blades becomes larger resulting in a significant decay of wake before reaching the later blades (see Figure 4.6 (c)). When the rotor radius is increased to $R = 0.9$ m ($\sigma = 0.33$, Figure 4.6 (d)), the wake interaction between the three turbine blades is extremely low and the blades can be treated independently.

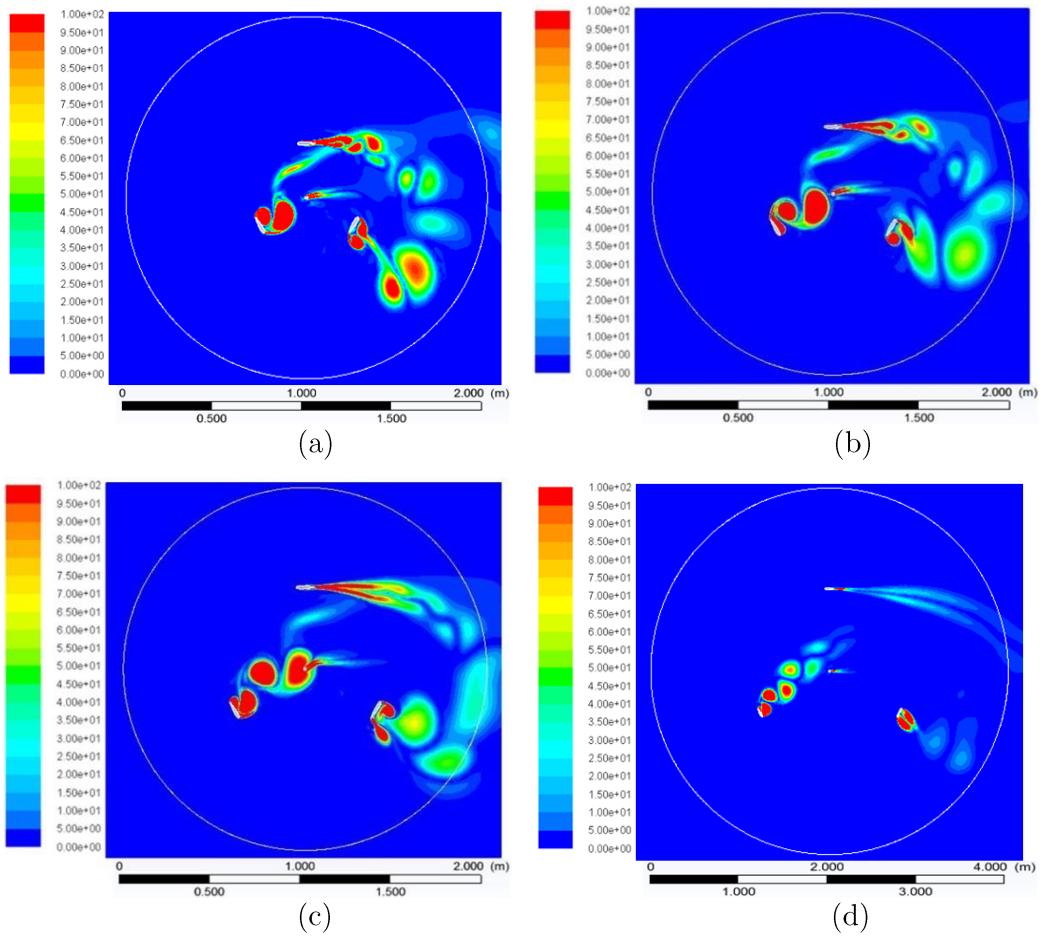

Figure 4.6 Flow structure (vorticity) at $\theta = 0^{\circ}$ and $\lambda = 0.8$ for turbines at different solidities: (a) $c = 0.1$ m, $R = 0.3$ m, $\sigma = 1$; (b) $c = 0.1$ m, $R = 0.37$ m, $\sigma = 0.81$; (c) $c = 0.1$ m, $R = 0.45$ m, $\sigma = 0.67$ and (d)$c = 0.1$ m, $R = 0.9$ m, $\sigma = 0.33$. NACA0018 and $V = 6$ m/s.

This wake interaction was further studied by looking at the blade tangential force which is plotted against the azimuth angle as the turbine is rotated (shown in Figure 4.7). It can be clearly seen that due to the strong wake interaction (larger solidity) the blade stalls later at a larger azimuth angle with higher peak thrust force. This is probably a result of increased turbulence intensity and flow curvature leading to the delayed stall, which was later experimentally examined in present study. However, the strong wake interaction for $\sigma = 1$ at this tip speed ratio of $\lambda = 0.8$ also results in a prolonged negative thrust band from $\theta \approx 80^{\circ}$ to $\theta \approx 180^{\circ}$ significantly reducing the overall averaged thrust (torque) force, which is consistent with the sudden C_p decrease shown in Figure 4.5.

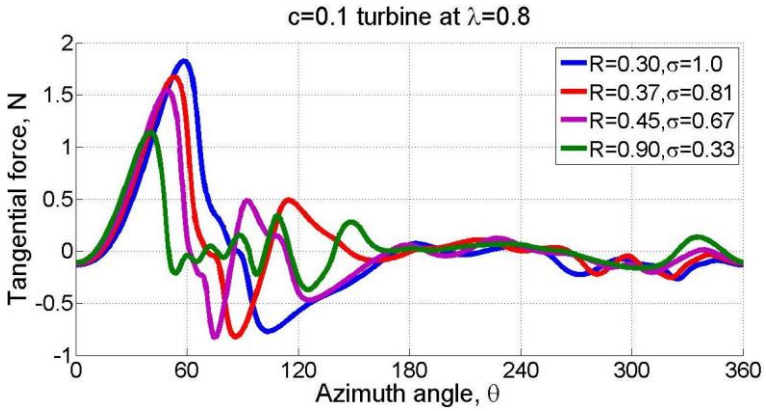

Figure 4.7 One blade thrust force against azimuth angle at different turbine solidity. NACA0018 and $V = 6\ \mathrm{m/s}$.

With regard to how solidity influences the turbine self-starting capability, the total power against tip speed ratio curve is plotted in Figure 4.8. Turbines with larger solidity clearly demonstrate a better self-starting capability since more power is extracted from the wind at low tip speed ratios (start-up period), although there are some fluctuations at certain tip speed ratios due to the strong mutual wake interaction explained above. Moreover, the low power period, which is responsible for the plateau behaviour or 'dead band' shown in Figure 2.4, is much shorter for turbines with larger solidity and this is also beneficial to a turbine designed to achieve self-starting.

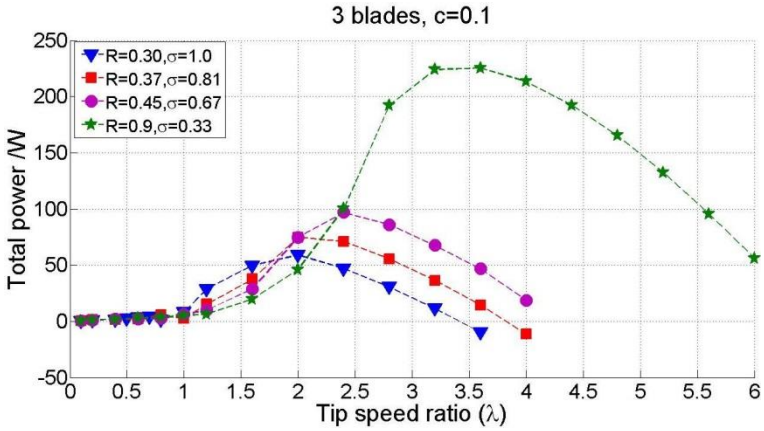

Figure 4.8 Total power extraction for the turbine under different solidities. Radius R and chord length c are in meters. NACA0018 and $V = 6\ \mathrm{m/s}$.

In conclusion, based on the CFD study turbines with larger solidity achieve their maximum power output at a lower tip speed ratio but with a lower absolute value of peak power coefficient. However, better turbine performance at low tip speed ratios is achieved, which benefits the turbine's ability to self-start. Therefore an optimal solidity could be determined in order to achieve quick turbine self-starting while maintaining relatively high efficiency.

4.2.2 Turbines performance under given solidity but with different combinations of turbine radius and blade chord length

Although the variation of turbine performance with different combinations of blade number and chord length was investigated by Castelli et al. [40] and Bedon et al. [143], this study focused on how the turbine performance was influenced by different combinations of turbine radius (R) and blade chord length (c) when solidity was kept constant. Three cases were examined: $c = 0.1\ \mathrm{m}, R = 0.3\ \mathrm{m}$; $c = 0.15\ \mathrm{m}, R = 0.45\ \mathrm{m}$; $c = 0.3\ \mathrm{m}, R = 0.9\ \mathrm{m}$. Case I with the smallest chord length and rotor radius was a reference case and the parameters were multiplied by factors of 1.5 and 3 in order to create case II and case III with the same solidity of $\sigma = 1.0$.

Figure 4.9 compares the turbine performance for the three different combinations with the same solidity of 1.0. It can be clearly seen that although the three cases show similar performance trends, the turbine with larger blade chord length indicates a better performance over the whole working range. This increase in turbine performance is expected since a larger blade chord length results in a larger blade Reynolds number and hence better blade performance (higher lift). Moreover, a larger blade chord length increases the blade surface area resulting in greater aerodynamic force.

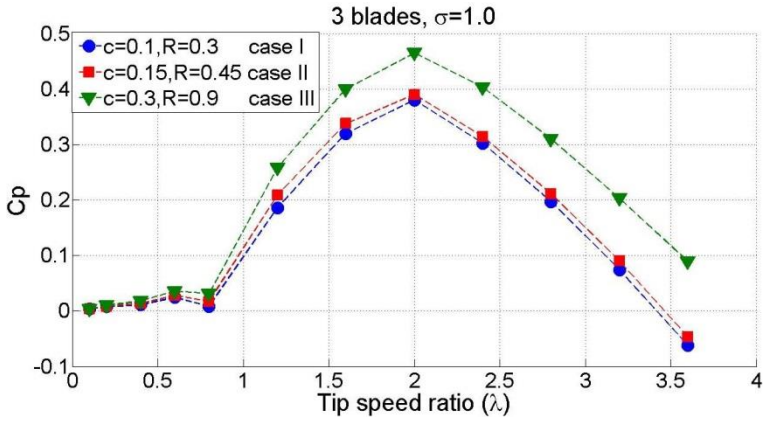

Figure 4.9 Turbines under the same solidity of $\sigma = 1.0$ with different combination of blade chord length and rotor radius. Radius R and chord length c are in meters. NACA0018 and $V = 6\ \mathrm{m/s}$.

The relationship between the chord length of the blades and the turbine performance was further studied by looking at the torque generated by a blade against the azimuth angle (shown in Figure 4.10) as the turbine was in rotation. At $\lambda = 0.4$, the peak torque generated by a blade with $c = 0.3\ \mathrm{m}$ reaches about $1.33\ \mathrm{N \cdot m}$. In comparison, the peak torque for $c = 0.15\ \mathrm{m}$ and $c = 0.1\ \mathrm{m}$ is $0.85\ \mathrm{N \cdot m}$ and $0.35\ \mathrm{N \cdot m}$ respectively. All three cases show similar behaviour since the peaks and troughs occur at very similar azimuth angles, following the same shape and trend. Between $0^{\circ} < \theta < 60^{\circ}$, the blade experiences dynamic stall and the stall angle for the above three cases increases with the increase of the blade Reynolds number (blade chord length). The predicted peak torque for the three cases occurs at $\alpha = 30.7^{\circ}$, $\alpha = 31.6^{\circ}$ and $\alpha = 32.6^{\circ}$ respectively, which is calculated from the azimuth angle.

It must be noted that the wind tunnel static measurement performed in this study (shown in Chapter 7) indicates the NACA0018 stall at around $\alpha = 14^{\circ}$. However the CFD study here for the turbine blade demonstrates a delayed blade stall due to the dynamic effect. Experimental measurements were performed in this study to further examine this dynamic stall effect.

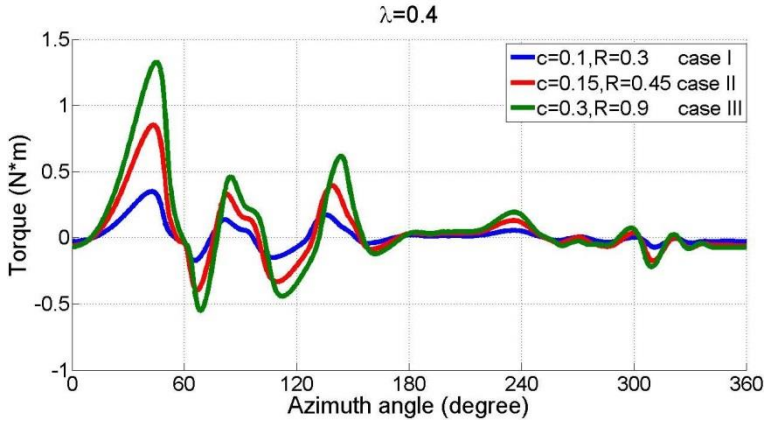

(a)

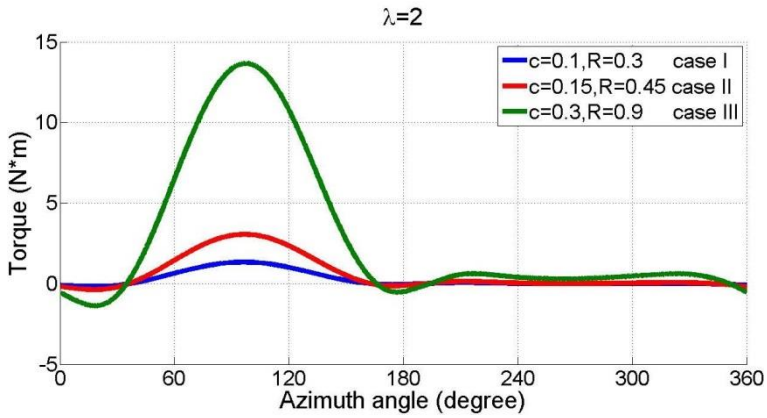

(b)

Figure 4.10 Blade torque against azimuth angle at two tip speed ratio of $\lambda = 0.4$ and $\lambda = 0.8$. NACA0018 and $V = 6\ \mathrm{m/s}$.

At $\lambda = 2$, the peak torque generated by a blade with $c = 0.3\ \mathrm{m}$ rockets to $13.6\ \mathrm{N \cdot m}$ which is almost 4 times and 9 times higher than that for $c = 0.15\ \mathrm{m}$ and $c = 0.1\ \mathrm{m}$, respectively. Nevertheless, the torque peak for the three cases at $\lambda = 2$ occurs at almost the same incidence angle (about $\theta = 96^{\circ}$, which corresponds to an incidence angle $\alpha = 27.8^{\circ}$) indicating at this relative high tip speed ratio the incidence range is significantly reduced and the blade no longer experiences dynamic stall. This was further confirmed by the examination of the turbine wake which illustrated similar flow structures for all three cases (shown in Figure 4.11 at $\theta = 0^{\circ}$).

Furthermore, it is interesting to note that although the blade Reynolds number increases with the increase of chord length, the torque generated by the blade in the downwind region ($180^{\circ} < \theta < 360^{\circ}$) for all three investigated cases shows very low values. This is consistent with previous studies that showed that most of the useful torque (power) was generated by the turbine in the upwind region [64, 123].

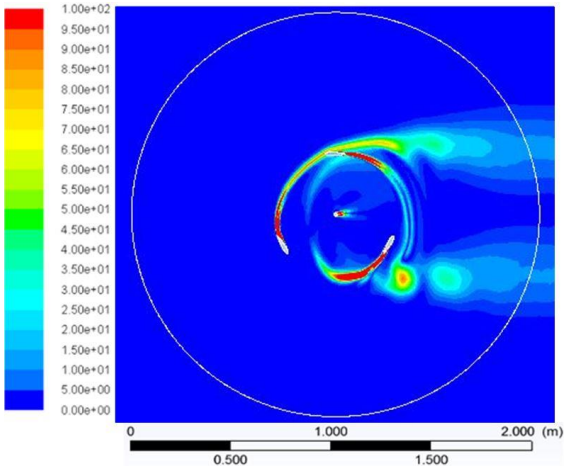

(a) Case I

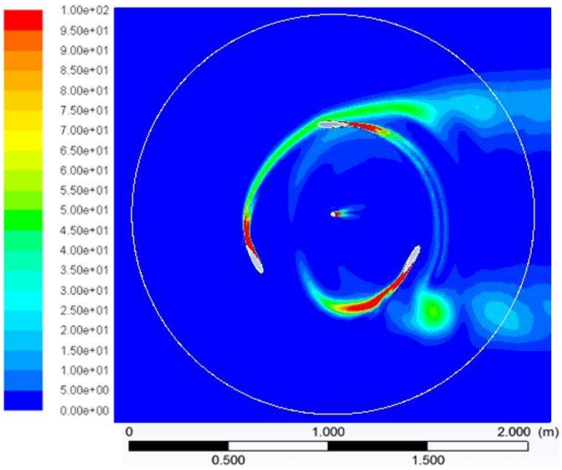

(b) Case II

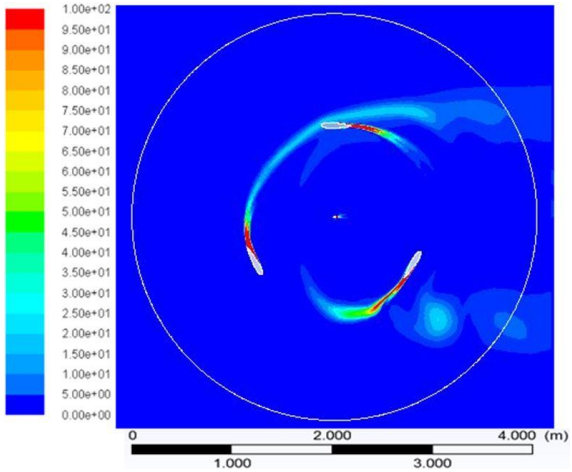

(c) Case III

Figure 4.11 Flow structure (vorticity) at $\lambda = 2$, $\theta = 0^{\circ}$ for turbines under the same solidity with different combinations: (a)$c = 0.1$ m, $R = 0.3$ m; (b)$c = 0.15$ m, $R = 0.45$ m; (c) $c = 0.4$ m, $R = 0.9$ m

With regard to turbine self-starting capability, although under given solidity turbine performance is improved for the larger combination of c and R, the blade mass is also increased resulting in larger turbine inertia and the spoke (support arm) length is increased as well leading to larger system resistance. Therefore there is no guarantee, based on this 2-D CFD study, that a turbine with a larger blade (under given solidity) has a better self-starting capability or that the self-starting time can be reduced. Further studies including Blade Element Momentum (BEM) and experimental measurements were performed to further examine the combination effect on the turbine self-starting capability and the results will be shown in the following chapters.

Some conclusions can be drawn according to the CFD study about turbines of a given solidity with different combinations of blade chord length and rotor radius:

- At a given solidity, turbines with larger blade chord length show better performance over the whole range of tip speed ratios. The CFD model successfully captured the blade dynamic stall behaviour at low tip speed ratios. Experimental data needs to be collected to further support the considerable large dynamic stall delay predicted by CFD.
- Further studies needs to be conducted to examine the combination effect on turbine self-starting capability considering turbine inertia and system resistance. No solid conclusion can be drawn based on the 2-D CFD study only.

4.2.3 Turbines with different blade profiles

Following a review of the literature, four typical and widely used blade profiles for small-scale VAWT were investigated and compared in this study. The blades of interest were:

- NACA0018 and NACA0021 because the symmetric NACA00xx series with relatively large thickness are the most widely used profiles and demonstrate relatively good turbine performance as explained in Chapter 2.
- The DU06W200 profile, which was designed specifically for VAWT application which has 20% thickness with 0.8% camber. This blade profile demonstrated better turbine performance especially during the starting period (low tip speed ratio) according to Claessens [57].
- The NACA4415 profile, which had a maximum camber of 4% and was suggested by Kirke and Lazauskas [43] as showing good turbine self-starting capability.

Tests and comparison were performed at two solidities of $\sigma = 0.67$ and $\sigma = 0.81$ by changing the rotor radius while keeping the chord length and number of blades constant. The results are presented in Figure 4.12 and Figure 4.13.

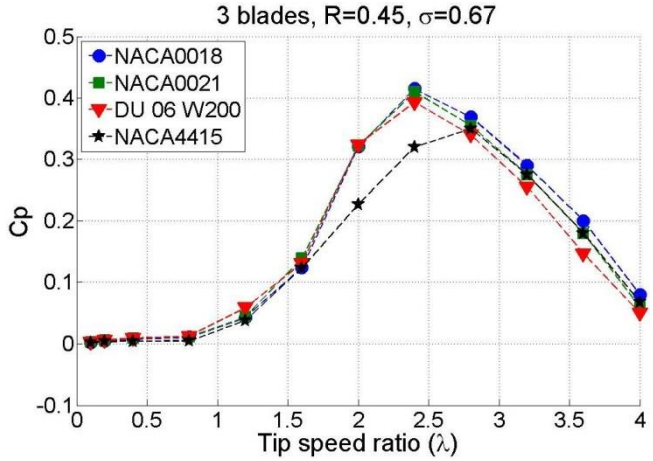

(a)

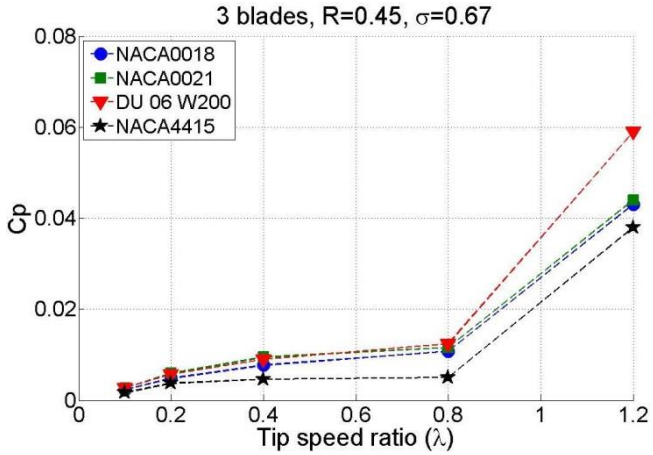

(b)

Figure 4.12 (a)Turbine performance comparison with different blades and (b) enlarged view at $\sigma = 0.67$. Radius R is in meters. $V = 6\ \mathrm{m/s}$.

At $\sigma = 0.67$, the NACA0018 reveals a very similar turbine performance to the NACA0021 over the entire working range. The NACA0018 demonstrates a slightly lower C_p compared with NACA0021 when $\lambda < 2$. In contrast, at high tip speed ratios where the incidence angle is reduced the NACA0018 shows better turbine performance than the NACA0021. This might be due to the larger drag force that results from the larger thickness of the NACA0021. In comparison with the NACA00xx series, the DU06W200 shows enhanced turbine performance at $\lambda < 1.2$ indicating potentially faster turbine self-starting capability. However the peak power predicted from the DU06W200 is 0.393, which is 5.6% lower than NACA0018 with a peak $C_p = 0.415$. Conversely, the cambered NACA4415 blade does not present any improvement at low tip speed ratios compared to the NACA00xx series (see Figure 4.12 (b)) and the predicted maximum C_p is significantly lower than any of the other three cases. In

addition the NACA4415 reaches its maximum C_p at a higher λ of approximately 2.8 than the other three cases, which reach theirs at a λ of about 2.4.

Similar conclusions can be drawn for $\sigma = 0.81$ (show in Figure 4.13) where the DU06W200 demonstrates the best profile in terms of turbine self-starting capability with slightly lower peak C_p compared with NACA00xx series. The cambered NACA4415 blade geometry does not show any improvement at low tip speed ratios and the turbine maximum C_p is significantly lower than the other blades studied.

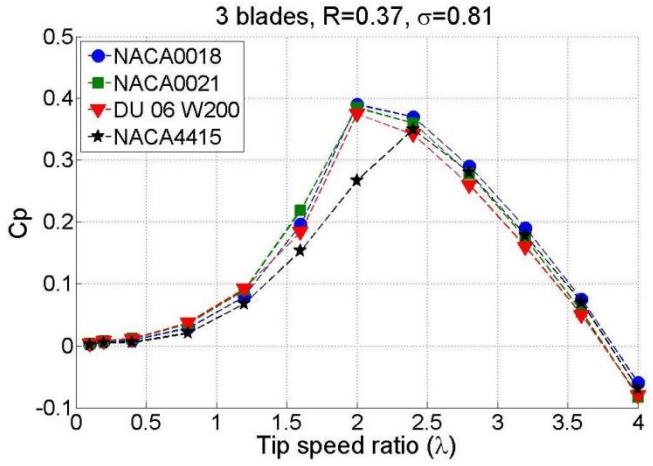

(a)

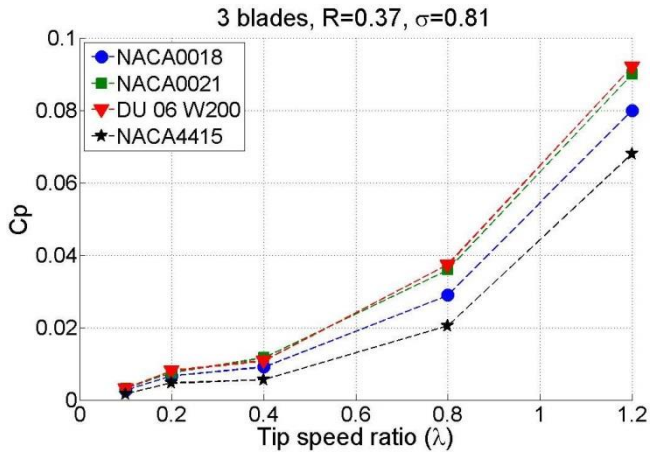

(b)

Figure 4.13 (a) Turbine performance comparison with different blades and (b) enlarged view at $\sigma = 0.81$. Radius R is in meters. $V = 6$ m/s.

In conclusion, these four different blade profiles all show positive C_p at low tip speed ratio demonstrating the turbine is able to self-start at the investigated solidity. The NACA4415 does not seem to bring any benefit compared with the other three blades which all represent good choices for a small-scale H-Darrieus wind turbine designed to achieve self-starting.

4.2.4 Turbines with fixed pitch angle

Pitch control can enable the turbine blades to generate the optimal thrust force at all azimuth angles, resulting in better turbine power output and efficiency. However, since the small-scale H-Darrieus wind turbine is the primary interest of this study, active pitch control is not considered due to its complexity. Instead, an alternative easy way to change the blades aerodynamics by using fixed pitch will be investigated numerically in this section.

CFD tests were performed at six values of pre-set pitch angle and the definition of pitch in this study is shown in Figure 2.16. These values were -8°, -4°, -2°, 0° (no pitch), 2°, 4°. The aerofoil profile was NACA0018 with a rotor radius of $R = 0.37$ m and blade chord length $c = 0.1$ m leading to a solidity of $\sigma = 0.81$. The upstream wind speed was $V = 7$ m/s. Figure 4.14 presents the results.

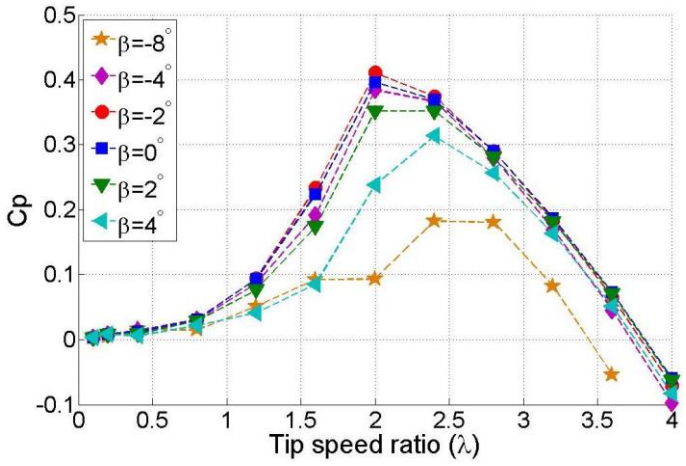

(a)

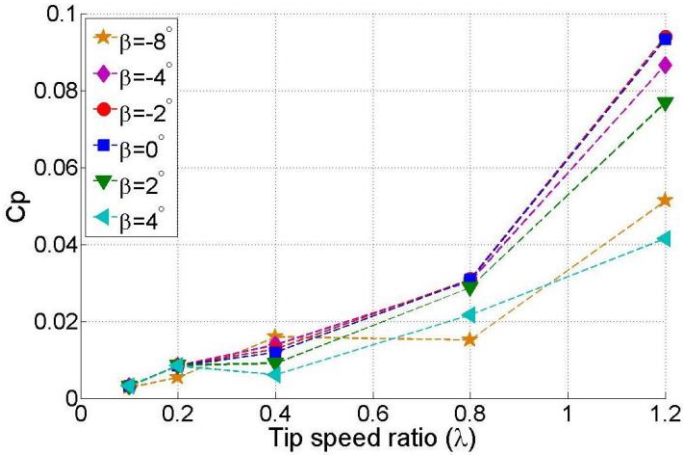

(b)

Figure 4.14 (a) Blade pitch effects on turbine power output and (b) enlarged view. $R = 0.37$ m, $c = 0.1$ m, $\sigma = 0.81$. NACA0018. $V = 7$ m/s

By applying a small negative pitch angle of $\beta = -2^{\circ}$, the turbine shows an improved performance at low tip speed ratio and peak power output. The maximum C_p for $\beta = -2^{\circ}$ is 0.41 which indicates a 5% increase compared with the no pitch case of $\beta = 0^{\circ}$. The blade dynamic stall is delayed in the upwind region due to the negative pitch resulting in the blade torque being produced for a greater portion of the revolution. However at high tip speed ratios the blade will no longer stall, this negative pitch will reduce the angle of attack in the upwind region, where the majority of torque is produced, leading to a slightly lower lift force produced and consequently lower C_p compared with $\beta = 0^{\circ}$.

In terms of larger negative pitch angle, the $\beta = -4^{\circ}$ case presents a similar $C_p - \lambda$ trend as the $\beta = 0^{\circ}$ case, but the turbine performance is worse for the whole tip speed ratio range as shown in Figure 4.14. Moreover, the overall turbine power output for $\beta = -8^{\circ}$ is considerably reduced showing the worst case for all the pitch angles investigated. Although the large negative pitch angle can delay the stall angle in the upwind half of the rotor, the incidence angle is increased in the downwind region leading to a decreased torque generation and deterioration of overall performance.

With regards to the two positive pitch angle cases of $\beta = 2^{\circ}$ and $\beta = 4^{\circ}$, the C_p is always lower than the $\beta = 0^{\circ}$ case. Moreover, the $C_p - \lambda$ curve for the two positive pitch angle cases are shifted right hampering turbine starting. The positive pitch angle does not bring any benefit to an H-Darrieus machine.

A further study was conducted by looking at the blade torque generation under different pitch angles as shown in Figure 4.15. At $\lambda = 1.6$ (Figure 4.15 (a)) where the blade still experiences dynamic stall, the peak torque for $\beta = 0^{\circ}$, $\beta = -2^{\circ}$ and $\beta = -4^{\circ}$ occurs at $\theta = 82^{\circ}$, $\theta = 86^{\circ}$ and $\theta = 89^{\circ}$ respectively. The negative pitch angle successfully delays the stall and enables the blade to generate more torque for a greater portion of the azimuth angle. However, blade performance at the downwind region $180^{\circ} < \theta < 360^{\circ}$ is significantly reduced by the large negative pitch angle. The $\beta = -4^{\circ}$ case illustrates a negative torque all the way from $\theta = 220^{\circ}$ to $\theta = 360^{\circ}$ which offsets the blade's positive contribution in the upwind region and consequently results in lower turbine performance. In contrast, the $\beta = -2^{\circ}$ shows better blade performance in the upwind region with slightly lower performance in the downwind region compared with no pitch, leading to an improved overall turbine performance at $\lambda = 1.6$. With regards to the positive pitch $\beta = 2^{\circ}$, the stall occurs earlier than the no pitch case at $\theta = 77^{\circ}$ as shown in Figure 4.15 (a). Although the positive pitch leads to better blade performance

in the downwind region, the much deteriorated performance in the upwind region makes the choice of positive pitch unreasonable.

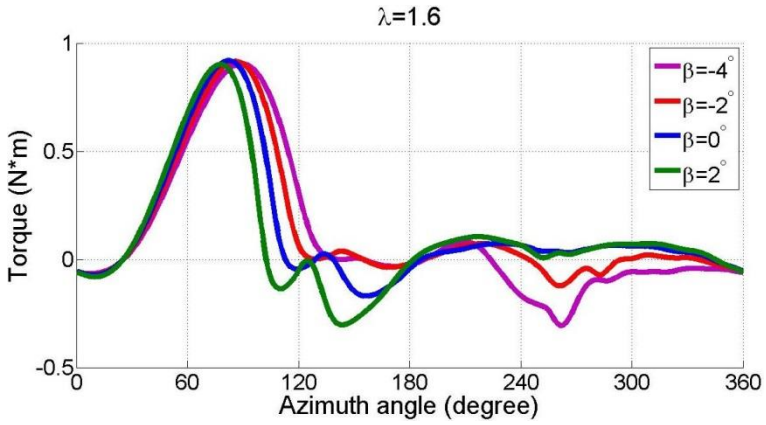

(a)

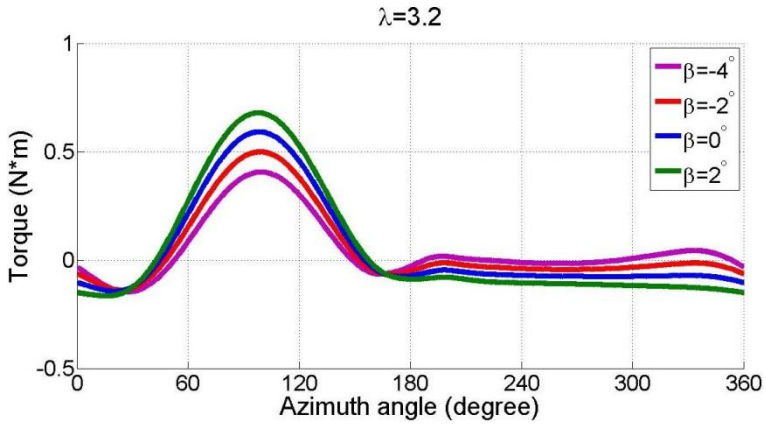

(b)

Figure 4.15 The blade torque under different pitch angle at two tip speed ratio: (a) $\lambda = 1.6$ and (b) $\lambda = 3.2$. $R = 0.37$ m, $c = 0.1$ m, $\sigma = 0.81$, $V = 7$ m/s. NACA0021.

Figure 4.15 (b) shows the blade torque at $\lambda = 3.2$. At this high tip speed ratio, the blade no longer experiences stall, therefore the peak torque for all cases investigated occurs at the same azimuth angle. Compared to the no pitch case of $\beta = 0^{\circ}$, a negative pitch ($\beta = -2^{\circ}$ or $\beta = -4^{\circ}$) increases blade performance in the downwind region, but the overall torque (and C_p) is reduced due to the reduced performance in the upwind region (lower incidence angle). Conversely, a positive pitch improves blade performance in the upwind region (by increasing the incidence angle) but reduces it in the downwind resulting in a reduced overall torque (and C_p).

In conclusion, a small variation in blade pre-set pitch leads to a large variation in blade aerodynamic performance and turbine power generation. Specifically, the maximum value of turbine C_p was approximately 115% greater than the minimum

values over the 12° range of pre-set pitch angle investigated here. Turbines with slightly negatively pitched blades ($\beta > -2^{\circ}$) clearly demonstrate a better performance at low tip speed ratios which is beneficial to the turbine's self-starting capability. However, a negatively pitched blade will result in a slightly lower turbine power output at high tip speed ratios.

4.2.5 Turbine performance at different Reynolds numbers

The aerodynamic performance of blades varies significantly at different Reynolds numbers, which will result in an improved or worsened turbine performance. Generally speaking, blades such as NACA00xx show higher lift and reduced drag at larger Reynolds numbers. Since the relative velocity varies against azimuth angles, the blade chord based Reynolds number is not a constant for an H-Darrieus turbine at a given tip speed ratios. In this study, the upstream wind speed was modified in order to change the Reynolds number and the maximum Reynolds number (Re_{max}) was calculated at $\lambda = 4$, $\theta = 0^{\circ}$ for comparison.

The tested blade profile was NACA0021 with a chord length of $c = 0.1$ m. The turbine's radii were $R = 0.37$ m and $R = 0.45$ m which result in solidities of $\sigma = 0.81$ and $\sigma = 0.67$. Upstream wind speeds were set at $V = 6$ m/s, $V = 7$ m/s and $V = 8$ m/s and the corresponding maximum Reynolds number at $\lambda = 4$, $\theta = 0^{\circ}$ was $\sim 2 \times 10^5$, $\sim 2.4 \times 10^5$ and $\sim 2.7 \times 10^5$. Results are presented in Figure 4.16 and Figure 4.17.

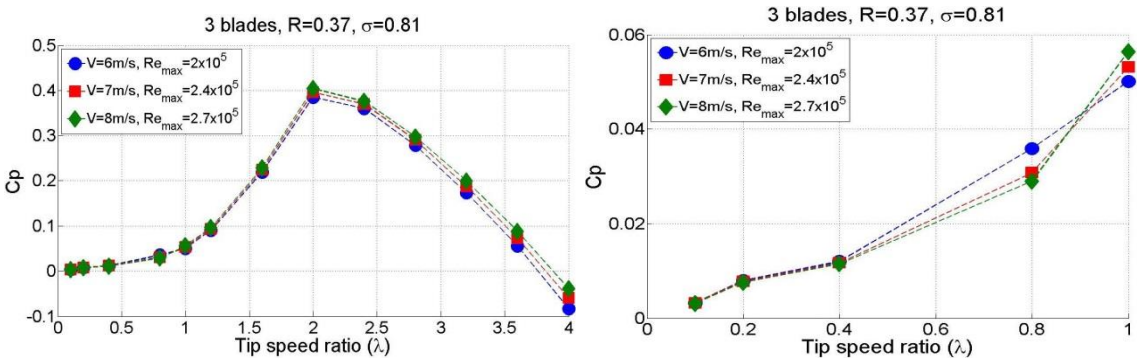

(a) (b)

Figure 4.16 (a) Reynolds effects on turbine power output and (b) enlarged view at $R = 0.37$ m and $\sigma = 0.81$.

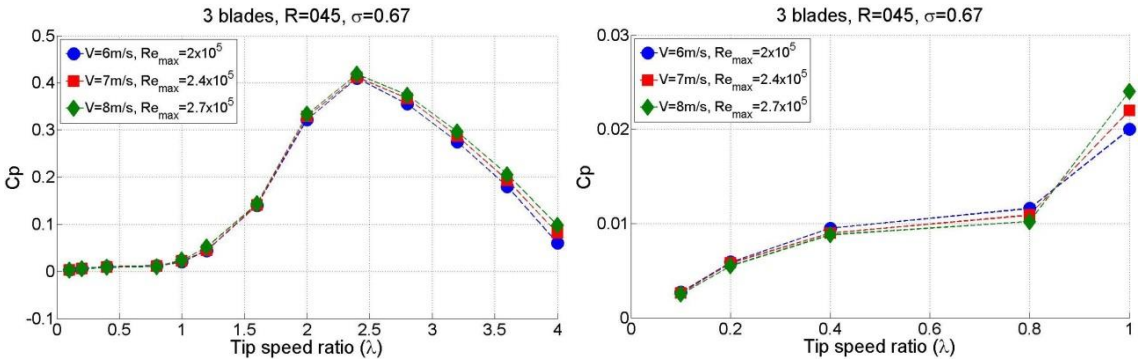

(a) (b)

Figure 4.17 (a) Reynolds effects on turbine power output and (b) enlarged view at $R = 0.45$ m and $\sigma = 0.67$

At both solidities of $\sigma = 0.67$ and $\sigma = 0.81$, the turbine power output at different upstream wind speeds shows very similar trends. The turbine peak C_p was increased by increasing the upstream wind speed and turbine performance at high tip speed ratios is also improved at higher Reynolds numbers due to the increase of lift and decrease of drag force. Nevertheless, the higher wind speed does not guarantee an improved performance for the entire turbine working range since Figure 4.16 (b) and Figure 4.17 (b) clearly illustrate a decrease of C_p with the increase of Reynolds number typically during the turbine start-up period of $\lambda \leq 0.8$. The blade torque against azimuth angle is plotted as shown in Figure 4.18 in order to further study and understand the blade force at different Reynolds numbers.

Torque at two tip speed ratios was investigated for turbine solidity of $\sigma = 0.81$. At $\lambda = 0.8$ (see Figure 4.18 (a)), the peak torque is slightly delayed with the increase of wind speed indicating a slightly delayed blade stall at higher Reynolds numbers. Between $\theta = 80^{\circ}$ and $\theta = 100^{\circ}$, a larger Reynolds number adversely affects blade performance showing a significant increase of negative torque. Moreover, for the turbine downwind region ($180^{\circ} < \theta < 360^{\circ}$), the blade generated torque is also reduced at larger Reynolds numbers. This explains the reduced turbine power output under larger Reynolds number at the start-up period ($\lambda < 0.8$) shown in Figure 4.16 and Figure 4.17.

In contrast, at $\lambda = 2.4$ (see Figure 4.18 (b)) the blade torque at all azimuth angles is increased by increasing the wind speed. The turbine blade no longer experiences dynamic stall since the peak torque occurs at the same azimuth angle for all Reynolds numbers. A larger Reynolds number leads to larger lift and lower drag force being generated at incidence angles below stall, which always improves the blade and turbine performance as shown in Figure 4.16 and Figure 4.17 at high λ.

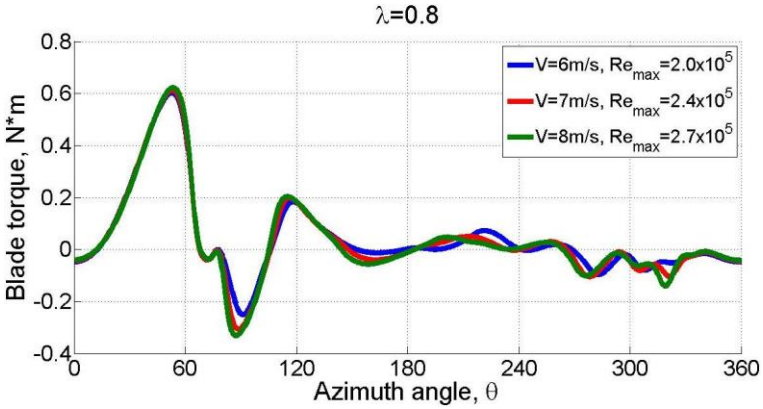

(a)

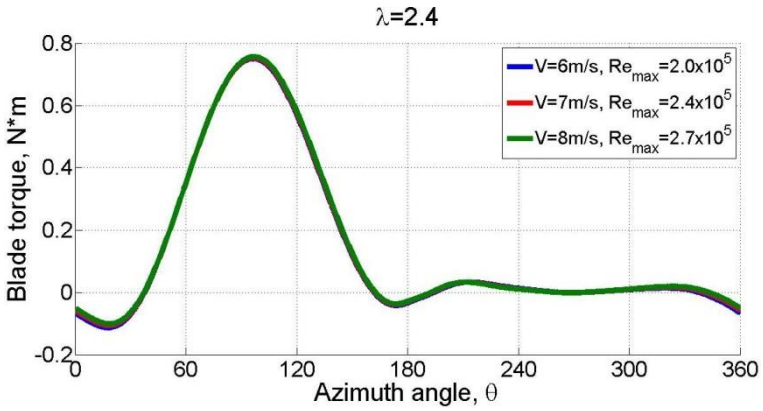

(b)

Figure 4.18 The blade torque against azimuth angle at different Reynolds number (upstream wind speed) at (a) $\lambda = 0.8$ and (b) $\lambda = 2.4$. $c = 0.1\,\mathrm{m}$, $R = 0.37\,\mathrm{m}$ and $\sigma = 0.81$.

In conclusion, the CFD study indicates that a higher wind speed does not contribute to improved turbine performance at low tip speed ratios ($\lambda < 0.8$). Larger Reynolds numbers lead to deteriorated blade performance at deep stall angles. However when the turbine approaches $\lambda \sim 1$, a larger Reynolds number enables the blade to produce more positive torque which will significantly reduce the turbine plateau period. It must be noted from previous experimental measurements that the plateau stage accounts for almost half of the turbine self-starting period (time). Therefore increasing the blade Reynolds number is able to reduce the turbine plateau stage ($\lambda \sim 1$) and hence turbine self-starting time although it slows the turbine slightly at extremely low tip speed ratios ($\lambda < 0.8$). Moreover, increasing the Reynolds number also increases turbine peak power output and performance at high λ.

4.3 Conclusion and discussion

A 2-D aerofoil model has been built and validated in this study in order to examine the accuracy of CFD model in predicting the blade's static aerodynamic forces. The lift and drag forces calculated by using Transition SST turbulence model show good agreement with those measured by experiments before stall. The laminar separation bubble is successfully captured by the CFD. Moreover, the bubble separation and reattachment location matches closely with the experimental measurements. However, the aerofoil stall angle is predicted at a higher incidence angle by CFD and the aerodynamic forces at deep stall angles are significantly over-predicted. When modelling an H-Darrieus wind turbine, these over-predicted aerodynamic forces at deep stall will result in an over-predicting of turbine performance at low tip speed ratios since the turbine blades will experience extremely large incidences at the low λ.

A 2-D H-Darrieus wind turbine model has been employed to investigate the turbine design parameters including: solidity, blade profile, pitch angle and Reynolds number. In terms of turbine self-starting capability, turbines with larger solidity demonstrate better performance during the start-up period (low tip speed ratios) although the peak power output is reduced. For turbines with given solidity, larger blade chord length (and correspondingly larger turbine radius) increases the blade Reynolds number and surface area, which results in more power produced for the whole working range. However no solid conclusion can be drawn about the larger combination effect on the turbine self-starting capability since the increased turbine inertia and system resistance are not considered in this 2-D CFD model. Experimental tests are designed to further study the effect of larger combinations of c and R on turbine performance during start-up period. The turbine with slightly negatively pitched blades is demonstrated to have better self-starting capability due to the improved performance at low tip speed ratios. Moreover, according to the CFD results the DU06W200 aerofoil section is shown to have slightly better performance at low tip speed ratios compared with symmetric NACA profiles with large thickness (NACA0018 and NACA0021). The cambered NACA4415 blade geometry does not show any improvement at low tip speed ratios and the turbine maximum C_p is significantly lower than the other blades that were studied. Finally, increasing the upstream wind speed (Reynolds number) has mixed effects on turbine performance. A Larger Reynolds number increases the turbine peak C_p and performance at high λ, whereas turbine performance at extremely low tip speed ratios ($\lambda < 0.8$) is slightly reduced. Nevertheless, an improved performance at the turbine

plateau stage ($\lambda \sim 1$) resulting from the increased Reynolds number might reduce the turbine's overall self-starting time.

The CFD results predicted in this study support the previous research performed by Worasinchai [31] at Durham university. Worasinchai claimed that aerofoils with high camber would lose their effectiveness in producing forward thrust when operating in the downwind region and the conventional symmetrical aerofoil such as NACA0018 was still a simple and attractive choice. Furthermore, based on the BEM study, Worasinchai also claimed that turbines under the solidity range of $0.72 < \sigma < 0.84$ could self-start. However, the present CFD study demonstrates turbines outside this solidity range can also produce positive power (or torque) at low tip speed ratios, indicating a self-starting capability.

This CFD study provides a first insight into turbine performance under different design parameters. All of the above information and conclusions will be used to guide the experimental design which will be detailed in Chapter 6. The CFD predictions will also be compared with the experimental results measured in this study in Chapter 7.

Chapter 5

Blade Element Momentum (BEM) based approaches in this study

The CFD study successfully demonstrated that design factors have strong effects on turbine performance including its critical turbine self-starting capability. In particular, it was demonstrated that for a given solidity, turbines with larger blade chord length, c, and correspondingly larger turbine radius, R, could achieve higher performance (C_p) over the entire working range due to larger local Reynolds number and larger blade surface area (see Figure 4.9). Nevertheless, in terms of turbine self-starting behaviour this larger combination did not guarantee better self-starting capability since the whole system inertia was increased along with increased system resistance. Since the CFD model employed was unable to model the dynamic turbine start-up process, a blade element momentum (BEM) based model referred to as the Start-Up model was developed to examine whether a larger combination of c and R could improve the turbine self-starting capability and reduce the self-starting time when the solidity was kept constant. This Start-Up model was first proposed by Worasinchai [31] and improved in this study making it more suitable for the study of small-scale H-Darrieus wind turbines.

In this Start-up model, the upstream wind was assumed to be steady and uniform across the whole rotor swept area. Moreover, each turbine blade was treated as independent which indicates there was no wake interaction within the turbine. The static wind tunnel aerodynamic lift and drag coefficients of the NACA0018 blade measured in a low-blockage wind tunnel during this study were used as the input for this model (details about the static wind tunnel measurements are provided in Chapter 7). The results were compared with experimental measurements in order to validate this improved Start-Up model.

It has been pointed out by Rossetti and Pavesi [64] that the principal limits of the BEM approach could be ascribed to the absence of high quality, well documented aerofoil databases. Therefore, another dataset of NACA0018 measured during this study in a closed-jet (high-blockage) tunnel was also tested so as to check the sensitivity of the Start-Up model to the quality of different aerofoil aerodynamic datasets. The final results were found to be significantly different from the prediction made using the dataset of NACA0018 measured in the low-blockage wind tunnel.

In order to further examine the effect of aerodynamic data quality on the BEM based prediction, another widely used BEM model, the double multiple streamtube model (DMST), was also built in this study. This DMST model was validated by using the aerodynamic dataset provided by Sheldahl and Klimas [62]. Modification of the aerodynamic dataset was made in terms of aerofoil stall behaviour and the results are compared with the original calculation in this chapter.

5.1 The Start-Up Model

5.1.1 Model description

A detailed description of this model can be found in [31]. This subsection only provides the basic equations relating to the turbine kinematics and emphasis is placed on the improvement of this model.

The Start-Up model predicts the turbine performance based on a time-stepping basis. At each time step the resultant speed (V_R) experienced by each blade is first calculated as:

$$V_R = V \times \sqrt{\lambda - 2\lambda cos\theta + 1} \qquad \text{Equation 5.1}$$

The corresponding blade Reynolds number can be then determined and the lift and drag forces are then calculated by interpolating from a look-up table based on the input aerodynamic database. Once the blade forces have been determined, the forces are resolved in the circumferential direction in order to establish the instantaneous torque and power:

$$C_t = C_l sin\alpha - C_d cos\alpha \qquad \text{Equation 5.2}$$

The tangential force and driving torque generated by one blade are:

$$F_{ti} = \frac{1}{2}\rho A_s V_R^2 C_t \qquad \text{Equation 5.3}$$

$$T_i = F_{ti}(\theta) \times R \qquad \text{Equation 5.4}$$

The total torque and power are then:

$$T = \sum_{i=1}^{n} T_i \qquad \text{Equation 5.5}$$

$$C_t = C_l sin\alpha - C_d cos\alpha \qquad \text{Equation 5.6}$$

where n is number of blades. Knowing the turbine's inertial, J, and any system resistance, R_s, the new rotational speed at the next time step can be determined as:

$$\omega_{t+1} = \omega_t + (\frac{T - R_s}{J})\delta t \quad \text{Equation 5.7}$$

Appling the new rotation speed over a short time interval, a new turbine position is determined and the process is repeated. Three dimensional effects such as blade tip loss are considered by applying Prandtl's tip loss correction factors [31, 145] to both ends of the blades as:

$$F_{loss} = F_1 \times F_2 \quad \text{Equation 5.8}$$

$$F_1 = \frac{2}{\pi}\cos^{-1} e^{-f_1} \text{ where } f_1 = \frac{n}{2}\frac{s-S}{Rsina} \quad \text{Equation 5.9}$$

$$F_2 = \frac{2}{\pi}\cos^{-1} e^{-f_2} \text{ where } f_2 = \frac{n}{2}\frac{S-s}{Rsina}$$

where s is a cetain location on the blade and S is the blade span length

Furthermore the semi-empirical dynamic stall model, the Leishman-Beddoes model [31, 95], is also incorporated in the Start-up model, which divides the important flow phenomena into three modules: attached-flow, separated-flow and vortex-induced flow modules.

Improvements to this Start-Up model that were made in the present study are as follows:

- New static aerodynamic lift and drag forces for the NACA0018, which was the input file to the Start-Up model, were measured in this study in a low-blockage wind tunnel. In contrast, the aerodynamic dataset employed in Worasinchai's study [31] was based on empirical equations. A well-documented aerodynamic dataset was essential for accurately predicting the torque force and also provided a better prediction of dynamic stall since some of the parameters (such as normal curve slope, critical normal force coefficient, static separation point, etc.) used in the Leishman-Beddoes model were deduced from static wind-tunnel measurements.
- The airloads for separated flow in the Leishman-Beddoes dynamic-stall model were modified for low Mach number applications according to Sheng et al.'s [146] study as:

$$C_n = C_{Na}(\alpha - \alpha_0)(\frac{1 + \sqrt{f'}}{2})^2 \quad \text{Equation 5.10}$$

$$C_t = \eta C_{Na}(\alpha - \alpha_0)^2(\sqrt{f'} - E_0) \quad \text{Equation 5.11}$$

where a_0 is the zero-lift angle of attack, C_{Na} is the slope of the normal force coefficient, $\eta = 0.95$ and $E_0 = 0.2$ for most NACA series aerofoils. The corresponding separation location, f', of the static case is modified as

$$f' = 1 - 0.4\exp\left(\frac{\alpha - \alpha_s}{S_1}\right), \ \alpha \le \alpha_s \quad \text{Equation 5.12}$$

$$f' = 0.02 + 0.58\exp\left(\frac{\alpha_s - \alpha}{S_2}\right), \ \alpha > \alpha_s$$

where a_s is the static aerofoil stall angle, S_1 and S_2 are functions of the free-stream Mach number which were empirically determined according to Chantharasenawong [147].

- The dynamic stall-onset criteria in the Leishman-Beddoes dynamic-stall model was improved by Sheng et al. [146] and employed in this study as follows:

$$\alpha' \ge \alpha_{cr} \quad \text{Equation 5.13}$$

where for the NACA0018 aerofoil

$$\alpha' = \alpha - 6.22k \quad \text{Equation 5.14}$$

$$\alpha_{cr} = 17.46^\circ, \ k \ge 0.01 \quad \text{Equation 5.15}$$

$$\alpha_{cr} = 14.68^\circ + \left(17.46^\circ - 14.68^\circ\right)\frac{k}{0.01}, \ k < 0.01$$

Where k is the reduced frequency, $= \frac{c}{D}\lambda$.

All other parameters and assumptions used in this Start-Up model were kept the same as those proposed by Worasinchai [31]. Readers are referred to Section 9.2 of [31] for more detailed information about this Start-Up model and the implementation of the Leishman-Beddoes dynamic-stall model.

5.1.2 Input aerodynamic dataset and validation test

Due to the unique operational characteristics of Darrieus wind turbines, studies based on BEM theory require detailed aerofoil aerodynamic datasets over the full 360° incidence range (or 180° incidence range for symmetrical aerofoil) at low Reynolds numbers. The most complete available dataset was published by Sheldahl and Klimas [62] who studied seven symmetrical aerofoils at angles of attack up to $180°$ and whose

data had provided the foundation for many VAWT performance studies (e.g.[11, 64, 148]). However, their actual measurements were conducted at three Reynolds numbers of $360{,}000,\ 500{,}000$ and $700{,}000$. Data for lower Reynolds numbers was extrapolated by using the computer code PROFILE [62]. Nevertheless some authors (e.g.[11, 64]) had questioned whether the extrapolated data were sufficiently accurate since aerofoil behaviour such as laminar separation at low Reynolds numbers was not captured [58]. Therefore the input aerodynamic dataset used in the Start-Up model was measured during this study using a NACA0018 profile. Measurements were performed at relatively low Reynolds numbers of $60{,}000,\ 100{,}000$ and $140{,}000$ in a low-blockage ($0.5\% \sim 3\%$) open-jet wind tunnel and examples are shown in Figure 5.1. Details about the experimental set-up, flow condition and measurements will be presented in Chapter 6 and 7

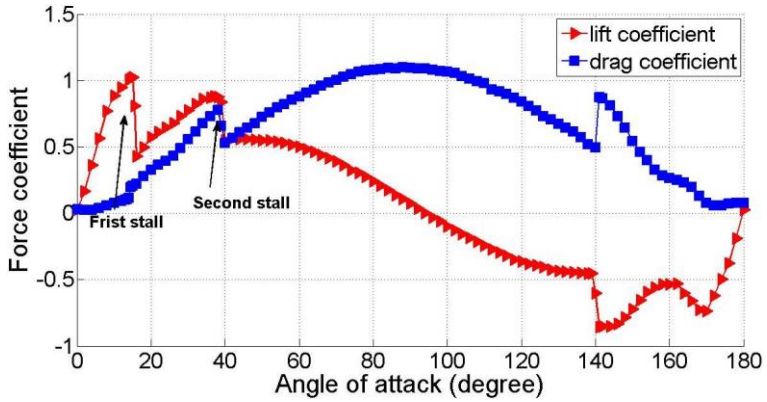

Figure 5.1 Example of aerodynamic dataset measured during this study in a low-blockage open-jet wind tunnel at $Re = 140{,}000$. NACA0018 profile.

It is noted that the experimental measurement also captured an aerofoil 'second-stall' behaviour at large angles of attack as shown in Figure 5.1. The lift and drag coefficient both illustrate a sudden decrease at an incidence angle around 40° and a sudden increase at around 140°. This sudden force change is due to the separation point near the leading edge which switches from the aerofoil suction side to the pressure side resulting in a significant change of wake structure, which will be explained in detail in Chapter 7. However, since the turbine is actually driven by the tangential force which is defined as $C_t = C_l sin\alpha - C_d cos\alpha$, a comparison of the tangential force from this study and Sheldahl and Klimas's [62] widely adopted study is presented here. It can be seen in Figure 5.2 that although the dataset from this study shows a sudden decrease both for lift and drag around 40°, the tangential force curve retains a gradual change similar to that of Sheldahl and Klimas's data. Hence this 'second-stall' will not result in

a sudden turbine performance change using the BEM method. Furthermore, at an incidence around 140° the present dataset illustrates a sudden increase of C_t. However since the turbine blades will only experience this extremely large incidence over a very limited azimuth range and only when $\lambda < 1$, this slight increase of tangential force has no significant effect on the final BEM based prediction of turbine performance. Nevertheless, experiments were performed in this study (Chapter 7) to examine how the 'second-stall' affects blade performance during the turbine start-up period.

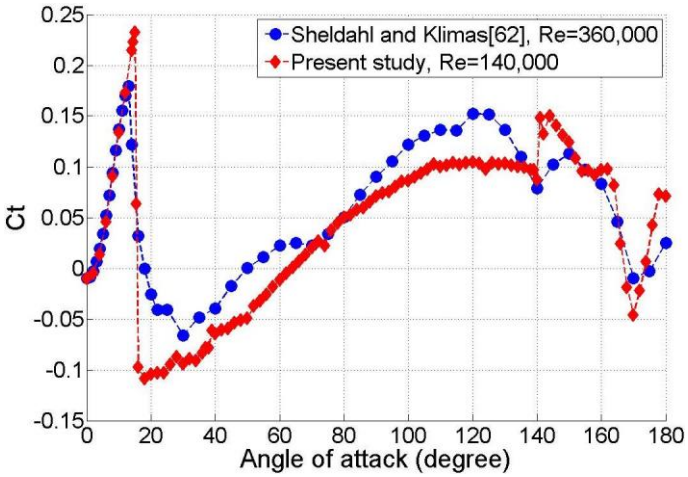

Figure 5.2 NACA0018 thrust coefficient comparison between aerodynamic data from this study [149] and Sheldahl and Klimas's study [62].

In order to check the sensitivity of the Start-Up model to the quality of different aerodynamic datasets that may arise, for example from blockage effects, closed-jet (high-blockage) wind tunnel data that were also measured during this study were employed for comparison (examples are shown in Figure 5.3, low-blockage data is shown in Figure 5.1). This dataset covers the same Reynolds range as the low-blockage open-jet dataset. It can be seen from Figure 5.3, a particular characteristic of this dataset is that its drag coefficient reaches an unusually high value of 3.42. The influence of this large drag on predicting turbine performance will be examined and discussed in the following section.

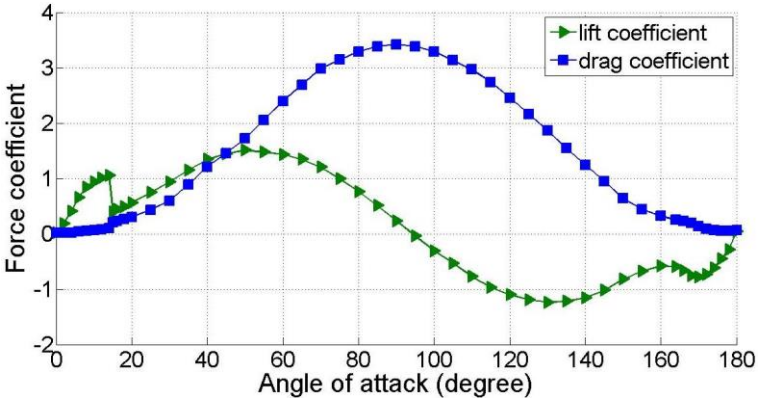

Figure 5.3 Example of aerodynamic data measured during this study in a high-blockage closed-jet at $Re = 140{,}000$. NACA0018 profile.

In this study a time step of $\delta t = 0.001s$ was applied and negligible system resistance was assumed. A validation test was performed and compared with Hill et al.'s [11] experimental measurements with the NACA0018 blades as can be seen in Figure 5.4. The simulation results show good agreement with experimental data although since no resistance is considered in the model, the turbine experiences a faster initial acceleration in the simulation. The turbine subsequently reaches a tip speed ratio plateau between approximately $\lambda = 0.9$ and $\lambda = 1.1$ where λ increases very slowly. In comparison, experimental measurements indicate the plateau occurs around $\lambda = 1.2$. Rapid turbine acceleration is predicted by the model above $\lambda = 1.5$ reaching a peak value of $\lambda = 3.2$ while the experimental results show the turbine peaks around $\lambda = 3$. Both experimental measurements and simulation demonstrate that it takes approximately 150 seconds for the turbine to self-start. The Start-Up model used in this study is demonstrated to be able to replicate the shape of the experimental curve and to display the Darrieus turbine dynamic start-up process.

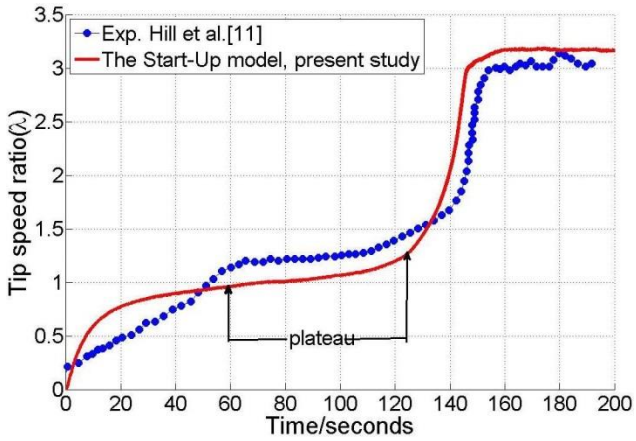

Figure 5.4 The Start-Up model validation test of NACA0018 blades with $c = 0.08\ \mathrm{m}$, $R = 0.37\ \mathrm{m}$, $\sigma = 0.65$ and upstream wind speed of $6\ \mathrm{m/s}$.

5.1.3 Turbine self-starting behaviour under given solidity but with different combinations of turbine radius and blade chord length

For H-Darrieus wind turbines under the same solidity, a larger combination of c and R leads to more power extracted from the wind over the whole turbine working range as was shown by the CFD prediction. However, the consequently larger system inertia and resistance might also increase the turbine self-starting time or even prevent the turbine from self-starting. In order to provide a clear answer to the impact of larger combinations of c and R on turbine self-starting behaviour, tests were performed using the Start-Up model.

The parameters for the two scenarios examined are summarised in Table 5.1.

	Scenario 1 Original	Scenario 2 Larger combination
Blade profile	NACA0018	NACA0018
Number of blades	3	3
Chord length/m	0.08	0.08×1.5
Turbine radius/m	0.37	0.37×1.5
Solidity	0.65	0.65
Upstream wind speed/ m/s	6	6

Table 5.1 Summary of two scenarios of wind turbines with the same solidity but with different combinations of blade chord length and rotor radius examined in the Start-Up model.

The power coefficient (C_p) for the above two scenarios is presented first and compared with the CFD prediction showing good agreement (Figure 5.5). It can be seen in Figure 5.5 that by increasing the turbine radius and blade chord length by 50% (scenario 2), the bin-averaged C_p shows similar results to those of scenario 1. This is consistent with the previous CFD study (Figure 4.9) that demonstrates that turbines having the same solidity but with different combinations of turbine radius and blade chord length show similar trends of C_p- λ with slightly higher C_p for turbines with a larger blade chord length combination.

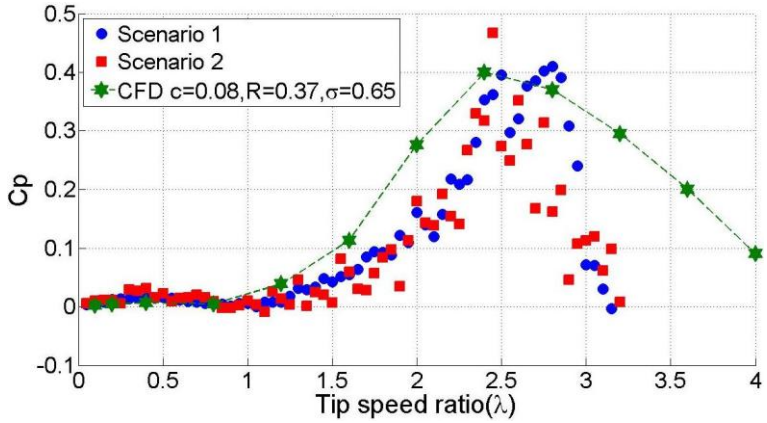

Figure 5.5 Power coefficient prediction from the Start-Up model for different scenarios compared with CFD prediction. Radius R and chord length c are in meters.

Both scenarios and the CFD results illustrate a sudden and significant power increase when the turbine tip speed ratio approaches approximately 1.5 and the turbine maximum performance is around $\lambda = 2.5$. As shown in Figure 5.5, the turbine in the Start-Up model is self-limited to a maximum rotational velocity corresponding to $\lambda = 3.2$ since the predicted C_p for both scenarios quickly drops towards 0 at the maximum rotational velocity. In contrast, large positive C_p is predicted beyond $\lambda = 3.2$ by the 2-D CFD since the blade tip loss and resistance are ignored.

Although the power coefficients are quite similar for the two scenarios, the turbine demonstrates significantly different dynamic start-up behaviour. As can be seen in Figure 5.6, for scenario 2 with the larger turbine radius (R) and blade chord length (c), the system inertia is larger than scenario 1 resulting in a slower initial acceleration. However during the plateau stage where λ increases very slowly, the rotor speed of scenario 1 is quickly overtaken by scenario 2 which consequently reaches its maximum speed much earlier, after 120 seconds. Detailed examination of the aerodynamics of the Darrieus turbine indicates that, at $\lambda < 1$, the turbine operates as a 'combined lift- and drag-driven' machine and only when the $\lambda > 1$ does the turbine begins to change its mode to a purely 'lift-driven' machine. Therefore, the turbine plateau stage will most likely happen around a tip speed ratio of 1 (see scenario 1) since the beneficial driving force associated with the drag will, from this point, becomes resistance for all azimuth angles. Nevertheless, with unsteadiness in the upstream wind (for example, a sudden drop of wind speed) [10], a careful selection of aerofoil profile with larger lift force [23] and a larger blade chord length (larger Reynolds number and consequently larger lift force), allows this plateau stage or 'dead band' to be more easily overcome and the turbine is able to self-start much more quickly. The results from the Start-Up model

confirm that, for a three-bladed Darrieus machine of given solidity, a larger combination of blade chord length and turbine radius (scenario 2) is preferred although the turbine will accelerate more slowly at first due to its increased inertia.

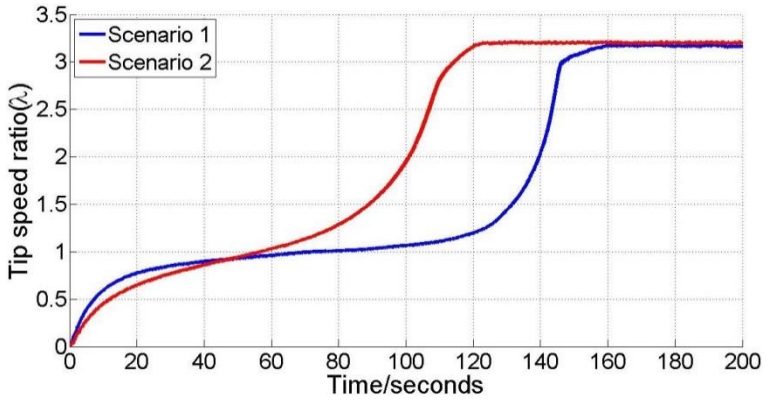

Figure 5.6 Predictions of the turbine dynamic start-up process for the same solidity with different combinations of turbine radius and blade chord length.

Furthermore, Figure 5.6 illustrates a rapid turbine acceleration starting at around $\lambda = 1.5$ which is consistent with the considerable increase of power output shown in the C_p- λ curve around the same λ (Figure 5.5). A detailed study of the incidence angle variation against the turbine rotational speed indicates that the incidence angle experienced by the blades reduces from 0°~90^{0} (when $\lambda = 1$) to 0°~42° (when $\lambda = 1.5$, shown in Figure 5.7). This remarkable reduction of incidence angle range results in a significant decrease of drag force generated by the blades at extreme incidences, which would lead to further rapid turbine acceleration until a new equilibrium is reached between total resistance and torque.

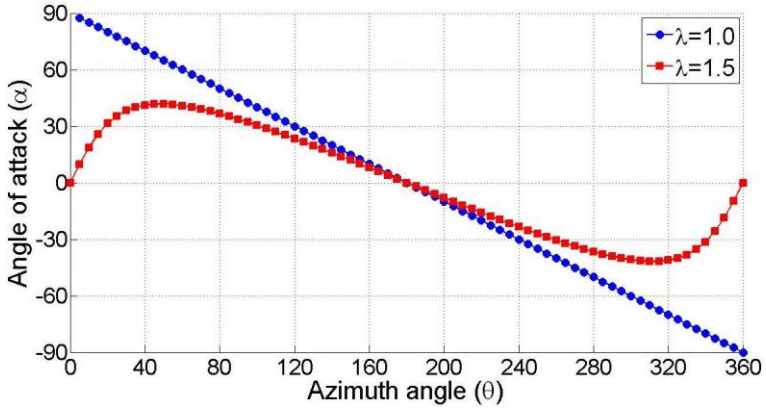

Figure 5.7 The angle of attack experienced by the turbine blades at different tip speed ratio

5.1.4 Sensitivity study of the BEM model to different aerodynamic datasets

The high-blockage, closed-jet wind tunnel dataset was also applied in this model in order to assess the model sensitivity to the accuracy of the input data and in particular to high drag configurations. This data with unusually high drag force is presented in Figure 5.3. As can be seen in Figure 5.8, the simulation predicts extremely fast initial turbine acceleration during the turbine 'combined lift- and drag- driven' phase ($\lambda < 1$) compared with the low-blockage open-jet dataset. However when the rotational speed reaches $\lambda \approx 1$, the large drag force switches from a driving force to a resistance and always prevents the turbine from self-starting. Therefore blades with large lift and appropriate drag are necessary for a self-starting Darrieus turbine. Moreover this study also demonstrates that the BEM based approaches, which usually employ aerofoil aerodynamic data as the model input, are sensitive to the dataset quality. Consequently differences that arise from measurements in different wind tunnel facilities may result in significantly different predictions of Darrieus wind turbine performance. It is suggested that the acquisition and publication of extensive, high quality data over the full-range of incidence that is experienced during VAWT start-up and at appropriate Reynolds numbers must be a high priority if turbine performance is to be predicted accurately.

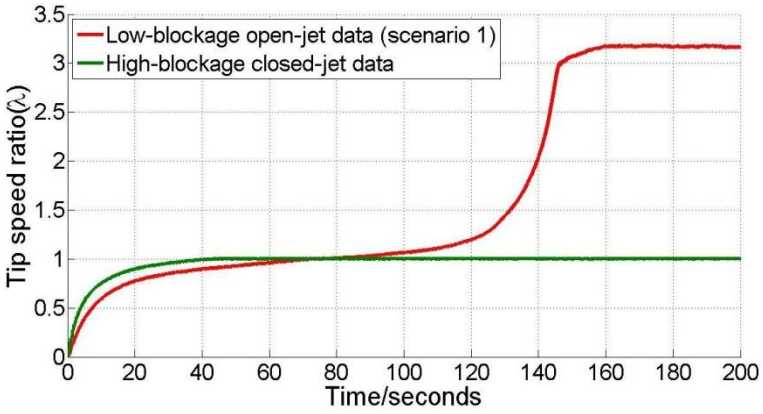

Figure 5.8 Predictions of the turbine dynamic start-up process with low-blockage open-jet data and high-blockage closed-jet data. $c = 0.08$ m, $R = 0.37$ m and $\sigma = 0.65$.

5.1.5 Conclusion

The Start-Up model was successfully improved and validated with a NACA0018 aerodynamic dataset measured during this study. This model was employed here in order to examine the turbine dynamic self-starting behaviour under a given solidity but

with different combinations of turbine radius and blade chord length. The following conclusions could be drawn based on the above results:

- Results from the Start-Up model further support the CFD prediction that for turbines of given solidity, larger blade chord length (and correspondingly larger turbine radius) demonstrates better turbine self-starting capability and the self-starting time is significantly reduced. Although the larger blades increase the inertia of the rotor which results in a slower initial acceleration, the turbine's plateau (or 'dead band') is overcome more easily as a consequence of the higher lift force. This design consideration is further explored by experimental measurements (detailed in Chapter 7) and the results support the above conclusion.
- The Start-Up model reveals that the BEM based approach is highly sensitive to the quality of aerodynamic data that is input to the model. The acquisition and publication of extensive, high quality data over the full-range of incidence that is experienced during VAWT start-up and at appropriate Reynolds numbers is shown to be a high priority for predicting turbine performance accurately.
- In terms of turbine self-starting, the tip speed ratio versus power coefficient curve $C_p - \lambda$ provides limited information. It is demonstrated that the turbine dynamic start-up process could be significantly different for similar $C_p - \lambda$ curves. Furthermore, the 2-D CFD model gives hypothetical results of C_p at user pre-set λ. Positive C_p is still predicted beyond the turbine working range since the blade tip loss and resistance are not considered.
- The turbine's plateau (or 'dead band' region) will most likely occur around $\lambda \approx 1$ since the beneficial driving force associated with the drag at low λ will, from this point, become resistance for all azimuth angles, which might prevent the turbine acceleration. Therefore, blades with large lift force and appropriate drag are crucial requirements for H-Darrieus turbines designed to be self-starting.

5.2 The Double Multiple Streamtube Model

5.2.1 Basic model description

The double multiple streamtube model (DMST) is based on the actuator disc theory as shown in Chapter 2 Figure 2.23. The development of the streamtube model is also detailed in Chapter 2. The most advanced DMST model extends the turbine boundary resulting in the division of the flow through the domain into many independent stream

tubes as shown in Figure 5.9 (a). The DMST model incorporates the differences in the upwind and downwind sections through the division of each stream tube further into two halves (upwind and downwind). Calculation of induction factors are performed for the upwind and downwind section separately. Since in this model the turbine interacts with the wind twice the predictions are thought to be more representative of the real flow. The general mathematical expression of the kinematics of a turbine blade at a specific location is presented below.

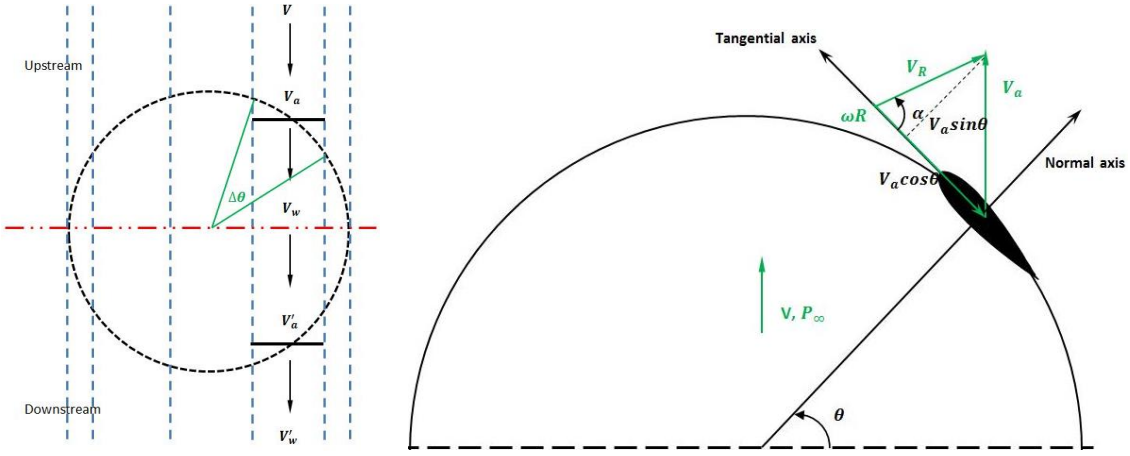

(a) (b)

Figure 5.9 (a) Example of DMST model with 5 streamtubes divided by uniform $\Delta\theta$. (b) Schematic diagram of turbine kinematics at a particular azimuth angle.

As can be seen in Figure 5.9 (b) the relative velocity (V_R) can be obtained from the chordwise velocity component and normal velocity component:

$$V_R = \sqrt{(V_a sin\theta)^2 + (\omega R - V_a cos\theta)^2} \qquad \text{Equation 5.16}$$

where V_a is the induced velocity through the rotor and ω is the rotational velocity. The relative velocity can be written in non-dimensional form using the free stream wind speed:

$$\frac{V_R}{V} = \sqrt{\left[\frac{V_a}{V} sin\theta\right]^2 + \left[\left(\frac{\omega R}{V}\right) - \left(\frac{V_a}{V} cos\theta\right)\right]^2} \qquad \text{Equation 5.17}$$

Referring back to $V_a = V(1 - \dot{a})$, Equation 5.17 can be re-written as:

$$\frac{V_R}{V} = \sqrt{((1 - \dot{a})sin\theta)^2 + (\lambda - (1 - \dot{a})cos\theta)^2} \qquad \text{Equation 5.18}$$

where $\dot{a}$ is the axial interference factor in the upwind region and λ is the tip speed ratio of the turbine.

According to Figure 5.9 (b) the local angle of attack can be expressed as:

$$\tan\alpha = \frac{V_a sin\theta}{\omega R - V_a cos\theta} \quad \text{Equation 5.19}$$

Non-dimensionalizing Equation 5.19 gives:

$$\tan\alpha = \frac{\frac{V_a}{V} sin\theta}{\frac{\omega R}{V} - \frac{V_a}{V} cos\theta} \quad \text{Equation 5.20}$$

$$\alpha = \tan^{-1}\left\{\frac{(1-\dot{a})sin\theta}{\lambda - (1-\dot{a})cos\theta}\right\} \quad \text{Equation 5.21}$$

The normal and tangential force coefficients can be expressed as:

$$C_n = C_l \cos\alpha + C_d \sin\alpha \quad \text{Equation 5.22}$$

$$C_t = C_l \sin\alpha + C_d \cos\alpha \quad \text{Equation 5.23}$$

where C_l and C_d are lift and drag coefficient at angle of attack α.

The instantaneous thrust force for one blade at a particular azimuth angle is:

$$K_i = \frac{1}{2}\rho V_R^2 (hc)(C_t \cos\theta - C_n \sin\theta) \quad \text{Equation 5.24}$$

where h is the blade height.

The instantaneous torque on the blade at a particular azimuth angle is:

$$T_i = \frac{1}{2}\rho V_R^2 (hc) C_t R \quad \text{Equation 5.25}$$

The momentum balance is carried out separately for each stream tube, allowing an arbitrary variation in inflow, resulting in $N_{\Delta\theta}$ (number of streamtube) induction factors for both upwind and downwind regions.

A single blade passes each streamtube in the upwind and downwind region and the time averaged thrust force acting in a streamtube in the upwind region by 'n' blades can be expressed as:

$$K_{ave} = n \times K_i \times \frac{\Delta\theta}{\pi} \quad \text{Equation 5.26}$$

Considering the swept area of the turbine for a single streamtube $A = hR\Delta\theta \sin\theta$, the average aerodynamic thrust can be non-dimensionalized into thrust coefficient as:

$$C_K = \frac{K_{ave}}{\frac{1}{2}\rho V^2(hR\Delta\theta \sin\theta)} = \left\{\frac{nc}{2R}\right\}\left\{\frac{V_R}{V}\right\}^2 \frac{1}{\pi}\left\{\frac{C_t \cos\theta}{\sin\theta} - C_n\right\} \quad \text{Equation 5.27}$$

The instantaneous torque is given in Equation 5.25. The average torque on the rotor for 'n' blades in the upwind half revolution is then given as:

$$T_{ave} = n \times \sum_{i=1}^{N_{\Delta\theta}} \frac{\left\{\frac{1}{2}\rho V_R^2 (hc) C_t R\right\}}{N_{\Delta\theta}} \quad \text{Equation 5.28}$$

The torque coefficient and power coefficient for the upwind half can be calculated as:

$$C_T = \frac{T_{ave}}{\frac{1}{2}\rho V^2 (2Rh) R} = \left\{\frac{nc}{2R}\right\} \sum_{i=1}^{N_{\Delta\theta}} \frac{\left\{(\frac{V_R}{V})^2 C_t\right\}}{N_{\Delta\theta}} \quad \text{Equation 5.29}$$

$$C_p = C_T \lambda \quad \text{Equation 5.30}$$

For the turbine's downwind region (see Figure 5.9 (a)), the downwind axial interference factor ($\dot{a}'$) and the induced velocity at downwind (V_a') are defined in Equation 5.31 and Equation 5.32 respectively.

$$\dot{a}' = \frac{V_w - V_a'}{V_w} \quad \text{Equation 5.31}$$

$$V_a' = V_w(1 - \dot{a}') \quad \text{Equation 5.32}$$

The relative velocity and angle of attack at downwind is then expressed as:

$$V_R' = \sqrt{(V_a' sin\theta)^2 + (\omega R - V_a' cos\theta)^2} \quad \text{Equation 5.33}$$

$$\alpha' = \tan^{-1}\left\{\frac{(1 - \dot{a}')sin\theta}{\lambda - (1 - \dot{a}')cos\theta}\right\} \quad \text{Equation 5.34}$$

Once the new relative velocity and incidence angle are found using the new induction factor, the thrust coefficient, torque coefficient and power coefficient for

downwind region can be calculated easily using Equation 5.27, Equation 5.29 and Equation 5.30. Finally the total thrust, torque and power are the sum of those in the upwind and downwind zones.

5.2.2 Computing methodology and model improvements

The solution method is based on the concept that the force of the wind on the blades transformed into the axial direction could be determined simultaneously using both momentum and blade element considerations. Both of these are functions of induction factor $\dot{a}$ (or $\dot{a}'$) because the force on the blades depends on how much energy is absorbed by the blades. Iterative schemes are employed to solve for an $\dot{a}$ at each streamtube where these two calculations for axial force balance. The procedure for carrying out computations on a specified streamtube is as follows:

- $\dot{a}$ at upwind region is set equal to zero which indicates $V_a = V$
- V_R is obtained from Equation 5.16
- α is calculated from Equation 5.21
- C_n and C_t are obtained from input aerofoil dataset
- C_K for blade element consideration is calculated based on Equation 5.27
- C_K is compared with that calculated from momentum consideration
- The process is repeated starting with a new $\dot{a}$ until the C_K from the two calculations above are equal or at a small, acceptable difference
- $\dot{a}'$ at the downwind region is then set to zero and the same procedure for finding $\dot{a}$ in the upwind region is applied until a particular value of $\dot{a}'$ resulting in the two calculations for axial force balance.
- Torque and power are calculated for both the upwind and downwind regions

In this study, the total number of streamtubes used for analysis was 45 with $\Delta\theta = 4^{\circ}$. Further reducing $\Delta\theta$ did not shown significant change of C_p. The iterative procedure used in the DMST model analysis is shown in Figure 5.10.

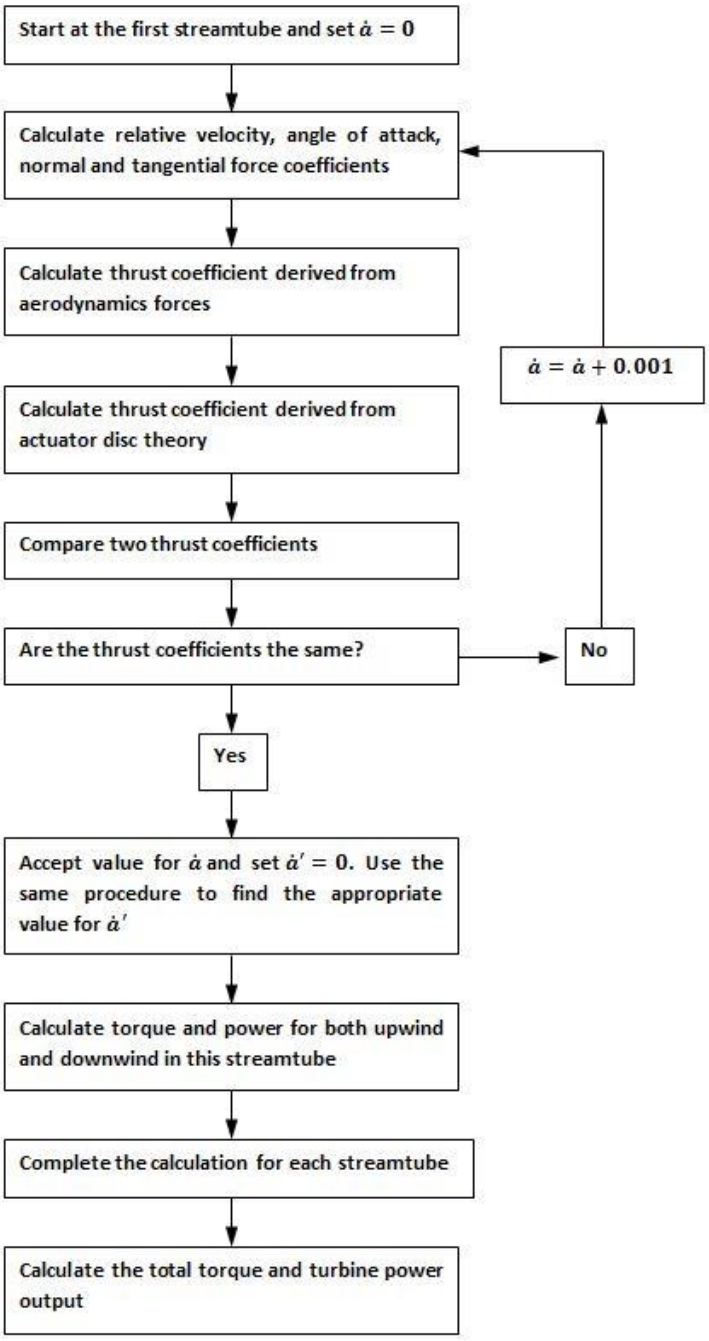

Figure 5.10 Iterative procedure used in DMST model to calculate the flow parameters and turbine power output

Based on the original DMST model, several improvements were made in order to provide more accurate results:

A. Glauert's correction

Thrust force in the axial direction due to the momentum consideration was based on actuator disk theory with Glauert's correction [150] since the original momentum

equation resulting from the axial equilibrium of the turbine was inappropriate for turbulent wakes as pointed out by Rossetti and Pavesi [64]:

$$C_{K\,mometum} = \begin{cases} 4\dot{a}(1-\dot{a}), & \dot{a} \leq \dot{a}_{\,thresh} \\ 1.215\dot{a} + 0.485, & \dot{a} \leq \dot{a}_{\,thresh} \end{cases} \quad \text{Equation 5.35}$$

$$\dot{a}_{\,thresh} = 1 - \frac{\sqrt{1.7}}{2} \quad \text{Equation 5.36}$$

The thrust coefficient from the blade element consideration is presented in Equation 5.27. For each streamtube the DMST model searched for the crossing points of $\dot{a}$ for the two methods outlined above with an adjustable step size increment in $\dot{a}$. Equations were solved twice in each streamtube for the upwind and downwind regions.

B. Streamtube expansion, flow curvature and tip loss

Streamtube expansion is the tendency for the flow to expand in the plane of rotation as it passes through the rotor due to conservation of mass and volume as the flow is retarded by the rotor. For wind turbines with high solidity or at high tip speed ratios, this phenomenon is most pronounced, causing the airflow to manoeuver around the turbine instead of pass through it.

The correction for streamtube expansion is difficult to apply to momentum models due to the difficulty with the definition of the boundaries between different streamtubes. This is because the azimuth position of these boundaries depends on the amount of flow expansion and thereby on the induction factors. In this study, the correction for streamtube expansion was based on Soraghan et al.'s approach [76] by making the approximation that the streamtubes were straight so that they can be defined initially in terms of the angle $\emptyset$ between the streamtube and a radial line protruding from the path of rotation as shown in Figure 5.11.

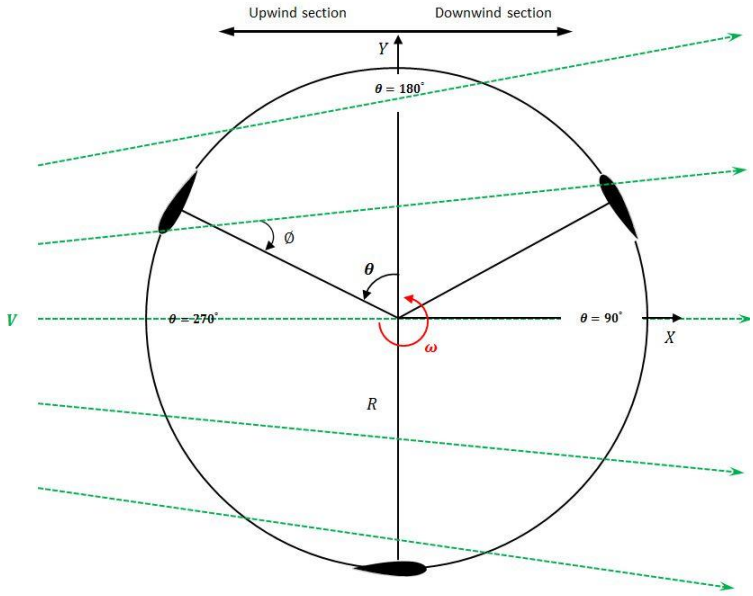

Figure 5.11 Schematic drawing of straight streamtube expansion

Therefore a correction factor was added to the equation of thrust coefficient predicted by blade element consideration based on Soraghan et al.'s study [76]:

$$C_K = \left\{\frac{Nc}{2R}\right\}\left\{\frac{V_R}{V}\right\}^2 \frac{1}{\pi}\left\{\frac{C_t \cos\theta}{\sin\theta} - C_n\right\}\left\{\sec(mod(\emptyset, \frac{\pi}{2}))\right\} \quad \text{Equation 5.37}$$

The correction for flow curvature was based on Sharpe's analysis [72] considering the additional normal force which acts toward the centre of rotation due to the orientation of virtual camber. The expression is shown in Chapter 2 Equation 2.2. Instead of estimating the derivative of C_l with respect to α, a constant value of 5.73 was used according to Soraghan et al.'s study [76]. This constant value was a good approximation for low α on the linear section of the $C_l - \alpha$ curve. The justification for this simplification was that the flow curvature will only become pronounced at high tip speed ratios where the blade incidence angle is inevitably very small.

With regard to the tip loss, Prandtl's tip loss correction factors [145] were applied to both ends of the blades as shown in Equation 5.8 and Equation 5.9.

C. Dynamic stall

The correction for dynamic stall used in this DMST model was based on Strickland's approach for VAWTs application [16]. This dynamic stall model assumed the blade thickness exceeds 12% and the flow was considered incompressible to eliminate the dependency on the Mach number. Furthermore, the dynamic coefficients were simplified for symmetrical blade profiles (all tests conducted in this section were using

the symmetrical NACA0012, NACA0015 or NACA0018 sections, which met those assumptions).

The modified reference angle of attack is expressed as:

$$\alpha_{ref} = \alpha - \gamma M_1 \sqrt{\left|\frac{c\dot{\alpha}}{2V}\right|} S_{\dot{\alpha}} \quad \text{Equation 5.38}$$

$$M_1 = 0.75 + 0.25 S_{\dot{\alpha}} \quad \text{Equation 5.39}$$

$$S_{\dot{\alpha}} = \begin{cases} -1, & \dot{\alpha} \geq 0 \\ 1, & \dot{\alpha} < 0 \end{cases} \quad \text{Equation 5.40}$$

$$\gamma = \begin{cases} 1.4 + 6.0(0.06 - t/c), & (lift) \\ 1.0 + 2.5(0.06 - t/c), & (drag) \end{cases} \quad \text{Equation 5.41}$$

where $\dot{\alpha}$ is the incidence difference between the previous and current one. The resulting aerodynamic force coefficients are then modified as:

$$C_{l_{dyn}} = \left(\frac{\alpha}{\alpha_{ref} - \alpha}\right) C_l(\alpha_{ref}) \quad \text{Equation 5.42}$$

$$C_{d_{dyn}} = C_d(\alpha_{ref}) \quad \text{Equation 5.43}$$

Since a VAWT blade usually encounters much higher angles of attack, to prevent overestimating the effect, Massé [96] proposed a method to interpolate between the static and dynamic blade data:

$$C_{l_{mod}} = \begin{cases} C_l + \dfrac{A_M \alpha_{ss} - \alpha}{A_M \alpha_{ss} - \alpha_{ss}} \left(C_{l_{dyn}} - C_l\right), & \alpha \leq A_M \alpha_{ss} \\ C_l, & \alpha > A_M \alpha_{ss} \end{cases} \quad \text{Equation 5.44}$$

$$C_{d_{mod}} = \begin{cases} C_d + \dfrac{A_M \alpha_{ss} - \alpha}{A_M \alpha_{ss} - \alpha_{ss}} \left(C_{d_{dyn}} - C_d\right), & \alpha \leq A_M \alpha_{ss} \\ C_d, & \alpha > A_M \alpha_{ss} \end{cases} \quad \text{Equation 5.45}$$

where A_M is an empirical constant of which Massé [96] suggested a value of 1.8. The α_{ss} then represents the angle at which the lift slope leaves the linear regime.

5.2.3 Input aerodynamic dataset and validation tests

Since there is only very limited blade aerodynamic data available in the literature for the full incidence range at low Reynolds numbers, the dataset of NACA0012, NACA0015 and NACA0018 from Sheldahl and Klimas [62] at the three Reynolds numbers they measured ($Re = 360{,}000$, $Re = 500{,}000$ and $Re = 700{,}000$) were applied for the validation tests in this DMST study. Their data at lower Reynolds numbers

were extrapolated by using the computer code PROFILE and is considered to be inaccurate here. Figure 5.12 and Figure 5.13 illustrate the aerodynamic data from Sheldahl and Klimas [62] compared with other recent aerodynamic data (measured only at low incidence angles since higher incidence data were not available).

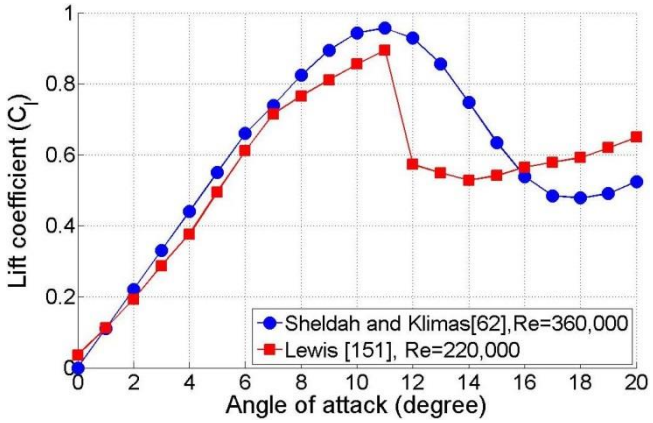

Figure 5.12 Example of lift coefficient comparison of NACA0015 between Sheldahl and Klimas [62] and Lewis [151]

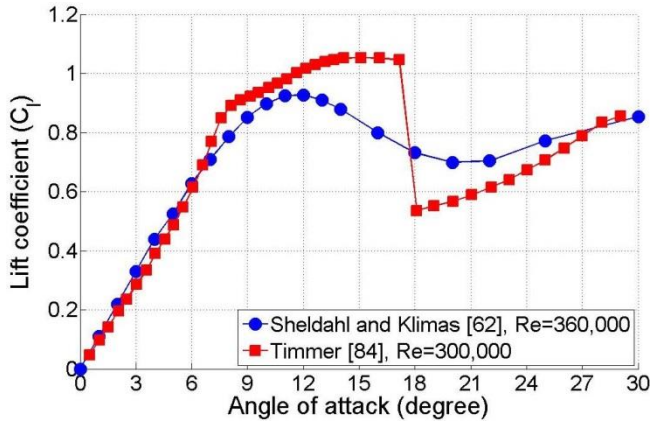

Figure 5.13 Example of lift coefficient comparison of NACA0018 between Sheldahl and Klimas [62] and Timmer [84]

As can be seen from the above comparisons, an apparent difference between these aerodynamic datasets is that measurements from Sheldahl and Klimas's study [62] always illustrate a gradual stall behaviour for all three Reynolds numbers. In contrast, aerofoil aerodynamic data at similar Reynolds numbers from other recent studies (e.g.[61, 70, 84, 151]) all demonstrate an aerofoil sudden stall behaviour. Nevertheless, without any better alternative data for the full incidence range at low Reynolds numbers available, Sheldahl and Klimas's measurement [62] was still employed in present study. Modification of Sheldahl and Klimas's original data and tests were

performed in order to examine whether these different stall behaviours changed the predicted turbine performance. Results are presented in the following sections.

Two validation tests were performed first in order to validate the DMST model. Results from the first validation test were compared with Strickland's [16] experimental measurements using NACA0012. The turbine radius is $R = 1.0\ \mathrm{m}$ and blade chord length is $c = 0.06\ \mathrm{m}$, which results in solidity of $\sigma = 0.18$. As can be seen from Figure 5.14, the DMST predicted results match the experimental measurements at low tip speed ratios but under-predict the performance around $\lambda = 3$. Both DMST model and experiments illustrate a peak turbine power output around $\lambda = 4.4$. Although the DMST model over-predicts the peak C_p and power output at high λ, it successfully captures the overall turbine performance trend.

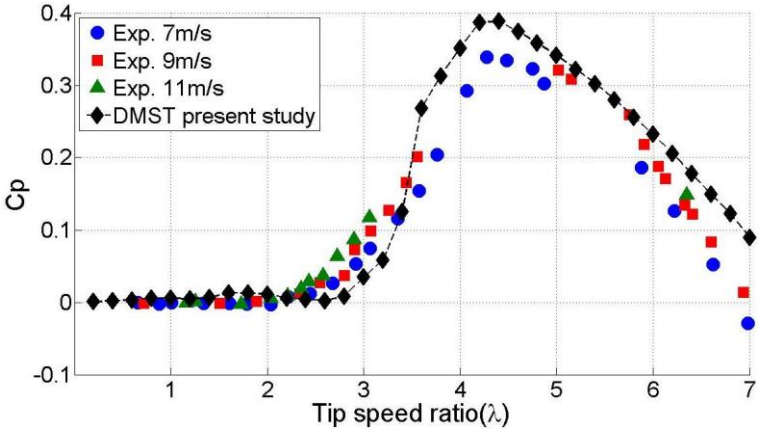

Figure 5.14 DMST model validation test for turbine with $R = 1.0\ \mathrm{m}, c = 0.06\ \mathrm{m}, \sigma = 0.18$. Upstream wind speed of $V = 7\ \mathrm{m/s}$. Experimental measurements from Strickland [16] with NACA0012

The second validation test was conducted by using a NACA0015 based turbine with $R = 1.0\ \mathrm{m}$ and $c = 0.15\ \mathrm{m}$. The result is compared with experimental measurements performed by Sheldahl et al. [15] and presented in Figure 5.15. The DMST model under-predicts the C_p at low tip speed ratios of $\lambda < 3$, which is thought to be partially due to the complex blade dynamic stall behaviour not being fully captured by the DMST model at low λ and partially because of the inadequate aerodynamic data at low Reynolds numbers. However the DMST model closely matches the experimental results at $\lambda > 5$. The DMST predicts a similar peak power output C_p but at earlier tip speed ratio of $\lambda = 4.4$ while the experiment shows the turbine peaks at $\lambda = 5.2$.

In general, the DMST model developed in this study is able to provide reasonably good predictions of turbine performance compared with experimental measurements. However, it must be noted that the input aerodynamic data from Sheldahl and Klimas

[62] is at $Re = 360{,}000$, $Re = 500{,}000$ and $Re = 700{,}000$. Data at lower Reynolds numbers is not available which might result in over-prediction for turbine performance at low tip speed ratios.

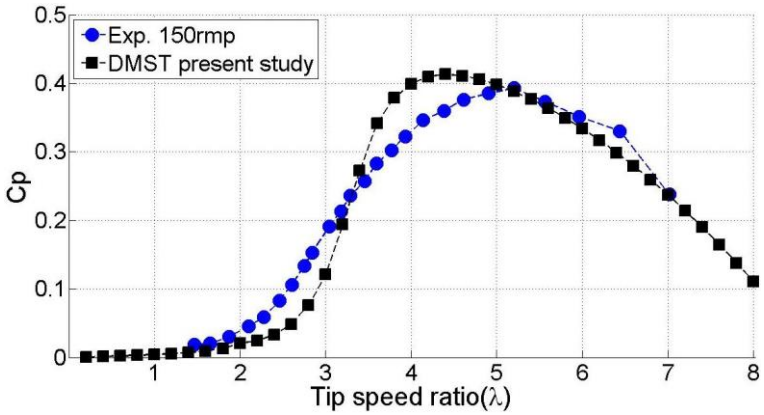

Figure 5.15 DMST model validation test for turbine with $R = 2.5\ \text{m}, c = 0.15\ \text{m}, \sigma = 0.18$. At constant rotation speed of $150\ \text{rpm}$. Experimental measurements from Sheldahl et al. [15] with NACA0015

5.2.4 DMST sensitivity study

As shown in Chapter 5.1, the BEM based model, the Start-Up model, is sensitive to input data quality. Different aerodynamic data or inaccurate measurements could result in totally different predictions and conclusions. In order to further analyse the influence of the input aerodynamic dataset on the prediction of turbine performance using the BEM based approach, the original Sheldahl and Klimas' data [62] for a NACA0018 with an aerofoil gradual stall behaviour was modified by a sudden stall based on Timmer's [84] and Gerakopulos et al.'s studies [83] of the NACA0018. Timmer's [84] and Gerakopulos et al.'s study [83] indicated the NACA0018 stall behaviour always leads to an approximately 50% drop of lift coefficient, therefore the original Sheldahl and Klimas' data [62] was modified based on this criteria and one example at $Re = 3.6 \times 10^5$ is shown in Figure 5.16 (a). The peak lift occurs at 12° followed by a gradual decrease of lift force to 22° shown by the original data. In contrast, the modified Sheldahl and Klimas' data illustrate a sudden stall of lift force from 0.92 at $12^\circ$to 0.46 at 13° (50% reduction). A straight line was created from 13° to intersect the original data at 22° in order to present the post-stall behaviour, which is similar to the typical NACA0018 post-stall behaviour based on Timmer's and Gerakopulos et al.'s experimental measurements. With regard to drag coefficient, a sudden increase of drag force occurs at the same incidence angle as the sudden decrease of lift based on

Timmer's measurement [84]. Therefore the sudden jump of drag coefficient is modified at 13° in this case and the value is estimated as a linear extension from 16° as can be seen in Figure 5.16 (b). No modification was made to the deep stall region. The same method was applied to the Sheldahl and Klimas' data [62] at other two Reynolds numbers of $Re = 500{,}000$ and $Re = 700{,}000$.

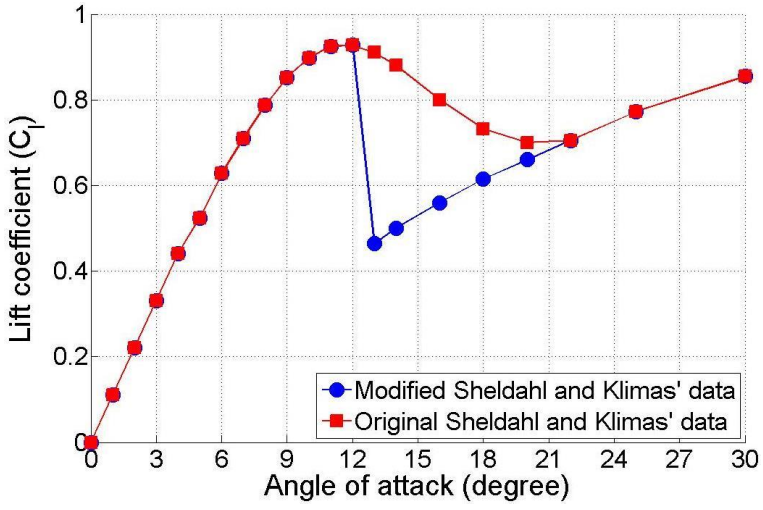

(a)

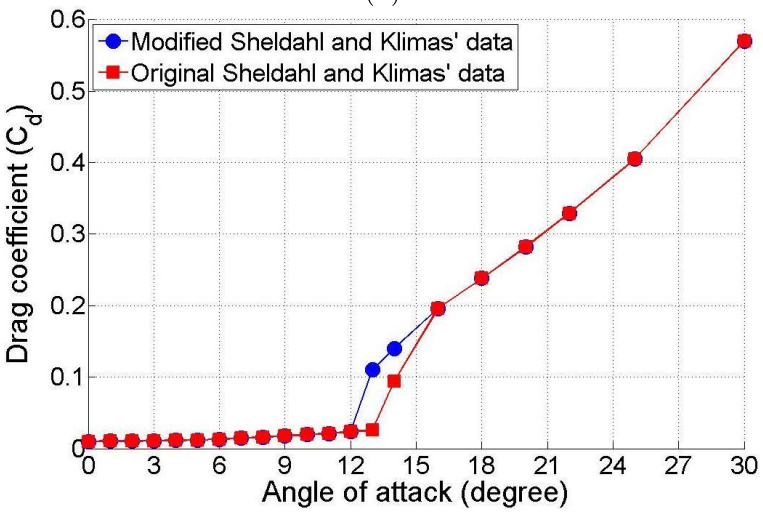

(b)

Figure 5.16 Original Sheldahl and Klimas' data of NACA0018 showing aerofoil gradual stall behaviour and example of modified Sheldahl and Klimas' data showing sudden stall characteristics. (a) Lift coefficient (b) Drag coefficient at $Re = 360{,}000$

The sensitivity tests were then performed by using these two different aerodynamic datasets: original Sheldahl and Klimas' data (referred to as original data), modified Sheldahl and Klimas' data (referred to as modified data). As can be seen in Figure 5.17, the original data significantly over-predicts the turbine performance all the way from $\lambda = 0$ to about $\lambda = 4.5$. The maximum over-prediction is about 141% and occurs at

$\lambda = 1.5$ with an averaged value of about 64% . The turbine extracts considerably more power using the original data and this would indicate a much stronger turbine self-starting capability. When the rotation speed reaches approximately $\lambda = 5.0$, the turbine blades will no longer experience incidence angles that are larger than the stall angle which leads to the predictions from the original data and modified data being the same. It must be noted that this over-prediction of turbine self-starting capability could result in up to 40% over-prediction of annual energy yield based on Worasinchai et al.'s study [152].

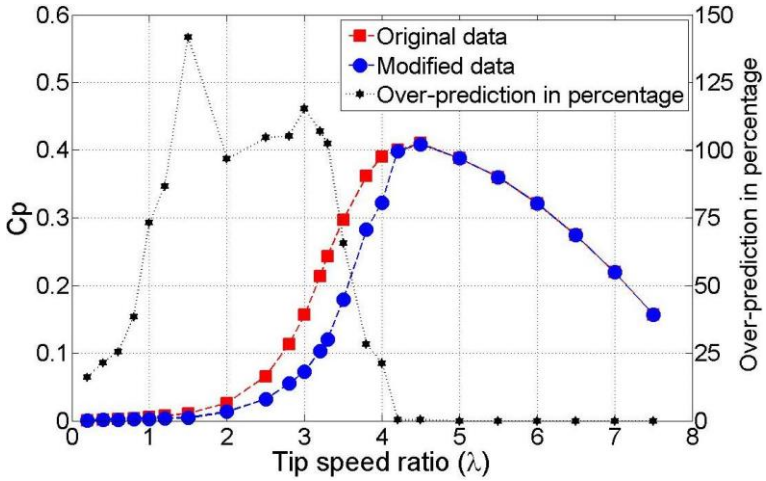

Figure 5.17 Comparison of predicted turbine performance by using original data from Sheldahl and Klimas [62] and the modified data. $V = 7$ m/s

Furthermore, the over-prediction from the original dataset is further studied by looking at the torque coefficient versus the blade azimuth position over a complete revolution at two tip speed ratios of $\lambda = 1.5$ and $\lambda = 3$ as shown in Figure 5.18. At $\lambda = 1.5$ (Figure 5.18 (a)), the blade experiences a large incidence range from about 0° to 42° and according to kinematic analysis, the sudden stall behaviour (modified data) results in the blade torque falling to a negative value much earlier than the gradual stall (original data) in the upwind region ($0^{\circ} < \theta < 180^{\circ}$). In the downwind region ($180^{\circ} < \theta < 360^{\circ}$), this sudden stall behaviour (modified data) delays the generation of positive torque to 319° while the original data predicts it much earlier, occurring at 303°. The blade with gradual stall behaviour (original data) enables the turbine to produce positive torque (and power) for a larger proportion of the revolution which finally results in the 141% larger C_p predicted as can be seen Figure 5.17.

At $\lambda = 3$ the angle of attack range reduces to 0°~20°, the gradual stall (original data) illustrates a positive torque for almost all azimuth angles (see Figure 5.18 (b)).

However, the sudden stall (modified data) still predicts two negative torque bands ($61^{\circ} < \theta < 149^{\circ}$ and ($215^{\circ} < \theta < 279^{\circ}$) due to the significant drop of lift (stall) and the corresponding increase of drag force.

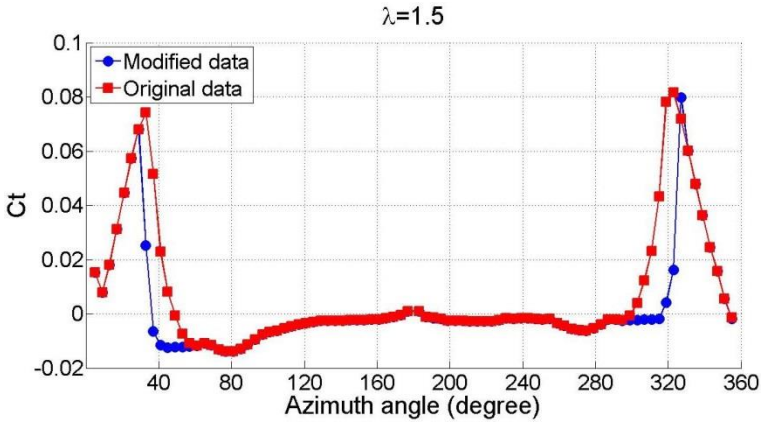

(a)

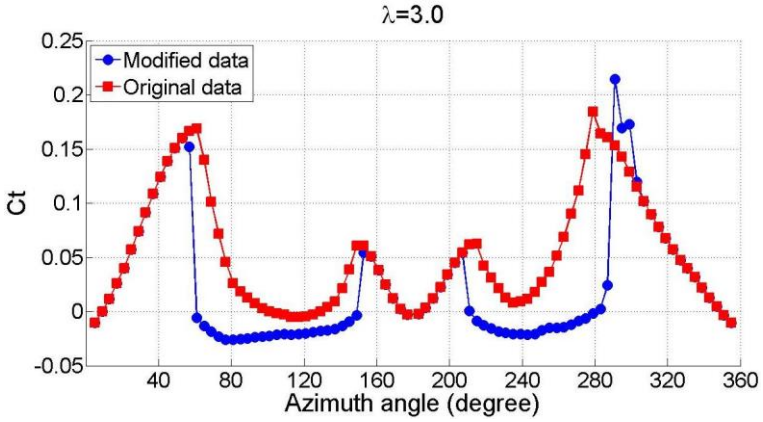

(b)

Figure 5.18 Comparison of predicted torque coefficient versus azimuth angle by using original data from Sheldahl and Klimas [62] and the modified data at (a) $\lambda = 1.5$ and (b) $\lambda = 3.0$

5.2.5 Conclusion and discussion

The sensitivity study performed using the DMST model further demonstrates that the predictions from BEM based approaches heavily depend on the input aerodynamic dataset quality. Particularly, the blade stall behaviour has a strong effect on the predicted turbine performance at relatively low tip speed ratios.

Nevertheless, from another perspective an important conclusion can be drawn is that blades with smooth stall behaviour (original data) may significantly improve the turbine performance and enhance the turbine self-starting capability. There is therefore a strong incentive to investigate methods to change the blade's sudden stall behaviour

to a gradual stall characteristic. It has been found that by creating tubercles around the blade leading edge the sudden stall can be successfully replaced by a more gradual stall behaviour. Detailed studies (BEM study and experimental study) of the blades with tubercle leading edges are therefore presented in Chapter 8.

Chapter 6

Experimental methods

6.1 Wind tunnel and test section

6.1.1 Durham $2\,m^2$ wind tunnel

The Durham $2\,m^2$, 3/4 open-jet, open-return wind tunnel was used to measure the H-Darrieus wind turbine performance and the aerofoil static aerodynamic performance at low Reynolds numbers, low blockage ratio in this thesis. The nozzle exit dimension is $1{,}150\,mm$ (height) $\times\, 1{,}730\,mm$ (width). A schematic drawing of the tunnel and a tunnel test section photograph are provided in Figure 6.1 (a) and Figure 6.1 (b).

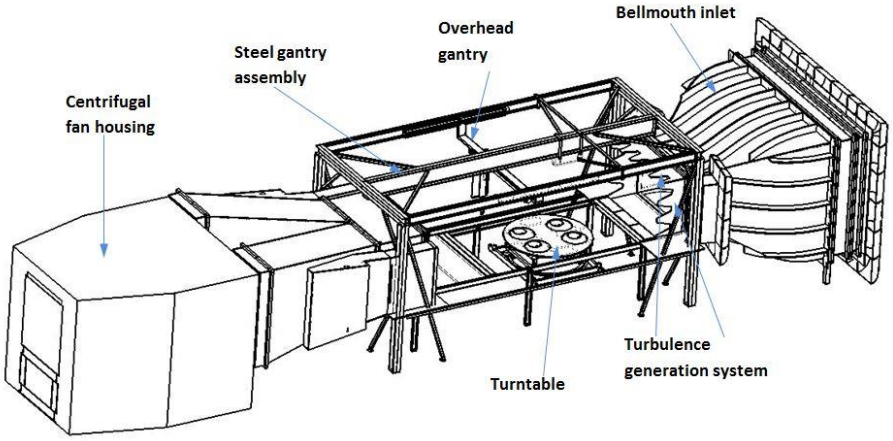

(a)

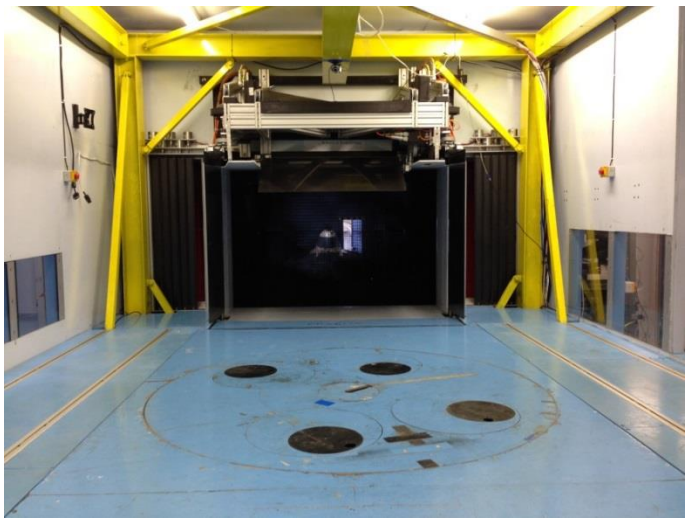

(b)

Figure 6.1 (a) Schematic drawing of the Durham $2\,m^2$, 3/4 open-jet, open-return wind tunnel and (b) working section (looking from downstream)

The tunnel is powered by two dual entry centrifugal fans which are located in the downstream fan housing. A honeycomb mesh at the inlet straightens the inlet flow and breaks up any large scale flow structures present in the room. The inlet contraction ratio is about $1:7.7$. A turbulence generation system (TGS) is installed at the inlet in order to generate large scale inlet turbulence if required but this feature was not used in this study. More details about the TGS can be found in Mankowski's study [153]. Mankowski's study also demonstrates that the flow through the inlet nozzle is uniform with no bulk yaw or pitch being induced when TGS is not being utilised. The turbulence intensity in the working section is less than 1%.

The tunnel has other features including floor boundary layer suction and a three axis overhead gantry traverse system for pressure probes. Readers are referred to Sims-Williams et al. [154] for more details about the design of the wind tunnel.

6.1.2 Durham $0.5\,\mathrm{m}^2$ Plint wind tunnel

Aerofoil static aerodynamic forces were also measured in the Durham $0.5\,\mathrm{m}^2$ Plint wind tunnel under open-jet and closed-jet flow conditions. The wind tunnel is an open circuit design which discharges the flow directly to the atmosphere as shown in Figure 6.2. The closed-jet test section, which has a square cross-section with solid walls measuring $460\,\mathrm{mm} \times 460\,\mathrm{mm}$, lies downstream from a bellmouth nozzle. An extended open-jet test section was also designed which has the same dimensions but without the top and bottom walls (see Figure 6.3). The flow in both the closed and open sections was uniform with less than 1% deviation of yaw and velocity across the test zone. The free-stream turbulence intensity in the test plane in both working sections was approximately 1%. These wind tunnel test conditions closely match those of the $2\,\mathrm{m}^2$ tunnel. For all of the wind tunnel tests in this study, the model was located in an established zone of negligible axial static pressure gradient in order to minimise horizontal buoyancy effects [154]. By controlling the fan speed, the upstream wind speed can be varied between $5\,\mathrm{m/s}$ and $20\,\mathrm{m/s}$. The aerofoil used in 2-D aerofoil study had a chord length of $130\,\mathrm{mm}$. Therefore the chord-to-tunnel height ratio was, $c/H = 130/460 \approx 0.28$, corresponding to a blockage range from 5% (zero incidence) to 28% (90° incidence). In contrast, the blockage ratio for static aerofoil testing in the Durham $2\,\mathrm{m}^2$ tunnel was 0.5% to 3% with a chord-to-tunnel width ratio of $c/H = 130/1730 \approx 0.075$ (note that the aerofoil's axis was placed vertically in the Durham $2\,\mathrm{m}^2$ tunnel and horizontally in the $0.5\,\mathrm{m}^2$ wind tunnel).

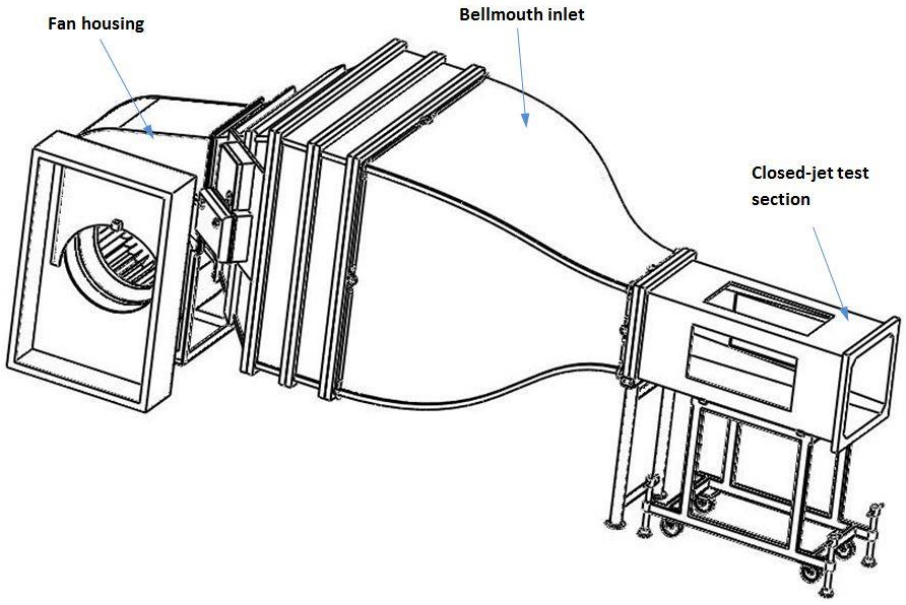

Figure 6.2 Schematic drawing of Durham $0.5\,\mathrm{m}^2$ Plint wind tunnel with only closed-jet test section

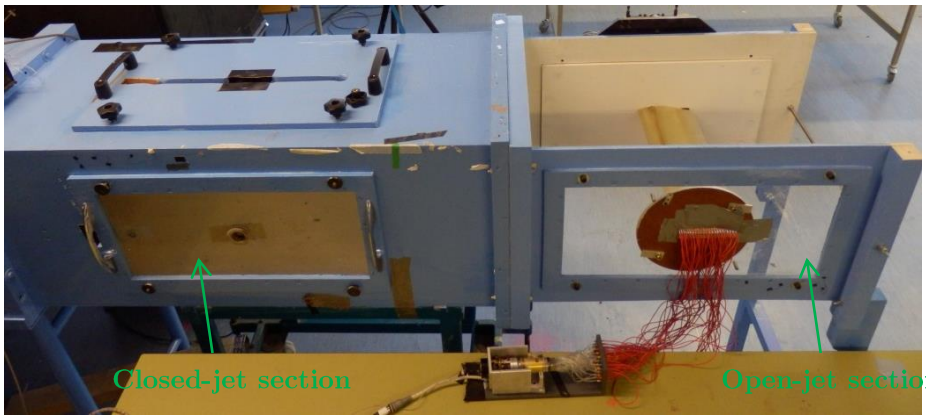

Figure 6.3 Photograph of Durham $0.5\,\mathrm{m}^2$ Plint wind tunnel showing both closed-jet test section and open-jet test section extension

6.2 Aerofoil model and testing methods

6.2.1 Aerofoil model

The aerofoil used for static wind tunnel measurement was the NACA0018 symmetric aerofoil since the NACA00xx series has been widely used in H-Darrieus wind turbine studies. The test aerofoil was manufactured by rapid prototyping from Fullcure 720, thus giving a high surface profile precision ($\pm 0.1\,\mathrm{mm}$). The aerofoil span was $460\,\mathrm{mm}$ which indicated that it could span the full width of the $0.5\,\mathrm{m}^2$ Plint wind tunnel test section in order to minimise, but not entirely eliminate, tip effects and hence to provide the best approximation of a two-dimensional flow along most of the aerofoil span. The

aerofoil was constructed around an $8\,\mathrm{mm}$ diameter steel bar which passed along its entire span and extended from one end to provide a rigid, cantilevered mounting from the force balance as can be seen in Figure 6.4 (a). A chord length of $130\,\mathrm{mm}$ was chosen to provide the required Reynolds number range and to provide a large-enough cross-sectional area to accommodate internal pressure instrumentation.

When used in the larger Durham $2\,\mathrm{m}^2$, $3/4$ open-return wind tunnel, two $380\,\mathrm{mm}$ radius circular endplates were fitted to each wing tip (shown in Figure 6.4 (b)) to mimic the nominally 2-D flow of the smaller test sections. The endplate edges were chamfered in order to minimise the impact on the flow. The aerofoil was placed in the middle of the flow in order to reduce any wall or shear layer boundary effects.

Measurements were performed at three different Reynolds numbers ($Re = 60{,}000$, $Re = 100{,}000$ and $Re = 140{,}000$) for angles of incidence ranging from 0° to 180° in both the $2\,\mathrm{m}^2$ and $0.5\,\mathrm{m}^2$ wind tunnels.

(a) (b) (c)

Figure 6.4 (a) NACA0018 aerofoil model (b) NACA0018 with two endplates (c) Side view of the pressure tappings

6.2.2 Measurements of static aerodynamic forces

Surface pressure measurements were obtained from 43 pressure tappings (each surface hole having a diameter of $0.8mm$, tapping locations are provided in Appendix A) symmetrically distributed at mid-span on the upper and lower surfaces of the aerofoil (the side view of the pressure tapping locations is presented in Figure 6.4 (c)). The static surface pressure measurements were obtained using a SensorTechnics 103LP10D

transducer through a Scanivalve at a sampling rate of $800\ \text{Hz}$ and averaged over a period of $3\ \text{s}$. The specifications of the pressure transducers is given in Table 6.1.

Operating pressure range	± 10 mbar
Sensitivity	0.25 V/mbar
Repeatability	$0.1\%\ FSO$
Response time	2 μsec
Linearity & Hysteresis	$1\%\ FSO$
Temperature (0-50^{0}C)	$0.5\%\ FSO$

Table 6.1 The specification of the pressure transducer, SensorTechnics 103LP10D

Data were acquired using a National Instruments USB-6218 ADC with 16 channels and a 16 bit resolution. This device has a sample rate up to $250kS/s$. In all the wind tunnels, the free stream total and static pressures at the test plane were obtained from a nozzle calibration based upon pressure measurements in the plenum and at the test section entry. The lift and drag coefficients were then calculated by integrating the pressure along the surface of the aerofoil based on Fuglsang et al.'s approach [155]:

$$C_n = \frac{1}{c}\oint C_{pp}(s)\vec{t}\cdot d\vec{s} \qquad \text{Equation 6.1}$$

$$C_t = \frac{1}{c}\oint C_{pp}(s)\vec{n}\cdot d\vec{s} \qquad \text{Equation 6.2}$$

where $\vec{t}$ is a unit vector aligned to the chord, $\vec{n}$ is a unit vector perpendicular to the chord and $d\vec{s}$ is running along the aerofoil surface.

$$C_l = C_n cos\alpha + C_c sin\alpha \qquad \text{Equation 6.3}$$

$$C_d = C_n sin\alpha - C_c cos\alpha \qquad \text{Equation 6.4}$$

where α is incidence angle.

Multiple measurements were performed to estimate the standard deviation and repeatability of the static pressure and force measurements. The uncertainties are summarised in Table 6.2.

Variable	Closed-jet	Open-jet	$2\ \mathrm{m}^2$ wind tunnel
Aerofoil profile	± 0.1 mm	± 0.1 mm	± 0.1 mm
Incidence angle	$\pm 0.5^{\circ}$	$\pm 0.5^{\circ}$	$\pm 0.1^{\circ}$
Reynolds numbers	± 850	± 900	± 1320
Pressure coefficient	± 0.035	± 0.033	± 0.042
Lift coefficient	± 0.023	± 0.025	± 0.028
Drag coefficient	± 0.011	± 0.011	± 0.014

Table 6.2 Uncertainties in static force coefficient measurements

6.2.3 Surface flow visualization

Surface flow visualization was performed in the $0.5\ \mathrm{m}^2$ Plint wind tunnel open- and closed-jet test sections at the Reynolds number of $Re = 140{,}000$ using a fluorescent pigment suspended in kerosene. The surface of the blade was painted black to maximise the contrast of the flow patterns. Visualization was conducted on a limited region centred about mid-span. The region was delimited by self-adhesive tape to improve the quality of the image. Small spanwise disturbances may be created locally by the tape but this does not significantly influence the flow at the centre of the area of interest. The aerofoil was removed from the wind tunnel to record the flow patterns photographically. The repeatability of the images in terms of the positional and angular alignment of the axes of the camera and the blade chord line was accurate to $1\ \mathrm{mm}$ and 1° respectively.

6.2.4 Wake velocity field measurements

The pressures, velocities and flow trajectories downstream from the aerofoil were measured using a conical-head five-hole pressure probe with a diameter of $5\ \mathrm{mm}$. The measurements were taken in both closed-jet and open-jet sections of the Durham $0.5\ \mathrm{m}^2$ Plint wind tunnel at Reynolds number of $Re = 100{,}000$ and $Re = 140{,}000$. The size of the probe limits the spatial resolution of flow structures that are smaller than the probe head but previous studies have demonstrated that there is no significant impact on the flow itself [156, 157]. The probe was calibrated for pitch and yaw (see Figure 6.5) within the range of $\pm 45°$ and for a range of velocities exceeding the peak test flow velocity. Details about the five-hole probe technique and calibration methods can be found in [157]. The five pressure signals were sampled at a frequency of $800\ \mathrm{Hz}$, and

averaged over a period of 10 seconds. Pressures, velocities and flow direction were obtained using in-house post-processing routines based on a calibration map that had been obtained using a dedicated probe calibration facility. Errors were estimated to be ± 0.3 m/s ($\pm 2\%$) for velocity magnitude and $\pm 0.5^{\circ}$ degrees for pitch angle.

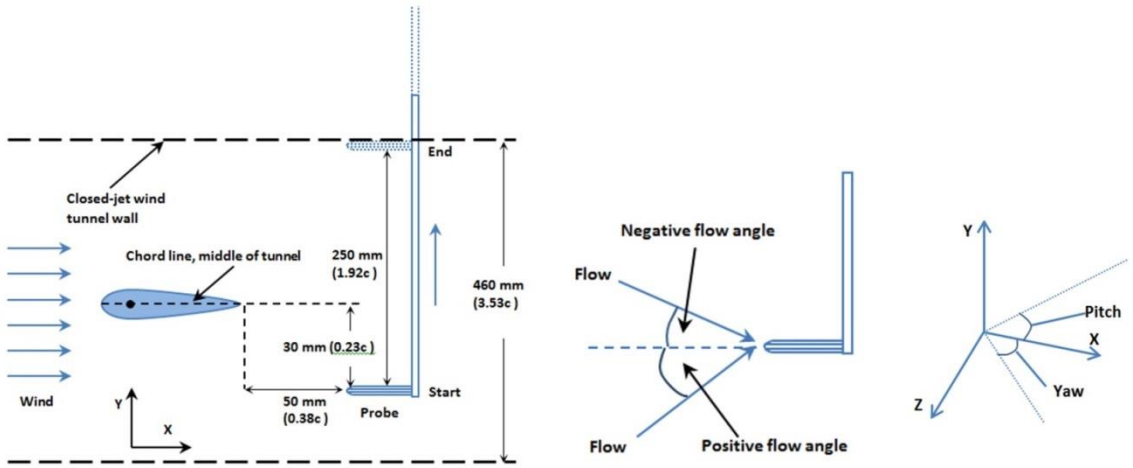

Figure 6.5 Schematic diagram of the side view of the five-hole probe in the wind tunnel and the pitch and yaw definition

As depicted in Figure 6.5, the aerofoil was mounted about a horizontal axis and the probe was placed 50 mm (0.38c) downstream of the trailing edge of the aerofoil (when set at zero incidence). The probe was traversed in the vertical direction with a positional resolution of 0.0025 mm over a distance of 250 mm (1.92c) with its starting position set 30 mm (0.23c) below the chord line of the aerofoil when set at zero incidence angle. The origin of the probe coordinate system was taken at the starting position of the probe throughout this study.

6.2.5 Aerofoil test matrix

Extensive static wind tunnel measurements were performed in three different wind tunnels at three low Reynolds numbers. The measured incidence ranges from 0° to 180°. In total there are almost 1,620 pressure distributions measured under different conditions. All the experimental tests using the NACA0018 aerofoil are summarised in Table 6.3 and the results are presented in the next chapter.

	Closed-jet	Open-jet	2 m^2 wind tunnel
Aerofoil profile	NACA0018	NACA0018	NACA0018
Aerodynamic force	0°~180°	0°~180°	0°~180°
Reynolds numbers	60,000 100,000 140,000	60,000 100,000 140,000	60,000 100,000 140,000
Surface flow visualization	8°~18° 40°~60°	8°~18° 40°~60°	No test
Wake measurement	12°~20° 40°~60°	12°~20° 40°~52°	No test

Table 6.3 Summary of aerofoil tests

6.3 Three bladed H-Darrieus wind turbine testing methods

6.3.1 Blade models

Three different blade profiles were employed in this study: NACA0021, DU06W200 and NACA4415. The chord length was $c = 100\,\text{mm}$ for all of the blades. In order to examine the turbine performance at a given solidity but with different combinations of blade chord length and turbine radius, a larger NACA0021 was created with $c = 150\,\text{mm}$. The profiles of all the blades tested in this study are shown in Figure 6.6. Each blade was made from laser cut plywood laminates of $10\,\text{mm}$ width. These wooden laminates were assembled to produce a complete blade. Two threaded bars were passed through holes cut into the laminates so sections could be assembled and clamped tightly together using nuts at the ends of both bars (shown in Figure 6.7). This arrangement leads to the easy modification of blade span and two blade span lengths were examined in this study: $S = 600\,\text{mm}$ and $S = 700\,\text{mm}$ corresponding to aspect raitos of 6 and 7 respectively. In order to reduce mass, the blades had central material removed but leaving a significant wall thickness to retain strength and stiffness as shown in Figure 6.6. After assembling the blade, sand paper was used to make a smoother blade surface.

In order to connect the blades to the turbine support arms with sufficient accuracy and strength, two additional laminates made from perspex were used as connection parts for each blade as shown in Figure 6.7. The perspex is much stronger than wood (at least an order of magnitude stronger in terms of tensile strength) and it can also

absorb high shock. Each blade was secured by two support arms. Furthermore, by changing the relative location of the two holes on the perspex laminates (see Figure 6.7), the blades could be fastened on the support arms at a pre-set pitch angle. Three pitch angles were investigated ($\beta = 0^{\circ}$, $\beta = -2^{\circ}$ and $\beta = -4^{\circ}$) which were selected based upon evidence of improved performance from previous CFD studies and studies performed by Klimas and Worstell [94].

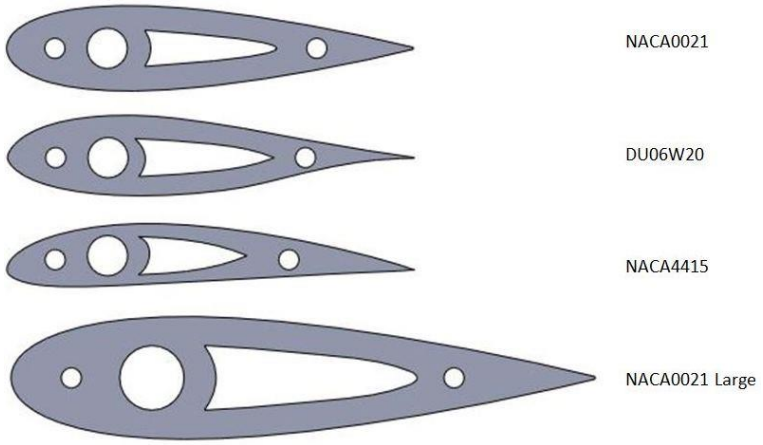

Figure 6.6 Side view of the blades profile of NACA0021, DU06W200, NACA4415 with $c = 100$ mm and the large NACA0021with $c = 150$ mm.

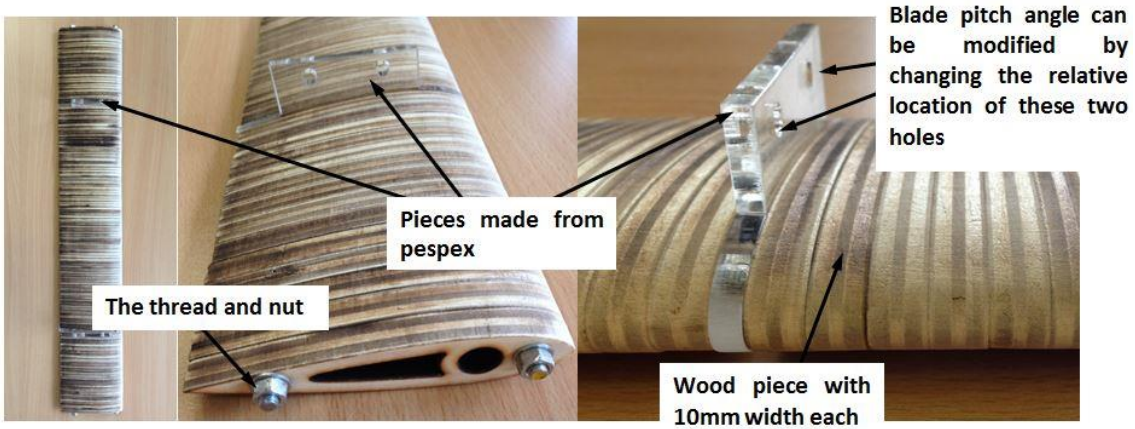

Figure 6.7 Photograph of the H-Darrieus blade showing threads, nuts, wood laminates and perspex mounting pieces. Pre-set blade pitch angle can be modified by replacing perspex pieces with different relative hole locations.

In respect to the study of blades with tubercle leading edge (see Chapter 8), the modification of blades was only made at $0 \leq x \leq 0.3c$, the remaining trailing part ($0.3c < x \leq 1.0c$) was kept the same as the standard NACA0021 profile. The blade chord length was $c = 100$ mm. To ensure that each of the tubercle leading edge sections

was produced with an acceptable compromise between accuracy and cost, the following procedures were followed:

- **Step1**: The tubercle leading edge part was drawn in Solidworks (Figure 6.8 step1)
- **Step2**: A male mould was manufactured by rapid prototyping from Fullcure 720 (Figure 6.8 step2)
- **Step3**: 20 layers of latex were applied to this mould in order to make a female rubber mould (Figure 6.8 step3)
- **Step4**: Plaster of Paris was mixed with water in appropriate ratio and then poured into this rubber mould to make a solid plaster cast (Figure 6.8 step4)
- **Step5**: Plastic tubercle leading edge models were then made by vacuum forming oven (Figure 6.8 step5). The maximum span length per section was limited by the forming oven width to 300 mm. Therefore in this study two sections were required to make one complete blade with a span length of 600 mm.
- **Step6**: wood laminate trailing edge pieces were cut by laser machine and assembled together using threads and nuts. In order to ensure a smooth connection between the leading part and the trailing part, the thickness of the plastic tubercle leading edge model (about 1 mm) was also considered by creating an indentation on the top and bottom of the wood trailing part. (Figure 6.8 step6)
- **Step7**: The plastic tubercle model was glued on the wood trailing part. Multipurpose filler was then used to fill any small gaps resulting from manufacture error. Sand paper was used to further smooth the surface
- **Step8**: Foil tape (about 15 mm width, and 0.03 mm thickness) was used at the connection area to create a smoother surface. (Figure 6.8 step8)

Step 1

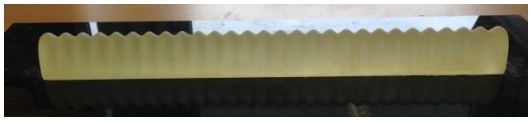

Step 2

Step 3

Step 4

Step 5

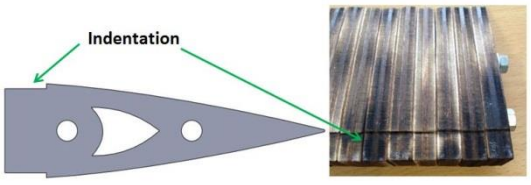

Step 6

Step 8

Figure 6.8 Manufacturing procedures of the blade with tubercle leading edge

It must be noted that sand paper was used to smooth the surface after applying the filler around the connection area. Any change in profile shape was negligible after sanding (less than $\pm 5\%$ deviation in aerofoil thickness) which kept the NACA0021 shape with a smooth transition from the plastic tubercle leading part to the wood trailing part.

The deviation of chord length of all the blades manufactured and used in this study was less than $\pm 1\,\text{mm}$, which resulted in about $\pm 1\%$ uncertainties about the calculated turbine solidity σ.

6.3.2 Blade surface roughness measurement

In order to examine the effects of blade surface roughness on H-Darrieus wind turbine performance including its self-starting capability, blades with two different surface finishes were tested and compared in this study. The original turbine blade was laser cut from high grade plywood resulting in a relatively rough surface. To reduce the surface roughness a new set of blades were manufactured and then coated with thin aluminium tape. The tape was extremely thin, $0.03\,\text{mm}$, so the effect of increased blade thickness can be ignored.

To quantify the roughness value, a ZETA-20 3-D profiler [158] was employed in this study to measure the surface roughness. The ZETA-20 is a fully integrated surface measurement system which can provide advanced 3-D imaging and metrology features of samples. This system measures the surface roughness by applying the theory of white light interference [159] and it mainly consists of a CCD camera, axis-drive mechanism and analysis software. The maximum resolution is up to $0.01\,\mu\text{m}$.

For each surface finish, measurements were repeated using three sample pieces ($30\,\text{mm} \times 30\,\text{mm}$) in order to calculate the averaged surface roughness value. Various

3-D roughness parameters including maximum height (S_z), maximum peak height (S_p), maximum valley depth (S_v), arithmetic mean height (S_a) and root mean squared height (S_q) were calculated and recorded along with the 3-D colour surface imaging. The mean results for the wood sample and the sample covered with thin aluminium tape are provided in Table 6.4. Examples of local 3-D colour imaging are also illustrated in Figure 6.9.

	S_a	S_q	S_z	S_p	S_v
Aluminium	0.2201	0.28045	2.719	1.747	0.9724
Wood	4.023	5.0265	33.155	17.745	15.4

Table 6.4 Measured surface roughness (mean value) of wood sample and the sample covered with thin aluminium tape. Unit: μm

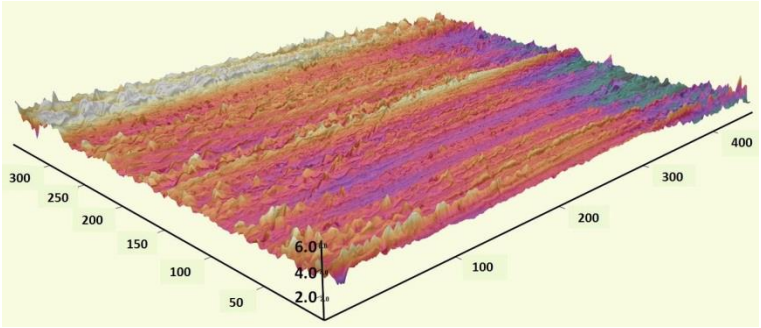

(a)

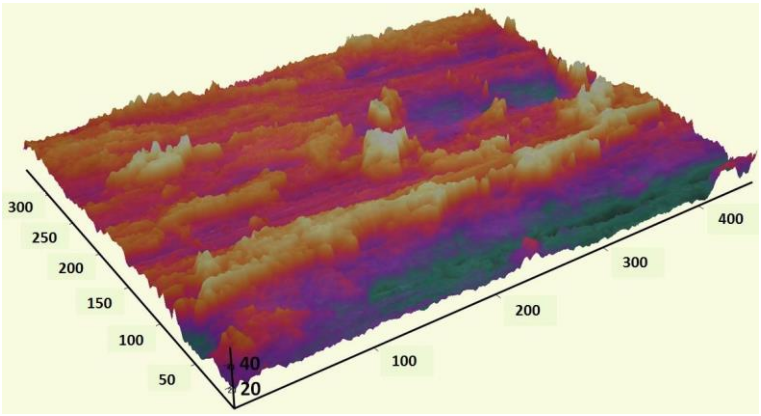

(b)

Figure 6.9 Local 3D colour imaging from ZETA-20 (a) aluminium (b) wood. Unit: μm

By examining the generally used parameters of S_a and S_q that represent an overall measurement of 3-D surface roughness, it can be clearly seen that the surface roughness of the wood sample was approximately 18 times larger than the one covered with aluminium tape. Moreover, the local 3-D colour imaging from the wood sample

illustrates much larger fluctuations of peaks and valleys than those from the aluminium surface, further demonstrating a lager surface roughness. The effects of this significant difference in blade surface roughness on turbine performance are examined in Chapter 7.

6.3.3 Support arms and H-Darrieus turbine arrangement

The turbine support arms were designed in Solidworks based on NACA0014 profiles of $60\,\text{mm}$ chord length and manufactured by 3-D printer. Each support arm was made of two (or three) pieces as shown in Figure 6.10. Bolts and nuts were used to connect pieces. Although these fastenings produce more air resistance to the turbine, this arrangement allows the turbine radius (length of the support arm) to be changed easily at low cost. In this study, three different radii were examined: $R = 300\,\text{mm}$, $R = 370\,\text{mm}$ and $R = 450\,\text{mm}$. Due to the manufacture and assembly tolerances the length of the support arms was slightly longer/shorter than the designed value, which results in the largest possible uncertainty of $\pm 0.67\%$ in terms of turbine solidity σ.

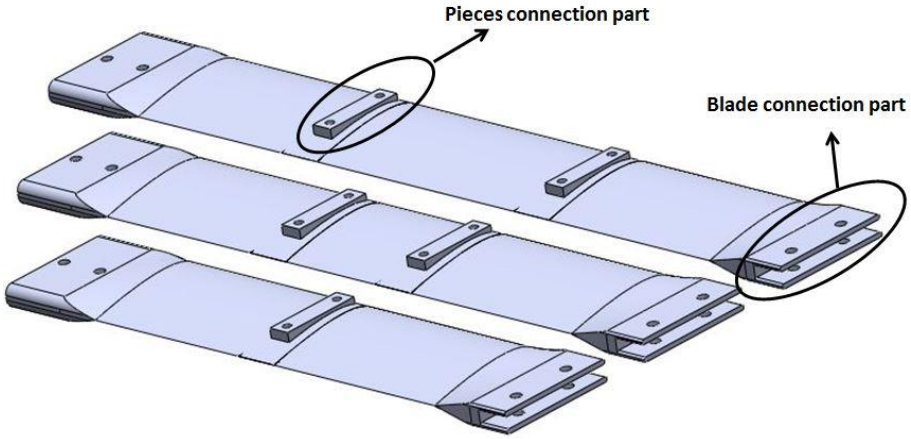

Figure 6.10 Support arms with different lengths

Each turbine blade was held by two support arms and the whole turbine was placed in the middle of the upstream flow in order to reduce shear layer and ground effects as shown in Figure 6.11(a). The turbine was mounted on a $15\,\text{mm}$ diameter central shaft which was supported by bearings at both ends so as to minimise vibration at large rotational speeds. The centre shaft was aligned vertically using digital inclinometer with a resolution of 0.1°.

At its base the shaft was attached to a permanet magnet torquemeter that could be used to apply load to the turbine. The torquemeter comprised a fixed lower aluminium disc to which were attached permanent magents. The upper disc was free to rotate with the turbine (see Figure 6.11 (b)). Changing the inter-disc spacing by raising the lower disc increased the resistance load. This torquemeter was used to provide 'brake' torque

which together with a drive motor enabled a constant rotational speed to be maintained if required.

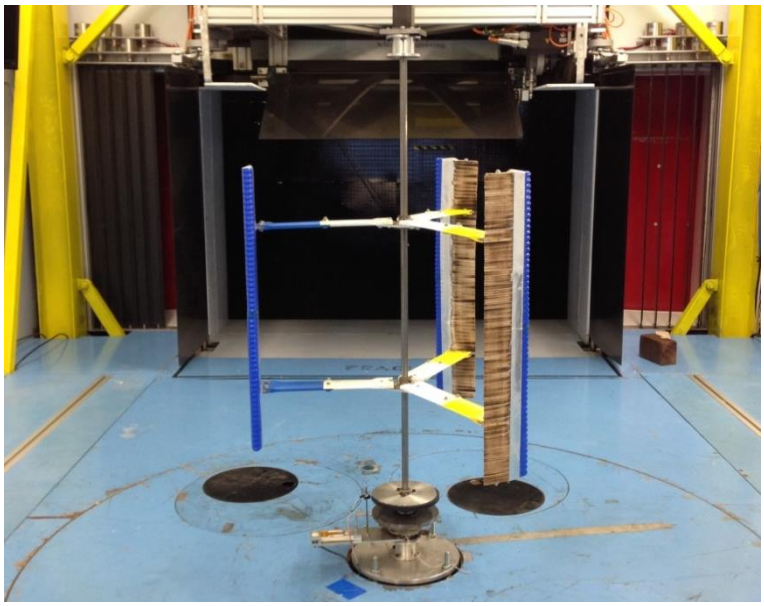

(a)

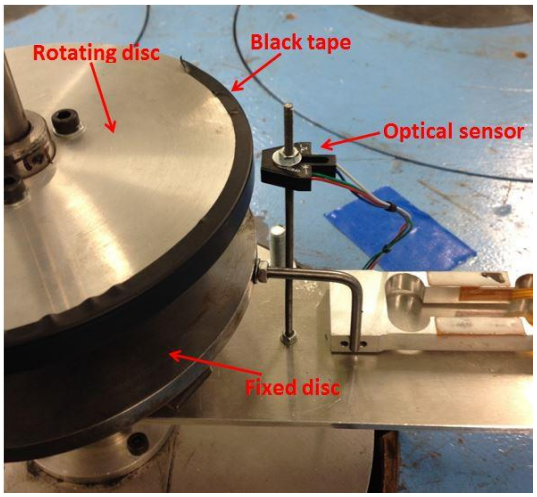

(b)

Figure 6.11 (a) Photograph of H-Darrieus wind turbine arrangement. (b) The torquemeter that consists of a lower rotating disc and an upper fixed disc

6.3.4 Rotational speed measurement

In this study, the H-Darrieus wind turbine rotational speed and acceleration (or deceleration) rate was measured by an optical sensor. The sensor was designed for remote mounting and consisted of an infrared light emitting diode and a NPN silicon phototransistor. When used as a non-contact reflective object sensor, the phototransistor responds to illumination from the emitter when a reflective object

passes within the field of view producing a high TTL voltage output. Otherwise, the voltage output is around zero.

The optical sensor was mounted beside the torquemeter's rotating disc within a distance at about 4 mm as suggested in the manual [158] (shown in Figure 6.11(b)). Part of the disc's perimeter was covered with black tape in order to create a non-reflective object. The voltage output was recorded using the National Instruments USB-6218 ADC and an example is shown in Figure 6.12.

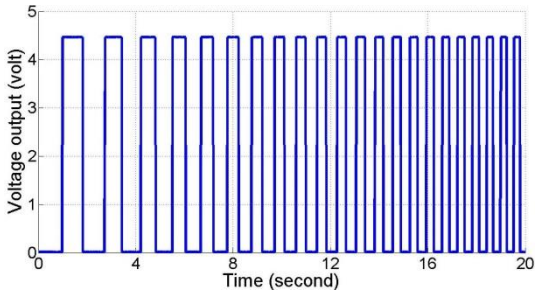

Figure 6.12 Example of TTL voltage output

6.3.5 Torque (and power) calculation

Since turbine performance is usually evaluated and compared in terms of torque coefficient C_T and power coefficient C_p, the torque (and power) generated by the turbine blades was then calculated in this study in order to compare with those predicted by 2-D CFD studies. Although the magnetic torquemeter provide useful load control, its torque measurement accuracy was insufficient for this study so an alternative method was adopted. The method employed to measure and calculate the blade torque (and power) followed the technique proposed by Edwards et al [6].

The force balance equation of the turbine system is determined by Equation 6.5. T_B is the net torque generated by all of the blades. T_{res} is the resistance torque generated by the whole system (excluding the blades). I_s is the whole system moment of inertia including blades and this value is calculated from the mass and geometry of the rig. The angular acceleration ξ is calculated from two readings of rotational speed (ω_1 and ω_2) measured by the optical sensor described above, and knowing the time between the readings taken at t_1 and t_2 the acceleration can be easily calculated by Equation 6.6.

$$T_B + T_{res} = I_s \xi \qquad \text{Equation 6.5}$$

$$\xi = \frac{\omega_2 - \omega_1}{t_2 - t_1} \qquad \text{Equation 6.6}$$

Knowing the blade torque, the torque coefficient and power coefficient can then be easily determined by Equation 6.7 and Equation 6.8 respectively.

$$C_T = T_B / 0.5\rho A V^3 \quad \text{Equation 6.7}$$

$$C_p = C_T \lambda \quad \text{Equation 6.8}$$

where ρ is air density, A is the frontal area of the turbine and V is upstream wind speed.

The following sections will detail the process for quantifying the system resistance T_{res} and system moment of inertia I_s in order to determine the torque generated by the blade T_B.

A. H-Darrieus wind turbine system resistance

Spin-down tests were performed without the blades in order to calculate the whole turbine system resistance. The turbine was first driven by a motor up to a high tip speed ratio which exceeds the maximum tip speed ratio for other tests. The motor was then disconnected from the turbine using a clutch mechanism and the turbine was free to spin down. The turbine deceleration rate ξ measured using the optical sensor and T_{res} was then deduced from Equation 6.9. It must be noted that the moment of inertia of the rig without blades I_{rig} was calculated from the mass and geometry of the rig.

$$T_{res} = I_{rig}\left(\frac{\omega_2 - \omega_1}{t_2 - t_1}\right) = I_{rig}\xi \quad \text{Equation 6.9}$$

Although the system resistance T_{res} varies continuously as the turbine spins down, a constant value was assumed across the time interval of $t_2 - t_1$. This assumption was justified by adopting a sensor sampling frequency of $200\ \text{Hz}$ which was much higher than the maximum frequency that the turbine could reach ($< 10\ \text{Hz}$). A series of readings could therefore be taken from peak rotational speed to zero, mapping out the $T_{res} - \omega$ curve. Moreover, the spin-down tests were repeated 6 times in order to calculate the averaged $T_{res} - \omega$ curve.

As demonstrated by Edwards et al [6], although the increased mass resulting from the addition of the blades might alter the bearing friction, the difference of T_{res} was negligible. Therefore the effect from the added blade mass on the bearing friction was ignored in this study. Furthermore, the spin-down tests in this study were conducted at different upstream wind speeds of $6, 7$ and $8\ \text{m/s}$. Negligible differences were found in

T_{res} indicating the resistance was dominated by ω and bearing resistance. This was consistent with Edwards et al.'s study [6].

B. Moment of inertia of the H-Darrieus wind turbine

The moment of inertia of the H-Darrieus wind turbine employed in this study mainly consisted of four parts: the three blades, the six support arms, the turbine centre shaft and the torquemeter disc at the base of the turbine (see Figure 6.12 (a)). The calculation is based on mass measurement and geometry simplification as detailed in Table 6.5.

Finally, the total inertia of the turbine system with and without blades is given by Equation 6.10 and Equation 6.11 respectively:

$$I_s = 3I_B + 6I_{arm} + I_t + I_d \qquad \text{Equation 6.10}$$

$$I_{rig} = 6I_{arm} + I_t + I_d \qquad \text{Equation 6.11}$$

For blades of essentially equivalent geometry, this was an acceptable approximation. Although fastenings (bolts and nuts) at discrete points along the support arms resulted in a non-uniform thin rectangular plate, the deviation was minor and as equivalent support arms were used for all of the tests in this study this error should not affect the comparison between experimental results. The maximum uncertainty of calculated power coefficients C_p due to the simplified inertia was estimated to be less than $\pm 5\%$.

Parts	Description	Schematic drawing	Equation
Blades	In this study, the turbine blades are simplified into solid cuboids with thickness of t_c equal to the maximum aerofoil thickness and width of c. The parallel axis theorem [160] is used to calculate the moment of inertia of the rectangles rotating around the turbine shaft.	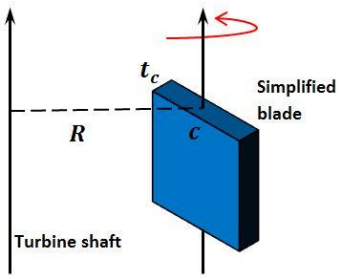	$I_B = \frac{m_b(c^2 + t_c^2)}{12} + m_b R^2$
Support arms	The turbine support arms are simplified into thin rectangular plates with length of R and width of d.	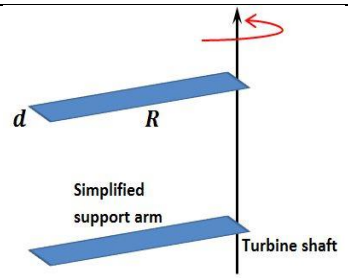	$I_{arm} = \frac{m_a R^2}{3} + \frac{m_a d^2}{12}$
Turbine shaft and torquemeter disc	Both the turbine centre shaft and the torquemeter disc are treated as equivalent solid cylinders with corresponding radius r_t and r_d.	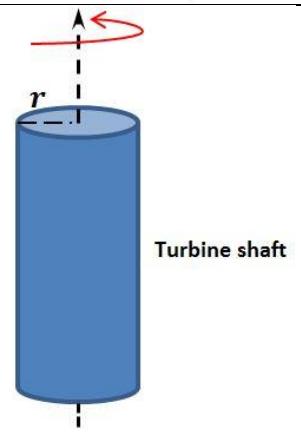	$I_t = \frac{m_t r_t^2}{2}$ And $I_d = \frac{m_d r_d^2}{2}$
Note: the 'm' in the above equations means the mass of corresponding part or averaged mass of corresponding parts (e.g. blades and support arms)			

Table 6.5 Equations for calculating the moment of inertia of different turbine parts.

6.3.6 On-board pressure measurement

It is difficult to measure the pressure variation around H-Darrieus wind turbine blades using traditional methods such as hot wires or pressure probes due to the rotating nature of the turbine. Moreover, since the turbine blades will experience a large range of incidence angle during one revolution, the pressure varies significantly around the blades with different turbine positions (azimuth angles), which makes the surface flow visualization method inappropriate for this application. Previous experimental studies focused on PIV methods to illustrate the instantaneous velocity field (and indirectly the pressure field) of the blade at different azimuth angles. This method undoubtedly improved the understanding of the aerodynamics of H-Darrieus wind turbines. However, in this study a new high frequency, time-accurate, on-board pressure measurement was proposed for directly measuring the instantaneous pressure change around the blade when the turbine was rotating. All of the measuring and recording components was placed on the turbine and rotated along with the blade. To the best of the authors' knowledge, this is the first time that the instantaneous pressure variation around the blade has been measured and recorded directly for an H-Darrieus wind turbine.

For the on-board pressure measurement, the H-Darrieus wind turbine was driven at constant tip speed ratios (λ) by a motor in conjunction with a torquemeter providing a stabilizing 'brake' torque. The pressure was then measured at corresponding constant pre-set intervals which equated to $\theta = 0.25^{\circ}$ leading to $1{,}440$ points measured for each revolution at the examined λ. The measurements were repeated for 100 revolutions in order to calculate the averaged pressure value at each azimuth angle and minimise any noise from the electronic components. More details are provided in section **C** below.

This on-board pressure measurement system mainly consisted of an instrumented blade section with pressure tappings, a microcontroller datalogger, a pressure scanner, an optical sensor, a bluetooth and a battery. Details are provided in the following sections:

A. The instrumented blade section

The blade profile was chosen to be the NACA0021 since it is widely used in VAWT researches and it has a relatively large thickness to accommodate the pressure tappings. The same wooden laminate construction was adopted with an additional perspex laminate containing 15 pressure tappings. Fourteen pressure tappings were distributed symmetrically on the pressure side and suction side with one tapping at the leading edge. The coordinates of these pressure tappings are provided in Table 6.6.

Unfortunately, due to the relatively small thickness near the blade trailing edge it was not possible to locate any tapping after $x/c = 0.6$ on the respective surfaces. The tappings were created by drilling holes perpendicular to the local blade surface into transverse internal tubes as can be seen in Figure 6.13. Each pressure tapping had a diameter of 0.5 mm.

Suction side		Pressure side		Leading edge	
Tapping No.	x/c	Tapping No.	x/c	Tapping No.	x/c
1	0.046	8	0.046	15	0
2	0.100	9	0.100		
3	0.200	10	0.200		
4	0.300	11	0.300		
5	0.400	12	0.400		
6	0.500	13	0.500		
7	0.600	14	0.600		

Table 6.6 Pressure tapping coordinates for on-board pressure measurement

In order to measure the surface pressure accurately and minimise any flow effect from the tubing, the tubing exit was placed sufficiently far from the pressure tapping position (see Figure 6.13). Moreover, the pressure tappings were placed at the mid-span of the blade so as to provide representative results with little or no tip loss effect although the laminated construction method provides the option to place the instrumented section at different spanwise locations.

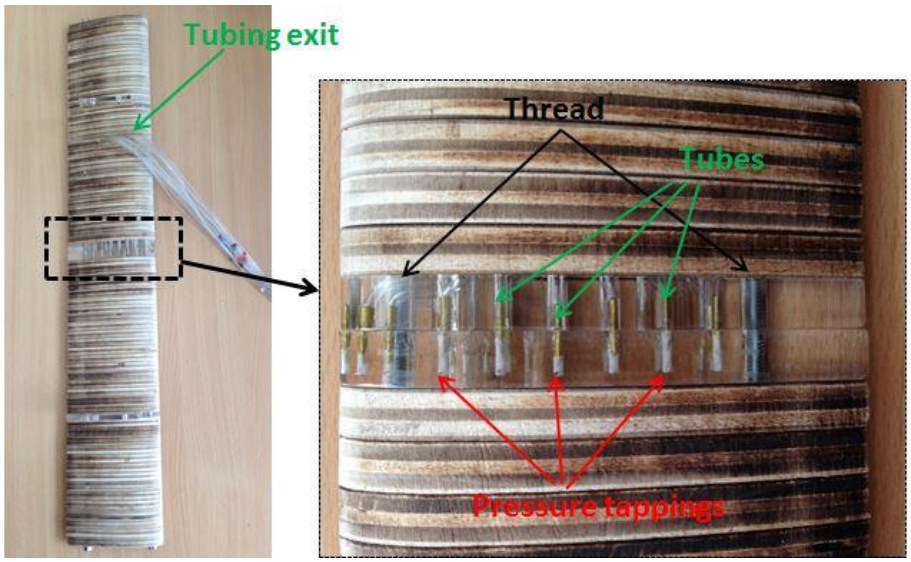

Figure 6.13 Photograph of the NACA0021 blade with the pressure tapping section made from perspex

B. The pressure scanner

A 16-channel miniature electronic pressure scanner ESP-16HD was employed in this study to convert pressure into an analog electrical signal (see Figure 6.14). The ESP electronic pressure scanners are differential pressure measurement units consisting of an array of silicon piezo-resistive pressure sensors, one for each pressure channel. The outputs from the sensors are electronically multiplexed through a single on-board instrumentation amplifier at rates up to 20,000 Hz.

Figure 6.14 The 16-channel miniature pressure scanner ESP-16HD.

This pressure scanner was selected to accommodate the size constraints of the rig and to allow all 15 pressure tappings on the blade to be measured in a single test, which significantly reduced the amount of time required and eliminated experimental error resulting from manually changing the tapping connections.

Each channel was calibrated using a micro-manometer and the calibration data for each channel of the scanner could be reduced into offset, sensitivity and non-linearity coefficients that were used to determine the measured pressures. In this study, the following fourth-order polynomial (Equation 6.12) resulting from a five-point calibration was used to calculate the pressure during data acquisition as suggested in the scanner's manual [161]. A linear function was found for each channel and the static error for the fourth-order correction was within $\pm 0.05\%$ of the full scale pressure range (± 2.5 kPa).

$$P_x = C_0 + C_1(V_x) + C_2(V_x)^2 + C_3(V_x)^3 + C_4(V_x)^4 \qquad \text{Equation 6.12}$$

where:

P_x is pressure to be measured

C_0 is offset (Pa)

C_1 is sensitivity (Pa/volt)

C_2 is non-linearity ($\mathrm{Pa/volt^2}$)

C_3 is non-linearity ($\mathrm{Pa/volt^3}$)

C_4 is non-linearity ($\mathrm{Pa/volt^4}$)

V_x is scanner voltage at P_x

The pressure channels on the scanner were connected to the corresponding pressure tappings on the blade using 500 mm long, 1 mm diameter flexible tubing. The reference pressure input for the scanner was provided by a tube with one end fastened on the centre shaft and located outside the wind tunnel jet. It was demonstrated that the reference pressure input did not vary significantly under different turbine rotational speeds. Moreover, the reference pressure input value for each test was also recorded by scanner channel No.16 for use in calibrating the other 15 channels during the data post-processing.

It is known that the use of tubing to connect the blade surface static pressure tappings to the pressure scanner can influence the system response. For pressure fluctuations close to the natural frequency of the system this can lead to signal amplification whereas at higher frequencies the signal may be attenuated. Studies [162, 163] have shown that for tubing configurations similar to those used in this study it is possible to determine and apply phase and amplitude corrections for measurement frequencies up to around 200 Hz. However, according to above studies for the low cycle frequency used in this study ($f \leq 9$ Hz) the attenuation errors were less than 1% and corrections were not applied.

C. The microcontroller datalogger, the optical sensor, the bluetooth and the battery

The microcontroller chosen in this study was an Olimexino-STM32 board, which was proposed and developed by Peter Baxendale from Durham University (technical details are provided in Appendix D). This is an Arduino-based system which can be powered by a single Li-Po battery and can save data to a MicroSD card as it can be seen in Figure 6.15. The MicroSD card is necessary due to the large amount of data to be recorded in a single run.

In this study, the microcontroller was controlled wirelessly by a laptop located outside the wind tunnel through bluetooth. Users are then able to modify the sample rate and scanner channel number during testing without stopping the turbine. The output data from the pressure scanner was recorded in conjunction with signals from an optical sensor to determine the rotor position and speed. Each time the blade with the pressure tappings passed the azimuth angle $\theta = 0^{\circ}$, a pulse would be generated (see example in Figure 6.12 (b)) from the optical sensor and transmitted to the microcontroller. This pulse would cause the microcontroller to stop and record a new set of data. Knowing the data starting position in the tunnel, this arrangement allowed all the pressure data collected at user pre-set sample rates to be mapped back to the blade position (azimuth angle) for each revolution when it was processed. The time delay between detecting the active pulse edge from the optical sensor and writing the new set of data to the MicroSD card was 5 microseconds and the azimuth angle shift resulting from this delay could also be considered during post-processing although the resulting azimuth angle shift for this study was very small ($\theta < 0.1^{\circ}$).

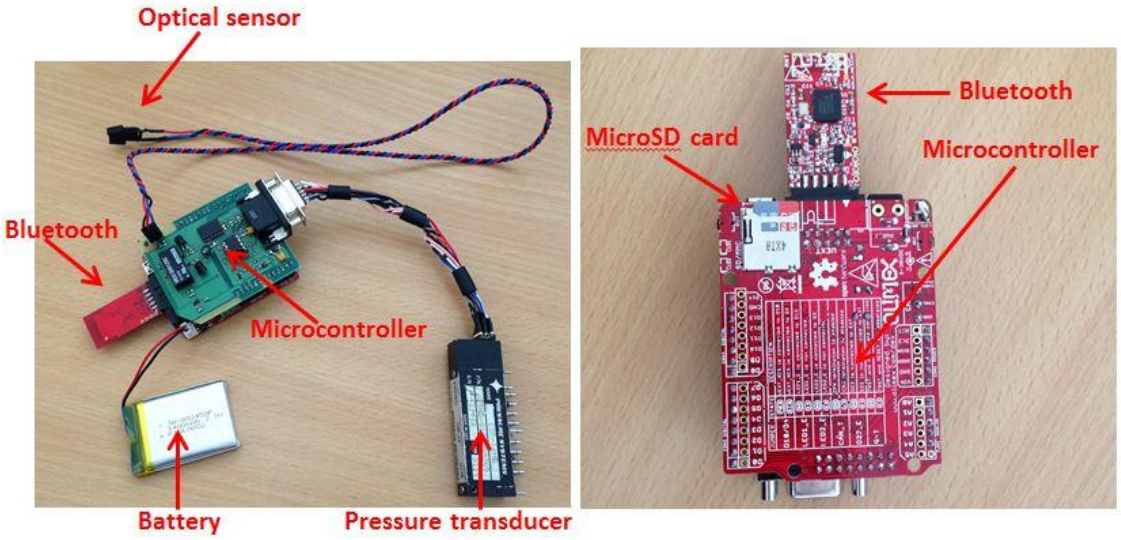

(a) (b)

Figure 6.15 (a) Front view of the microcontroller, bluetooth, battery, optical sensor and pressure scanner (b) Back view of the microcontroller, microSD card and bluetooth

The turbine was driven at constant tip speed ratios (λ) by a motor and a pre-set fixed sample rate at a particular λ enabled the microcontroller datalogger to record the pressure value (for a particular channel) at a constant time step. The time step was chosen to be $\theta = 0.25^{\circ}$ for all tip speed ratios, which indicates that for each turbine revolution there were $360^{\circ}/0.25^{\circ} = 1{,}440$ sample positions. Moreover in order to remove any noise from electronic components, pressure measurements were repeated for

100 revolutions with the help of the optical sensor and the averaged pressure value for each sample position was calculated. Some typical sample rates used in this study are shown in Table 6.7.

Fixed tip speed ratio	Upstream wind speed (m/s)	Fixed motor speed (Hz)	Time step (degree)	No. of sample points per revolution	Fixed sample frequency (Hz)
0.5	7	1.24	$\theta = 0.25^{\circ}$	1,440	1,782
0.8	7	1.98	$\theta = 0.25^{\circ}$	1,440	2,852
1	7	2.48	$\theta = 0.25^{\circ}$	1,440	3,565
1.5	7	3.71	$\theta = 0.25^{\circ}$	1,440	5,347
2	7	4.95	$\theta = 0.25^{\circ}$	1,440	7,130

Table 6.7 Typical parameters used in this study for on-board pressure measurement with turbine radius $R = 0.45$ m

A schematic diagram of the whole on-board pressure measurement system is provided in Figure 6.16 (a) along with a detailed flow chart to describe the microcontroller datalogger working process in Figure 6.16 (b).

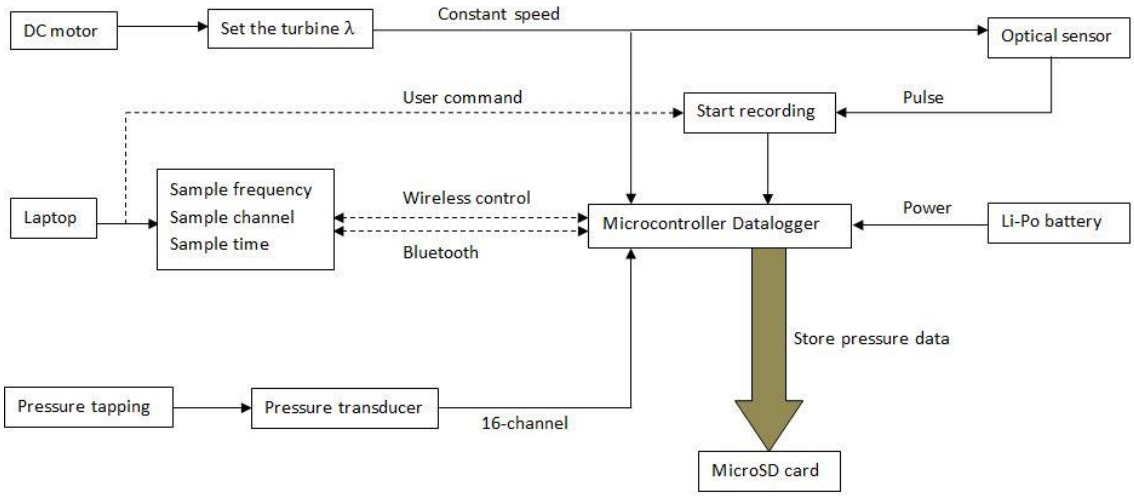

(a)

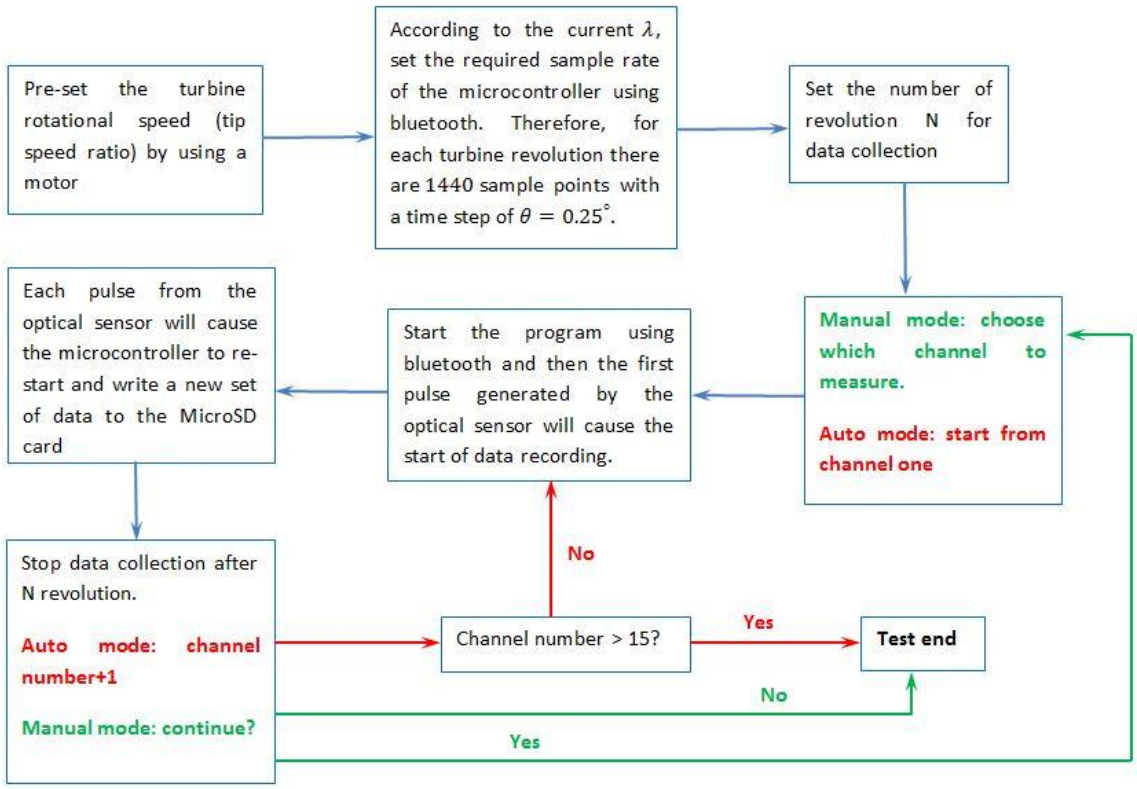

(b)

Figure 6.16 (a) On-board pressure measurement system schematic diagram and (b) Flow chart of the microcontroller datalogger working process

D. Mounting arrangement

The microcontroller datalogger (including battery) and pressure scanner were placed close to the turbine centre shaft in order to reduce their effect on the flow. Self-adhesive tape was used to hold the components of the measurement system on the support arms as can be seen in Figure 6.17. Pressure variation around the turbine blades was measured by the pressure scanner though 15 pressure tubes and recorded on the MicroSD card by the microcontroller datalogger. A laser pen was used to ensure the optical sensor generated the pulse signal when the instrumented blade (right hand side of Figure 6.17) passed the azimuth angle of $\theta = 0^{\circ}$. This alignment was accurate to $\theta = 0^{\circ} \pm 2^{\circ}$. Therefore the pressure distribution presented at a particular azimuth angle θ in Chapter 7 should be understood as $\theta \pm 2^{\circ}$. Nevertheless, this small uncertainty of azimuth angle will not affect the final conclusions according to the measured blade behaviour and the overall performance.

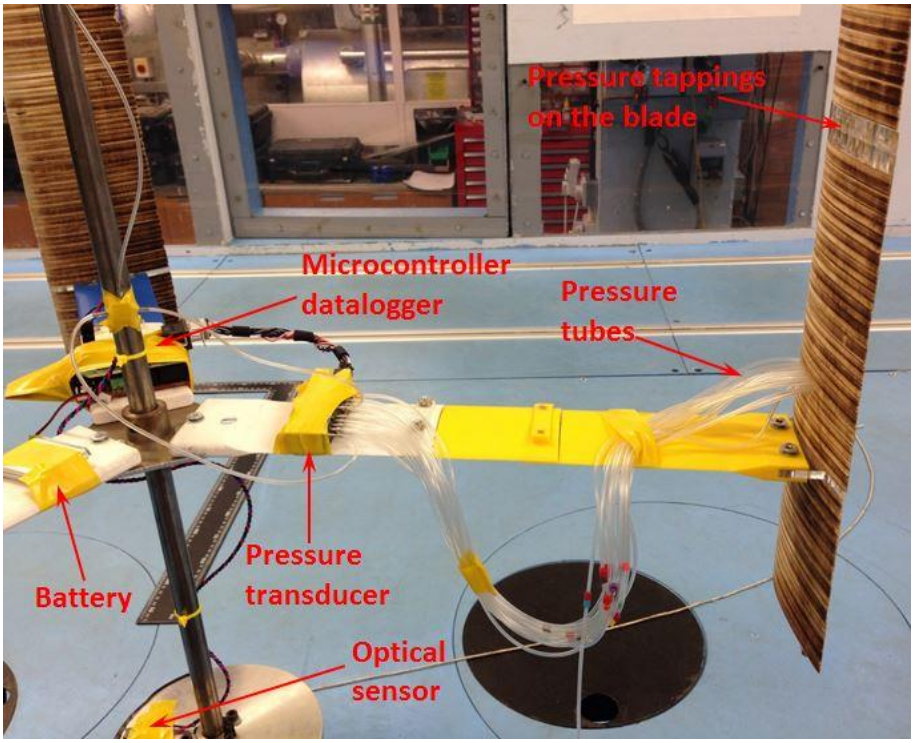

Figure 6.17 Arrangement of on-board pressure measurement components

6.3.7 Experimental data post-processing

A. Turbine self-starting time-varying results

The turbine self-starting behaviour was examined in this study by measuring and recording the turbine's time-varying rotational speed. Experimental measurements were performed in various geometrical configurations and upstream wind conditions. For each scenario, the measurements were conducted 3 times and showed good repeatability and low standard deviation as demonstrated by the example shown in Figure 6.18. The frequency outputs were calculated from the optical sensor signal over an average of 2 revolutions. The beginning of each dataset was defined as when the turbine rotational speed became greater than 0.5 Hz.

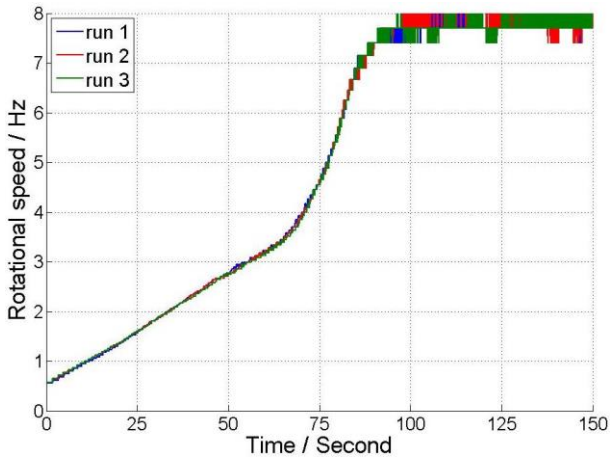

Figure 6.18 Example of experimental measurements of turbine self-starting time-varying results. $V = 6\ \mathrm{m/s}, R = 300\ \mathrm{mm}$

In theory, the more runs that were performed the more representative the mean data is (more confident about the mean data). However limited by the time and the large amount of different tests designed in this study, 3 runs were performed for each scenario and the standard error (also known as the standard deviation of the mean) was calculated at different measuring points, showing the confidence range of the mean value as illustrated in Figure 6.19. This format will be used in the rest of the thesis to present the turbine time-varying self-starting behaviour.

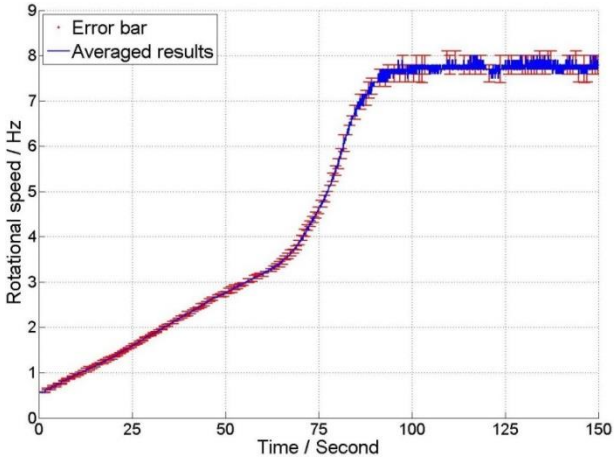

Figure 6.19 Averaged results with error bar (standard error)

B. Turbine resistance torque calculation

The system resistance torque T_{res} was measured by spin down tests without blades for each turbine radii ($R = 300\ \mathrm{mm}, R = 370\ \mathrm{mm}$ and $R = 450\ \mathrm{mm}$) at different upstream wind speeds. For each scenario, 6 runs were performed in order to calculate the

averaged $T_{res} - \omega$ curve based on Equation 6.9. Since I_{rig} is determined by the mass of the system components which is a constant, the relationship between T_{res} and ω was simplified into $\xi - \omega$. Examples of the raw data are illustrated in Figure 6.20 (a) and Figure 6.21 (a).

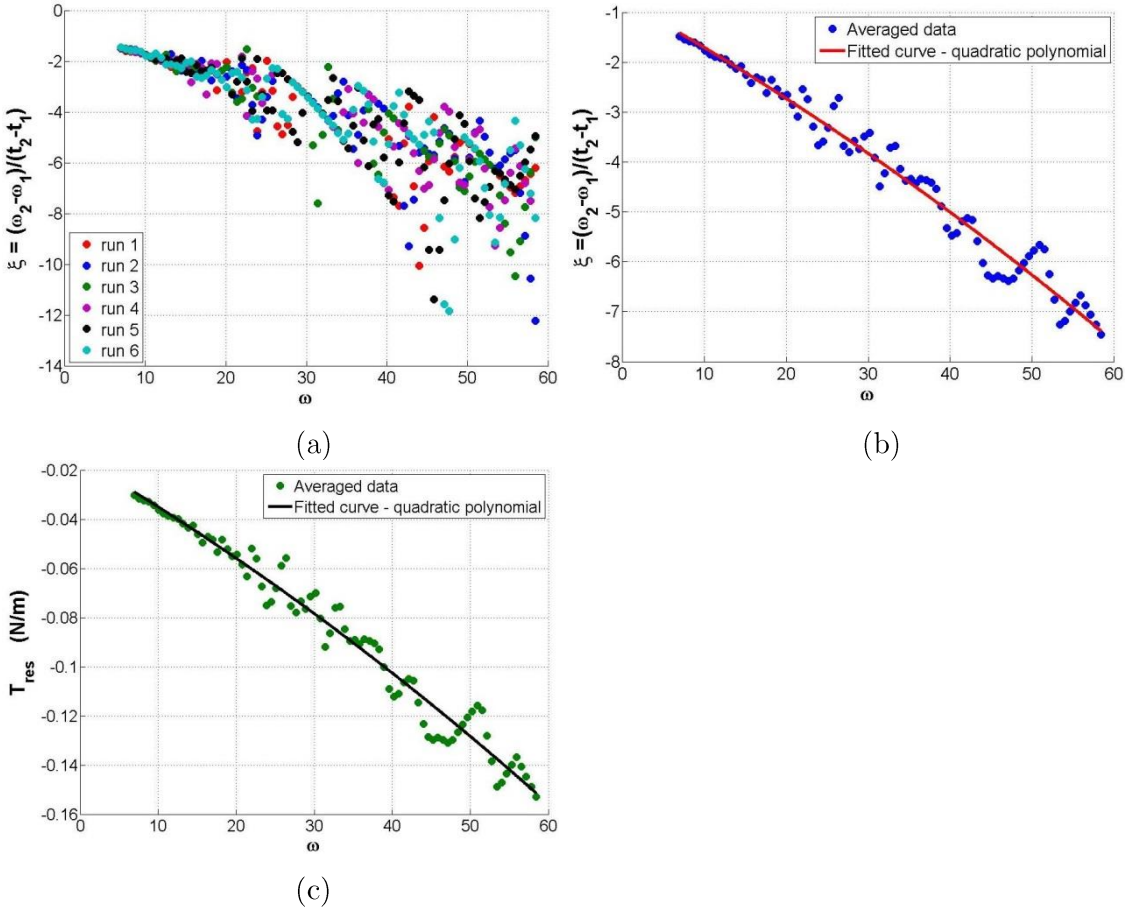

Figure 6.20 Example of measured turbine resistance. (a) $\xi - \omega$ curve, raw data. (b) $\xi - \omega$ curve, averaged data with quadratic polynomial fitted curve. (c) Final $T_{res} - \omega$ curve, averaged data with quadratic polynomial fitted curve. $V = 6\ \mathrm{m/s},\ R = 300\ \mathrm{mm}$.

Since T_{res} and ω have a second-order relationship, a quadratic polynomial fitting curve was produced based on the averaged value of the 6 runs as can be seen in Figure 6.20 (b) and Figure 6.21 (b). Finally, by considering the turbine inertia I_{rig} for each scenario, the corresponding $T_{res} - \omega$ curve can be produced as can be seen in Figure 6.20 (c) and Figure 6.21 (c). This $T_{res} - \omega$ fitted curve matches well with the averaged data throughout the rotational speed range and therefore it will be used as a 'look-up' table for calculating blade torque (T_B) which is detailed in the following section.

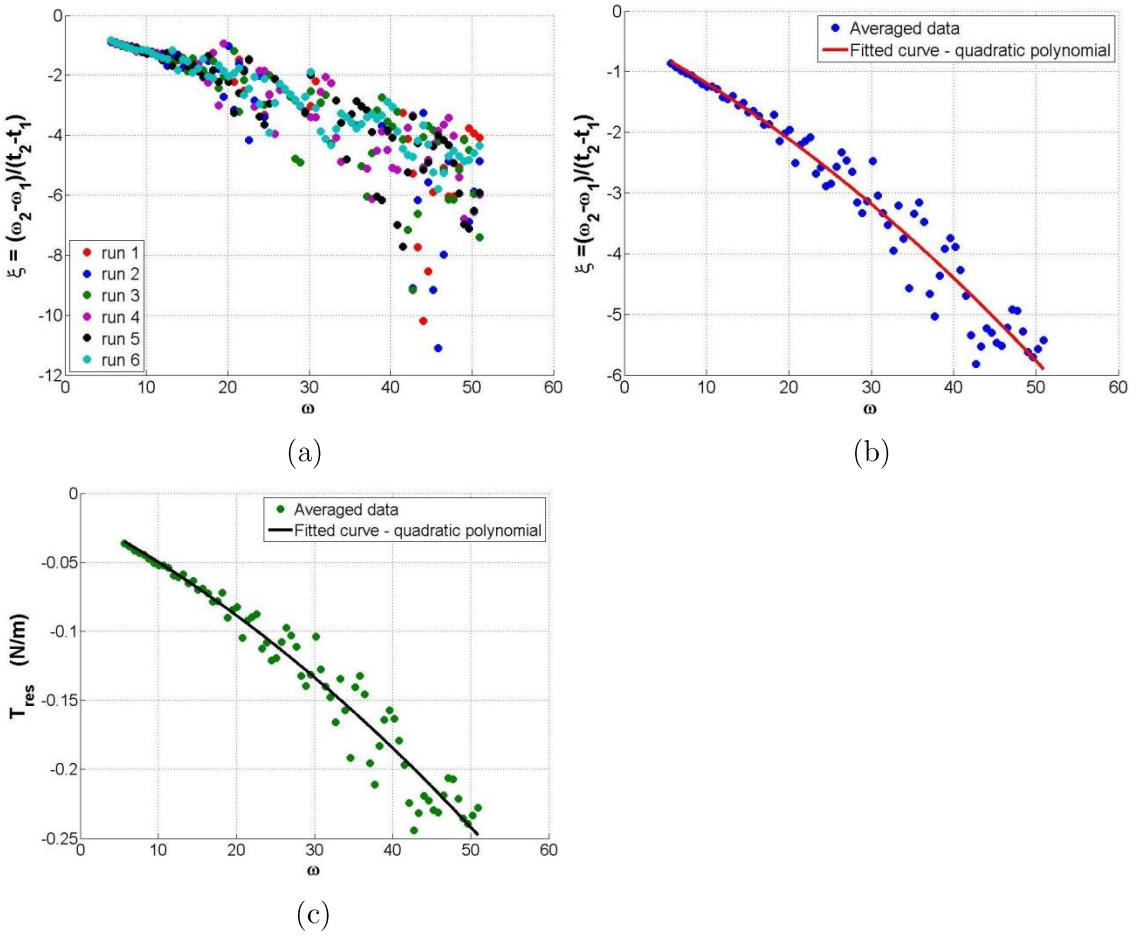

Figure 6.21 Example of measured turbine resistance. (a) $\xi - \omega$ curve, raw data. (b) $\xi - \omega$ curve, averaged data with quadratic polynomial fitted curve. (c) Final $T_{res} - \omega$ curve, averaged data with quadratic polynomial fitted curve. $V = 7\ \mathrm{m/s},\ R = 370\ \mathrm{mm}$.

C. Blade torque and power calculation

In order to compare the experimental results with those predicted by CFD, the instantaneous torque generated by the turbine blades (T_B) was calculated based on Equation 6.5 and Equation 6.6. The instantaneous turbine rotational speed was measured by the optical sensor and the mean value from 3 runs (example see Figure 6.19) was then used to calculate the instantaneous acceleration ξ. Knowing the instantaneous system resistance T_{res}, the relationship between blade torque and tip speed ratio ($T_B \sim \lambda$) can be easily established, where the tip speed ratio $\lambda = \frac{\omega R}{V} = \frac{2\pi f R}{V}$.

Examples are shown in Figure 6.22. The measured experimental results are presented with the standard error (standard deviation of the mean) showing the confidence range of the mean results from the 3 runs. Meanwhile, a fitted curve (smoothed spline) is added in order to show the overall trend of the experimental results against turbine tip speed ratio. Since under this testing condition the turbine

was purely driven by the wind, the self-starting process was highly unsteady, leading to the scatter in the $T_B \sim \lambda$ data. The fitted curve shows very good agreement with the experimental measurements at low tip speed ratios although some discrepancies exist between the fitted curve and the experimental results in the turbine's maximum torque region. However, even here the fitted curve still falls within the standard error range (standard deviation of the mean) from the 3 runs for most of the measured points, providing reasonably good guidance. It should be noted that due to the limited number of runs, the calculated standard error might not represent the true value especial at turbine unstable region (high tip speed ratios). Therefore, these discrepancies between fit curve and the experimental data are simply due to the relatively small number of data sets from which the results were averaged.

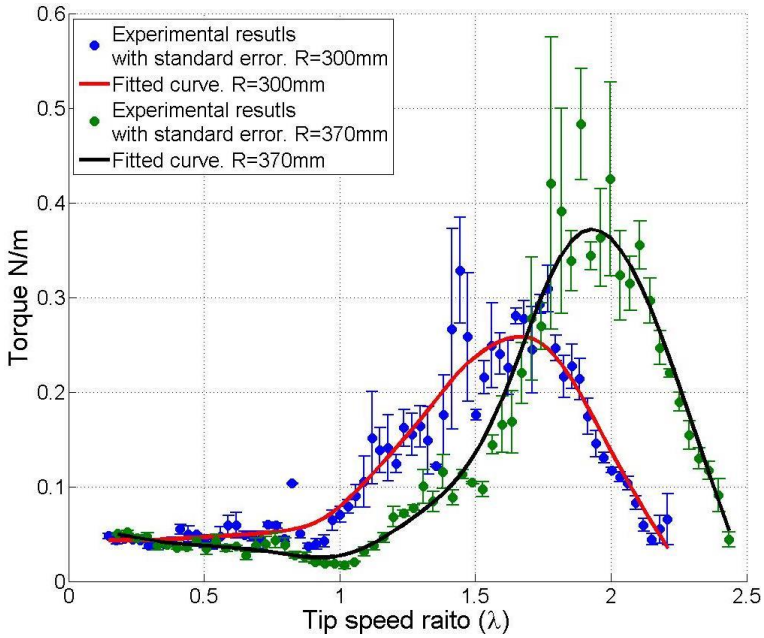

Figure 6.22 Examples of experimental measured torque with standard error and fitted curve. $V = 6\ \mathrm{m/s}$

Once the torque has been determined, the power coefficient can be calculated based on Equation 6.7 and Equation 6.8. Examples are illustrated in Figure 6.23 below.

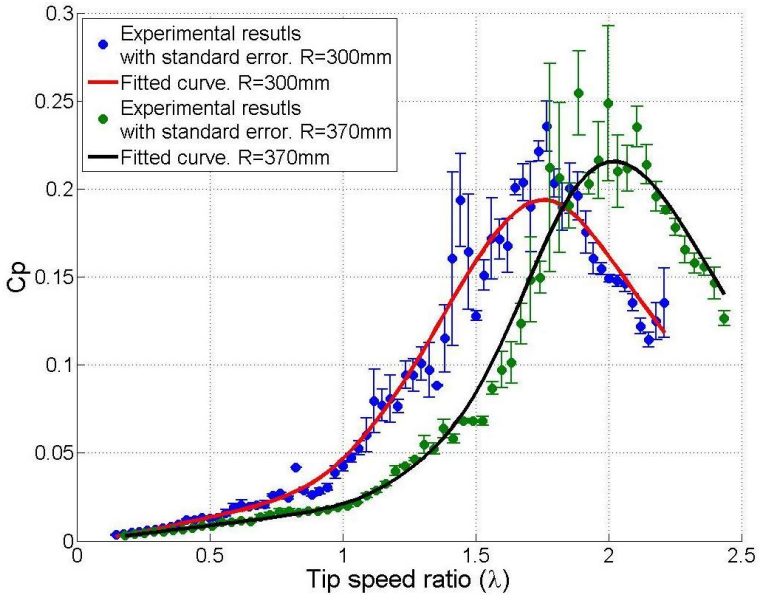

Figure 6.23 Examples of experimental measured power coefficient (C_p) with standard error and fitted curve. $V = 6\ \mathrm{m/s}$

In conclusion, the experimental measured turbine torque and power from this study are presented in the format of both discrete point with standard error and fitted curve for the rest of the thesis. The smoothing parameter, p, which was used to produce the smoothing spline was kept constant as $p = 0.995$ in this study in order to keep all the following results consistent (it is noted that $p = 0$ produces a least-squares straight-line fit to the data while $p = 1$ produces a cubic spline interpolant).

D. On-board pressure measurement data interpolation

The on-board pressure measurement was designed to be performed at constant turbine tip speed ratios. Under wind-driven conditions, the turbine's torque characteristics mean that tip speed ratios can only be achieved during transient start-up but cannot be maintained at a steady state. To achieve those steady conditions in the wind tunnel or achieve λ above peak power it is necessary to drive the turbine electronically. This was achieved by using a motor to drive the turbine at constant rotational speeds with the help of the torquemeter providing 'brake' resistance. The time interval between each measurement was pre-set to record $1{,}440$ points for one revolution (a constant step of $\theta = 0.25^{\circ}$). Nevertheless, in reality it was impossible to keep the motor speed/turbine speed absolutely constant. Instead, the motor speed would vary slightly (less than $\pm 1\%$ in RPM) around the designed value resulting in more or less than $1{,}440$ points measured in one revolution. Thanks to the synchronised signal from the optical sensor, the first point recorded by the datalogger would always occur at $\theta = 0^{\circ}$

and the remaining measured positions can then be calculated. For example if 1,436 points were measured for a particular revolution, it means the actual time step is $\theta = \frac{360^{\circ}}{1436} = 0.2507^{\circ}$ and the last point is measured at $\theta = 359.7493^{\circ}$. Knowing all the pressure values at the actual measured positions for each revolution, the values at the designated positions (time step of $\theta = 0.25^{\circ}$) could be interpolated for each revolution and the values were averaged for 100 revolutions. A diagram is provided in Figure 6.24 to show this process.

Revolution X		
Actual number of measured points	**Actual measured position /θ**	**value**
1432	0°	993
Actual step	0.2514°	999
$\theta = 0.2514^{\circ}$	0.5028°	998
	0.7542°	997
	⋮	⋮
	358.9992°	999
	359.2506°	998
	359.502°	998
	359.7534°	997

Revolution X	
Designed position /θ	**Interpolated value**
0°	993
0.25°	998.9333
0.5°	998.0167
0.75°	997.0222
⋮	⋮
359°	998.9833
359.25°	998
359.5°	997.9944
359.75°	997.0002

Figure 6.24 Example of on-board pressure measurement data interpolation process

E. Sensitivity study for on-board pressure measurement

In order to minimize the effect of any unwanted ambient electrical noise from or picked up by the electronic components, the pressure measurement for each pressure tapping (scanner channel) was repeated for N revolutions in order to calculate the mean pressure value at each azimuth angle. A sensitivity study was performed to examine the number of revolutions required to produce a reasonably good result with low standard deviation. Five random azimuth angles were picked as examples along with the overall averaged value. Results are illustrated in Table 6.8.

It can be seen in Table 6.8 that after approximately 100 turbine revolutions the standard deviation (SD) for all five azimuth angles examined become relatively stable, which indicates that further increasing the measured revolutions and sampling time will not significantly improve the data quality. Although the mean value seems to be very

stable after a few revolutions, the overall pressure distribution against azimuth angle shown in Figure 6.25 demonstrates that the curve becomes significantly smoother after averaging the pressure value at each azimuth angle for approximately 100 revolutions.

Therefore, in this study the on-board pressure measurement for each scanner channel/tapping was repeated for 100 revolutions. The largest uncertainty of the measured pressure was found to be less than ± 10 Pa and the corresponding uncertainty of the pressure coefficient (C_{pp}) was less than ± 0.5. However, it should be noted that this apparently high value is a consequence of pressures in this study being non-dimensionalized by the upstream wind speed rather than the much higher but cyclic resultant speed, therefore the blade surface C_{pp} at even low incidence angles was much larger than 0.5. This non-dimensionalisation by the free stream dynamic head is commonly used for studying dynamic problems in the literature (e.g. [138, 164]).

$\theta = 10^{\circ}$						
Revolutions	10	30	50	80	90	100
SD/ Pa	7.7594	7.2189	6.9685	**6.3982**	**6.3633**	**6.351**
$\theta = 30^{\circ}$						
Revolutions	10	30	50	80	90	100
SD/ Pa	9.1323	6.9464	**5.9902**	**6.0082**	**6.0055**	**5.9842**
$\theta = 100^{\circ}$						
Revolutions	10	30	50	80	90	100
SD/ Pa	9.3031	8.8585	7.4326	6.87	**6.6544**	**6.6577**
$\theta = 200^{\circ}$						
Revolutions	10	30	50	80	90	100
SD/ Pa	10.3832	9.8223	9.4839	**9.1418**	**9.1664**	**9.1057**
$\theta = 300^{\circ}$						
Revolutions	10	30	50	80	90	100
SD/ Pa	7.8865	7.6931	7.7	**7.4935**	**7.5163**	**7.507**
Mean						
Revolutions	10	30	50	80	90	100
SD/ Pa	**0.97**	**1.06**	**0.982**	**1.04**	**1.02**	**1.01**

Table 6.8 The calculated standard deviation (SD) of 5 random azimuth angles and mean value under different number of revolutions. Scanner channel 1/Tapping 1.

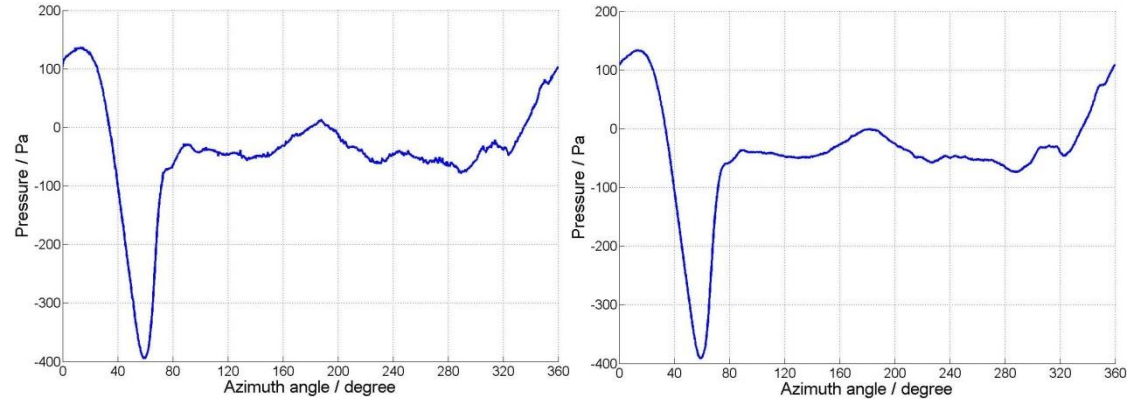

(a) (b)

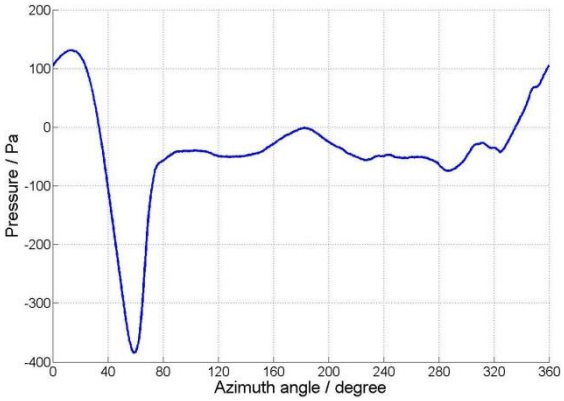

(c)

Figure 6.25 Measured pressure variation against azimuth angle for scanner channel 1. (a) Mean value over 10 revolutions. (b) Mean value over 50 revolutions. (c) Mean value over 100 revolutions.

6.3.8 H-Darrieus wind turbine test matrix

All experimental tests on the three-bladed H-Darrieus wind turbine performed in this study are summarised in Table 6.9 below. A total of approximately 300 wind tunnel tests were performed. The results are presented and discussed in Chapter 7 and Chapter 8.

	Blade type and chord length	Tip speed ratio	Turbine radius	Wind speed	Pitch degree	Blade span
H-Darrieus wind turbine self-starting behaviour	NACA0021; $c = 100mm$; NACA4415; $c = 100mm$; DU06 W200; $c = 100mm$; NACA0021; $c = 150mm$;	$\lambda = 0{\sim}3.5$	$R = 0.30m$; $R = 0.37m$; $R = 0.45m$;	$V = 6m/s$; $V = 7m/s$;	$\beta = 0^{\circ}$	$S = 600mm$; $S = 700mm$;
Torque calculation	NACA0021; $c = 100mm$; NACA4415; $c = 100mm$; DU06 W200; $c = 100mm$; NACA0021; $c = 150mm$;	$\lambda = 0{\sim}3.5$	$R = 0.30m$; $R = 0.37m$; $R = 0.45m$;	$V = 6m/s$; $V = 7m/s$;	$\beta = 0^{\circ}$	$S = 600mm$; $S = 700mm$;
Effect of blade surface roughness	NACA0021; $c = 100mm$; DU06 W200; $c = 100mm$;	$\lambda = 0{\sim}3.5$	$R = 0.30m$; $R = 0.37m$; $R = 0.45m$;	$V = 6m/s$; $V = 7m/s$;	$\beta = 0^{\circ}$	$S = 700mm$;
Effect of blade pitch angle	NACA0021; $c = 100mm$; NACA4415; $c = 100mm$; DU06 W200; $c = 100mm$;	$\lambda = 0{\sim}3.5$	$R = 0.30m$; $R = 0.37m$; $R = 0.45m$;	$V = 6m/s$; $V = 7m/s$;	$\beta = 0^{\circ}$; $\beta = 2^{\circ}$; $\beta = 4^{\circ}$;	$S = 600mm$; $S = 700mm$;
Same turbine solidity with different combinations of blade chord length and turbine radius	NACA0021; $c = 100mm$; NACA0021; $c = 150mm$;	$\lambda = 0{\sim}3.5$	$R = 0.30m$; $R = 0.45m$;	$V = 6m/s$; $V = 7m/s$;	$\beta = 0^{\circ}$	$S = 700mm$;
Dynamic pressure measurement (On-board pressure measurement)	NACA0021; $c = 100mm$;	$\lambda = 0.5$; $\lambda = 0.8$; $\lambda = 1.0$; $\lambda = 1.5$; $\lambda = 2.0$; $\lambda = 2.5$; $\lambda = 3.0$;	$R = 0.30m$; $R = 0.37m$; $R = 0.45m$;	$V = 7m/s$;	$\beta = 0^{\circ}$	$S = 700mm$;
Blade with tubercle leading edge	NACA0021 with tubercle leading edge. $c = 100mm$;	$\lambda = 0{\sim}3.5$	$R = 0.30m$; $R = 0.37m$; $R = 0.45m$;	$V = 6m/s$; $V = 7m/s$;	$\beta = 0^{\circ}$	$S = 600mm$;

Table 6.9 Summary of experimental tests on the three-bladed H-Darrieus wind turbine

Chapter 7

Experimental results

This chapter presents all the experimental results measured during this study. The aerofoil static wind tunnel measurements and the associated wake structure are presented in Section 7.1. Explanations of the aerofoil 'second-stall' behaviour at large angles of attack are provided. In Section 7.2, three-bladed H-Darrieus wind turbine performance including self-starting capability under different geometrical and wind conditions is illustrated. The experimentally measured turbine performance is also compared with the available CFD and BEM predictions performed in this study. Finally in Section 7.3, the results from on-board pressure measurement are presented and discussed.

7.1 Aerofoil study

7.1.1 Static aerodynamic force measurements

This study examines the performance of a NACA0018 aerofoil (a widely adopted aerofoil for VAWTs) over the whole range of angles of attack and at low Reynolds numbers relevant to VAWT applications. Only the static data is considered here. Tests were performed in three different wind tunnel test sections: a closed-jet with a relatively large chord-to-tunnel height ratio, ($^{c}/_{H}$), which is the measure of the maximum blockage (referred to as the 'closed-jet tunnel' in later figures); an open-jet with identical dimensions (referred to as the 'open-jet tunnel' in later figures); and a second open-jet section of the Durham $2\,\mathrm{m}^2$ tunnel having a very small $^{c}/_{H}$ ratio, which acted as a low-blockage reference tunnel (referred to as the 'reference tunnel' in later figures).

Figure 7.1 shows the variation of lift coefficient with incidence measured in the closed-jet wind tunnel at the Reynolds number of $140{,}000$ over a limited range of incidence from 0° to 20° for which comparative data from other sources is readily available [83, 84] and this is used to validate the pressure derived loads obtained from this study. All of the data relate to uncorrected closed section tests at similar Reynolds numbers and the corresponding blockage ratios at zero incidence were 4% in the study by Gerakopilos et al. [83] and 3.6% in Timmer et al. [84]. Prior to stall, there are two distinct regions in the lift curve. At low angles of incidence, from 0° to

approximately 6°, the lift coefficient grows almost linearly following the ideal lift slope [165]. Above 6°, the lift coefficient increases more slowly as the angle of incidence tends towards the stall angle. These two regions of the lift curve are closely related to the advancing rate of the laminar separation bubble at the aerofoil suction surface as shown in Figure 4.4 (CFD results).

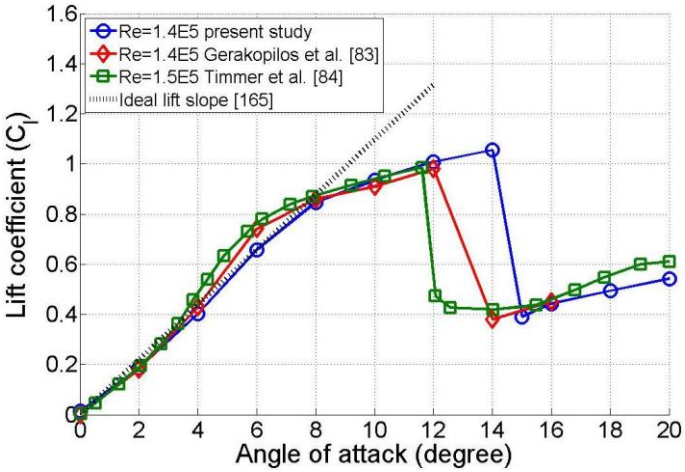

Figure 7.1 Lift coefficient comparison with previous investigations at similar Reynolds numbers

The peak lift coefficient value in this study is 1.05 at 14° while other researchers found a peak in the lift coefficient at approximately 12° with a value closer to 1.0. The larger stall angle and the slightly lower lift coefficient around 6° is thought to be due to higher turbulence intensity in the wind tunnel used for this study (1%) compared to Gerakopulos et al.'s [83] and Timmer et al.'s [84] studies, which were 0.3% and 0.02% respectively. This is consistent with Swalwell et al.'s experimental measurements [166] on a NACA0021 aerofoil, which showed that larger turbulence intensity will result in a delayed stall with slightly lower lift force around 6°. Moreover the aerofoils investigated in those studies were made from polished aluminium, which results in lower surface roughness than in this study where unpolished RP material was used. Fuglsang et al. [155] demonstrated that a rough surface also delays the stall angle of an aerofoil.

At the low Reynolds numbers considered here, all three sets of data show a similar behaviour at stall, where the loss of lift force occurs very suddenly with increasing angle of incidence. It may be noted that the results obtained by Gerakopulos et al. [83] seem to show a more gradual stall but it is believed that this is an artefact due to inadequate data point resolution near the stall angle. This behaviour differs significantly from what is observed at higher Reynolds numbers where the transition to stall is usually more

gradual. For example, Sheldahl and Klimas [62] demonstrated a more gradual stall behaviour from about 10° to 20° at $Re = 360{,}000$.

Lift coefficients at $Re = 140{,}000$ over the full incidence range are presented in Figure 7.2 (a), measured in all three Durham wind tunnel test sections with an enlarged view of the small incidence characteristics given in Figure 7.2 (b). Results from the reference tunnel lie between the smaller closed- and open-jet data. The stall angles in the closed tunnel, reference tunnel and open tunnel are approximately 15°, 16° and 18° respectively and the corresponding peak values of the lift coefficient are 1.05 (at 14°), 1.02 (at 15°) and 0.94 (at 17°) respectively. These results are consistent with the classic wind tunnel blockage correction theory, i.e. that a relatively larger/smaller lift will be measured in the closed/open tunnel when compared with the lift for the same model in the absence of any blockage or other boundary effects [167, 168]. In addition, due to the curvature of the flow resulting from the tunnel wall effect, the effective angle of attack in the closed and open tunnels is increased and reduced respectively compared with the reference results.

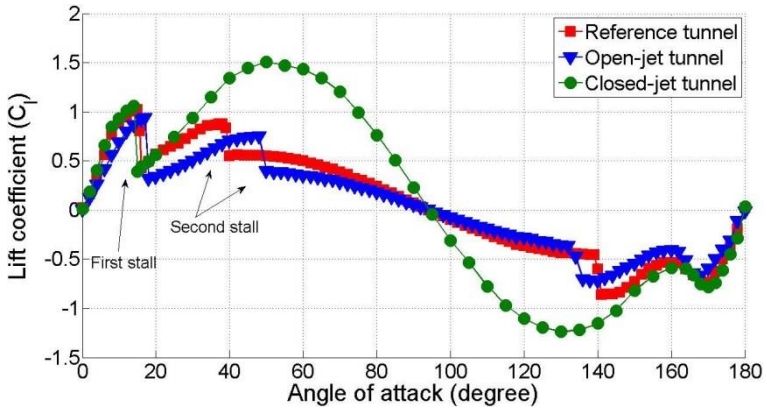

(a)

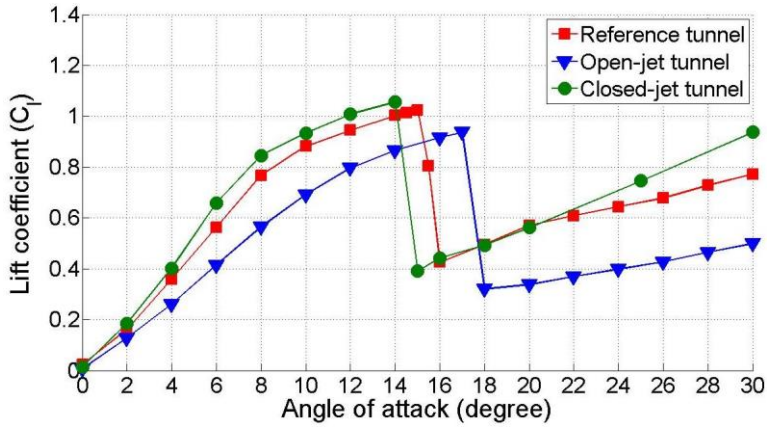

(b)

Figure 7.2 (a) Lift coefficient comparison among different wind tunnel configurations and (b) enlarged view. $Re = 140{,}000$

The most interesting phenomenon to observe from Figure 7.2 (a) is a "second-stall" captured in both the open-jet and reference wind tunnels but not in the closed-jet test section. In the reference tunnel, the lift coefficient gradually increases from its post-stall minimum of 0.42 at 16° to 0.83 at 39° before suddenly dropping to 0.55 at 40°. The characteristic is mirrored about 90° albeit with lower lift coefficient values when the apparent wind is from behind the aerofoil. Here the conventional but more gradual stall is observed at 168°, with a sudden second-stall at 140°.

Similar second-stall behaviour was observed in the open-jet tunnel but with a delayed second-stall angle at 50°. In contrast, the closed-jet tunnel results show a gradual increase in lift coefficient from 15° to 50° followed by a gradual decrease to zero lift at 90° (see Figure 7.2 (a)). No second-stall was observed.

Figure 7.3 presents the drag coefficient measured in the three different wind tunnel configurations. The drag coefficient shows a sudden decrease at the corresponding second-stall angle in open-jet and reference tunnels. The drag coefficient for the closed-jet section reaches an unusually high value of 3.42 as a consequence of its high blockage ratio at 90° incidence.

These results confirm the existence of the second-stall phenomenon that has previously been measured by Worasinchai et al. [31, 70] and Swalwell et al. [166].

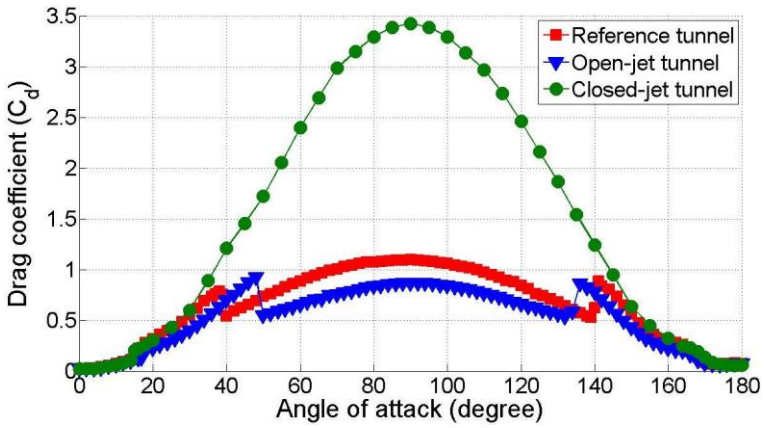

Figure 7.3 Drag coefficient comparison among different wind tunnel configurations

Since no significant differences in flow behaviour were observed at different Reynolds numbers in this study, the results presented and discussed here (including the following sections) focus on just one test condition ($Re = 140{,}000$) although dataset obtained at other Reynolds numbers of $Re = 100{,}000$ and $Re = 60{,}000$ have been plotted in Figure 7.4 and Figure 7.5. The dataset is also provided in Appendix B.

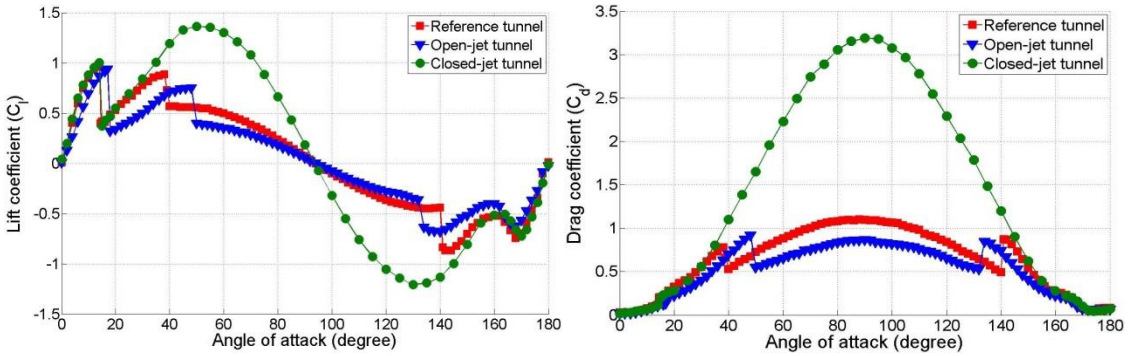

(a) (b)

Figure 7.4 Aerodynamic force comparison among different wind tunnel configurations at $Re = 100{,}000$. (a) Lift coefficient and (b) drag coefficient

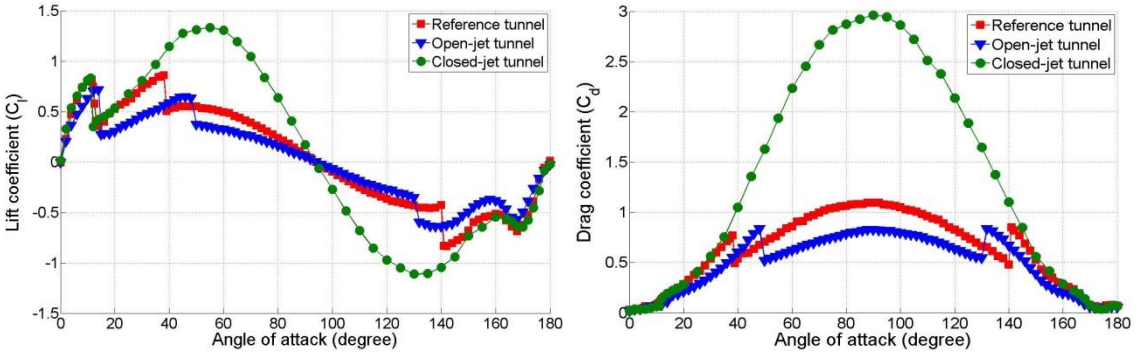

(a) (b)

Figure 7.5 Aerodynamic force comparison among different wind tunnel configurations at $Re = 60{,}000$. (a) Lift coefficient and (b) drag coefficient

7.1.2 Wind tunnel corrections

The vast majority of previous aerofoil studies have been conducted in closed wind tunnels (e.g. [61, 62, 165]) at low incidence and low blockage (e.g.[61, 80, 83, 165]) but even under those conditions extraneous forces due to boundary effects may occur as the flow about the model is constrained by the walls. The first investigations of these boundary interference effects date back to the 1920s [167] and since then numerous models have been developed to correct for the effect of blockage and other boundary effects on measured aerodynamic coefficients (e.g. [167, 168]). However, applications which require aerofoil data at large angles of attack stretch the capabilities of closed wind tunnel working sections and the validity of blockage correction becomes questionable, particularly during the transition from predominantly attached, pre-stall flow to wake dominated bluff-body flow. Open-jet wind tunnels partially alleviate the problems that are associated with increased wall blockage at high incidence in closed working sections but such configurations themselves affect the flow as the streamline

curvature at the boundary of an open-jet is greater than that for an infinite jet flow since there is no external flow to resist the deformation [169]. Corrections for open-jet measurements of the flow around aerofoils exist (e.g. [167, 168]), but there has been little attempt to validate them for extreme angles of attack.

In this study, attempts were made to correct the wind tunnel measurements from both open-jet and closed-jet sections by applying the classic wind tunnel corrections. Corrected results are compared with those measured from the Durham $2m^2$ low-blockage reference tunnel.

In a closed-jet wind tunnel, the correction of the aerodynamic forces includes the effects of solid blockage, wake blockage and separation blockage. The solid blockage is the blockage induced by the volume of the model itself. The corresponding correction factor, ε_s, is given by [167, 168]

$$\varepsilon_s = \frac{\pi}{6}\left\{1 + 1.2\gamma\left({}^{t_c}/_{c}\right)\right\}\frac{A_c}{\gamma^3 H^2} \qquad \text{Equation 7.1}$$

Where ${}^{t_c}/_{c}$ is the thickness-to-chord ratio, A_c is the cross-section area of the aerofoil, H is wind tunnel height and $\gamma = \sqrt{1 - M^2}$ is the Prandtl-Glauert factor accounting for compressibility effects with M the Mach number. At the low flow velocities considered here, M is small and therefore $\gamma \approx 1$.

The wake blockage relates to the velocity increment induced by the presence of the wake in the tunnel section. The correction factor for the wake blockage is [167]

$$\varepsilon_w = 0.25({}^{c}/_{H})\frac{1 + 0.4M^2}{\gamma^2}C_{du} \qquad \text{Equation 7.2}$$

Where $\mathrm{C_{du}}$ is the uncorrected drag coefficient.

For aerofoils at large angles of attack, the flow will separate from the aerofoil suction side and, therefore, an additional correction for the separated flow should also be considered. Maskell [170] performed a series of studies about flat plates (i.e. bluff bodies) in a closed-jet wind tunnel, which yielded the following correction factor for separation blockage:

$$\varepsilon_{sep} = 0.5\Omega({}^{c}/_{H})C_{du} \qquad \text{Equation 7.3}$$

where Ω is the separation blockage factor. It is suggested that the separation factor be 0.96 for two-dimensional flow [168], based on experimental results obtained by Maskell.

In addition to the effect of blockage on the measured data, interference between the lift created by the aerofoil and the tunnel solid boundaries needs to be accounted for. Assuming that the model is located at the centre of the test section, the corresponding residual corrections to lift and drag forces, as well as incidence angle are given by [167, 168]

$$\Delta C_l = C_{lu}\left\{-\frac{\pi^2}{48}\left(\frac{c}{\gamma H}\right)^2 + \frac{7\pi^4}{3072}\left(\frac{c}{\gamma H}\right)^4\right\} \quad \text{Equation 7.4}$$

$$\Delta C_d = -C_{du}(1 + 0.4M^2)\varepsilon_s \quad \text{Equation 7.5}$$

$$\Delta\alpha = C_{lu}\frac{\pi c^2}{96\gamma H^2}\left\{1 - 0.3897\gamma\left({}^{t_c}/_{c}\right)\right\} - C_{lu}\frac{\pi^3 c^4}{92160\gamma^3 H^4}\left\{41 + 67.33\gamma\left({}^{t_c}/_{c}\right)\right\} \quad \text{Equation 7.6}$$

where C_{lu} is the uncorrected lift coefficient.

Finally, the corrected dynamic pressure (q_c), lift coefficient(C_{lc}), drag coefficient (C_{dc}) and incidence angle (α_c) are given by [167, 168]

$$q_c = q_u\{1 + \varepsilon_T(2.0 - M^2)\} \quad \text{Equation 7.7}$$

$$C_{lc} = (C_{lu} + \Delta C_l)\frac{q_u}{q_c} \quad \text{Equation 7.8}$$

$$C_{dc} = (C_{du} + \Delta C_d)\frac{q_u}{q_c} \quad \text{Equation 7.9}$$

$$\alpha_c = \alpha_u + \Delta\alpha \quad \text{Equation 7.10}$$

where q_u and α_u are the uncorrected dynamic pressure and incidence angle, respectively, and $\varepsilon_T = \varepsilon_s + \varepsilon_w + \varepsilon_{sep}$.

In an open-jet wind tunnel, the flow is free to expand and therefore the solid and wake blockages (including separation blockages) are usually negligible. However, the effect of streamline curvature on the measurements, due to the diverging nature of the jet, needs to be corrected for. The correction applied in the present study is based on Garner et al.'s approach [167]. The effect of downwash is neglected, as suggested by Fuglsang et al. [155]. The final corrections for the open-jet are [167, 168]

$$C_{lc} = C_{lu} + C_{lu}\frac{\pi^2}{24}\left(\frac{c}{\gamma H}\right)^2 \quad \text{Equation 7.11}$$

$$C_{dc} = C_{du} - \frac{1}{2\pi}\left(\frac{L_0}{L} - 1\right)C_{lu}^2 \quad \text{Equation 7.12}$$

$$\alpha_c = \alpha_u - \frac{1}{2\pi}\left(\frac{L_0}{L} - 1\right)C_{lu} \qquad \text{Equation 7.13}$$

where L_0/L is a function of the chord-to-tunnel height ratio (c/H) explained in [167].

Figure 7.6 shows the corrected lift coefficient at $Re = 140{,}000$ for all three tunnels although for the $2m^2$ low-blockage reference measurements the correction is negligible.

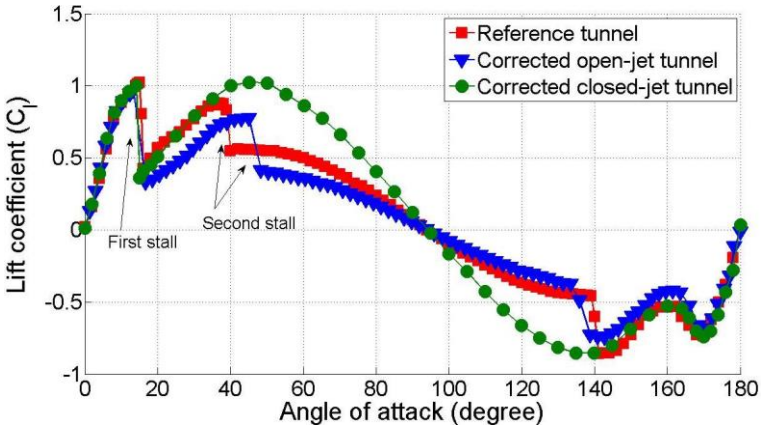

(a)

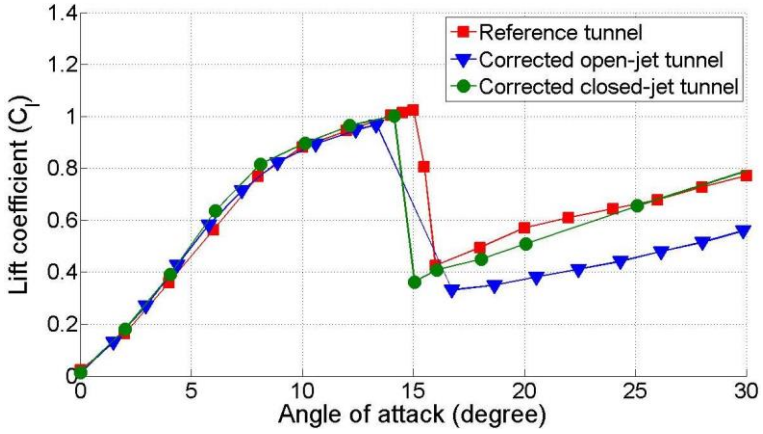

(b)

Figure 7.6 (a) Reference tunnel lift coefficient compared with corrected open-jet and closed-jet results and (b) enlarged view. $Re = 140{,}000$

Before the first-stall angle (about 14°) the corrected results for both open- and closed-jet wind tunnels closely match the reference data, save for some slight discrepancies near the stall angle. With increasing incidence the corrected data from the closed-jet tunnel matches the reference measurements until the second-stall at about 40°. Since no second-stall was observed in the closed-jet, the lift continues to increase to a peak at approximately 50°. Corrected data from the open-jet tests capture the second-stall but under-predict the lift force between the first- and second-stall angles. Although the blockage correction converges the first-stall data for all three test

sections that is not true of the second-stall where the phenomenon continues to be seen almost 8° later than the reference case, possibly as a consequence of there being no proper downwash correction. The effect of downwash is usually small at low angles of incidence for a nominal 2-D test [155], but it might become comparable to the effect of streamline curvature when the flow is separated at large incidence, the flow is highly unsteady and the jet dimension exceeds the aerofoil section dimension. Unfortunately, existing downwash and streamline curvature corrections cannot be applied simultaneously as they rely on conflicting assumptions [155].

Corrected drag coefficients are presented in Figure 7.7. Like the lift coefficient curves, the corrected closed-jet results match the reference until the second-stall occurs whereas the corrected open-jet data results in lower drag coefficients after the first-stall angle.

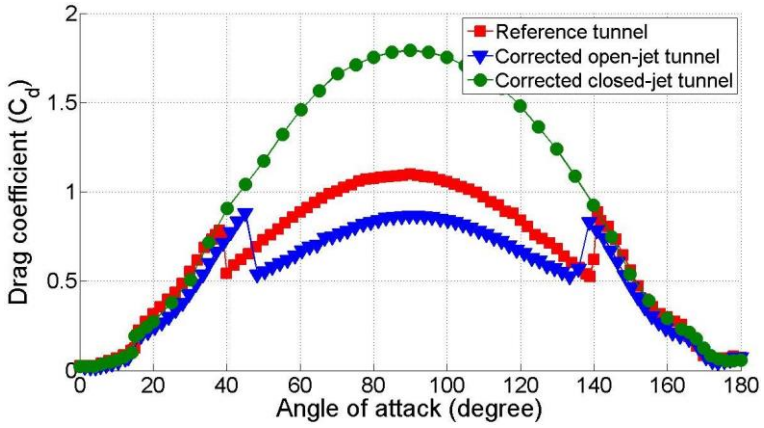

Figure 7.7 Reference tunnel drag coefficient compared with corrected open-jet and closed-jet results. $Re = 140{,}000$

The results for the other two Reynolds numbers of $Re = 100{,}000$ and $Re = 60{,}000$ show a very similar trend that the corrected closed-jet results match the reference until the second stall incidence angle while the corrected open-jet results under-predict the value. The corrected dataset is also provided in Appendix C.

7.1.3 Surface flow visualisation

Surface flow visualisation was used to further investigate the characteristics of the flow near both the first- and second-stall angles, in the closed- and open-jet test sections. Figure 7.8 (a), (b) and (c) present the results of suction side surface flow visualisation along with corresponding pressure distributions at three angles of incidence before first-stall (12°, 14° and 16°) and at the stall angle (18°). Results are only presented for the open-jet case but very similar flow features were observed from the closed-jet tunnel tests up to the first-stall. Before first-stall, a laminar separation bubble is clearly

indicated by both the surface flow and pressure data (pressure coefficient C_{pp}) with the separation and re-attachment lines highlighted by dashed red lines in the figures. Increasing the angle of incidence causes the separation bubble to move upstream and to reduce in length, which is qualitatively consistent with the study performed by previous researchers such as Gerakopulos et al. in a closed-jet wind tunnel [83]. The spanwise non-uniformities at both the top and bottom of the visualisation pictures are experimental artefacts created by the presence of tape at the edges of the visualisation region. Tape affects the flow direction only locally and the flow of interest along the centreline of the images remains undisturbed. When the aerofoil stalls at 18° (Figure 7.8(d)), the bubble bursts resulting in full leading-edge stall characterised by a sudden and significant reduction in the suction pressure peak (negative) and lift coefficient.

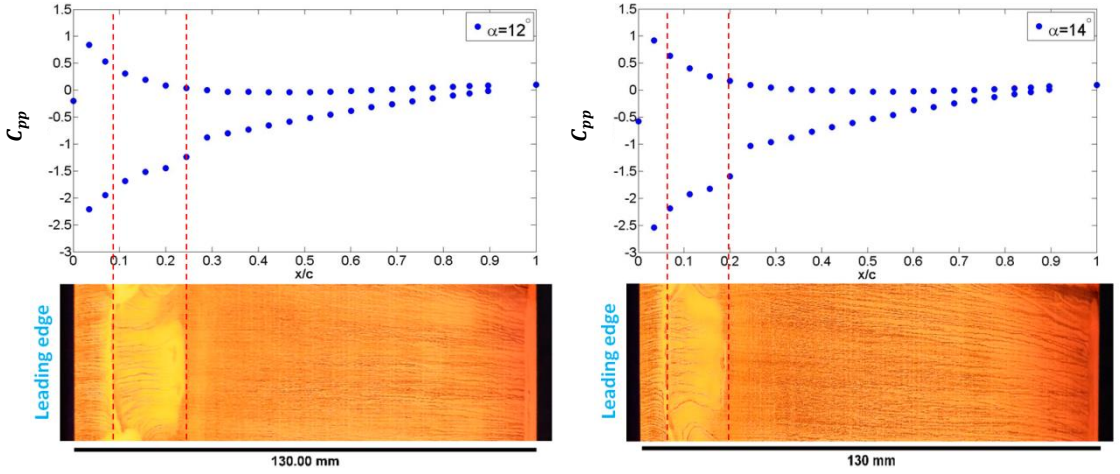

(a)

(b)

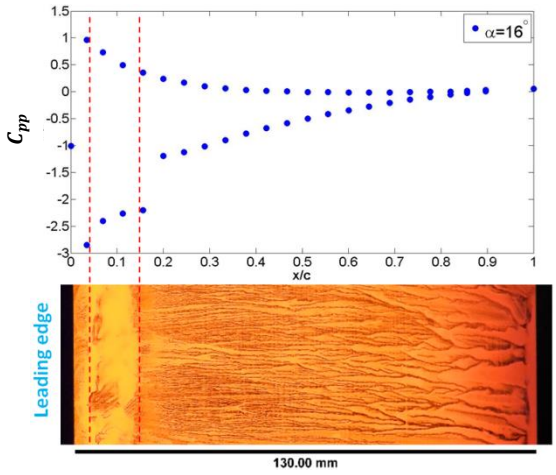

(c)

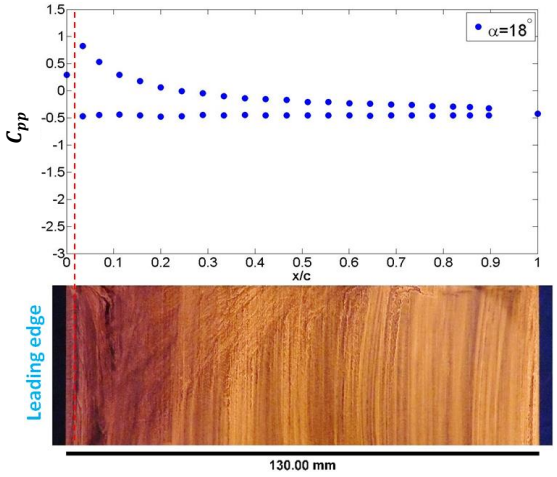

(d)

Figure 7.8 Open-jet surface flow visualisation at 12°(a), 14°(b), 16°(c) and 18°(d) compared with pressure measurement at $Re = 140{,}000$.

Figure 7.9 (a) illustrates the pressure distribution measured at incidence angles before and after the second-stall in the open-jet tunnel while Figure 7.9 (b) shows the pressure distribution in the closed-jet tunnel for a similar incidence range. Since the flow is fully separated from the aerofoil leading edge after first-stall, suction surface flow visualisation provides no useful information and is therefore not shown. It can be seen from Figure 7.9 (a), by examination of the pressure coefficients at incidence angles before and after the second-stall (48° and 50° respectively) that after the second-stall the suction surface pressure is significantly increased (less negative). This sudden pressure change is also captured in the reference tunnel tests around the corresponding second-stall angle and its magnitude suggests that a significant change of flow structure must have occurred in the wake of the fully stalled aerofoil. Further investigation drew focus to small changes in the leading edge separation point. Data from the closed-jet tunnel show no sudden change but a more progressive pressure increase with increasing incidence as can be seen in Figure 7.9 (b). It should also be noted that the suction surface pressures in closed-jet are much lower (more negative).

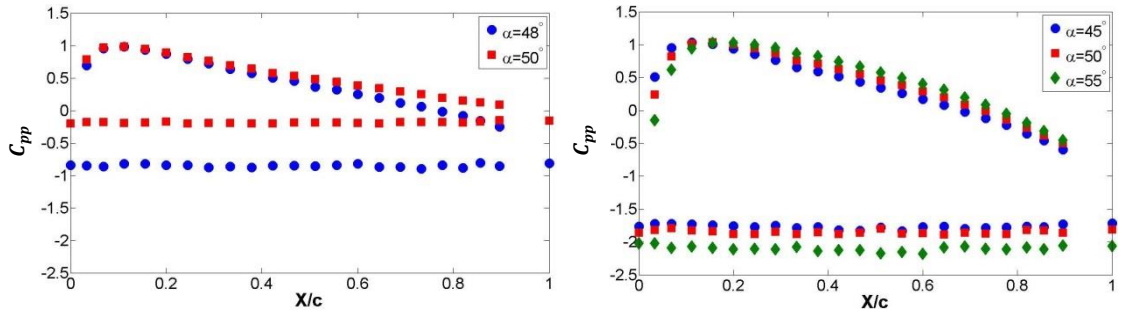

(a) (b)

Figure 7.9 (a) Aerofoil pressure distribution in the open-jet tunnel before and after the "second-stall" and (b) in the closed-jet tunnel for the similar incidence range. $Re = 140{,}000$.

To further investigate the second-stall phenomenon, close attention was paid to the location of the leading edge separation line and its impact on the wake structure. The open-jet results are considered first. The images in Figure 7.10 ~ Figure 7.13 were taken parallel to the chord line of the aerofoil and the leading-edge pressure tapping was used as a reference to ensure a consistent identification of the leading edge. Graph paper was wrapped around the leading edge to provide a measure of the location of the separation line relative to that datum. Figure 7.10 (a) shows that at an incidence of 40° the separation line lies approximately $1\ \mathrm{mm}$ downstream from the leading edge on the suction side ($^{s}/_{s_0} = 6.7 \times 10^{-3}$) where s is the total distance measured along the

suction surface and s_0 is the surface length of flow separation. As the angle of incidence increases, the separation point moves towards the leading edge as the stagnation point moves further onto the pressure side of the aerofoil and at 48° (Figure 7.11 (a)), which corresponds to the second peak observed in the lift curve of the open-jet test (Figure 7.2 (a)), the separation line almost coincides with the leading edge. Further increase of the angle of incidence causes the flow to separate on the pressure side of the leading edge (Figure 7.12 (a) and Figure 7.13 (a)). At 60° incidence, the separation line has moved $1.4\,\text{mm}$ from the geometric leading edge on the pressure side. The second-stall corresponds to the angle for which the flow starts to separate on the pressure side rather than on the suction side.

Investigation of the location of the separation line for the closed-jet tunnel yields almost identical results to those obtained for the open-jet (Figure 7.10 (b) ~ Figure 7.13 (b)). However, it is known that there is no second-stall in that test section so the likelihood of a second-stall occurring cannot be due to the location of the separation point alone.

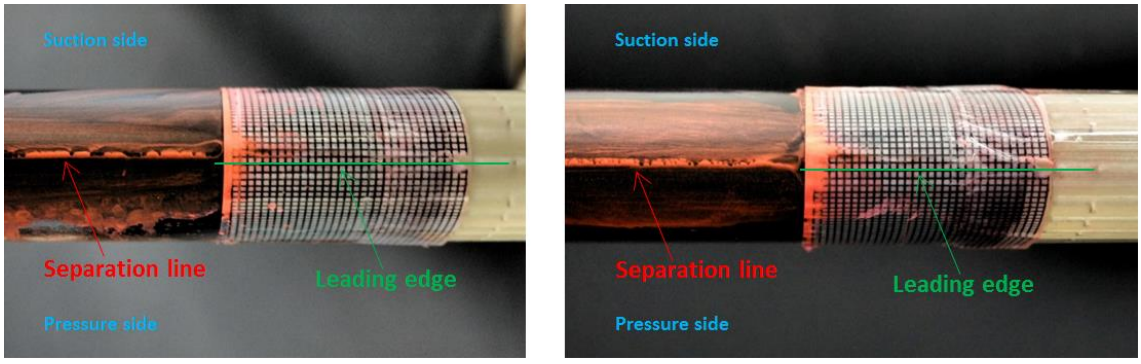

(a) (b)

Figure 7.10 (a) Visualisation of flow separation point at 40° in the open-jet and (b) in the closed-jet. $Re = 140{,}000$.

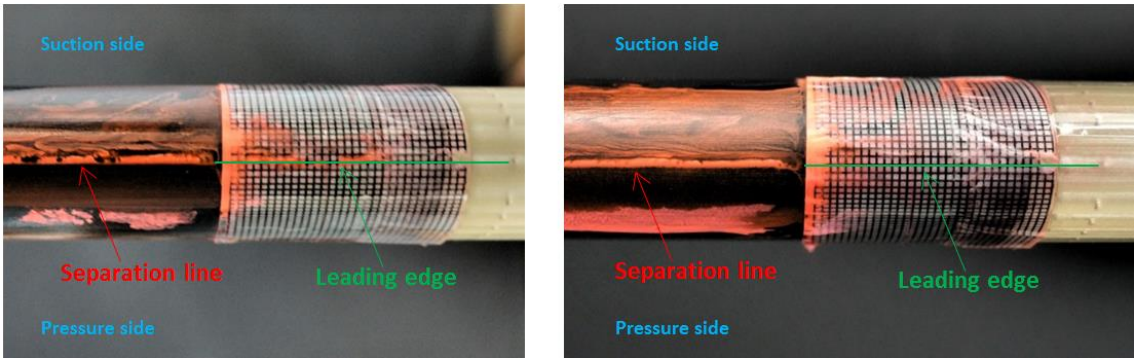

(a) (b)

Figure 7.11 (a) Visualisation of flow separation point at 48° in the open-jet and (b) in the closed-jet. $Re = 140{,}000$.

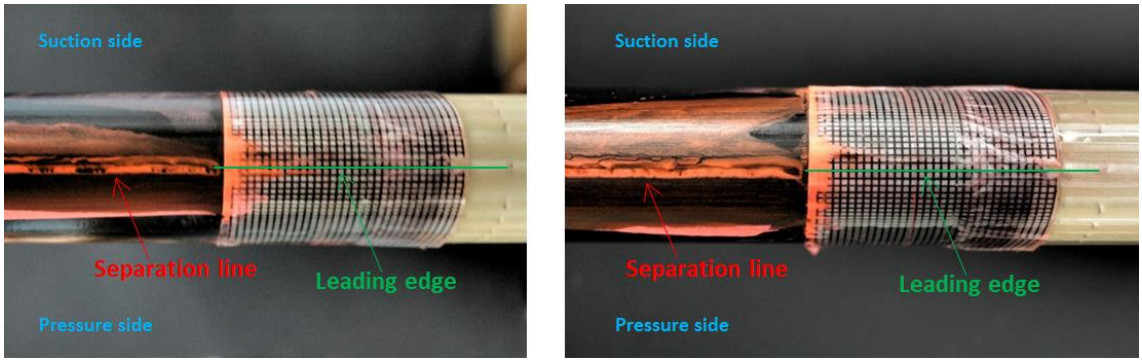

(a) (b)

Figure 7.12 (a) Visualisation of flow separation point at 52° in the open-jet and (b) in the closed-jet. $Re = 140{,}000$.

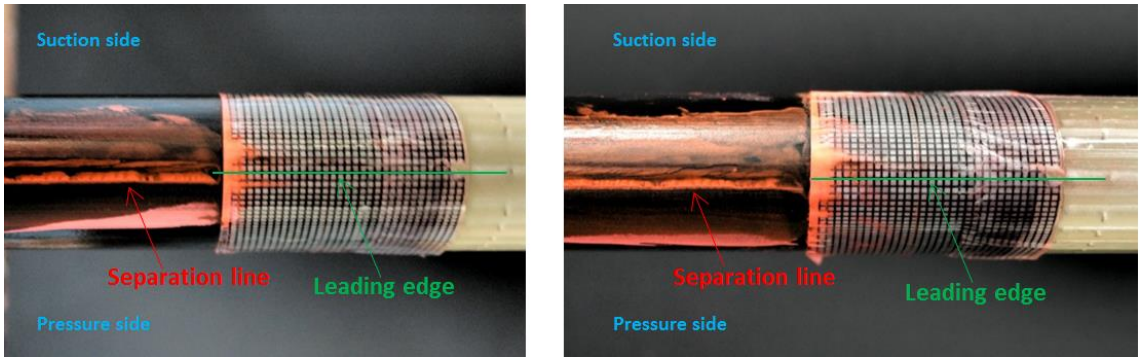

(a) (b)

Figure 7.13 (a) Visualisation of flow separation point at 60° in the open-jet and (b) in the closed-jet. $Re = 140{,}000$.

7.1.4 Characterisation of the wake

7.1.4.1 Open-jet

In order to explain the sudden increase in pressure along the suction side that is associated with the second-stall, it was necessary to characterise the wake of the aerofoil and data were acquired using a five-hole pressure probe at $Re = 140{,}000$.

Figure 7.14 (a) shows the measured flow angle in the open-jet test section for angles of incidence around the first-stall. Before the stall angle, i.e. at 12°, 14° and 16°, the flow is attached resulting in a downwash that decreases gently with increasing distance from the probe starting position to $Y/c \approx 1.3$. Above that point, the flow begins to interact with the upper free boundary which has itself been pulled downwards slightly by the turning caused by the aerofoil. Here the flow angle tends to zero as the flow is allowed to freely expand. As expected, when the aerofoil stalls the turning of the

downstream flow is reduced across the entire working section and the wake extends to $0.54c$. In the wake, the flow is highly unsteady and the probe experiences large, local flow angle fluctuations which may exceed the probe calibration limit ($\pm 45^{\circ}$) and are therefore not shown in the figure. Since the detail of the wake structure is an effect and not the cause of the second-stall phenomenon no additional attempt was made to investigate the flow using alternative techniques.

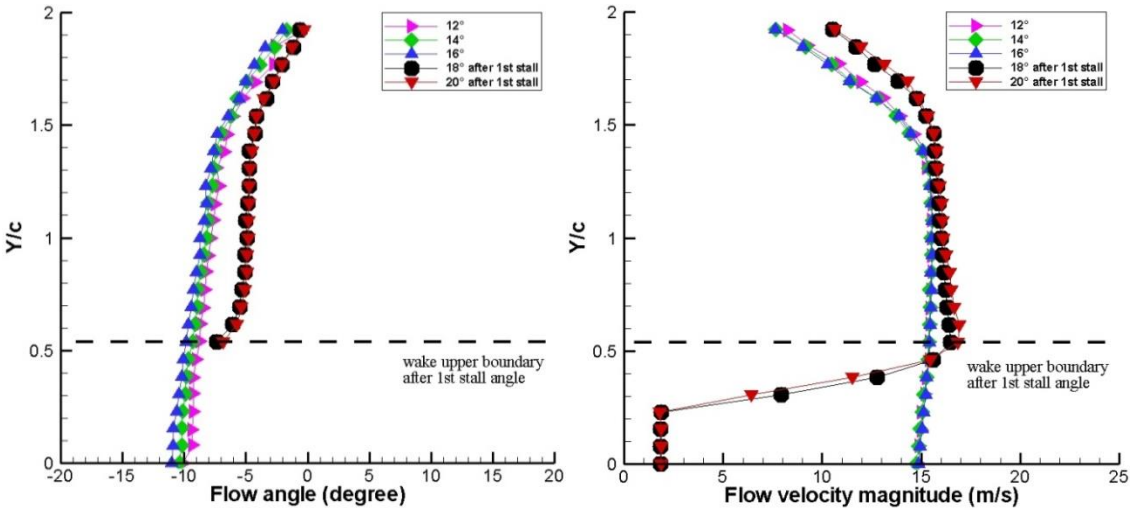

(a) (b)

Figure 7.14 (a) Open-jet downstream flow angle and (b) velocity around first-stall. $Re = 140{,}000$.

Figure 7.14 (b) displays the velocity profile downstream of the aerofoil for the same configuration. When the flow is attached, i.e. before stall, the wake is so thin that it is not resolved by the measurements. Mixing in the shear layer of the open-jet reduces the wind speed at the top of the test section but does not significantly influence the velocity profile in the region of the aerofoil itself. When the aerofoil stalls ($\alpha > 18^{\circ}$), the time-averaged, mean flow speed in the wake ($Y < 0.23c$) is approximately $1.8m/s$ (neglecting out of range data points). A velocity recovery occurs between $0.23c$ and $0.54c$. The reduced net downwash in the stalled case results in the upper jet shear layer being located higher in the working section.

Figure 7.15 shows the corresponding results for angles of incidence either side of the second-stall. In Figure 7.15 (a), the downstream flow-angle characteristics just before the second-stall (46° and 48°), are very similar to those observed after the first-stall (at 18° and 20°) with surprisingly little change of direction in the main flow and with a wake that is only very slightly thicker as a consequence of the doubling of the angle of attack. After the second-stall there is a remarkable change of flow angle with the

downwash switching to upwash of almost identical magnitude which is explained by the seemingly small change of separation point that was observed from the flow visualisation. When the incidence angle was lower than the second-stall angle it was noted that the flow remained attached over the first few millimetres of the suction side of the aerofoil (Figure 7.10 (a)). Because of the strong curvature at the leading edge the flow has already achieved a significant downwash velocity when it separates even after having travelled such a short distance from its stagnation point. For angles of incidence above the second-stall, it has been noted that movement of the stagnation point leads the flow to separate on the pressure side where its trajectory along the surface still has a strong upward component leading to a broadening wake (Figure 7.16).

The downstream velocity distribution presented in Figure 7.15 (b) further supports this hypothesis. At high pre-second-stall angles (46° and 48°) the velocity characteristics are similar to those observed after the first-stall, i.e. at 18° and 20°. After the second-stall angle, the wake boundary moves upwards by $0.3c$ and the upward component of the bulk flow pushes the jet shear layer upwards to the extent that there is no longer any evidence of it within the test section. The small change in the location of the separation line at the leading edge of the aerofoil and the associated change in the wake pattern cause a sudden rise in the pressure along the suction surface (i.e. a decrease in velocity) with a consequent sudden loss of lift as observed in Figure 7.2, at around 40° in the reference tunnel (Durham $2\ \mathrm{m}^2$ wind tunnel) and 50° in the open-jet tunnel (Durham $0.5\ \mathrm{m}^2$ Plint wind tunnel).

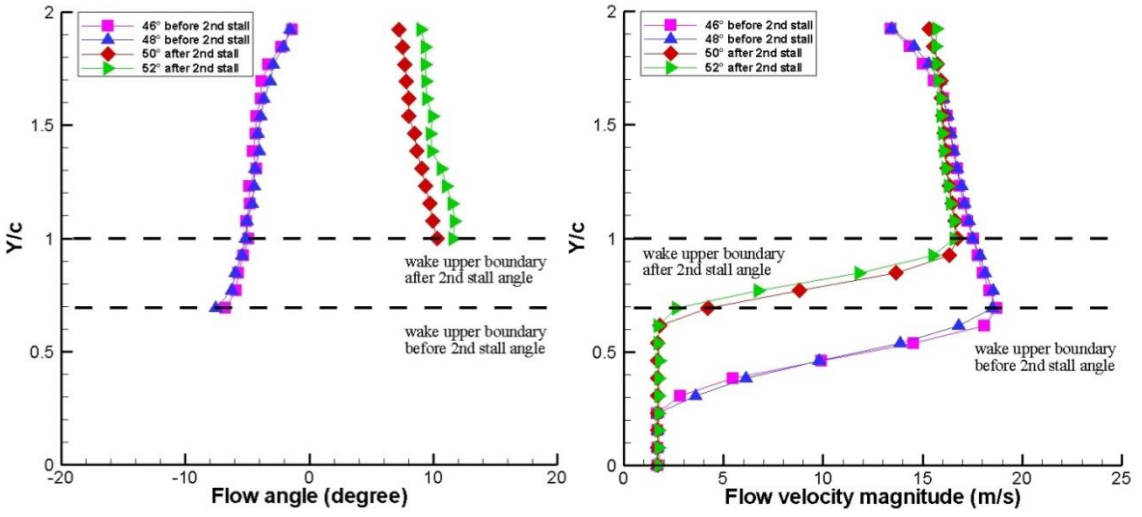

(a) (b)

Figure 7.15 (a) Open-jet downstream flow angle and (b) velocity around second-stall, $Re = 140{,}000$

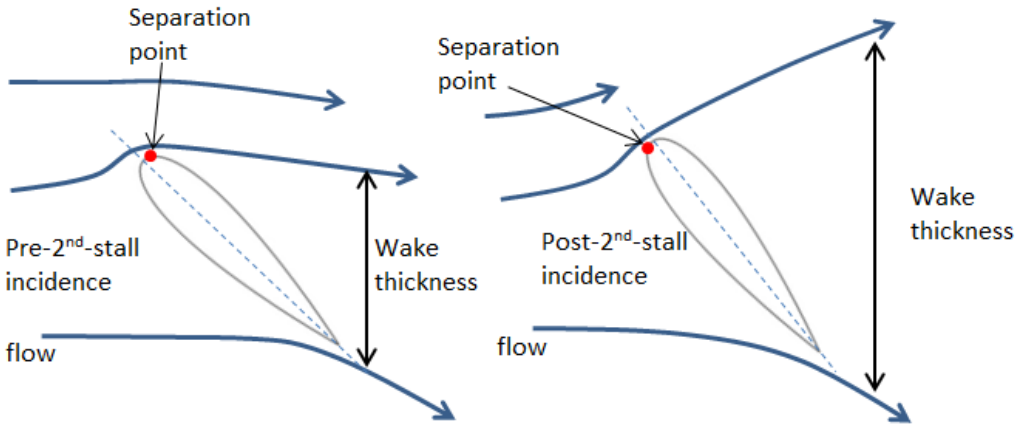

Figure 7.16 Schematic diagrams of flow structure for separation point movement from aerofoil suction side to pressure side in an open-jet wind tunnel

7.1.4.2 Closed-jet

Figure 7.17 (a) and (b) show the downstream flow angle and velocity profiles for an incidence range (48°, 50°, 52° and 60°) corresponding to the second-stall region that was observed in the open-jet study. The wake is similar regardless of the angle of incidence even though, from the flow visualisation, it has been noted that the separation line moves from the suction side to the pressure side over this range of incidence. Here the upper solid wall prevents any vertical flow component at that boundary which prevents the flow from switching to the second-stall flow regime (Figure 7.18). Note also that the measured downstream, bulk flow velocity is higher than that in the open-jet for the same incidence angle which is consistent with wind tunnel blockage correction concepts [167].

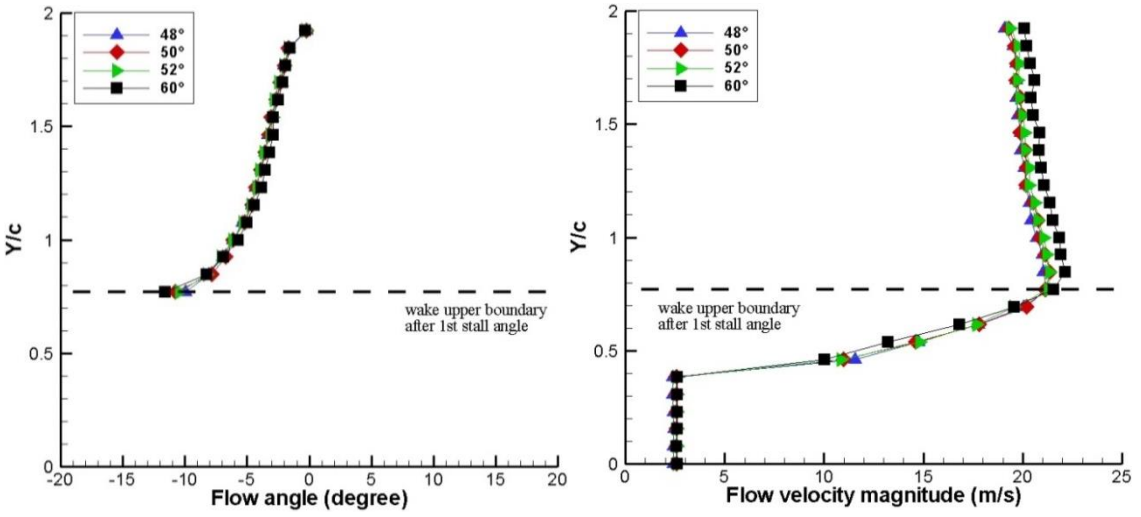

(a) (b)

Figure 7.17 (a) Closed-jet downstream flow angle and (b) velocity at incidence angle of 48°, 50°, 52° and 60°. $Re = 140{,}000$.

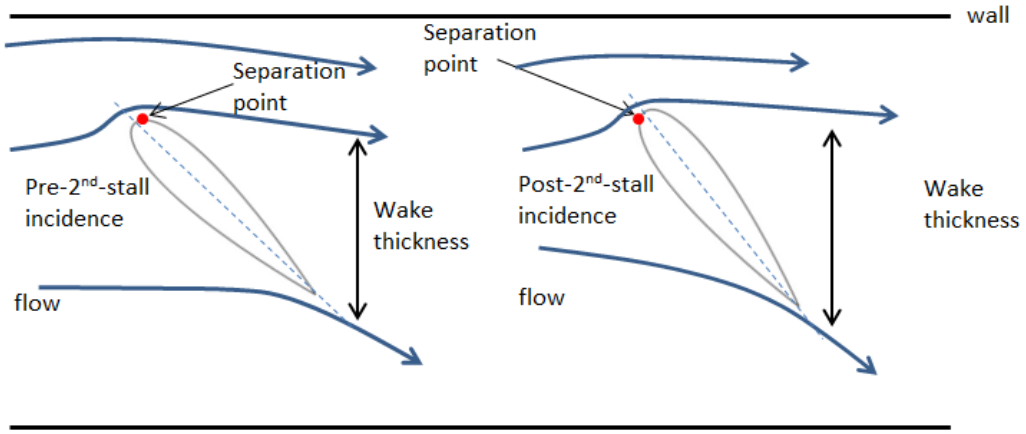

Figure 7.18 Schematic diagrams of flow structure for separation point movement from aerofoil suction side to pressure side in a closed-jet wind tunnel

7.1.5 Conclusion

The static aerodynamic characteristics of a NACA0018 aerofoil have been measured for the entire possible range of incidence, from 0° to 180°, in both open-jet and closed-jet wind tunnels at three Reynolds numbers: $Re = 60{,}000$, $Re = 100{,}000$ and $Re = 140{,}000$. Tests were also performed in an open-jet tunnel with a very low blockage ratio in order to provide a reference, eliminating significant blockage or other boundary effects. Results from both the reference and open-jet wind tunnel test sections demonstrated a "second-stall" phenomenon, at angles of incidence of 40° and 50° respectively, which is characterised by a sudden loss of both lift and drag forces. In contrast, the second-stall behaviour was not detected in the large blockage ratio closed-jet tunnel.

Classic wind tunnel corrections for the blockage and other boundary effects were applied to the open- and closed-jet data and compared with the reference case. Both corrected datasets closely match the results from the reference tunnel before the first-stall angle and the corrected closed-jet data remain in very good agreement up to an incidence of 39°, above which the aerofoil in the reference tunnel undergoes its second-stall. The blockage-corrected open-jet data captures the second-stall, although delayed, but always under-predicts the aerodynamic forces between the first- and second-stalls. Thus the limits of existing wind tunnel corrections for open-jet wind tunnels seem to be exceeded under deep-stall conditions, probably as a consequence of inadequate consideration of the effect of downwash on streamline curvature under the bluff-body conditions of deep-stall. A downwash correction was proposed by Mangler [171] but it

cannot be used jointly with the streamline curvature correction because of incompatible assumptions.

The second-stall was found to occur at the angle of attack where the separation point near the leading edge switches from the suction side to the pressure side of the aerofoil. Before the second-stall, the flow remains attached to the suction side of the aerofoil over a short but sufficient distance to induce downwash but when the separation line moves to the pressure side the separated flow has a significant upwash component. It is this small movement of the separation line about the leading edge which, because of the severe curvature at this location, results in the remarkable changes in wake size, flow direction and force generation.

In a large-blockage closed-jet tunnel even at angles above the nominal onset of second-stall, the wake behind the aerofoil is restricted by the solid boundaries of the tunnel and despite similar movement of the separation point there is no sudden change in the wake structure and therefore no corresponding loss of lift and drag forces.

Finally, the following recommendations are proposed:

1. The aerodynamic behaviour of aerofoils at high angles of attack for Reynolds numbers ranging between $\sim 60{,}000$ and $\sim 140{,}000$ should be examined in wind tunnels with a low blockage ratio (low chord to tunnel height ratio) or in open-jet tunnels as closed-jet tunnels with a large blockage ratio do not capture the "second-stall". Aerodynamic data measured in closed-jet tunnels with large blockage at this Reynolds range must be viewed with caution.
2. The limits of existing wind-tunnel corrections for open-jet tunnels are reached at high angles of incidence and better correction methods are necessary.
3. The impact of the "second-stall" on the start-up behaviour of VAWTs has yet to be determined. In addition, the next step in modelling VAWTs will be to assess how dynamic effects impact the aerodynamic performances of the aerofoil.

7.2 Three-bladed H-Darrieus wind turbine study

All experimental tests on the H-Darrieus wind turbine were performed in the Durham $2\ \mathrm{m}^2$ wind tunnel in this study. The turbine performance under various geometrical and wind conditions was examined. The parameters studied included: turbine solidity, blade profile, blade surface roughness, Reynolds number, blade pitch, blade aspect ratio and surface pressure measurements (Section 7.3). For each parameter, special attention is paid to turbine performance at low tip speed ratios and turbine self-starting capability.

7.2.1 Turbine performance under different solidities

In this study, the turbine solidity is modified by changing the turbine radius, R, while keeping the blade chord length, c, as a constant. The parameters are kept the same as those employed in the CFD study in order to make the comparison easier. Details are summarised in Table 7.1 below.

Solidity	R	c	S	V	Blade profile
$\sigma = 1.0$	300 mm	100 mm	700 mm	6 m/s and 7 m/s	NACA0021
$\sigma = 0.81$	370 mm	100 mm	700 mm	6 m/s and 7 m/s	NACA0021
$\sigma = 0.67$	450 mm	100 mm	700 mm	6 m/s and 7 m/s	NACA0021

Table 7.1 Parameters for studies of turbine under different solidities

Turbine self-starting behaviour is presented first in the time-varying format as can be seen in Figure 7.19. For scenarios of $\sigma = 1.0$ and $\sigma = 0.81$, the turbine successfully self-starts at both upstream wind speeds of $V = 6$ m/s and $V = 7$ m/s. For $= 6$ m/s , the turbine of $\sigma = 1.0$ reaches the maximum rotational speed of $\lambda \approx 2.3$ after approximately 100 seconds as shown in Figure 7.19 (a). In comparison, the turbine of $\sigma = 0.81$ peaks at $\lambda \approx 2.5$ after about 180 seconds under the same testing conditions. The results demonstrate that by increasing the solidity, turbine self-starting time can be reduced significantly at the expense of lower maximum rotational speed. Nevertheless, the turbine of $\sigma = 0.67$ failed to self-start during the testing period of 250 seconds as shown in Figure 7.19 (a). After the turbine accelerates to about $\lambda = 0.65$, the rotational speed becomes constant indicating that there is no net positive torque generated by the turbine at this λ.

For the test condition of $V = 7$ m/s as shown in Figure 7.19 (b), the turbine for each solidity can reach a higher peak tip speed ratio than the corresponding results at $V = 6$ m/s. The turbine self-starting time for $\sigma = 1.0$ and $\sigma = 0.81$ is reduced 20% and 33% respectively due to the increased Reynolds number.

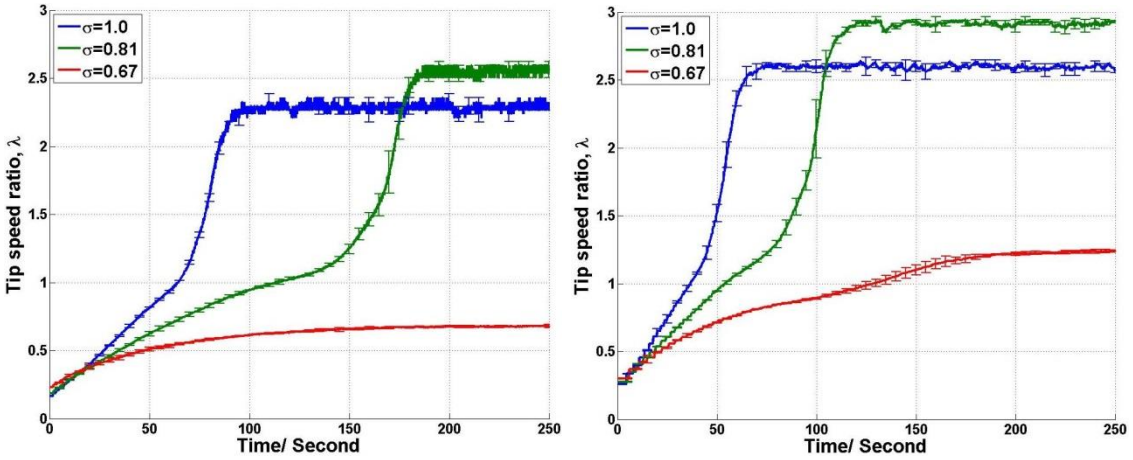

(a) (b)

Figure 7.19 Turbine self-starting behaviour under different solidities (showing standard error, also known as the standard deviation of the mean as detailed in Chapter 6). NACA0021. (a) $V = 6\ \mathrm{m/s}$. (b) $V = 7\ \mathrm{m/s}$.

Turbine performance under different solidities can be studied further by looking at the turbine torque (T) and blade power coefficient (C_p). The results for $V = 6\ \mathrm{m/s}$ are presented in Figure 7.20 (a) and (b) respectively.

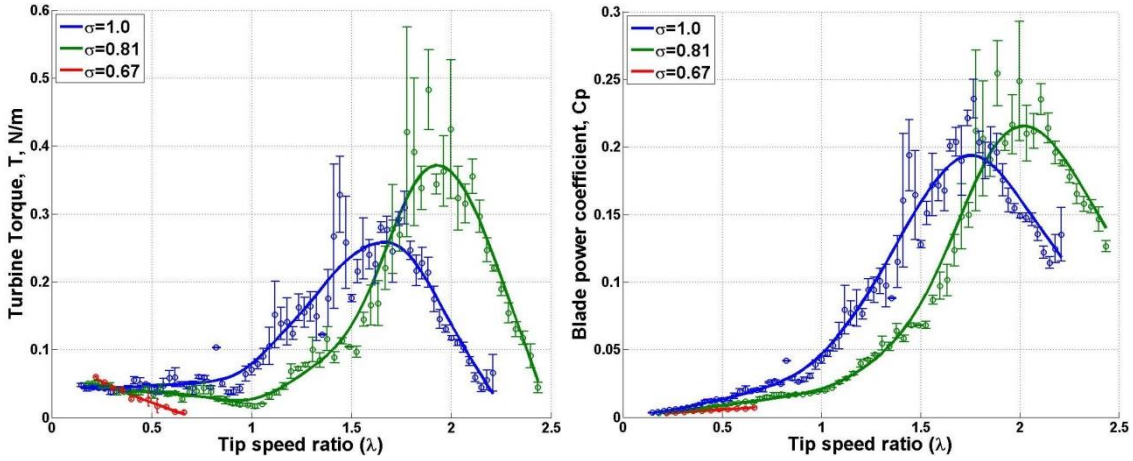

(a) (b)

Figure 7.20 (a) Turbine torque and (b) blade power coefficient under different solidities for $V = 6\ \mathrm{m/s}$.

The fitted curves clearly illustrate the relationship of $T \sim \lambda$ and $C_p \sim \lambda$. It is noticed that some large uncertainties exist at the turbine peak torque and power region, but the fitted curve falls within the standard error range (also known as the standard deviation of the mean) for most of the measured points, demonstrating clearly the overall trend. As can be seen in Figure 7.20 (a), the turbine of $\sigma = 1.0$ shows a

relatively constant positive torque produced at $0 < \lambda < 1$. The corresponding turbine self-starting behaviour shown in Figure 7.19 (a) indicates a linear acceleration in this λ range. However, when $\lambda > 1$ the net torque generated by the turbine increases significantly with the increase of λ and the turbine experiences an extremely fast acceleration as shown in Figure 7.19 (a). A maximum turbine torque of about $T = 0.26\ \mathrm{N/m}$ is measured around $\lambda = 1.8$ as shown in Figure 7.20 (a). Finally the turbine net torque value gradually decreases to 0 around a tip speed ratio of $\lambda \approx 2.3$, indicating the turbine reaches a new equilibrium state.

For a turbine of $\sigma = 0.81$, the net torque generated by the turbine is lower than that for the turbine of $\sigma = 1.0$ at low tip speed ratios. Moreover, the torque decreases with the increase of turbine rotational speed when $\lambda < 1$ as can be seen in Figure 7.20 (a). Although this torque behaviour results in the turbine of $\sigma = 0.81$ accelerating much more slowly than the turbine of $\sigma = 1.0$, a net positive torque is still measured at low tip speed ratios leading to the turbine finally self-starting. Further reducing turbine solidity to $\sigma = 0.67$, the turbine can no longer generate positive torque around $\lambda \approx 0.65$, resulting in the 'dead band' being created which prevents the turbine from self-starting.

With regard to the blade power coefficient (C_p) shown in Figure 7.20 (b), the experimental measurements indicate that the turbine of $\sigma = 1.0$ reaches a maximum blade $C_p \approx 0.19$ at $\lambda = 1.8$. In comparison, the peak blade power coefficient for the turbine of $\sigma = 0.81$ increases to about $C_p \approx 0.22$ but at a higher tip speed ratio of $\lambda = 2.0$. The experimental results support the CFD predictions that turbines of higher solidity achieve their maximum power output at a lower tip speed ratio but with a lower absolute value of peak power coefficient.

The experimental results are also compared directly with the CFD prediction for the same geometry as shown in Figure 7.21. For scenario of $\sigma = 1.0$ (Figure 7.21 (a)), the CFD under-predicts the power coefficient when $\lambda < 0.8$ but over-predicts the performance at high tip speed ratios. The $C_p \sim \lambda$ curves from CFD follow the same trend as that measured by the experiment and shows the turbine peaks around $\lambda = 1.9$ with a maximum $C_p = 0.36$. For $\sigma = 0.81$ (Figure 7.21 (b)), the CFD model over-predicts the turbine performance for the whole working range. The peak C_p is predicted around $\lambda = 2.1$ which is very close to that measured in the experiment at $\lambda = 2.0$. Considering the CFD model employed in this study is a two-dimensional model, 3-D effects such as blade tip loss and spoke drag are not considered. Therefore these large discrepancies, especially at high λ, between the CFD results and experimental measurements are understandable. The results measured in this study are consistent with the previous

investigation performed by Howell et al. [39]. According to their study, 2-D CFD significantly over-predicts the turbine power output at high λ compared to their experimental results and the turbine's maximum C_p measured from their experiment is only half of that predicted from their 2-D CFD. Nevertheless, the results from Howell et al.'s 3-D CFD model closely follow the experimental $C_p \sim \lambda$ curve, further demonstrating the significance of 3-D effects at high tip speed ratios [39].

Ignoring the 3-D effects also results in positive torque/power predicted by CFD for a turbine of $\sigma = 0.67$ at $\lambda > 0.6$ (see Figure 7.21 (c)), but experiments show the turbine cannot produce net positive torque beyond this tip speed ratio and the turbine fails to self-start.

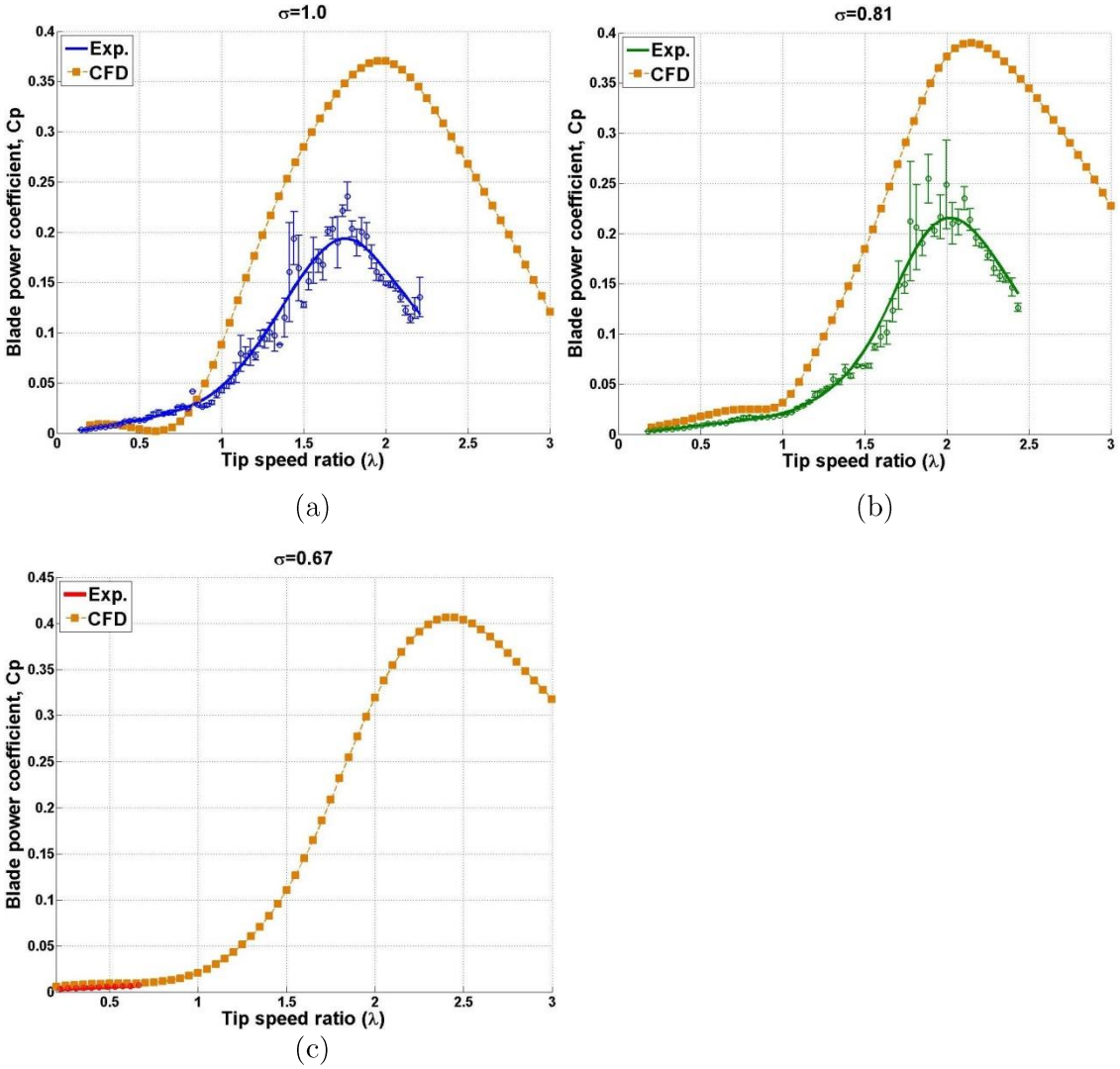

Figure 7.21 Experimental measurements compared with CFD prediction for $V = 6\ \mathrm{m/s}$. (a) $\sigma = 1.0$. (b) $\sigma = 0.81$. (c) $\sigma = 0.67$.

Measurements were also performed at upstream wind $V = 7$ m/s. Since the results show similar conclusions and no significant differences in turbine performance were observed, the data will not be discussed but data are presented in Figure 7.22 for completeness.

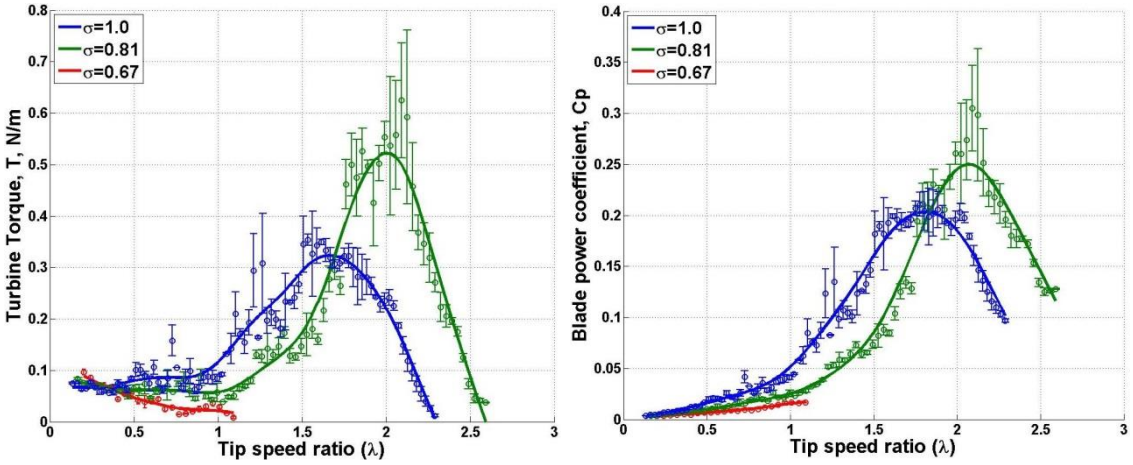

(a) (b)

Figure 7.22 Turbine torque (a) and blade power coefficient (b) under different solidities for $V = 7$ m/s.

In conclusion, Table 7.2 summarises the above experimental results

Solidity	Tested V (m/s)	Self-starting capability	Self-starting time (s)	Maximum C_p
$\sigma = 1.0$	6 // 7	Yes // Yes	100 // 80	0.19 // 0.2
$\sigma = 0.81$	6 // 7	Yes // Yes	180 // 120	0.22 // 0.25
$\sigma = 0.67$	6 // 7	No // No	N/A	N/A

Table 7.2 Summary table of turbine performance under different solidities for $V = 6$ m/s (blue) and $V = 7$ m/s (red)

7.2.2 Turbine performance under given solidity but with different combinations of turbine radius and blade chord length

Although the CFD model indicates that for a given solidity the turbine with the larger combination of turbine radius R and blade chord length c is able to generate more power over the whole working range, the increased system inertia and resistance cannot guarantee that this larger combination will improve turbine self-starting capability and reduce self-starting time. Therefore, a larger NACA0021 was manufactured and tested along with the original NACA0021 blades in order to examine how turbine performance,

including the critical self-starting behaviour, is affected by different combinations of R and c when the solidity is kept constant. The test parameters are summarised in Table 7.3.

Blade profile	R	c	σ	m	I_s	S	V
NACA0021 (Case I)	300 mm	100 mm	1.0	460 g	1	700 mm	6 m/s and 7 m/s
NACA0021 Large (Case II)	450 mm	150 mm	1.0	735 g	3.6	700 mm	6 m/s and 7 m/s

Note: Turbine inertia I_s is non-dimensionalised by inertia value of Case I

Table 7.3 Parameters for studies of the two turbines under same solidity with different R and c. m is the mass of the blade.

The turbine self-starting, time-varying results for $V = 6$ m/s are illustrated in Figure 7.23. Although the turbine inertia for Case II is more than 3 times than that for Case I, the turbine still demonstrates considerable improvement in turbine self-starting capability. The self-starting time is reduced from approximately 100 seconds to about 80 seconds (20% reduction). It was shown in the previous experimental study [11] that the turbine 'plateau stage', where turbine rotational speed increases very slowly, is mainly responsible for the long self-starting time required. Therefore the larger aerodynamic force generated by the blades (Case II) at these low tip speed ratios is able to help the turbine pass through the 'plateau stage' more quickly resulting in a much faster turbine self-starting.

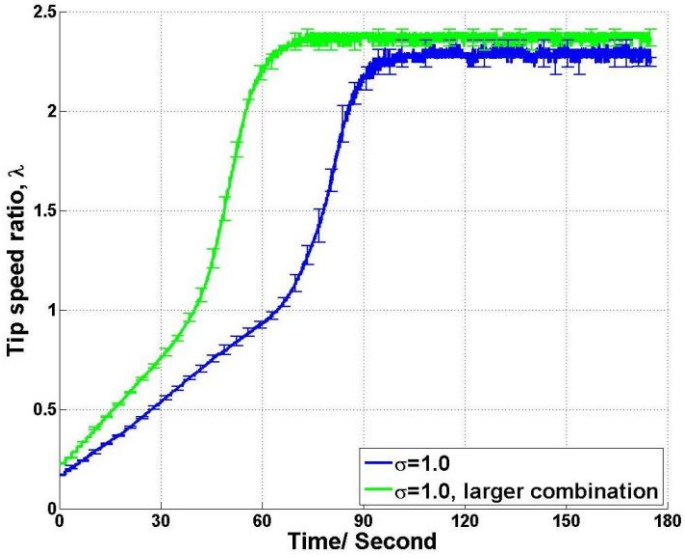

Figure 7.23 Turbine self-starting behaviour under the same solidity but with different combinations of R and c. $V = 6$ m/s

It must be noted that for Case II the system resistance is larger than that in Case I since the turbine support arms (R) are longer. Meanwhile the blade aspect ratio (c/S) in Case II is also reduced, which results in more blade tip loss than that in Case I. Nevertheless, in spite of the above weakness, Case II can still not only reduce turbine self-starting time but also increase the turbine maximum rotational speed as shown in Figure 7.23. The experimental results support the BEM study conducted in this study. The BEM study also demonstrates that a larger combination of R and c is beneficial for a turbine designed to self-start although the initial acceleration might be slightly slower due to the increased inertia.

The relationship between C_p and λ is also presented in Figure 7.24 in order to compare with those predicted by CFD.

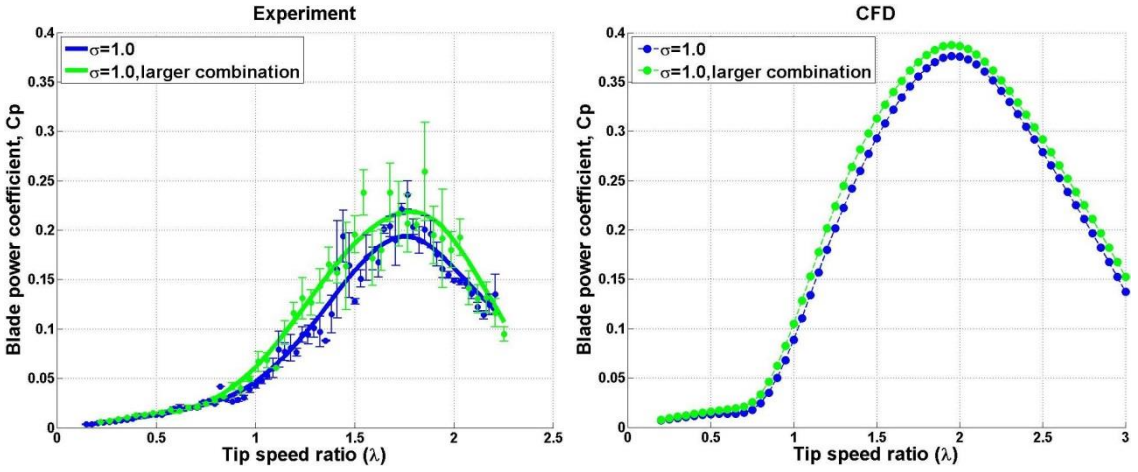

(a) (b)

Figure 7.24 $C_p \sim \lambda$ curve for turbine under the same solidity but with different combination of R and c from (a) experiment, (b) CFD. $V = 6\ \mathrm{m/s}$

As can be seen in Figure 7.24 (a), experimental measurements further support the CFD prediction that a larger combination of R and c (Case II) illustrates a similar $C_p \sim \lambda$ trend compared with that of Case I and the turbine performance is improved over the whole working range. CFD over-predicts C_p since 3-D effects were not taken into consideration in the 2-D model. The larger aerodynamic force generated by this larger blade (Case II) overwhelms the increased system resistance and inertia resulting in better turbine self-starting capability and overall performance.

Again, experimental tests were performed at an upstream wind speed of $V = 7\ \mathrm{m/s}$ which demonstrated similar results and conclusions. Therefore the discussion will not be repeated for $V = 7\ \mathrm{m/s}$ but data is provided in Figure 7.25 for completeness.

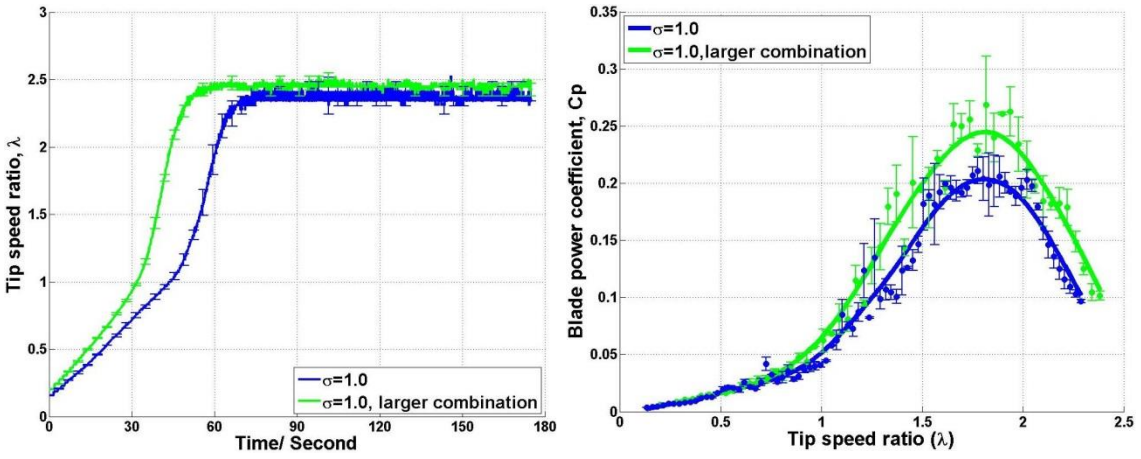

(a) (b)

Figure 7.25 Turbine performance under the same solidity but with different combination of R and c. $V = 7$ m/s. (a) Self-starting, time varying results. (b) $C_p \sim \lambda$ curve

In conclusion, Table 7.4 summarise the experimental results and conclusions in this subsection:

	Tested V (m/s)	Self-starting capability	Self-starting time (s)	Maximum C_p
Case I	6 // 7	Yes // Yes	100 // 80	0.19 // 0.2
Case II	6 // 7	Yes // Yes	80 // 60	0.22 // 0.24

Table 7.4 Summary table of turbine performance with different combination of R and c when solidity is kept constant. $V = 6$ m/s (blue) and $V = 7$ m/s (red)

7.2.3 Turbine performance with different blade profiles

In this section, the turbine performance is examined using different blade profiles. Three typical blades were tested: NACA0021, DU06W200 and NACA4415. Experimental measurements were conducted at various geometrical and wind conditions as summarised in Table 7.5 below. No test was performed for the NACA0018 section since the CFD predictions demonstrated that the NAC0018 and NACA0021 have almost the same behaviour in terms of turbine overall performance. Furthermore the NACA0021 has a greater thickness which is beneficial for other tests performed in this study.

Blade profile	Solidity	V	S	c	m
NACA0021	$\sigma = 1.0$; $\sigma = 0.81$; $\sigma = 0.67$	6 m/s and 7 m/s	700 mm	100 mm	460 g
DU06W200	$\sigma = 1.0$; $\sigma = 0.81$; $\sigma = 0.67$	6 m/s and 7 m/s	700 mm	100 mm	414 g
NACA4415	$\sigma = 1.0$; $\sigma = 0.81$; $\sigma = 0.67$	6 m/s and 7 m/s	700 mm	100 mm	388 g

Table 7.5 Testing parameters for studies of turbine performance with different blade profiles. m is the mass of the blade.

7.2.3.1 V = 6 m/s

The results for solidity, $\sigma = 1.0$ are illustrated in Figure 7.26. Turbine self-starting, time-varying data is shown along with the corresponding $C_p \sim \lambda$ curve. The experimental measurements indicate the turbine with NACA0021 or DU06W200 blades can self-start but the turbine with NACA4415 blades fails to self-start. Compared with the NACA0021 blade as shown in Figure 7.26 (a), the recently proposed blade DU06W200 blade does not improve the turbine self-starting capability despite its lighter weight and lower inertia. With regard to the turbine's maximum power output, the DU06W200 peaks at the same tip speed ratio of $\lambda = 1.8$ as NACA0021 and it demonstrates a slightly higher power coefficient of approximately $C_p = 0.21$ as shown in Figure 7.26 (b).

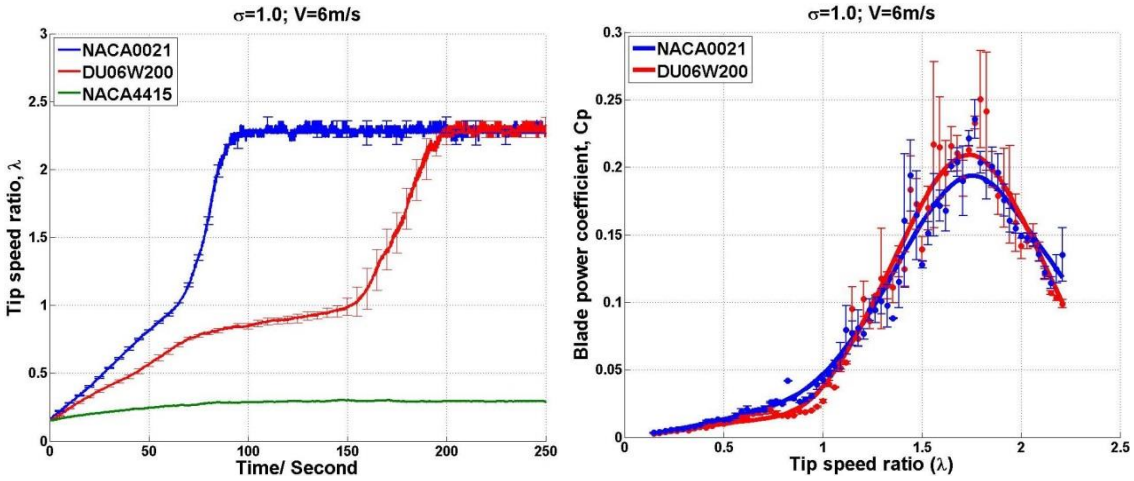

(a) (b)

Figure 7.26 Turbine performance with three different blade profiles for $\sigma = 1.0$ and $V = 6$ m/s. (a) Self-starting, time-varying results. (b) $C_p \sim \lambda$ curve

Although the cambered NACA4415 blade performed better during the upwind sector the gain is more than offset by the loss in the downstream sector because of its

unfavourable incidence angle. As a consequence, turbines with NACA4415 cannot pass the 'dead band' region and fail to self-start at the highest solidity tested in this study. This is the opposite conclusion from that drawn by Kirke and Lazauskas [43] who claimed the turbine with NACA4415 blades is able to self-start easily according to their BEM studies. It has also been demonstrated in this study that the BEM model is highly sensitive to the quality of the input aerodynamic dataset which could have had an impact on their results.

For turbine solidities of $\sigma = 0.81$ and $\sigma = 0.67$, the results are presented in Figure 7.27. By decreasing turbine solidity, the turbine self-starting capability with any blade profile is reduced as discussed in the previous section. DU06W200 failed to self-start at $\sigma = 0.81$ and all blades failed to self-start at $\sigma = 0.67$. The $C_p \sim \lambda$ curve is not plotted here since it provides no useful information if the turbine cannot self-start.

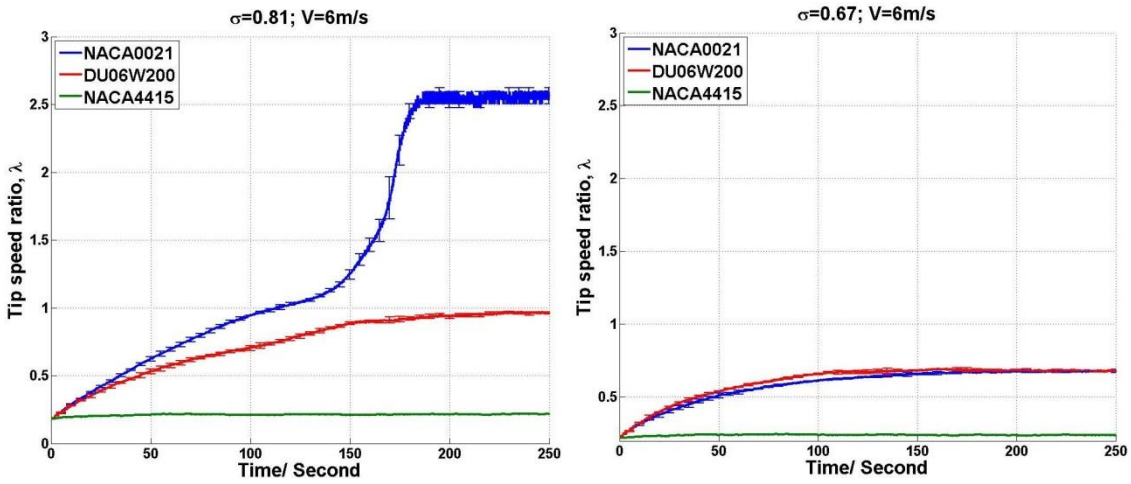

(a) (b)

Figure 7.27 Turbine self-starting behaviour with different blade profiles. $V = 6$ m/s. (a) $\sigma = 0.81$. (b) $\sigma = 0.67$.

7.3.1.1 $V = 7$ m/s

Measurements at $V = 7m/s$ under all three turbine solidities were also performed. Results are provided in Figure 7.28, Figure 7.29 and Figure 7.30. Similar turbine behaviour is found at this upstream wind speed and the results further confirm that NACA0021 is better than DU06W200 in terms of turbine self-starting capability. DU06W200 demonstrates higher maximum C_p but the power coefficient at low tip speed ratios is lower than that measured from NACA0021. Furthermore, the NACA4415 cannot produce positive net torque at low tip speed ratios and failed to self-start for all tested conditions.

The CFD study indicates that DU06W200 has better performance than NACA0021 at low tip speed ratios (see Figure 4.12) but the experimental results show a different conclusion. This discrepancy might result from the incapability of the CFD model to accurately predict the blade performance in the stalled region at low turbine λ. However for the NACA4415, the CFD model also demonstrates that this cambered blade shows significantly lower C_p over the whole working range compared with NACA0021 and this conclusion is supported by the experiments.

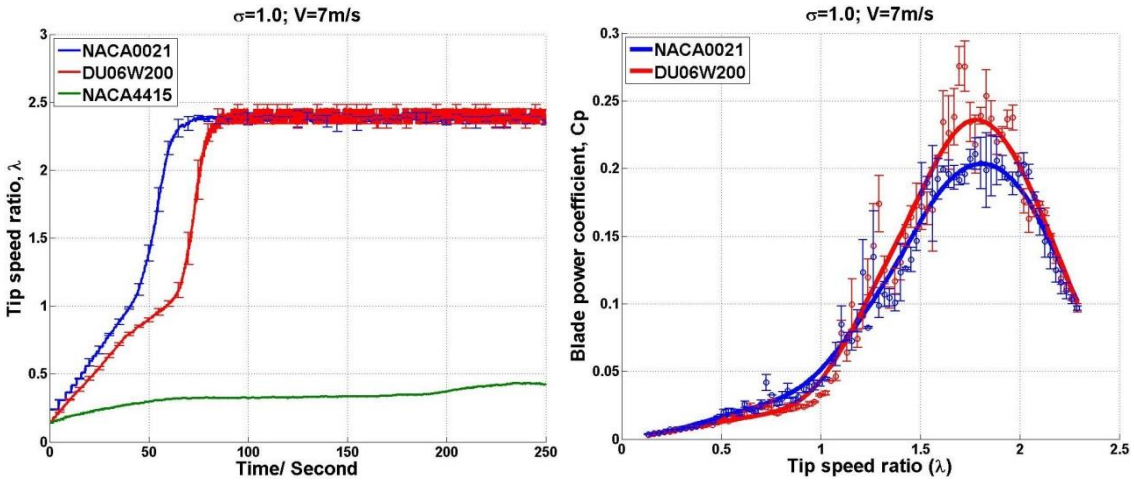

(a) (b)

Figure 7.28 Turbine performance with three different blade profiles for $\sigma = 1.0$ and $V = 7\ \mathrm{m/s}$. (a) Self-starting, time-varying results. (b) $C_p \sim \lambda$ curve

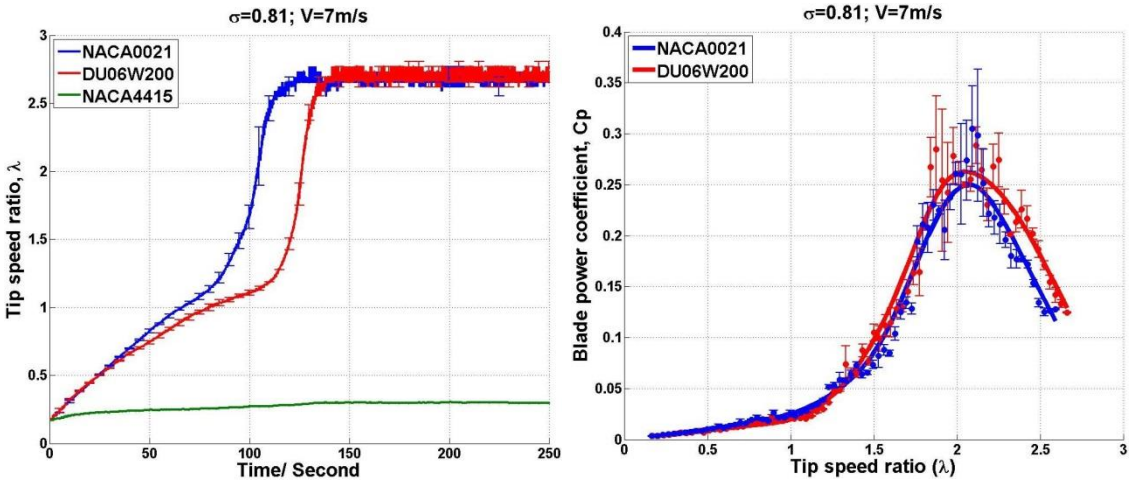

(a) (b)

Figure 7.29 Turbine performance with three different blade profiles for $\sigma = 0.81$ and $V = 7\ \mathrm{m/s}$. (a) Self-starting, time-varying results. (b) $C_p \sim \lambda$ curve

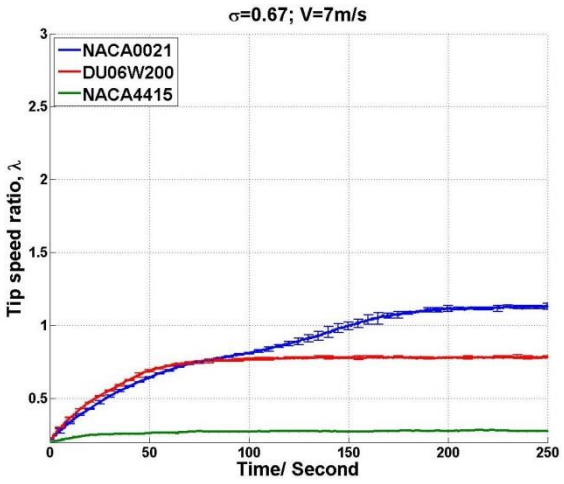

Figure 7.30 Turbine self-starting behaviour with different blade profiles. $\sigma = 0.67$ and $V = 7$ m/s.

In conclusion, Table 7.6 and Table 7.7 summarise the results and conclusions:

	NACA0021	DU06W200	NACA4415
$\sigma = 1.0$	100 s	200 s	Fail
$\sigma = 0.81$	190 s	Fail	Fail
$\sigma = 0.67$	Fail	Fail	Fail

Table 7.6 Turbine self-starting time with different blade profiles under three solidities. $V = 6$ m/s. Unit: second.

	NACA0021	DU06W200	NACA4415
$\sigma = 1.0$	75 s	90 s	Fail
$\sigma = 0.81$	130 s	150 s	Fail
$\sigma = 0.67$	Fail	Fail	Fail

Table 7.7 Turbine self-starting time with different blade profiles under three solidities. $V = 7$ m/s. Unit: second.

7.2.4 Turbine performance with different blade pitch angles

The CFD study shows that the pre-set blade pitch angle plays an important role in turbine overall performance and small negatively pitched blades lead to a better turbine performance at low tip speed ratios. Based upon the results from the CFD study, three pitch angles were chosen to be examined experimentally: $\beta = 0^{\circ}$, $\beta = -2^{\circ}$ and $\beta = -4^{\circ}$.

The NAC0021 is chosen as the tested blade and other testing conditions are summarised in Table 7.8.

Pitch angle	Solidity	V	S	c
$\beta = 0^{\circ}$	$\sigma = 1.0$; $\sigma = 0.81$; $\sigma = 0.67$	6 m/s and 7 m/s	700 mm	100 mm
$\beta = -2^{\circ}$	$\sigma = 1.0$; $\sigma = 0.81$; $\sigma = 0.67$	6 m/s and 7 m/s	700 mm	100 mm
$\beta = -4^{\circ}$.	$\sigma = 1.0$; $\sigma = 0.81$; $\sigma = 0.67$	6 m/s and 7 m/s	700 mm	100 mm

Table 7.8 Testing parameters for studies of turbine performance with different blade pitch angles using NACA0021 blade.

For an upstream wind speed of $V = 7$ m/s, the results at $\sigma = 1.0$ are presented in Figure 7.31. The time-varying data illustrates that the negative pitched blades are able to improve turbine self-starting capability at low tip speed ratios as shown in Figure 7.31 (a). However the turbine with its blades at $\beta = -2^{\circ}$ reaches the maximum speed at almost the same time as the blade without pitch and the turbine with $\beta = -4^{\circ}$ peaks about 30 seconds later. From the $C_p \sim \lambda$ curve shown in Figure 7.31 (b), it is not hard to see that negative pitched blades increase the turbine C_p at $\lambda < 0.9$. However, when $\lambda > 1.0$ both $\beta = -2^{\circ}$ and $\beta = -4^{\circ}$blades produce less power than $\beta = 0^{\circ}$. Although $\beta = -2^{\circ}$ shows similar peak power output, $\beta = -4^{\circ}$ significantly degrades the turbine maximum performance.

Since the majority of the torque is produced by the blade in the upwind region, at low λ a negative pitched blade is able to delay the blade stall and help the blade produce more power over a greater portion of the upwind region. This delayed stall is responsible for the improved turbine performance measured at low λ. With an increase of turbine rotational speed, the blade incidence range is significantly reduced and above a critical λ the blade will no longer experience stall for the whole revolution. At relatively high λ, a negative pitch angle will decrease the blade incidence in the upwind region resulting in less torque being generated. Although it is argued that this negative pitch angle will also increase the blade incidence in the downwind region, the blade produces lower torque in the downwind region leading to a decrease of net torque (or power) when integrated over a whole revolution. Therefore compared with $\beta = 0^{\circ}$, the turbine with $\beta = -4^{\circ}$ produces significantly lower power at $1.3 < \lambda < 2$ as shown in Figure 7.31 (b) resulting in a much slower turbine acceleration at high λ and the turbine self-starts much later (Figure 7.31 (a)).

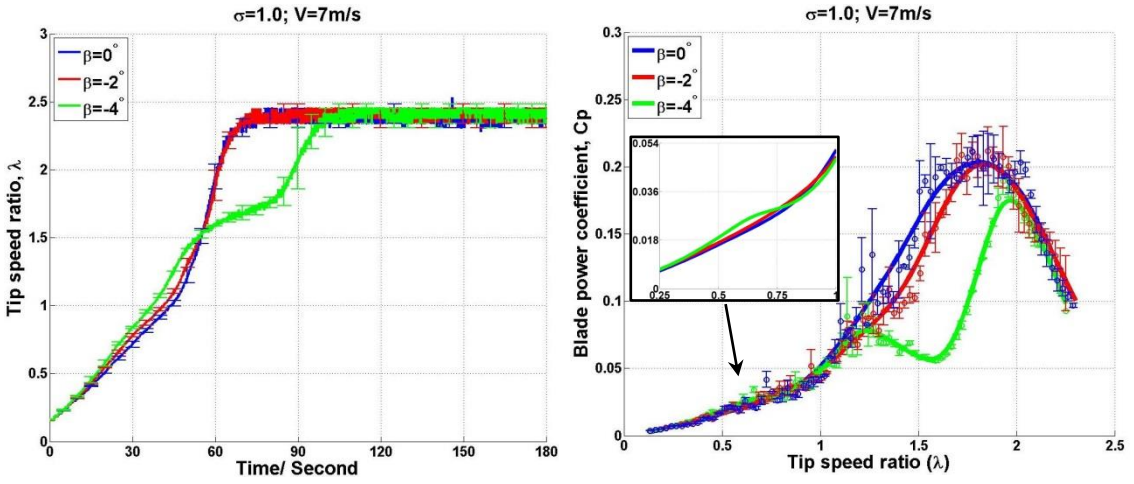

(a) (b)

Figure 7.31 Blade pitch effects on turbine performance at $\sigma = 1.0$ and $V = 7\ \mathrm{m/s}$. (a) Self-starting, time-varying results. (b) $C_p \sim \lambda$ curve.

At solidity, $\sigma = 0.81$, the advantages and disadvantages of negative blade pitch become clearer. As can be seen in Figure 7.32, blades of $\beta = -2^\circ$ and $\beta = -4^\circ$ improve turbine performance only at low tip speed ratios $\lambda < 1.3$, which leads to a faster initial acceleration. However negative pitch angle ($\beta = -2^\circ$) slows down the turbine acceleration rate when $\lambda > 1.3$ and too much negative pitch, $\beta = -4^\circ$, prevents the turbine from self-starting.

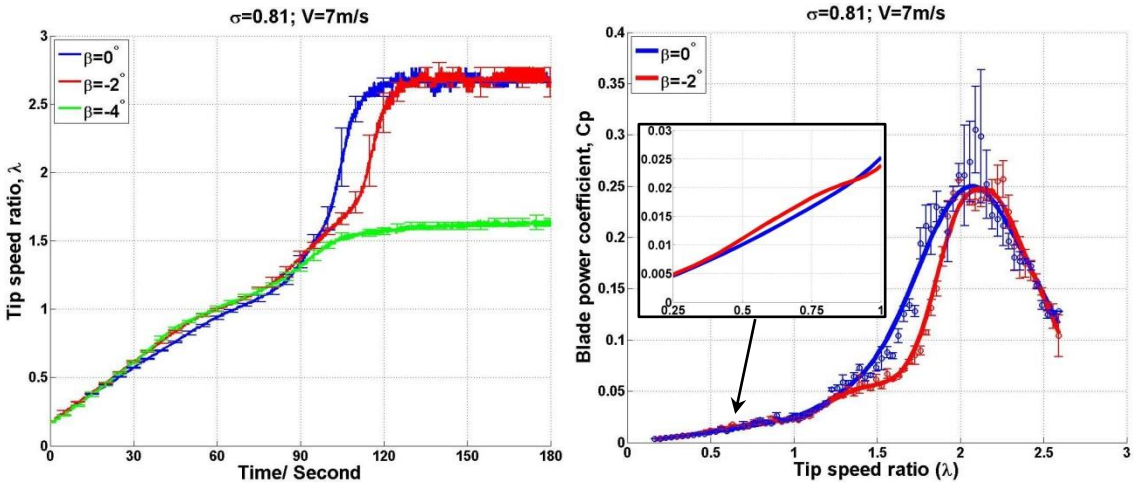

(a) (b)

Figure 7.32 Blade pitch effects on turbine performance at $\sigma = 0.81$ and $V = 7\ \mathrm{m/s}$. (a) Self-starting, time-varying results. (b) $C_p \sim \lambda$ curve.

At a solidity of $\sigma = 0.67$ (see Figure 7.33), no turbine is able to self-start at this wind speed but the turbine with negatively pitched blades still clearly demonstrates a

better initial turbine performance further supporting the above results and conclusions that slightly negatively pitched blades can improve the turbine performance during the start-up period (low tip speed ratios).

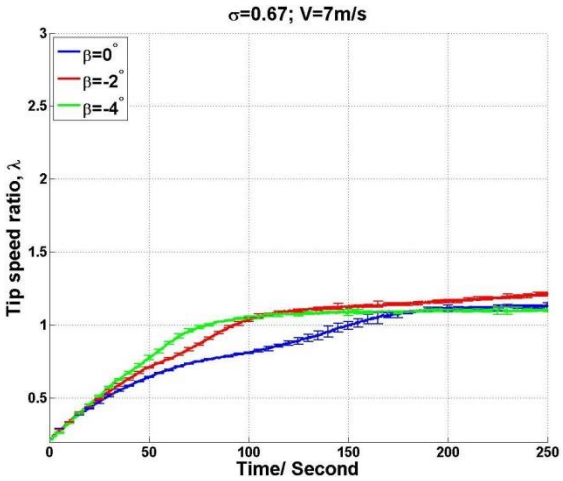

Figure 7.33 Blade pitch effects on turbine performance at $\sigma = 0.67$ and $V = 7\ \mathrm{m/s}$. Self-starting, time-varying results.

Measurements performed at $V = 6\ \mathrm{m/s}$ for $\sigma = 1.0$, $\sigma = 0.81$ and $\sigma = 0.67$ are presented in Figure 7.34, Figure 7.35 and Figure 7.36 respectively showing consistent results and conclusions.

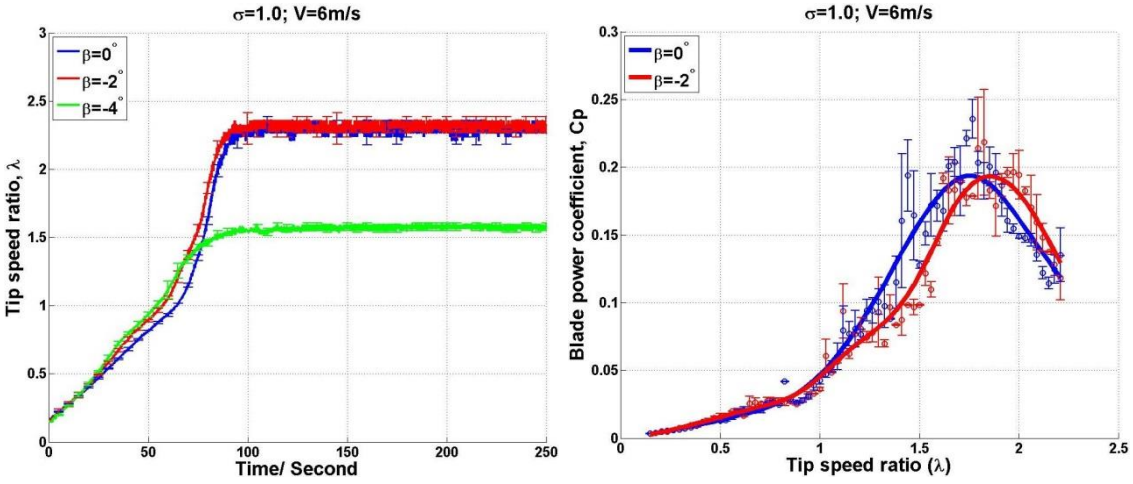

(a) (b)

Figure 7.34 Blade pitch effects on turbine performance at $\sigma = 1.0$ and $V = 6\ \mathrm{m/s}$. (a) Self-starting, time-varying results. (b) $C_p \sim \lambda$ curve.

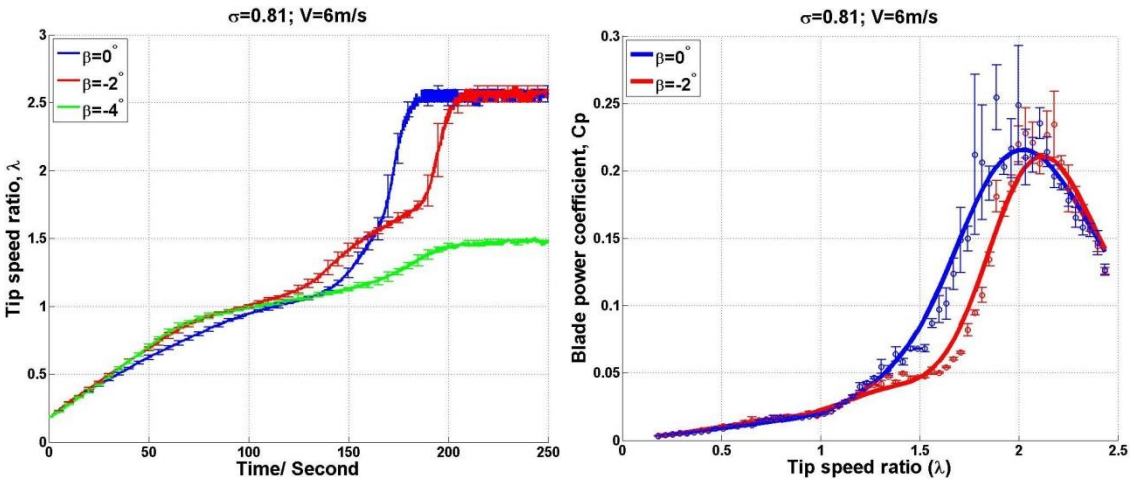

(a) (b)

Figure 7.35 Blade pitch effects on turbine performance at $\sigma = 0.81$ and $V = 6\ \mathrm{m/s}$. (a) Self-starting, time-varying results. (b) $C_p \sim \lambda$ curve

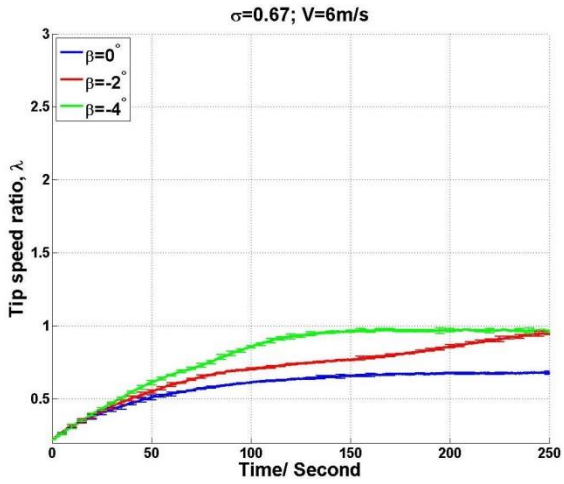

Figure 7.36 Blade pitch effects on turbine performance at $\sigma = 0.67$ and $V = 6\ \mathrm{m/s}$. Self-starting, time-varying results.

In conclusion, the experimental results support the CFD predictions (see Figure 4.14), which demonstrate that a slightly negatively pitched blade is able to improve the turbine power output at low tip speed ratios. Although the negatively pitched blade has mixed effects on the turbine performance in different λ regions, it is thought that slightly negative blade pitch ($\beta > -2^{\circ}$) is still beneficial to a turbine design to achieve self-starting since the 'dead band' region is usually located at relatively low λ. Any slightly improved blade performance at this low λ region might help the turbine pass its plateau stage and results in the turbine's successful self-starting.

7.2.5 Turbine performance with different blade surface roughness

According to the literature, the turbine blade surface roughness will affect turbine performance to some extent. This is an important factor that needs to be considered since the blade surface roughness will be altered during turbine operation through erosion or contamination. Experimental tests were performed using NACA0021 blades with two different surface finishes: wood and aluminium. The overall performance was compared and special attention was paid to the turbine's critical self-starting behaviour. A ZETA-20 3D profiler [158] was used to quantify the surface roughness and details of the machine and methods are discussed in Chapter 5.3.2. Measurements were conducted at turbine solidity of $\sigma = 1.0$; $\sigma = 0.81$ and $\sigma = 0.67$. Other parameters are summarised in Table 7.9.

Surface finish	V	S	c	m	S_q	S_a
Wood (rough)	6 m/s and 7 m/s	700 mm	100 mm	460 g	5.027 μm	4.023 μm
Aluminium (smooth)	6 m/s and 7 m/s	700 mm	100 mm	465 g	0.2805 μm	0.2201 μm

Note: S_q is root mean squared height of surface roughness. S_a is arithmetic mean height of surface roughness.

Table 7.9 Testing parameters for studies of turbines with different blade surface roughness. m is the mass of the blade.

Widely used 3-D surface roughness parameters, S_a and S_q, indicate that the wood surface is about 18 times coarser than the aluminium surface, which enables that the roughness comparison tests are representative and meaningful. The results for a turbine of $\sigma = 1.0$ at $V = 6$ m/s and $V = 7$ m/s are first presented in Figure 7.37 and Figure 7.38 respectively.

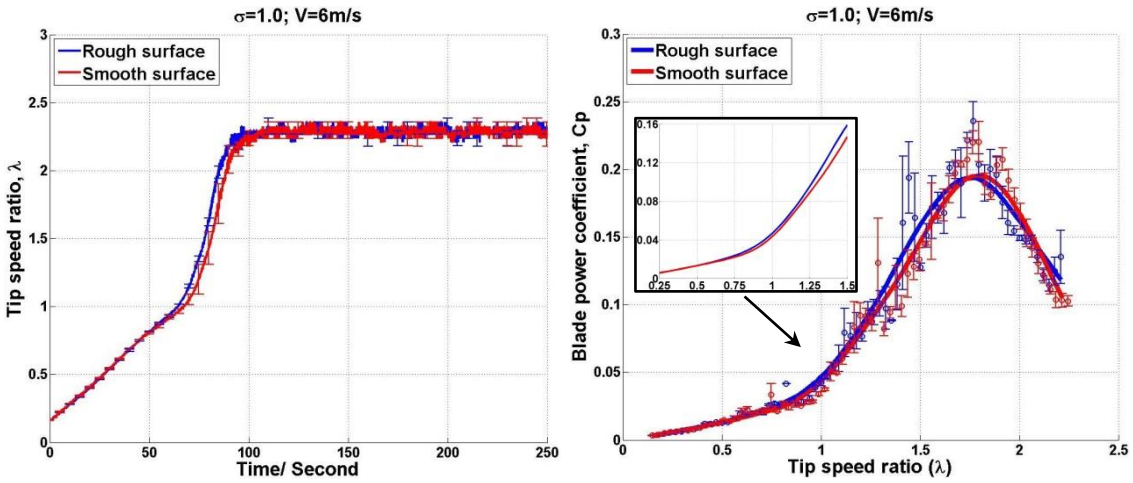

(a) (b)

Figure 7.37 Blade surface roughness effect on turbine performance at $\sigma = 1.0$ and $V = 6\ \mathrm{m/s}$. (a) Self-starting, time-varying results. (b) $C_p \sim \lambda$ curve

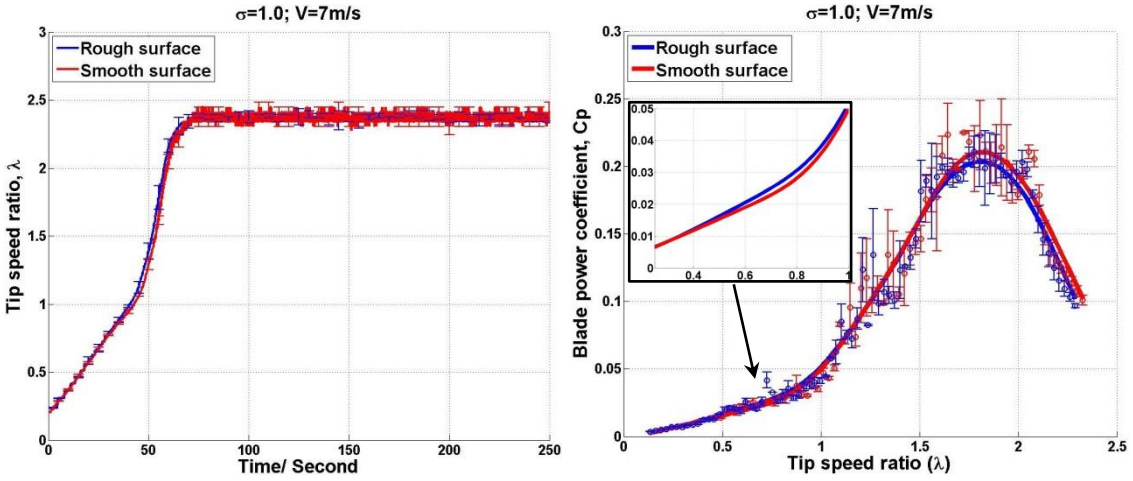

(a) (b)

Figure 7.38 Blade surface roughness effect on turbine performance at $\sigma = 1.0$ and $V = 7\ \mathrm{m/s}$. (a) Self-starting, time-varying results. (b) $C_p \sim \lambda$ curve

Both the rough blade and the smooth blade demonstrate almost identical starting behaviour. The relatively rough surface finish (wood) is able to make the turbine self-start slightly faster at low λ compared with the smooth blade as shown in Figure 7.37 (a) and Figure 7.38 (a). However, in terms of the $C_p \sim \lambda$ performance as shown in Figure 7.37 (b) and Figure 7.38 (b), the rough blade produces more power than the smooth blade at low tip speed ratios (approximately $\lambda < 1.6$), but the smooth surface improves the turbine performance at high λ ($\lambda > 1.6$).

Similar results are observed for the turbine of $\sigma = 0.81$ as shown in Figure 7.39 and Figure 7.40. Although the smooth surface shows slightly lower turbine performance at

low λ, the turbine peak C_p and turbine power output at high λ are both improved. These test results are consistent with the experimental studies performed by Howell et al. [39] and Ashwill [78].

The improved performance from the rough blade is explained by the earlier laminar to turbulent boundary layer transition due to the rougher surface. Those tiny peaks and valleys on the rough surface trip the boundary layer into turbulent leading to the flow being more inclined to attach to the aerofoil surface. Therefore a rough surface is able to delay the aerofoil stall and reduce the associated large drag force at low tip speed ratios. However when the turbine rotational speed is increased, the incidence range is significantly reduced and the rotational zone in which the aerofoil stalls is much reduced or even eliminated. Here the increased skin friction drag resulting from the rough surface will outweigh the benefit from delayed stall resulting in lower performance than a smooth blade at high λ.

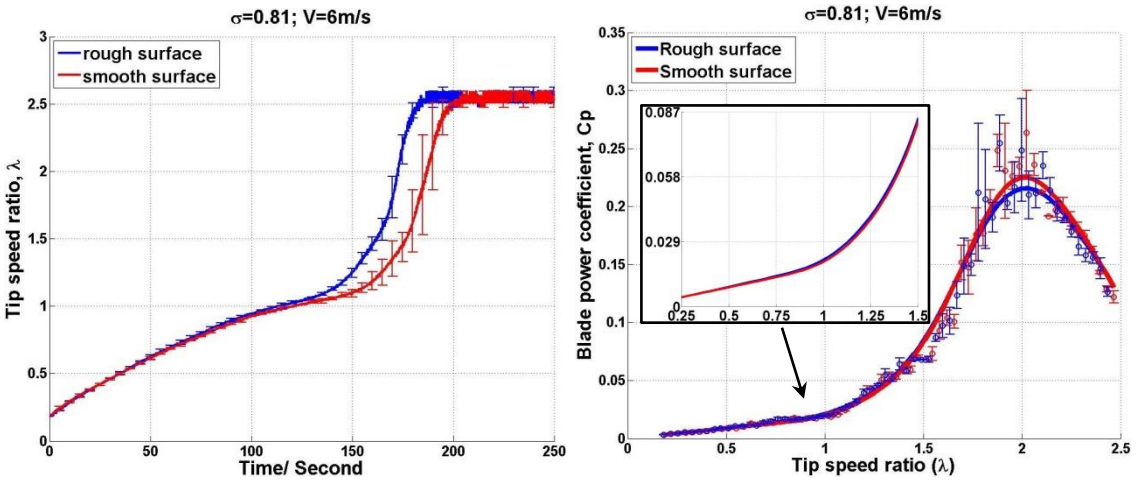

(a) (b)

Figure 7.39 Blade surface roughness effect on turbine performance at $\sigma = 0.81$ and $V = 6\,\mathrm{m/s}$. (a) Self-starting, time-varying results. (b) $C_p \sim \lambda$ curve

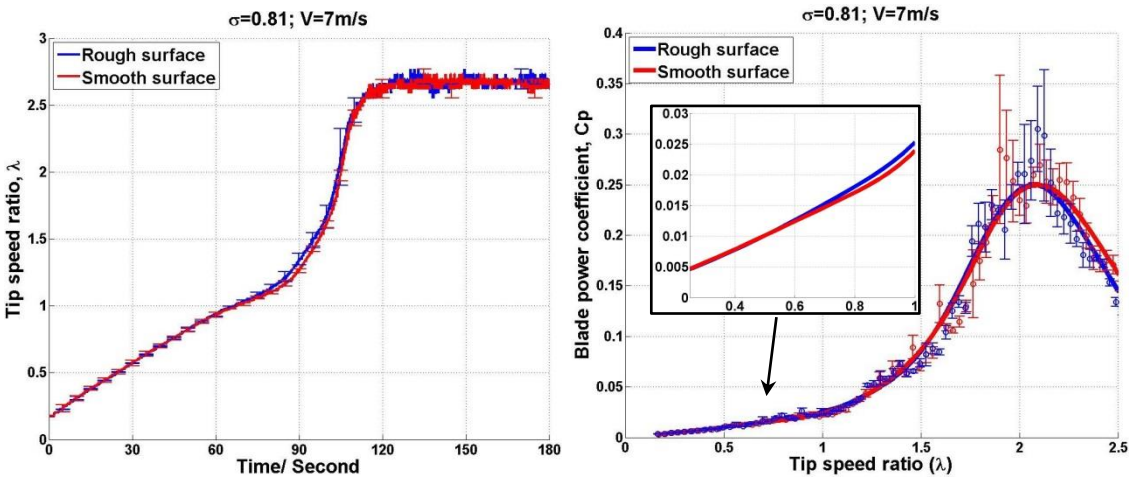

(a) (b)

Figure 7.40 Blade surface roughness effect on turbine performance at $\sigma = 0.81$ and $V = 7\ \mathrm{m/s}$. (a) Self-starting, time-varying results. (b) $C_p \sim \lambda$ curve

However, it is interesting to note that for turbine solidity, $\sigma = 0.67$, the experimental results shown in Figure 7.41 indicate the opposite conclusion to that drawn above. The smooth blade demonstrates better performance at both wind speeds $V = 6\ \mathrm{m/s}$ and $V = 7\ \mathrm{m/s}$. Particularly, at $V = 7\ \mathrm{m/s}$ the smooth blade successfully enables the turbine to self-start while the rough blade turbine fails to self-start. It seems that at this low turbine solidity the smooth blade actually improves the turbine performance at low λ.

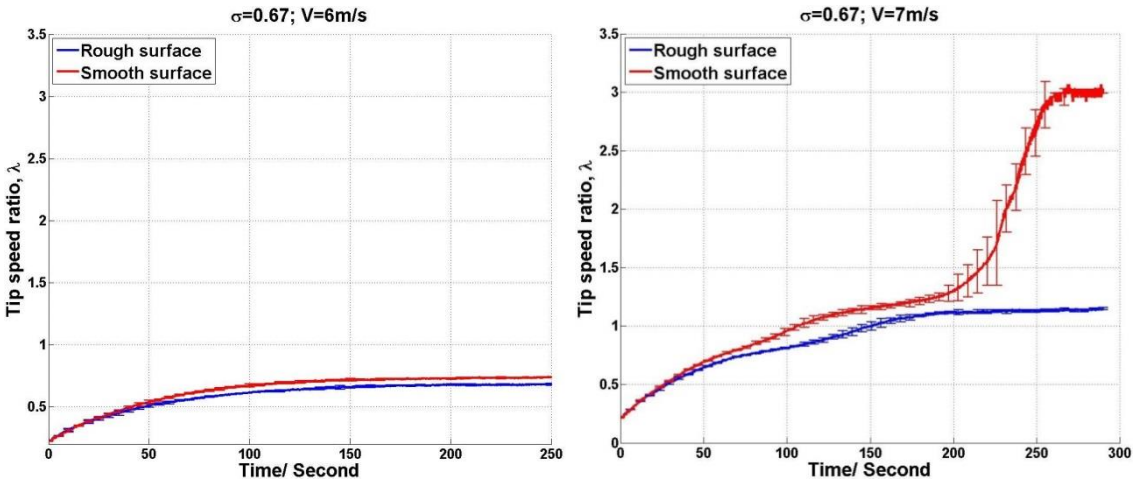

(a) (b)

Figure 7.41 Blade surface roughness effect on turbine performance at $\sigma = 0.67$. (a) $V = 6\ \mathrm{m/s}$. (b) $V = 7\ \mathrm{m/s}$.

One possible explanation for this phenomenon is that by further reducing the turbine solidity, the flow blockage is then reduced resulting in blade stalls over a larger

portion of azimuth angle in the upstream zone. The benefit from the delayed stall of a rough surface becomes limited in this low solidity situation, and cannot make up the loss from the increased skin friction drag. Therefore for a low solidity turbine blade experiencing stall over much of its revolution at low λ, a rough blade might not produce more net torque compared with a smooth blade. Nevertheless, it must be noted that the surface roughness effect on a blade's boundary layer is dependent on the blade Reynolds number, which varies with the rotational speed and azimuth angle. This varying blade Reynolds number inevitably makes the problem more complex and more studies need be performed to analyse the dynamic effect of blade surface roughness on turbine performance.

7.2.6 Turbine performance at different Reynolds numbers

As noted in previous studies, the upstream wind speed will affect the turbine performance since the blade Reynolds number is altered. This section will directly compare the measured results for wind turbine under $V = 6\ \mathrm{m/s}$ and $V = 7\ \mathrm{m/s}$ by using a NACA0021 blade. Three turbine solidities are examined and parameters are summarised in Table 7.10.

	σ	R	c	S
Scenario I	$\sigma = 1.0$	300 mm	100 mm	700 mm
Scenario II	$\sigma = 0.81$	370 mm	100 mm	700 mm
Scenario III	$\sigma = 0.67$	450 mm	100 mm	700 mm

Table 7.10 Parameters for studies of turbine performance under different upstream wind speeds of $V = 6\ \mathrm{m/s}$ and $V = 7\ \mathrm{m/s}$.

Results for turbine solidity of $\sigma = 1.0$, $\sigma = 0.81$ and $\sigma = 0.67$ are presented in Figure 7.42, Figure 7.43 and Figure 7.44 respectively. It can be seen that for scenarios I and II, increasing the upstream wind speed increases the turbine self-starting capability and reduces the self-start time significantly (20% for scenario I and 33% for scenario II). Moreover the blades demonstrate higher C_p over the whole working range indicating a better turbine performance. Although for scenario III the turbine fails to self-start under solidity of $\sigma = 0.67$ for both wind speeds, the turbine blades still accelerate faster at low tip speed ratios at $V = 7\ \mathrm{m/s}$.

In the low Reynolds range ($\sim 10^4\ to\ 10^5$) the blade lift coefficient increases with the increase of Reynolds number as demonstrated in static wind tunnel measurements

conducted in this study, resulting in more torque being generated at the upwind region. Therefore turbine performance at relatively high λ (no blade stall) is considerably increased at high wind speeds showing consistency with the CFD prediction. The CFD results shown in Figure 4.16 and Figure 4.17 indicate lower C_p at low λ for turbines operating at higher wind speeds, resulting from a reduced blade performance in the stall region at higher wind speeds. However, this is not captured by experimental measurements since all three scenarios demonstrate faster turbine acceleration and higher C_p at low λ at higher wind speeds.

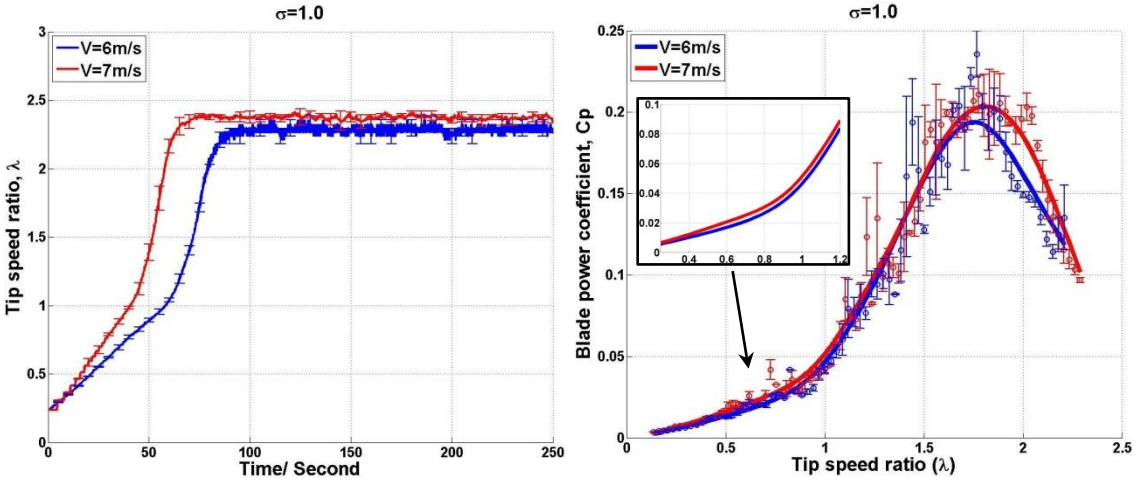

(a) (b)

Figure 7.42 Scenario I, $\sigma = 1.0$, turbine performance under different upstream wind speeds of $V = 6\ \mathrm{m/s}$ and $V = 7\ \mathrm{m/s}$. (a) Self-starting, time-varying results. (b) $C_p \sim \lambda$ curve.

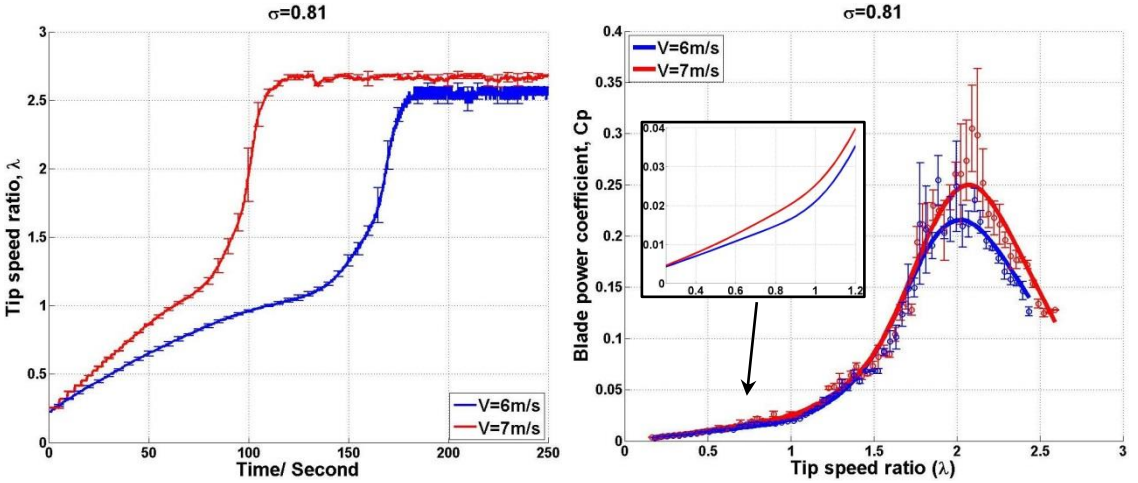

(a) (b)

Figure 7.43 Scenario II, $\sigma = 0.81$, turbine performance under different upstream wind speeds of $V = 6\ \mathrm{m/s}$ and $V = 7\ \mathrm{m/s}$. (a) Self-starting, time-varying results. (b) $C_p \sim \lambda$ curve.

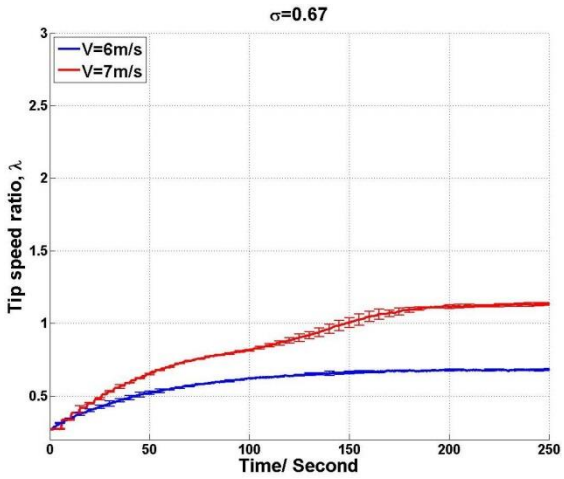

Figure 7.44 Scenario III, $\sigma = 0.67$, turbine performance under different upstream wind speeds of $V = 6\ \mathrm{m/s}$ and $V = 7\ \mathrm{m/s}$. Self-starting, time-varying results.

7.2.7 Turbine performance with different blade aspect ratios

The blade aspect ratio, which is defined as $AR = S/c$, plays a key role in determining the performance of a three dimensional blade. It is generally acknowledged that the tip loss phenomenon will degrade the blade performance and this is worsened if the AR is low. Previous experimental studies performed by Chua [32] and Hill et al [11] both demonstrate the turbine self-starting capability by using a large blade aspect ratio of $AR \approx 7$. Moreover, recent BEM studies conducted by Worasinchai [31] also indicate a blade aspect ratio $AR > 5.7$ is a requisite for a turbine achieving self-starting and experimental measurements are presented here to validate that conclusion.

It is implied in the literature that the blade span, S, must be considered together with the turbine solidity in the design of an H-Darrieus wind turbine for commercial application. Therefore, the aim of this study is to find the minimum value of AR to ensure the turbine is able to self-start. The tests will start from $AR = 6$ since $AR = 7$ has been shown to ensure turbine self-start as demonstrated in the previous sections. The tested blade is NACA0021 and other parameters are summarised in Table 7.11.

	Solidity	V	c	m
$AR = 6$	$\sigma = 1.0$; $\sigma = 0.81$; $\sigma = 0.67$	$6\ \mathrm{m/s}$ and $7\ \mathrm{m/s}$	$100\ \mathrm{mm}$	$395\ \mathrm{g}$
$AR = 7$	$\sigma = 1.0$; $\sigma = 0.81$; $\sigma = 0.67$	$6\ \mathrm{m/s}$ and $7\ \mathrm{m/s}$	$100\ \mathrm{mm}$	$460\ \mathrm{g}$

Table 7.11 Parameters for studies of turbine under different blade aspect ratio. m is the mass of the blade.

It is surprising to find that by reducing the blade aspect ratio to $AR = 6$, the turbine failed to self-start under any of the investigated solidities. Examples at

$V = 7\ \mathrm{m/s}$ are illustrated in Figure 7.45. As can be seen, the turbine with blades of $AR = 6$ accelerates much more slowly from the start at all solidities although the system inertia is reduced. Even at the highest solidity of $\sigma = 1.0$, shown in Figure 7.45 (a), the turbine produce very limited net positive torque thus achieving a maximum tip speed ratio of $\lambda = 0.85$. It seems that the removed $100\ \mathrm{mm}$ (14%) of blade span was just enough to overcome system resistance and enable the turbine to self-start. For the delicate process of H-Darrieus self-starting, any small loss of useful torque might be fatal to the turbine.

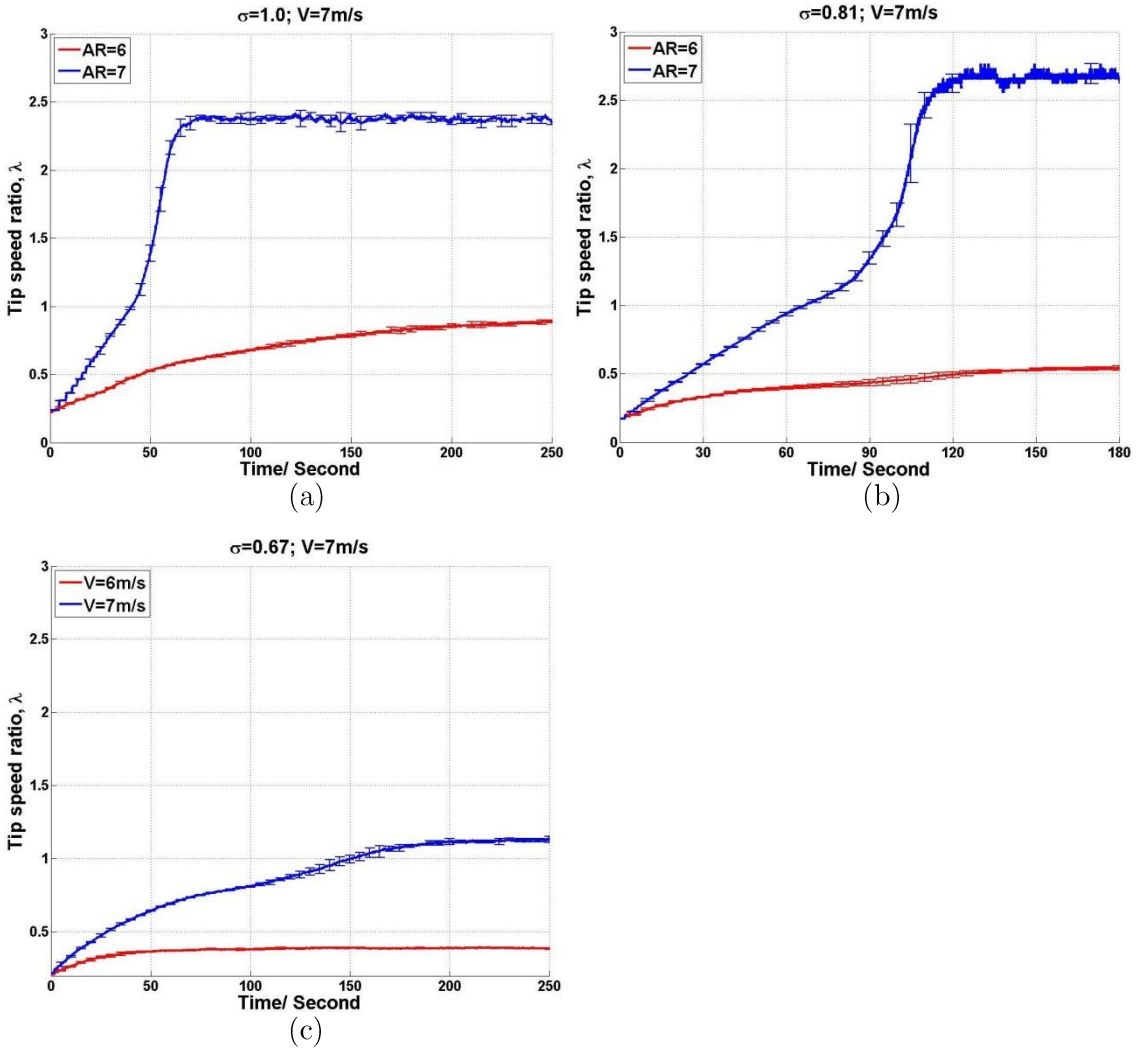

Figure 7.45 Self-starting time-varying results for turbine with different blade aspect ratios. (a) $\sigma = 1.0$. (b) $\sigma = 0.81$. (c) $\sigma = 0.67$.

The tests were performed by using the DU06W200 blades and yield the same conclusion, that a turbine cannot self-start under any test condition with the blade aspect ratio of $AR = 6$. Therefore, $AR = 7$ is the minimum value for a commercial H-Darrieus wind turbine to achieve self-starting at an the average wind speed of $V = 6\sim7\ \mathrm{m/s}$.

7.2.8 Conclusion

A three-bladed H-Darrieus wind turbine was experimentally tested in this study to investigate the effect of design parameters including turbine solidity, blade profile, surface roughness, pitch angle and aspect ratio. Turbine self-starting, time-varying data has been presented together with overall $C_p \sim \lambda$ performance data. Moreover, the experimentally measured results were also compared with the available CFD and BEM predictions conducted in this study. In order to fill the gaps in the literature, this study focused on turbine self-starting capability and turbine performance at low tip speed ratios, which have not been extensively studied in the past.

According to the experimental results, several important conclusions can be drawn:

- Turbines with high solidity are able to self-start faster than turbines with low solidity due to the increased flow blockage (explained in detail in Section 7.3). However this is achieved at the expense of lower peak power output.
- For a given turbine solidity, a combination of larger turbine radius and larger blade chord length is able to improve the turbine self-starting capability and to reduce the self-starting time despite increased system inertia and resistance. The experimental measurements further support the BEM predictions performed in this study.
- Among the three different blade profiles that were tested, the DU06W200 demonstrates higher peak C_p compared with that of NACA0021. However turbine self-starting time is reduced by using the NACA0021 section since it generates more power at low λ. The worst turbine performance is produced by the cambered blade NACA4415, which shows consistent low performance from CFD predictions. Nevertheless, the CFD over-predicts the DU06W200 performance at low λ compared with experimental results.
- Slightly negative blade pitch ($\beta > -2^{\circ}$) can delay the blade stall in the upwind region resulting in more torque generated at low λ. Although the blade performance at relatively high λ is degraded, it is thought blades with a small negative pitch angle can help the turbine pass through the plateau stage more easily. The experimental results support the CFD study.
- Blades with a rough surface tend to have an earlier laminar to turbulent boundary layer transition compared with smooth surfaces, which results in the flow becoming more inclined to remain attached to the aerofoil surface. Therefore blade stall is delayed with a rough surface leading to a better performance at low λ. However it seems the increased turbine performance only occurs for high turbine solidity. This

is because the flow blockage is reduced at low turbine solidity resulting in the blade stalling in a larger portion of the revolution. Thus the benefit from the delayed stall of a rough surface becomes limited and cannot make up for the loss from the increased skin friction drag.

- The present study demonstrates that in order to design an H-Darrieus wind turbine that can self-start, the blade aspect ratio should be larger than 7 in order to have enough area to drive the turbine and make up the loss from the tips.
- Higher upstream wind speed results in larger blade Reynolds number, which is illustrated to be able to reduce turbine self-starting time. Although the CFD indicates a reduced turbine performance at low λ at higher V, this might just be due to the incapability of CFD to accurately predict the blade performance in the stalled region.

Conclusions are summarised in Table 7.12.

	Increase	**decrease**
Solidity, σ	Better turbine performance at low λ and better self-starting capability. Lower maximum C_p	Lower turbine performance at low λ and lower self-starting capability. Higher maximum C_p
Blade pitch, $(0^\circ > \beta > -2^\circ)$	Better turbine performance at low λ and better self-starting capability. Slightly lower maximum C_p	Lower turbine performance at low λ and lower self-starting capability. Slightly higher maximum C_p
Aspect ratio, AR	Better turbine performance at low λ and better self-starting capability. Better to have $AR > 7$ blades	Lower turbine performance at low λ and lower self-starting capability. Turbines with blades $AR \leq 7$ fail to self-start
Reynolds, Re	Better turbine performance at low λ and better self-starting capability. Higher maximum C_p	Lower turbine performance at low λ and lower self-starting capability. Lower maximum C_p
Blade surface roughness	For $\sigma = 0.81$ and $\sigma = 1.0$, better turbine performance at low λ and better self-starting capability. Lower maximum C_p For $\sigma = 0.67$, lower turbine performance at low λ	For $\sigma = 0.81$ and $\sigma = 1.0$, lower turbine performance at low λ and lower self-starting capability. Higher maximum C_p For $\sigma = 0.67$, better turbine performance at low λ

Table 7.12 Summary table for design parameters' effect on turbine performance including self-starting capability

One of the main concerns of this study is to provide a clear answer to the question of how to design an H-Darrieus wind turbine that will self-start. Therefore according to experimental measurements the following design consideration should be followed:

- A relatively high turbine solidity σ
- For a given σ, choose larger combinations of R and c (if n is a constant)
- Traditional symmetrical NACA series blades with large thickness are still demonstrated to be a good choice for H-Darrieus wind turbines
- Blades with rough surface finish, especially for turbine of high σ
- A slightly negatively pitched blade ($\beta > -2^{\circ}$)
- The blade aspect ratio should be maximised (under the premise of structural strength), the suggested value is at least $AR > 7$.

7.3 On-board pressure measurement

The instantaneous blade pressure distribution and its variation during H-Darrieus wind turbine rotation were measured directly by employing the new on-board pressure measurement technique. Tests were conducted under different turbine geometrical and wind conditions. Table 7.13 provides a summary of the main parameters used for this study. For each tip speed ratio, the corresponding pre-set measurement interval was a constant equal to $\theta = 0.25^{\circ}$ and the measurements were repeated for 100 revolutions in order to calculate the averaged results as described in Chapter 6. The sign convention is shown in Figure 7.46.

Solidity	c	S	V	Blade profile	λ
$\sigma = 1.0$	100 mm	700 mm	6 m/s and 7 m/s	NACA0021	0.5,0.8,1.0,1.5,2.0
$\sigma = 0.81$	100 mm	700 mm	6 m/s and 7 m/s	NACA0021	0.5,0.8,1.0,1.5,2.0
$\sigma = 0.67$	100 mm	700 mm	6 m/s and 7 m/s	NACA0021	0.5,0.8,1.0,1.5,2.0

Table 7.13 Parameters for study of on-board pressure measurement

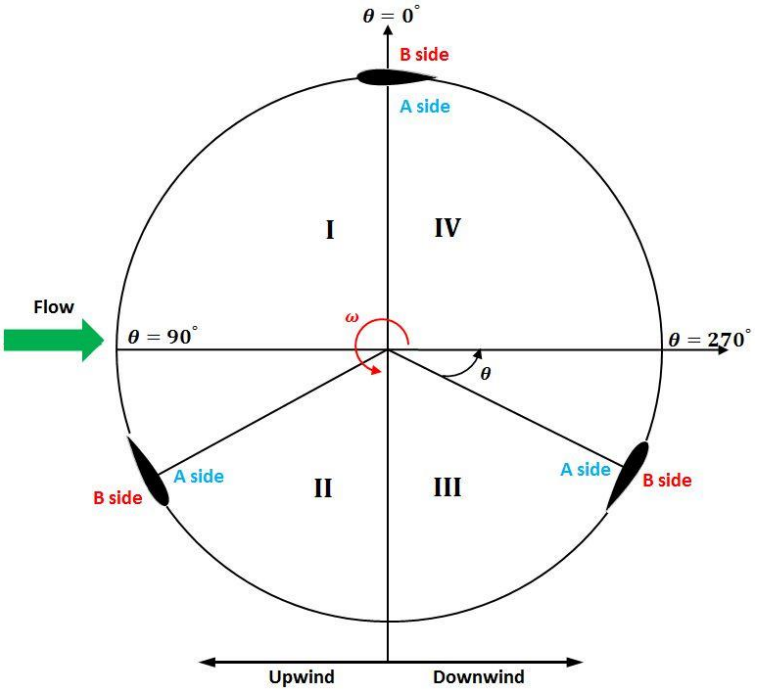

Figure 7.46 Sign convection for on-board pressure measurement study

The main study interests included blade dynamic stall, laminar separation and blade path curvature effects. The results are presented in this section along with discussion and conclusions. Since the two wind speeds examined did not result in a significant blade behaviour change, the data discussed here focuses on $V = 7\ \mathrm{m/s}$.

7.3.1 Flow physics at turbine solidity of $\sigma = 1.0$

Dynamic stall is an important flow phenomenon that considerably affects turbine performance. Blades will experience stall at low turbine tip speed ratio since the incidence range exceeds the static stall angle during rotation. However, in a dynamic process the stall angle is delayed to incidences above the static angle of attack resulting in higher peak lift value. In this study, the blade dynamic stall process and the laminar separation bubble are successfully captured and recorded along with the curvature effect using the on-board pressure measurement system. The results at three typical λ (low $\lambda = 0.5$; medium $\lambda = 1.5$; high $\lambda = 2.0$) are presented in terms of pressure coefficient distribution (C_{pp}), which is non-dimensionalised by the upstream wind speed.

7.3.1.1 $\lambda = 0.5$

Before discussing the results some terms need to be further explained. Firstly, the blade's **A** side is defined as the blade's inner surface (close to the axis) while the **B** side is defined as the blade's outer surface as shown in Figure 7.46. Secondly, the theoretical

incidence angle α is calculated based on the turbine kinematics. It must be noted that the kinematic analysis does not take any wake or flow curvature effect into consideration. It assumes a uniform flow through the whole domain. The results at the low tip speed ratio of $\lambda = 0.5$ are presented first in Figure 7.47.

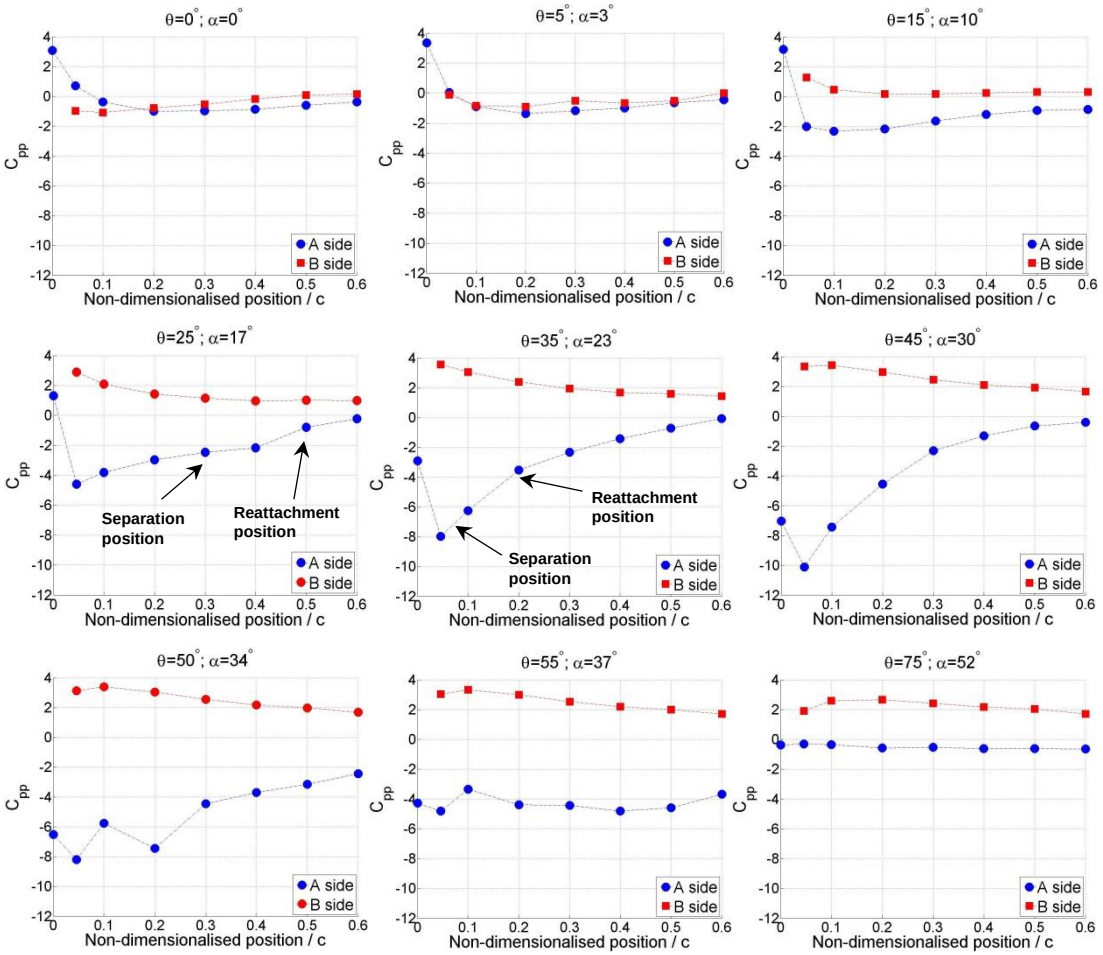

Figure 7.47 Instantaneous blade pressure measurements in the upwind quadrant I. $\sigma = 1.0$, $\lambda = 0.5$, $V = 7\ \mathrm{m/s}$.

It can be seen, at this relatively low tip speed ratio of $\lambda = 0.5$ that the symmetrical pressure distribution occurs at approximately $\theta = 5^{\circ}$ rather than $\theta = 0^{\circ}$. This differs from the theoretical analysis that assumes symmetry when the blade is parallel to flow at $\theta = 0^{\circ}$. This is becasue the measurements were taken after the turbine reached its pre-set speed and the rotor effect, in this case the curvature effect, becomes significant. A curvilinear flow results in a symmetrical blade becoming a virtual cambered aerofoil as pointed out by Migliore et al. [71]. It could also be argued that this small azimuth difference might result from the inaccurate alignment of the blade with the upstream flow. However, a sensitivity study indicates the error for alignment is within $\theta = \pm 2^{\circ}$.

This curvature effect becomes more pronounced at high λ as will be shown in the following discussion.

The blade incidence angle α further increases with the increase of azimuth angle θ and the blade's **A** side becomes the suction side while the **B** side becomes the pressure side (the resultant flow approaches from the **B** side after $\theta > 5^{\circ}$). According to static wind tunnel measurements and CFD studies, a laminar separation bubble forms at the blade trailing edge and moves towards the leading edge with the increasing angle of attack. However since there is no pressure tapping at the blade trailing edge in this study, the laminar separation bubble is not captured until $\theta = 15^{\circ}$, around a blade position of $0.4c \sim 0.6c$ (**A** side). It becomes more apparent at $\theta = 25^{\circ}$ where the bubble separation and re-attachment positions are around $0.3c$ and $0.5c$ respectively. It should be noted that due to the limited number of pressure tappings, the location of the bubble separation and re-attachment positions are not exact.

The maximum negative pressure coefficient for the blade suction side (**A** side) keeps decreasing with the increase of azimuth angle from $C_{pp} = -4.5$ at $\theta = 25^{\circ}$ to $C_{pp} = -10$ at $\theta = 45^{\circ}$. At this stage the blade generates significant torque due to the increasing lift force and the laminar separation bubble moves further towards the leading edge along with the reduction of bubble length. Within the resolution provided by the pressure tappings, the laminar separation bubble can be roughly identified at around $0.1c \sim 0.2c$ for $\theta = 35^{\circ}$ and $\theta = 45^{\circ}$ (see Figure 7.47). It must be noted that at $\theta = 45^{\circ}$, the theoretical incidence angle is about $\alpha = 30^{\circ}$ which is already far beyond the static stall angle of $\sim 13^{\circ}$ at similar Reynolds numbers [172]. Even taking the curvature effect into consideration, the dynamic stall effect which significantly delays the stall angle is successfully captured in this study. The laminar separation bubble bursts when the blade reaches about $\theta = 50^{\circ}$ showing pressure fluctuation at the leading edge and the blade totally stalls at around $\theta = 55^{\circ}$. The stalled blade produces no or limited positive torque at quadrant II and quadrant III.

It must be noted that an aerofoil second-stall behaviour around $\alpha = 40^{\circ}$ was captured in the static wind tunnel measurement performed in this study. However it is not noticed in the on-board pressure measurements. The blade stalls around $\alpha = 34^{\circ}$ as shown in Figure 7.47 and a gradual pressure change is measured afterwards. This might be because the wake structure in a dynamic process cannot change suddenly as it did when measured in a static wind tunnel.

The results for the blade behaviour in downwind quadrant IV are presented in Figure 7.48. From a quasi-steady consideration of a symmetrical blade, its behaviour in

quadrant IV would be expected to minor that in quadrant I except the flow comes from the A side which becomes the pressure side while the B side becomes the suction side. However it can be seen that the blade still stalls at $\theta = 325^{\circ}$ ($\alpha = -23^{\circ}$) due to the dynamic hysteresis, which delays the onset of flow reattachment. The flow subsequently reattaches on the suction side (**B** side) at low enough incidence when the turbine reaches $\theta = 345^{\circ}$ and no laminar separation bubble is captured in quadrant IV.

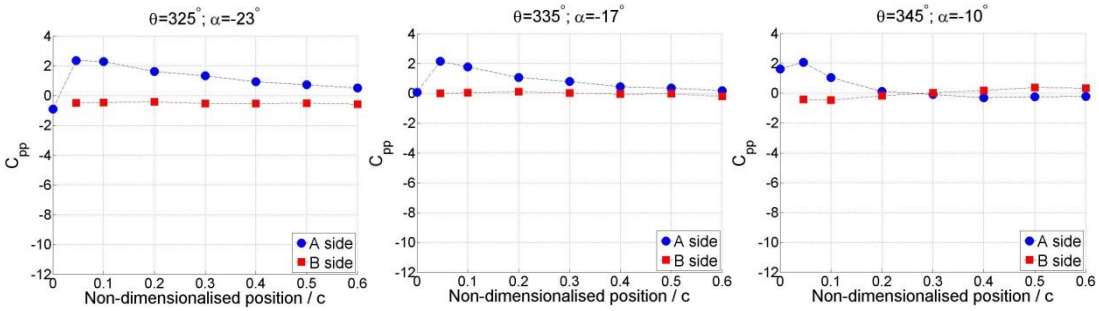

Figure 7.48 Instantaneous blade pressure measurements in the downwind quadrant IV. $\sigma = 1.0$, $\lambda = 0.5$, $V = 7\ \mathrm{m/s}$.

7.3.1.2 $\lambda = 1.5$

At the medium tip speed ratio of $\lambda = 1.5$, the blade incidence range is significantly reduced. However the curvature effect becomes more pronounced and the blade zero incidence occurs at $\theta = 24^{\circ}$ while the theoretical angle of attack at this position is $\alpha = 10^{\circ}$ as shown in Figure 7.49. The resultant flow still approaches from the blade's **A** side at the geometrical zero position of $\theta = 0^{\circ}$ indicating the symmetrical blade is virtually cambered. When the blade reaches $\theta = 45^{\circ}$, a laminar separation bubble is then captured around $0.4c \sim 0.6c$. Increasing the angle of incidence causes the separation bubble to move forward and to reduce in length and the bubble is captured around blade $0.1c \sim 0.2c$ at $\theta = 70^{\circ}$.

An interesting phenomenon is observed when the turbine reaches $\theta = 90^{\circ}$. The pressure measurements demonstrate that the peak negative pressure point starts to traverse along the blade surface from $\theta = 90^{\circ}$. As can be seen in Figure 7.49 the corresponding peak suction points for $\theta = 90^{\circ}$, $\theta = 95^{\circ}$, $\theta = 100^{\circ}$, $\theta = 105^{\circ}$ and $\theta = 110^{\circ}$ are around $0.05c$, $0.25c$, $0.35c$, $0.45c$ and $0.6c$. This wave-like C_{pp} distribution illustrates that the dynamic-stall vortex formed at the blade leading edge convects along the blade as the incidence (azimuth angle) keeps increasing. This vortex is finally shed into the wake after $\theta = 110^{\circ}$ (since there is no pressure tapping after $0.6c$, it is not possible to know the exact θ). It seems that this dynamic stall vortex is

not the laminar separation bubble captured at lower incidence (azimuth angle) since the maximum pressure coefficient at the beginning of convection of $\theta = 95^{\circ}$ is only $C_{pp} = -14$ while the laminar separation bubble has a peak value of $C_{pp} = -22$ around $\theta = 70^{\circ}$. A more reasonable explanation is that the laminar separation bubble bursts around $\theta = 90^{\circ}$ and a new dynamic vortex with lower strength is then formed at the blade leading edge due to the fast rotation (reduced frequency). This newly formed vortex also might be part of the burst laminar separation bubble.

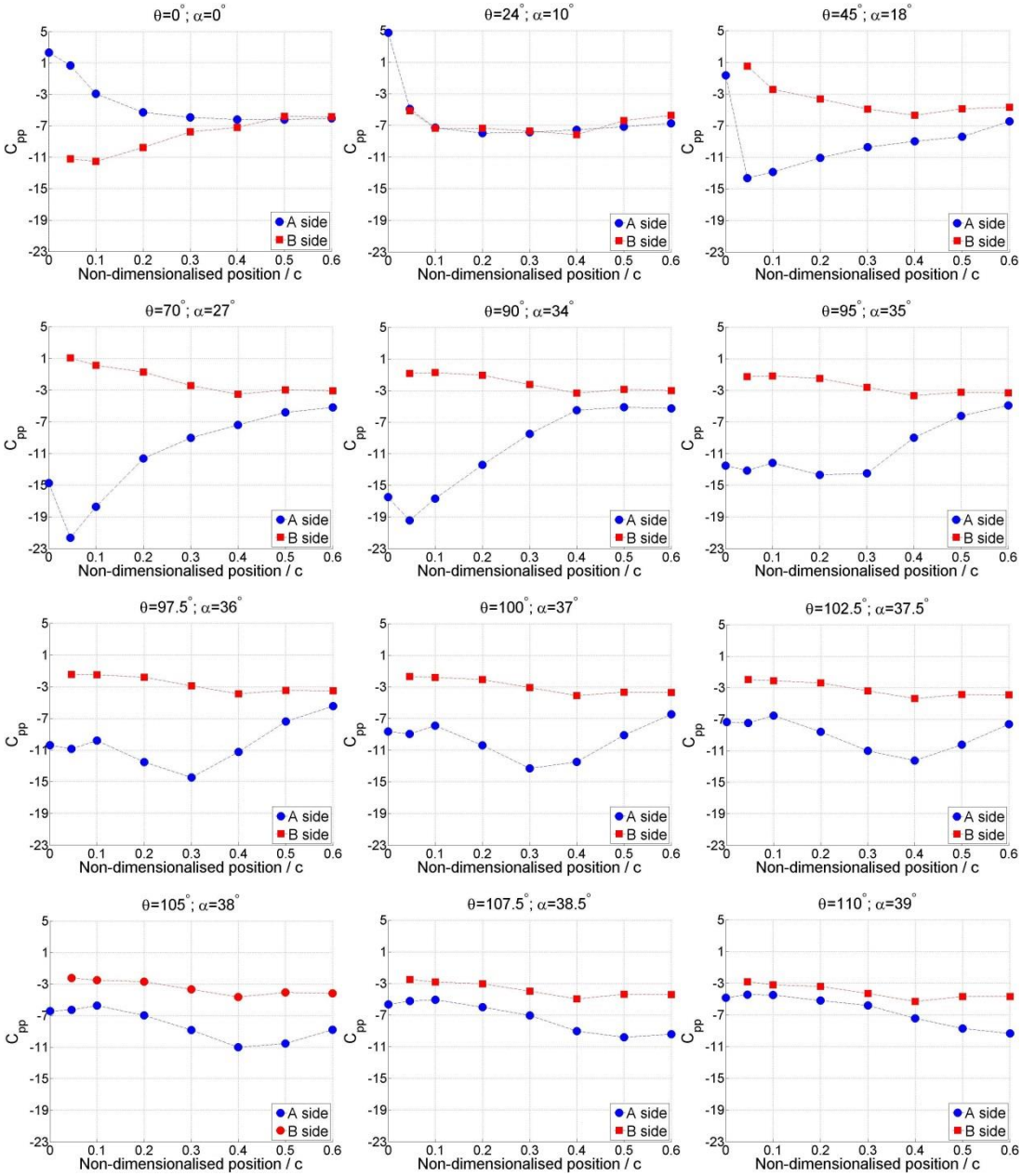

Figure 7.49 Instantaneous blade pressure measurements in the upwind quadrant I and quadrant II. $\sigma = 1.0$, $\lambda = 1.5$, $V = 7$ m/s.

A previous study performed by Worasinchai [31] at Durham University also captured the dynamic vortex convection along the aerofoil surface by purely pitching the aerofoil. Worasinchai claimed that the strength of the dynamic stall vortex increases with the increase of reduced frequency of pitching and the aerofoil stall angle is considerably delayed at the highest reduced frequency examined ($k = 0.25$). For H-Darrieus wind turbine operation, the reduced frequency can be also defined as $k = \frac{c}{D}\lambda$ as shown in Equation 2.3. Therefore, the corresponding reduced frequency for the above two tip speed ratios examined here, $\lambda = 0.5$ and $\lambda = 1.5$, are $k = 0.08$ and $k = 0.25$ respectively.

For pressure measurement at $\lambda = 0.5$, as shown in Figure 7.48, the dynamic vortex convection is not captured (or not clearly captured). The laminar separation bubble bursts at $\theta = 50^{\circ}$ and the blade totally stalls at $\theta = 55^{\circ}$. This might be because at this low tip speed ratio (low reduced frequency), the strength of the dynamic vortex is too low to attach and convect on the blade surface and is quickly shed into the wake. In contrast, at $\lambda = 1.5$ (relatively large reduced frequency) the dynamic stall vortex is finally shed into the wake after the blade travels through more than 20° (azimuth angle). The convection of the dynamic stall vortex is also captured at $\lambda = 0.8$ and $\lambda = 1.0$.

The measurements in the downwind region indicate the blade produces little torque in quadrant III and quadrant IV since the blade stalls for the majority of the downwind portion. Due to the blade dynamic hysteresis, the flow reattaches to the blade surface only when the incidence is low enough around $\theta = 345^{\circ}$ as shown in Figure 7.50.

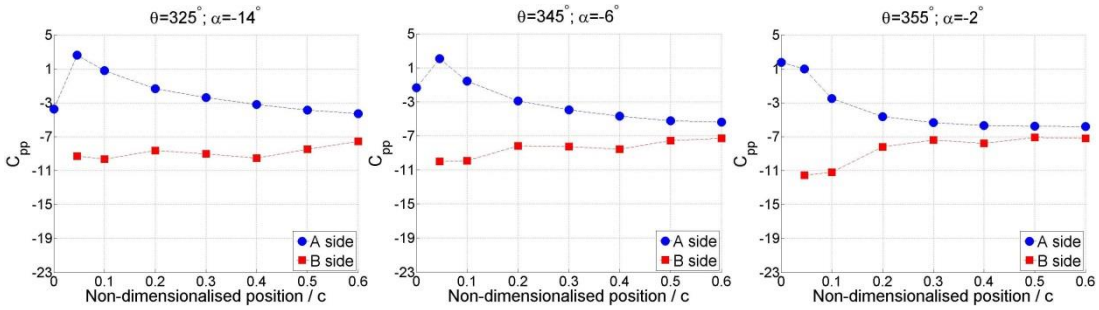

Figure 7.50 Instantaneous blade pressure measurements in the downwind quadrant IV. $\sigma = 1.0$, $\lambda = 1.5$, $V = 7$ m/s.

7.3.1.3 $\lambda = 2.0$

Pressure measurements were also performed at the relatively high tip speed ratio of $\lambda = 2.0$ and the results are shown in Figure 7.51. With the further increase of turbine

rotational speed, the curvature impact is also exacerbated as the pressure symmetry in the upwind region is captured at an azimuth angle around $\theta = 33^{\circ}$. After $\theta = 33^{\circ}$, the resultant flow is incident upon the blade **B** side which becomes the pressure side while the **A** side becomes the suction side. Meanwhile a laminar separation bubble is captured at $\theta = 60^{\circ}$ around blade position of $0.4c \sim 0.6c$. This laminar separation bubble moves further towards the leading edge at $\theta = 80^{\circ}$ and $\theta = 100^{\circ}$ along with the increase of incidence.

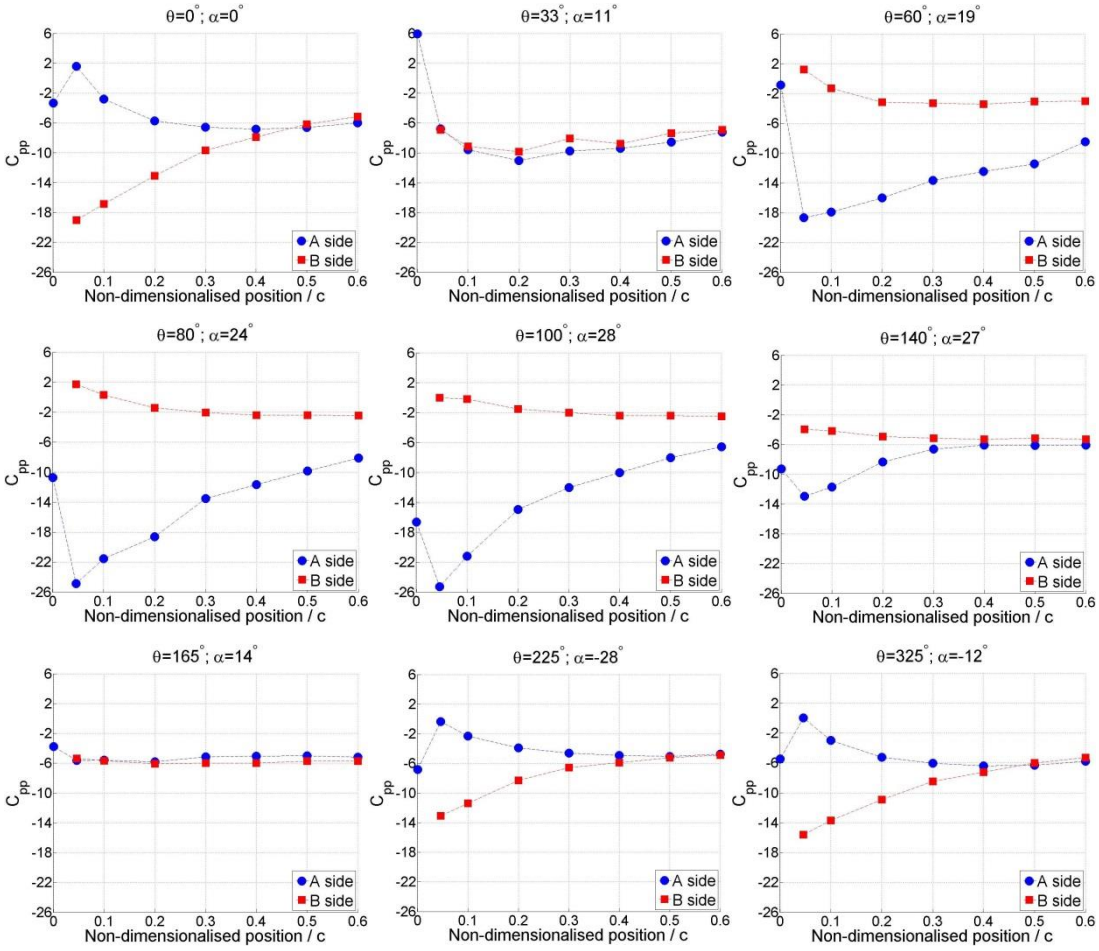

Figure 7.51 Instantaneous blade pressure measurements for the whole revolution. $\sigma = 1.0$, $\lambda = 2.0$, $V = 7\ \mathrm{m/s}$.

Since the high tip speed ratios significantly reduce the incidence range that the blade will experience, the theoretical angle of attack actually starts to decrease around $\theta = 140^{\circ}$ compared with that at $\theta = 100^{\circ}$. The measured pressure distribution also demonstrates that the blade does not stall at $\theta = 140^{\circ}$ but experiences a lower peak pressure coefficient of $C_{pp} = -13.5$ compared with $C_{pp} = -25.5$ at $\theta = 100^{\circ}$. This lower negative C_{pp} at $\theta = 140^{\circ}$ indicates lower incidence angle. Moreover the effective angle of attack becomes zero again at an azimuth angle of $\theta = 165^{\circ}$, after which the resultant

flow is incident upon the blade's **A** side as can be seen at $\theta = 225^{\circ}$ and $\theta = 325^{\circ}$. The turbine produces considerable power at this high tip speed ratio since the blade does not stall for the whole revolution and torque can be generated at all azimuth angles. However, it must be noted that the peak negative torque in the downwind region is only around $C_{pp} = -18$ which is significantly lower than that of $C_{pp} = -26$ in the upwind region. This lower peak negative pressure coefficient demonstrates that the majority of the torque is generated by the blade in the upwind region.

7.3.2 Flow physics at turbine solidities of $\sigma = 0.81$ and $\sigma = 0.67$

In this study, the turbine solidity is modified by changing the turbine radius R, in other words the length of the support arms. It must be noted that when the turbine solidity is increased the flow blockage is also increased, further increasing the flow curvature effect as was pointed out by Kirke [23]. It has been demonstrated that the curvature effect reduces the incidence angle in the upwind region where the majority of useful torque is generated. Therefore, increasing the solidity tends to move the peak power coefficient (C_p) to lower λ since the blade stall is delayed at relatively low λ due to the large blockage effect. This increased flow curvature effect at high turbine solidity is captured in this study as follows:

7.3.2.1 $\lambda = 0.5$

Instantaneous blade pressure distributions for $\sigma = 1.0$, $\sigma = 0.81$ and $\sigma = 0.67$ at the same tip speed ratio of $\lambda = 0.5$ are compared in Figure 7.52. At $\theta = 0^{\circ}$ the three solidities show similar pressure distributions. It should be noted that all three solidities indicate the blade does not experience zero incidence at the geometrical zero position due to the curvilinear flow. However when the turbine reaches $\theta = 25^{\circ}$, the blockage effect becomes apparent. $\sigma = 0.67$ shows the largest incidence followed by $\sigma = 0.81$ and $\sigma = 1.0$ demonstrates a reduced incidence angle due to the large blockage (increased curvature effect). Differences between the three solidities become clearer as the turbine rotates to $\theta = 45^{\circ}$. At this azimuth angle, the peak negative pressure coefficient for $\sigma = 0.81$ is about $C_{pp} = -11$ which is larger than that of $C_{pp} = -10$ for $\sigma = 1.0$ indicating a higher incidence angle. However the pressure distribution for $\sigma = 0.67$ illustrates the blade experiences very large incidence and a laminar separation bubble is already about to burst. The situation at $\theta = 55^{\circ}$ further demonstrates that the blade experiences reduced incidence for higher turbine solidities.

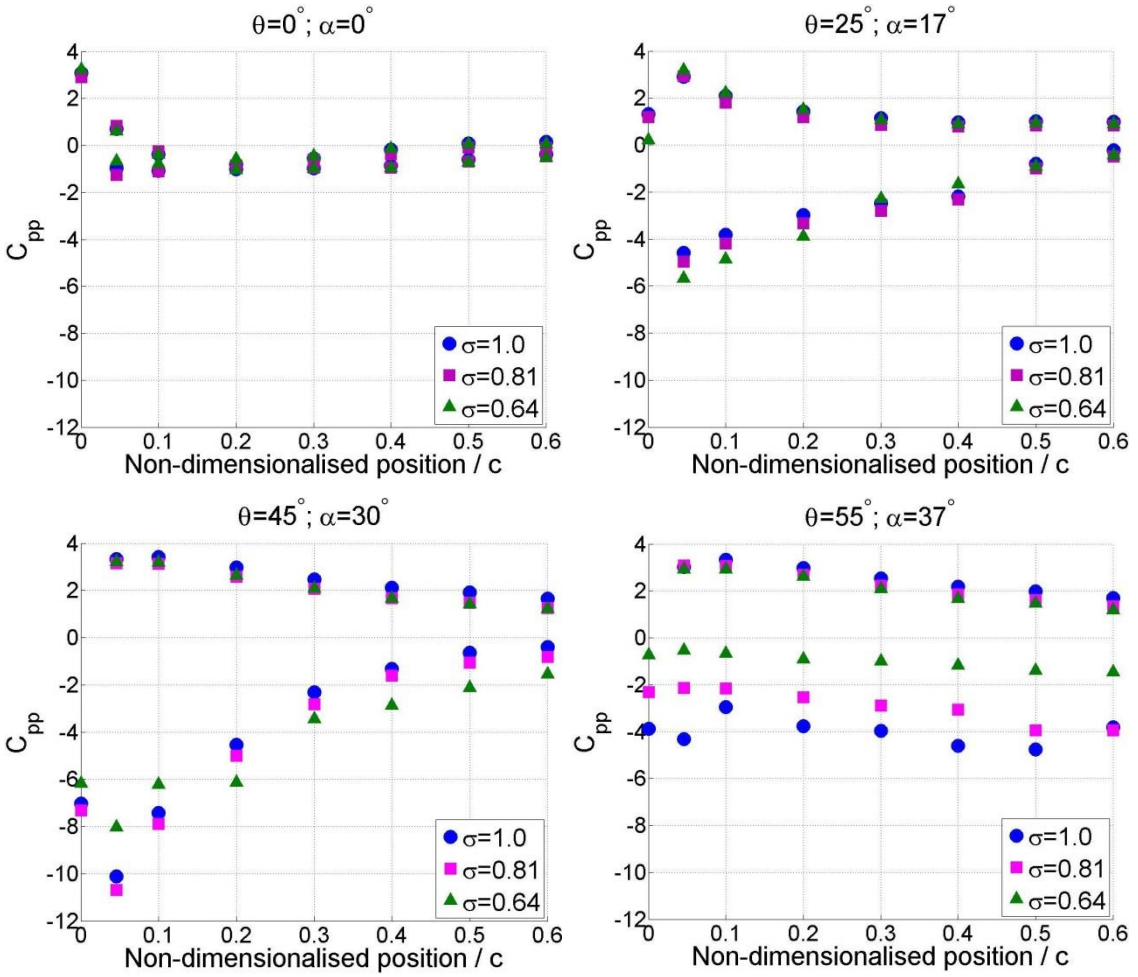

Figure 7.52 Instantaneous blade pressure measurements for three turbine solidities at $\lambda = 0.5$, $V = 7$ m/s.

The measurements show identical overall blade behaviour for all three solidities except for the increased curvature effect for turbine with higher solidity. The reduced incidence in the upwind region, resulting from the curvature effect, successfully delays the blade stall angle and enables the blade to produce more torque for a greater portion of the revolution at low tip speed ratios.

7.3.2.2 $\lambda = 1.5$

The convection of the dynamic stall vortex along the blade surface that was illustrated above for $\sigma = 1.0$ is also captured for $\sigma = 0.81$ and $\sigma = 0.67$ at this medium tip speed ratio as can be seen in Figure 7.53. The only difference is that this convection occurs earlier in the upwind region for $\sigma = 0.81$ and $\sigma = 0.67$ due to lower blockage. For example, at $\theta = 90^{\circ}$ the dynamic vortex exists at approximately $0.35c$ for the turbine of $\sigma = 0.67$. In contrast, the laminar separation bubble still attaches on the

blade leading edge for turbines of $\sigma = 1.0$ and $\sigma = 0.81$ and there is no dynamic stall vortex formed due to the reduced incidence. Moreover at $\theta = 100^{\circ}$, the pressure measurement illustrates the dynamic stall vortex for $\sigma = 0.81$ traverses faster than that for $\sigma = 1.0$ while the vortex for $\sigma = 0.67$ is already shed into the wake.

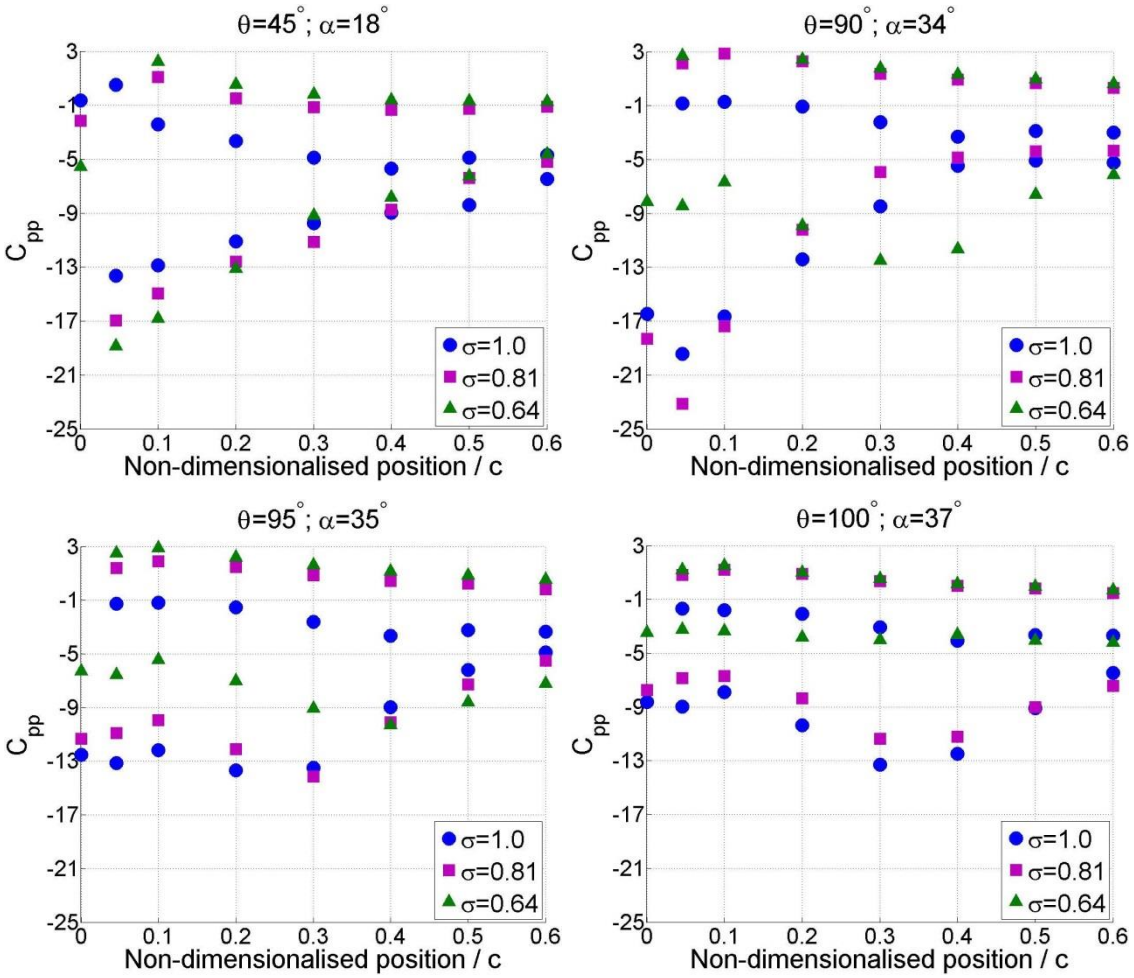

Figure 7.53 Instantaneous blade pressure measurements for three turbine solidities at $\lambda = 1.5$, $V = 7$ m/s.

At this medium tip speed ratio, the pressure measurement under the three different solidities examined also demonstrated similar overall blade behaviour. The increased curvature effect resulting from the larger flow blockage seems to shift the effective blade behaviour to a lower azimuth angle. On the contrary, blades under low blockage (low solidity, low curvature effect) seem to experience the equivalent flow at larger azimuth angles.

7.3.2.3 $\lambda = 2.0$

At the high tip speed ratio of $\lambda = 2.0$, the blade illustrates similar overall behaviour for all three different turbines. The blade no longer stalls for the whole revolution and produces torque in both the upwind and downwind regions. However, as shown in Figure 7.54, the blade overall behaviour of $\sigma = 0.67$ seems to be shifted forward in terms of azimuth angle and the peak negative pressure coefficient is larger than that of $\sigma = 0.81$ at $\theta = 60^{\circ}$ and at $\theta = 80^{\circ}$. In contrast, for the blade of $\sigma = 1.0$ the pressure distribution seems to be shifted backward in terms of azimuth angle compared with that of $\sigma = 0.81$. The pressure measurement for the three solidities at the same rational speed of $\lambda = 2.0$ further confirms that the increased curvature effect for the large blockage (high solidity) condition reduces the incidence angle that the blade experiences in the upwind region. This reduced incidence angle however at this high tip speed ratio will result in less overall power/torque generated by the blade since the blade no longer experiences stall during the whole revolution.

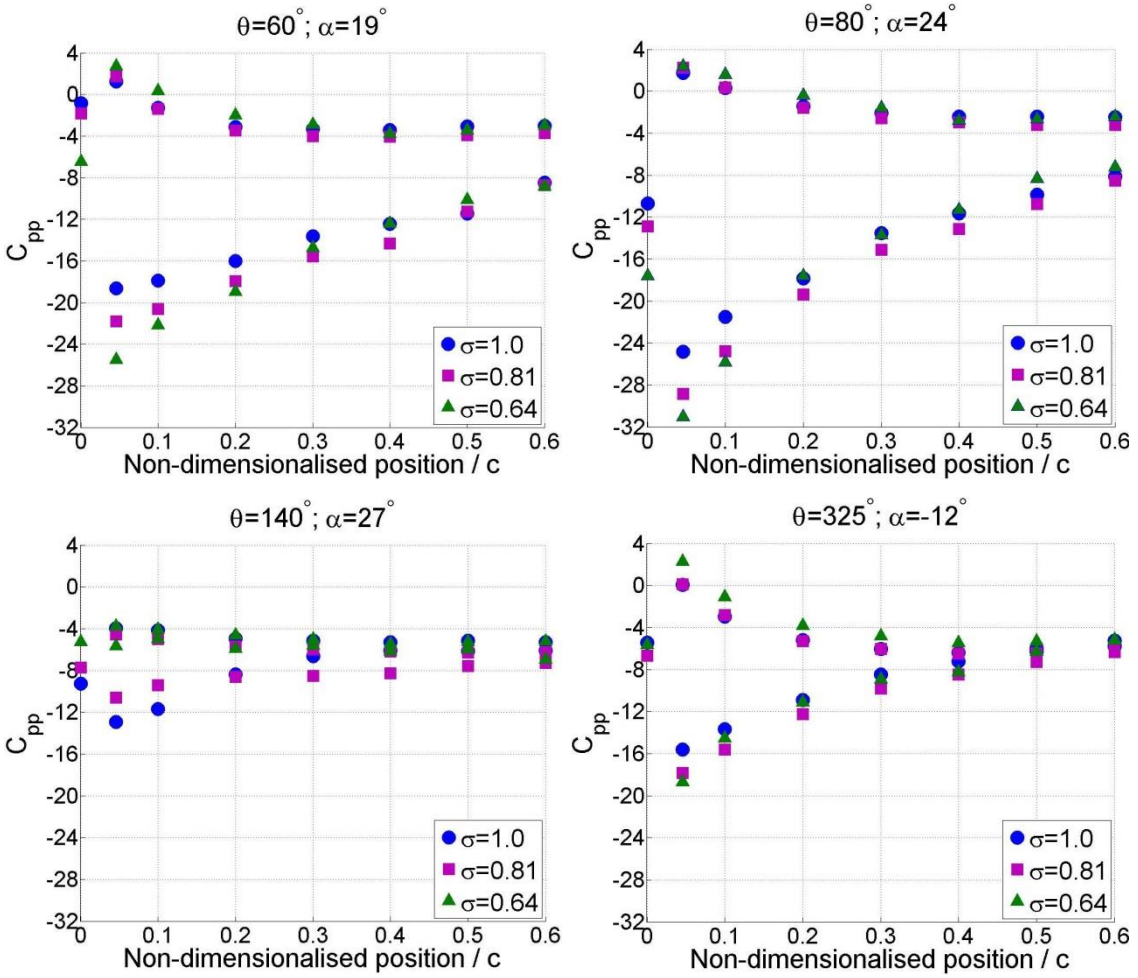

Figure 7.54 Instantaneous blade pressure measurements for three turbine solidities at $\lambda = 2.0$, $V = 7$ m/s.

7.3.3 Conclusion

The on-board pressure measurement technique was successfully employed to measure the instantaneous blade pressure distribution and its variation during the rotation. Dynamic stall and laminar separation bubbles were clearly captured along with the flow curvature effect. Furthermore, the convection of the dynamic stall vortex along the blade surface at large reduced frequency (high tip speed ratio) was also clearly recorded. To the best of the author's knowledge, this is the first time that this technique has been used in the study of H-Darrieus wind turbines.

The following conclusions can be drawn based on the measurements:

- A symmetrical blade moving in a curved path has the same aerodynamic characteristics as a cambered aerofoil moving in a rectilinear flow field with a virtual angle of incidence. The experimental results indicate the curvature effect will not affect the blade overall behaviour but just shift the behaviour forward or backward in terms of azimuth angle.
- The curvature effect increases with the increase of turbine solidity and tip speed ratio. Blade incidence angles in the upwind region are reduced due to the curvature, leading to a delayed stall and better performance at low λ. However, since the blade will no longer experience stall at high λ, this reduced incidence angle in the upwind region results in less torque generated by the blade at high turbine solidity.
- The instantaneous pressure measurements indicate that the dynamic stall vortex can only convect along the blade surface at large reduced frequency (high tip speed ratios). At low tip speed ratio (or low turbine solidity), the vortex strength is too low to attach and convect along the surface.

Chapter 8

Bio-inspired blades with tubercle leading edges

The humpback whale is exceptional among the large baleen whales in its ability to undertake aquabatic manoeuvres to catch prey [173, 174]. Humpback whales utilise extremely mobile, wing-like flippers for banking and turning [173, 174]. Large rounded tubercles along the leading edge of the flipper (see Figure 8.1) are morphological structures that are unique in nature [175]. It is suggested that the tubercles on the leading edge act as passive-flow control devices that enhance lift force and allow flow to remain attached for a larger range of attack angles, thus delaying stall [176]. The physics of delaying stall by the tubercles has been studied by many authors (e.g. [172, 176-180]). One explanation is the generation of streamwise vortices since the flow is sheared into the trough's centre. These vortices are convected along the chord and the spanwise arrangement of vortices is in a pair on each side of the tubercle crest with opposite spins. The tangential velocities of the inward facing flows of the pair of vortices are directed toward the trailing edge of the wing section. The flow from the tubercle peak is accelerated posteriorly due to the interaction with the vortex pair. These effects prevent the local boundary layer downstream of the tubercles from separating and push the stall line further toward the trailing edge.

Figure 8.1 Photographs of humpback whales' flippers with tubercle leading edge from [175]

According to the double multiple streamtube (DMST) model study performed in this study, blades with a gradual stall behaviour are able to improve turbine performance especially at low tip speed ratios. Therefore it is thought that a blade with

a tubercle leading edge is a very promising candidate to improve turbine self-starting capability since those tubercles might alter the flow-field at the leading edge resulting in gradual blade stall behaviour.

Hansen et al. [172] performed static wind tunnel measurements by using a NACA0021 blade with tubercle leading edges at $Re = 120{,}000$, which is comparable to the blade Reynolds number experienced by small-scale H-Darrieus wind turbine. The force measurements were undertaken in an open section of the $0.5\ \text{m} \times 0.5\ \text{m}$ open-return wind tunnel for different combinations of wavelength (ζ) and amplitude (A) as defined in Figure 8.2. The tested amplitudes were $A = 2\ \text{mm}\ (0.03c)$, $A = 4\ \text{mm}\ (0.06c)$ and $A = 8\ \text{mm}\ (0.11c)$ and the corresponding wavelengths were$\zeta = 7.5\ \text{mm}\ (0.11c)$, $\zeta = 15\ \text{mm}\ (0.21c)$ and $\zeta = 30\ \text{mm}\ (0.43c)$ respectively. According to their study [172], the tubercles at the blade leading edge increase the lift performance in the post-stall regime for all cases but at the expense of degraded lift performance in the pre-stall regime as shown in Figure 8.3. Nevertheless, they found that through optimising the amplitude and wavelength of the tubercles, it was possible to improve the pre-stall lift performance making it close to the values attained by the unmodified NACA0012 profile [172].

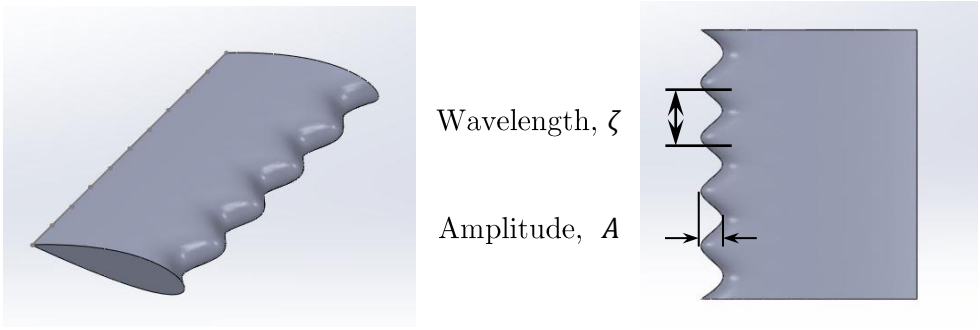

Figure 8.2 Definition of tubercle Wavelength, ζ and Amplitude, A

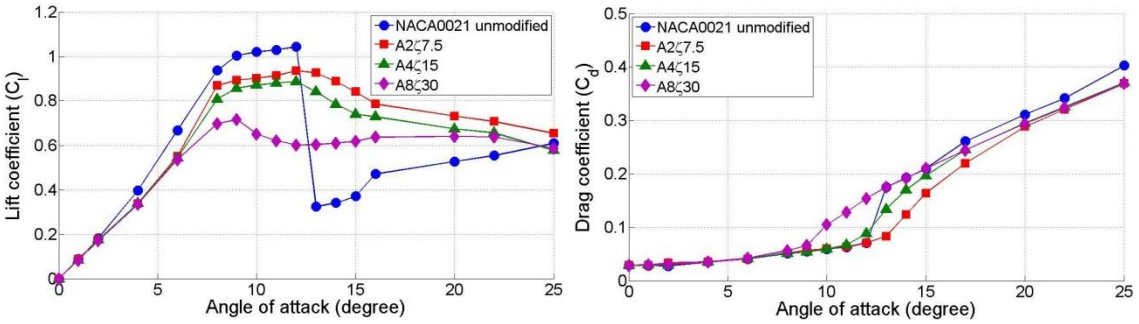

(a) (b)

Figure 8.3 Static wind tunnel measurement of NACA0021 compared with modified tubercle leading edge at $Re = 120{,}000$ [172].

As can be seen in Figure 8.3, the tubercle, $A2\zeta7.5$, presents the best combination showing only slightly lower lift force in the pre-stall regime. There is negligible difference in the drag coefficient for the $A2\zeta7.5$ profile in the pre-stall regime compared to the unmodified profile. However, a marked improvement is observed for both lift and drag in the post-stall regime for $A2\zeta7.5$ profile.

The enhanced lift and lower drag characteristics at post-stall are beneficial for aerofoils (or blades) operating near stall or post-stall. Therefore, blades with tubercle leading edges are very promising candidates for the H-Darrieus wind turbine. They might significantly improve turbine self-starting capability and reduce self-starting time. This hypothesis is tested using BEM and experimental studies in this chapter.

8.1 BEM study

In order to examine the above hypothesis, tests were first conducted using the DMST model. Two datasets were examined: the first one is the modified blade sudden stall dataset based on the original Sheldahl and Klimas' dataset (referred to as the 'sharp stall data'). The second one is the blade with tubercle leading edge dataset (referred to as the 'tubercle data') as shown in Figure 8.4. In order to mimic the tubercle effects according to Hansen et al.'s measurement, the lift force of the tubercle blade at pre-stall regime is lower than that of the sharp stall dataset but the post-stall performance has a more gradual stall behaviour. Lift coefficients after $\alpha > 25^{\circ}$ were kept the same for both blades. Although Hansen et al.'s study [172] illustrates the blade drag is also improved by the tubercles at post-stall regime (see Figure 8.3 (b)), no modification was performed for drag in this study.

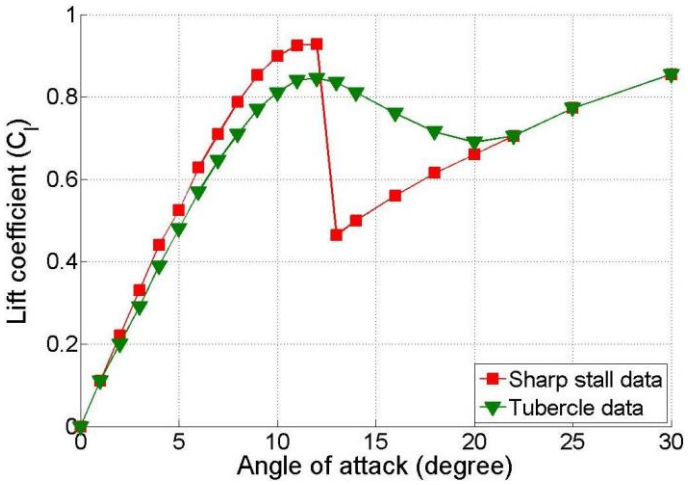

Figure 8.4 NACA0018 sharp stall data modified from original Sheldahl and Klimas' measurement [62] and tubercle data with a gradual stall behaviour. $Re = 360{,}000$.

Results are presented in Figure 8.5 where Figure 8.5 (b) is enlarged to show more clearly the C_p~λ data from Figure 8.5 (a). As can be seen, the tubercle dataset demonstrates a significant improvement of power output at low tip speed ratios of $\lambda < 4$, which enhances the turbine self-starting capability. The turbine peak C_p and performance at high tip speed ratios predicted by the tubercle dataset is slightly lower than the sudden stall dataset since the blade at high λ will no longer stall and the pre-stall lift force for the tubercle blade is lower.

The slightly lower lift for the tubercle blade at pre-stall incidence angle is offset by the considerably enhanced lift performance at post-stall regime, which consequently results in more torque (and power) generated by the turbine blade over a complete revolution at low λ.

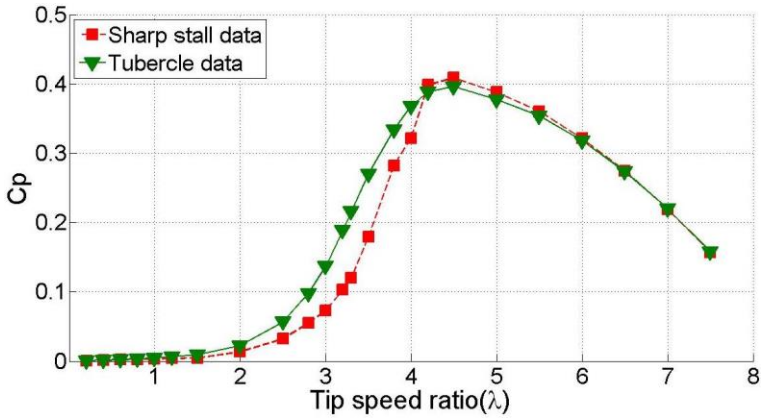

(a)

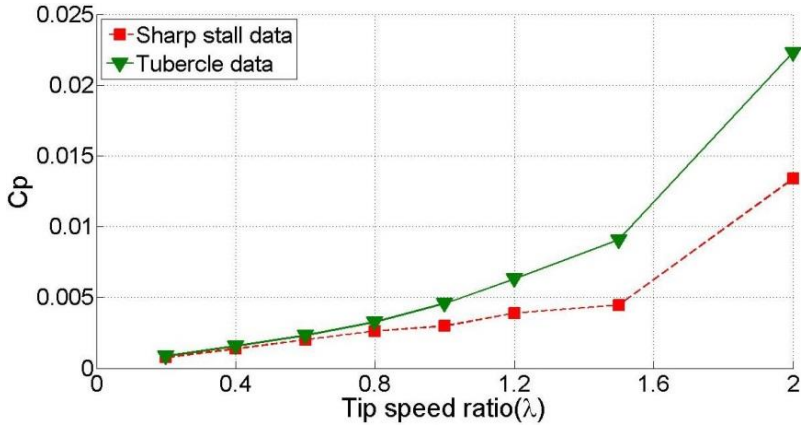

(b)

Figure 8.5 Prediction of turbine performance using sharp stall data and tubercle data

In conclusion, this DMST study confirms that blades with tubercle leading edges can further enhance the H-Darrieus turbine self-starting capability by modifying the blade sudden stall behaviour to a more gradual and smooth stall. The slightly degraded turbine performance with tubercle blades at high λ is compensated by a turbine that

self-starts quickly (although the improvement depends on the number of starts as mentioned by Worasinchai et al. [152]). The DMST results are supported by the experimental measurements performed in this study which are detailed in following the section.

8.2 Experimental study

The bio-inspired tubercle leading edge blade is able to improve the NACA0021 blade post-stall characteristic by creating a gradual stall behaviour instead of the original sudden stall as demonstrated by Hansen et al. [172]. The BEM simulation performed in this study supports the above hypothesis showing higher C_p predicted at low tip speed ratios for turbines with tubercle leading edge blades. In order to experimentally prove the above hypothesis and provide solid conclusions, three blades with tubercle leading edges (amplitude A$= 2$ mm and wavelength $\zeta = 7.5$ mm) were built and tested. The manufacture process and details are described in Chapter 6.3.1. The modification was only made at $0 \leq x \leq 0.3c$, the remaining trailing part of the blade ($0.3c < x \leq 1.0c$) was kept the same as the standard NACA0021. The blade span was chosen to be $S = 600$ mm as described in Chapter 6.3.1, resulting in an aspect ratio of $AR = 6$. Testing parameters are summarised in Table 8.1.

Blade	Solidity	V	c	m	AR
NACA0021 with tubercle leading edge	$\sigma = 1.0$; $\sigma = 0.81$; $\sigma = 0.67$	6 m/s and 7 m/s	100 mm	445 g	6
NACA0021	$\sigma = 1.0$; $\sigma = 0.81$; $\sigma = 0.67$	6 m/s and 7 m/s	100 mm	395 g	6

Table 8.1 Parameters for studies of turbine with tubercle leading edge blades. m is the mass of the blade.

The experimental results for blades with tubercle leading edges are compared with those for standard NACA0021 blades ($AR = 6$). Although it was demonstrated in the previous chapter that the turbine cannot self-start with NACA0021 of $AR = 6$, the tubercle leading edge blades clearly illustrate a considerable improvement in turbine performance since the turbine successfully self-started under $\sigma = 1.0$ and $\sigma = 0.81$ as shown in Figure 8.6 (a) and Figure 8.7 (a). It must be noted that the system inertia for NACA0021 with tubercle leading edges is also about 5% larger than the system with standard NACA0021. Nevertheless, the NACA0021 with the tubercle leading edges

produced significantly more positive torque than the standard NACA0021 at low tip speed ratios resulting in a much faster turbine initial acceleration. Meanwhile the turbines of $\sigma = 1.0$ and $\sigma = 0.81$ reach the maximum rotational speed approximately 105 s and 195 s respectively which is fast considering the blade aspect ratio is just $AR = 6$ and the increased system inertia. For the lowest turbine solidity of $\sigma = 0.67$, blades with tubercle leading edges still show improved performance compared with standard NACA0021 although the turbines fail to self-start in both cases (Figure 8.8).

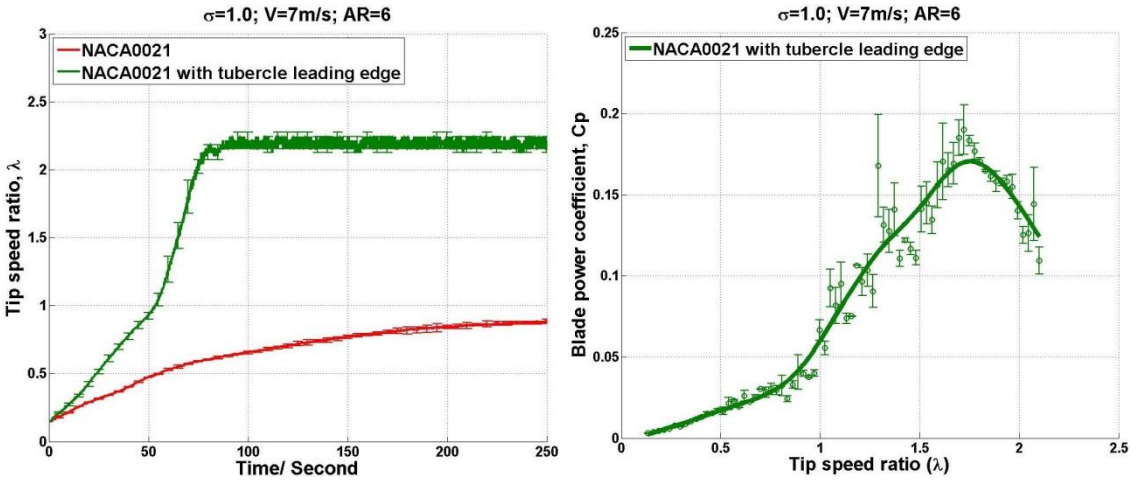

(a) (b)

Figure 8.6 Turbine performance for standard NACA0021 blade and NACA0021 with tubercle leading edge. $V = 7$ m/s, $\sigma = 1.0$. (a) Self-starting, time-varying results. (b) $C_p \sim \lambda$ curve.

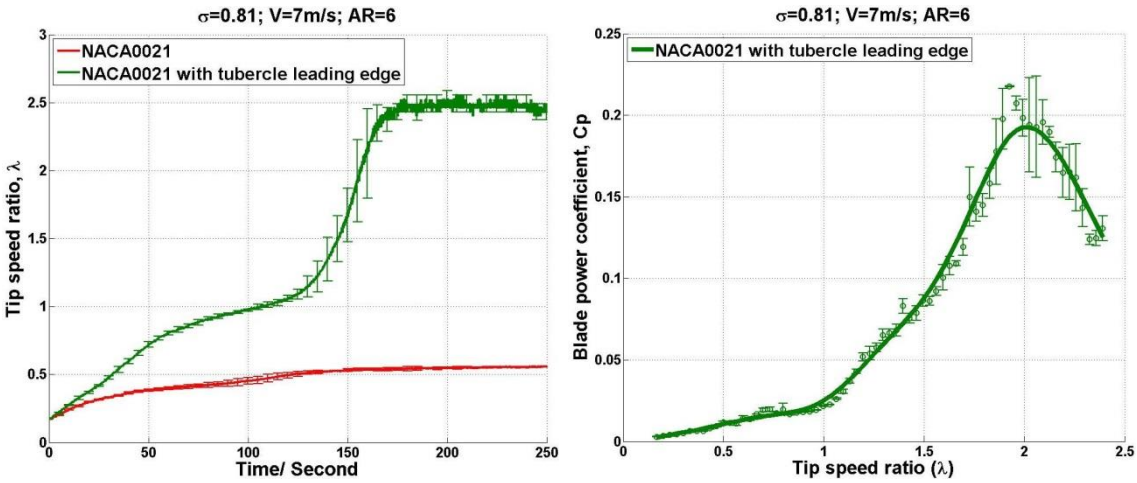

(a) (b)

Figure 8.7 Turbine performance for standard NACA0021 blade and NACA0021 with tubercle leading edge. $V = 7$ m/s, $\sigma = 0.81$. (a) Self-starting, time-varying results. (b) $C_p \sim \lambda$ curve.

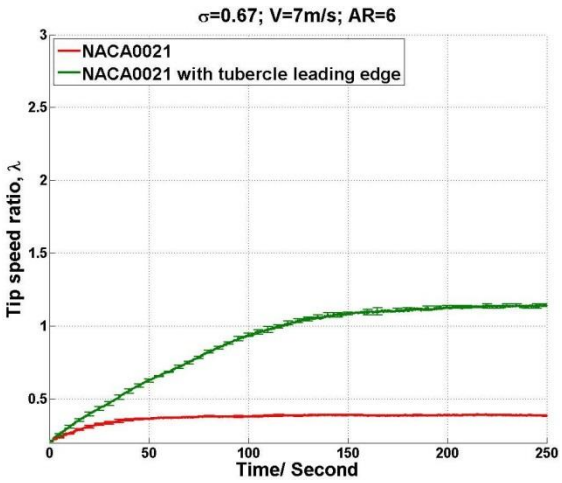

Figure 8.8 Turbine self-starting, time-varying results for standard NACA0021 blade and NACA0021 with tubercle leading edge. $V = 7\ \mathrm{m/s}$, $\sigma = 0.67$.

In terms of power coefficient C_p, the maximum value is about $C_p = 0.17$ and $C_p = 0.19$ for $\sigma = 1.0$ and $\sigma = 0.81$ respectively as shown in Figure 8.6 (b) and Figure 8.7 (b). Since the standard NACA0021 with $AR = 6$ fails to self-start, no direct comparison can be made. However based on static wind tunnel measurements performed by Hansen et al. [172], it is assumed that the maximum C_p for the tubercle blade will be slightly lower than the standard NACA0021(if the turbine with standard NACA0021 can self-start) since the improved post-stall behaviour is achieved at the expense of lower lift force at low incidence angles.

If comparing the turbine performance for tubercle blades of $AR = 6$ with standard NACA0021 blades of $AR = 7$, the tubercle blades still demonstrate good performance with only approximately 20% increase in self-starting time and 20% reduction of peak C_p. It must be noted that the turbine with standard NACA0021 blades of $AR = 6$ fails to self-start or produce any useful power.

According to the experimental results, those small tubercles at the blade leading edge successfully improve the blade post-stall behaviour resulting in more torque generated at a greater portion of the revolution, especially at turbine low tip speed ratios. It is thought that the tubercles work as passive-flow control devices which delay the stall and change the blade stall behaviour from a sudden stall to a more beneficial gradual characteristic. Moreover based on the study of on-board pressure measurement presented in Chapter 7.3.1.2, the dynamic vortices convect along the blade surface only at large reduced frequency, which delays the blade stall and enables more torque to be generated. Therefore proper tubercle distribution at the blade leading edge might significantly increase the local flow unsteadiness and 'manually' produces many vortices

at the blade leading edge during the turbine's rotation. Although at turbine low tip speed ratios the calculated reduced frequency ($k = \frac{c}{D}\lambda$) is low, this increased local blade unsteadiness and reduced frequency would enable those vortices formed at the blade leading edge to attach and convect along the blade surface and finally delay the stall resulting in improved turbine performance.

One possible argument for this study is that the surface roughness of the blade with tubercle leading edge is different from the standard NACA0021. This different surface roughness might be responsible for the different blade performance. However, as shown in Chapter 7.2.5, by modifying the blade surface roughness the turbine performance will be either improved or degraded only slightly. It is not believed that the surface roughness will lead to such a tremendous turbine performance change as measured in this chapter.

All in all, the blades with tubercle leading edges (with appropriate wave length and amplitude) are beneficial to an H-Darrieus wind turbine designed to achieve self-starting. The measurements for wind speed $V = 6\,\mathrm{m/s}$ are presented in Figure 8.9, Figure 8.10 and Figure 8.11 for completeness.

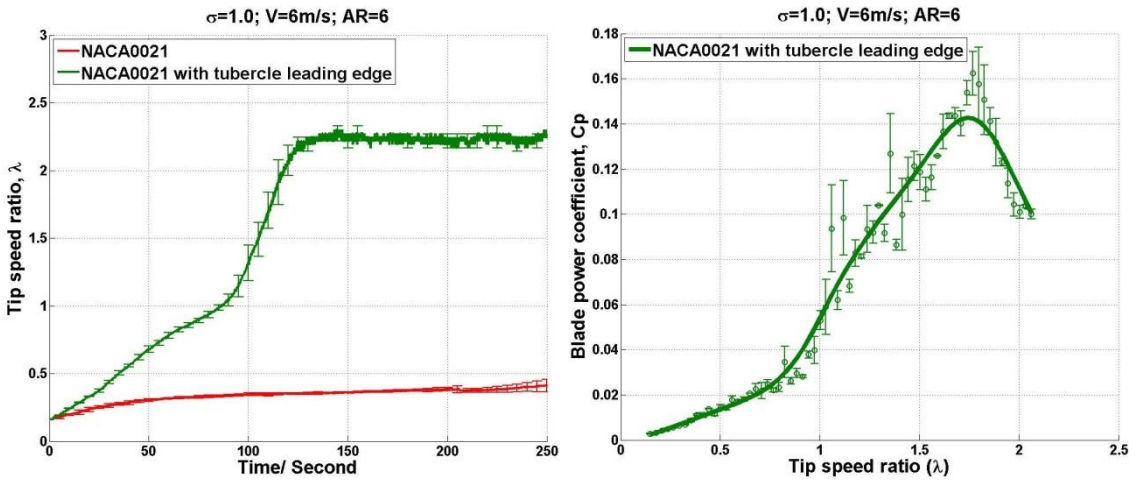

(a) (b)

Figure 8.9 Turbine performance for standard NACA0021 blade and NACA0021 with tubercle leading edge. $V = 6\,\mathrm{m/s}$, $\sigma = 1.0$. (a) Self-starting, time-varying results. (b) $C_p \sim \lambda$ curve.

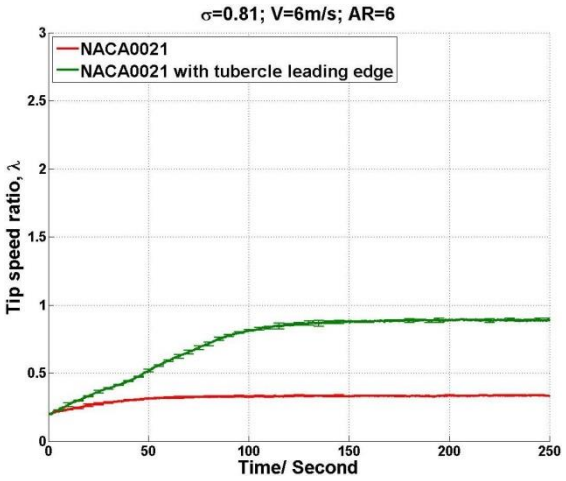

Figure 8.10 Turbine self-starting, time-varying results for standard NACA0021 blade and NACA0021 with tubercle leading edge. $V = 6\ \mathrm{m/s}$, $\sigma = 0.81$.

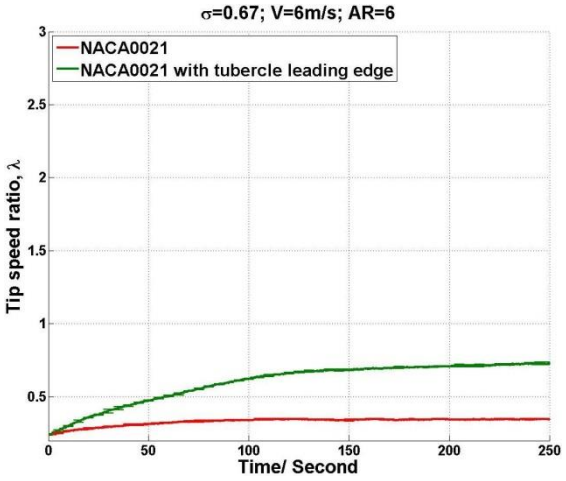

Figure 8.11 Turbine self-starting, time-varying results for standard NACA0021 blade and NACA0021 with tubercle leading edge. $V = 6\ \mathrm{m/s}$, $\sigma = 0.67$.

8.3 Conclusion

Bio-inspired blades with tubercle leading edges are demonstrated experimentally and numerically to be beneficial for a turbine designed to achieve self-starting. The locally increased unsteadiness and the reduced frequency resulting from those tubercles might enable the dynamic vortex to attach and convect along the blade's surface and change the blade sudden stall behaviour into a gradual stall. This tubercle design can be widely used in commercial H-Darrieus wind turbines without bringing significant extra cost since the modification is limited to the blade's leading edge. More detailed studies are worth performing in the future to examine the benefits that could be gained from tubercle blades.

Following the work described in the chapter a UK patent (GB2451670) by Joseph Emans [181] was discovered. The patent does not however contain any reference to experimental work and to the best of the author's knowledge this chapter represents the first tests on such a configuration.

Chapter 9

Conclusions and recommendations

The ultimate goal of this thesis was to examine small-scale H-Darrieus wind turbine performance at low tip speed ratios. Since the majority of studies in the literature focus on turbine peak power output and turbine performance at relatively high tip speed ratios, very limited data (especially experimental data) were available illustrating the turbine performance at low tip speed ratios. A series of experimental tests and simulations has been carried out in order to examine how different design parameters affect the turbine self-starting capability and overall performance. This chapter summarises the main findings and contributions from this study. Recommendations for future work are also provided.

9.1 Conclusions

9.1.1 CFD model for studying H-Darrieus wind turbines

The 2-D H-Darrieus wind turbine model with transition SST turbulence was demonstrated to be able to capture the overall turbine performance trend in terms of power coefficient C_p against λ. However, compared with the experimental measurements performed under the same testing condition, the 2-D results significantly over-predicted the turbine performance, especially at high tip speed ratios. This over-prediction was mainly due to the ignoring of blade tip loss, which significantly degraded the blade performance in 3-D. Moreover, the discrepancies observed at relatively low λ resulted from the incapability of the CFD model to accurately predict the blade performance in the deep-stall region. This was clearly shown in the 2-D static aerofoil study (using the transition SST turbulence model) as the CFD prediction failed to match those data from static wind tunnel measurements at similar Reynolds numbers.

Although discrepancies were noticed between 2-D CFD model and experimental measurements, CFD is able to examine a number of blade profiles without the need for a blade aerodynamic database and can visualise the flow structure. Therefore, it provides a useful tool to get a first insight into the turbine performance under different design parameters.

9.1.2 BEM model for studying H-Darrieus wind turbines

Two blade element momentum (BEM) based models were built in order to examine the H-Darrieus wind turbine performance. However a common problem for BEM based models is that they require an accurate aerodynamic dataset over the whole incidence range and at an appropriate Reynolds range, which is scarce in the literature. Therefore, static wind tunnel measurements were performed and correction factors were applied to correct the blockage effects. An aerofoil second-stall behaviour at relatively large angles of attack was also captured under the low blockage testing condition. Further studies demonstrated that this second-stall was due to the flow separation point near the leading edge switching from the suction side to the pressure side of the aerofoil resulting in a significant flow change in the wake. However, in a closed-jet tunnel (large blockage testing condition) the wake behind the aerofoil was restricted by the solid boundary leading to a much smaller change in the wake structure. Therefore no second-stall was captured in the closed-jet tunnel. With regard to aerofoil/blade torque, it was found that this second-stall behaviour does not result in a sudden change of torque force since the lift and drag decrease or increase simultaneously.

The Start-Up model, which employed the static aerodynamic dataset as the model input, successfully replicated the turbine self-starting process when compared with experiments. Further studies illustrated that for a given turbine solidity, a larger combination of turbine radius (R) and blade chord length (c) is beneficial to a turbine designed to achieve self-starting despite the system inertia and resistance being increased. This conclusion was later supported by the experimental tests performed.

The double multiple streamtube model (DMST) that was created indicated that blade with a gradual stall behaviour instead of sudden stall is able to significantly improve turbine performance at low λ and therefore improves turbine self-starting capability. Based on this finding, the blade with a tubercle leading edge was proposed and tested experimentally. Results supported the DMST conclusion.

It was demonstrated that the BEM based model was highly sensitive to the accuracy of the aerodynamic database used as input. Differences that arise from measurements in different wind tunnel facilities may result in significantly different predictions. Therefore, the acquisition and publication of extensive, high quality data over the full-range of incidence and at appropriate Reynolds range must be a high priority if the turbine performance is to be predicted accurately.

9.1.3 How to design an H-Darrieus wind turbine that can self-start

An H-Darrieus wind turbine will lose most of its advantages compared with a HAWT if it cannot self-start or requires external power to start-up. Therefore a number of design parameters were examined in order to answer the question of how to design an H-Darrieus wind turbine that can self-start. The conclusions according to all the tests performed are summarized here:

- Choose a three-bladed turbine rather than two-bladed or one-bladed.
- Choose a relative high turbine solidity. A balance must be struck between stronger self-starting capability and larger peak power output.
- For a given solidity, choose larger combinations of R and c (if n is a constant).
- The traditional symmetrical NACA aerofoil series with large thickness are good choices while it seems that the cambered blade does not bring any benefit.
- With a relatively high turbine solidity, blades with rough surfaces are preferred although the peak power output is slightly degraded.
- A slightly negatively pitched blade ($\beta > -2^{\circ}$) is preferred.
- The blade aspect ratio should be maximised (under the premise of structural strength). The suggested value is at least $AR \geq 7$.
- Blades with tubercle leading edges are preferred since they improve the blade performance significantly at low λ.

9.1.4 Dynamic stall, laminar separation and curvature effects

The on-board pressure measurement technique was employed for the first time in studying an H-Darrieus wind turbine. The instantaneous blade pressure distribution and variation were successfully captured and recorded. The pressure measurement demonstrated that in the upwind region the dynamic stall effect considerably delays the blade stall compared with that measured in static wind tunnel tests. Moreover, in the downwind region the dynamic stall effect also delays the onset of flow reattachment. The flow only reattaches on the blade surface at a low enough incidence angle.

A laminar separation bubble was clearly illustrated by the on-board pressure measurements. The bubble forms at the blade trailing edge at low incidence and travels upwards with the increase of incidence. Meanwhile the bubble size is reduced. The burst of the laminar separation bubble results in the stall of the blade at relatively low λ. However at high λ due to the increased reduced frequency ($k = \frac{c}{D}\lambda$), a new dynamic stall vortex is formed at the blade leading edge after the burst of the laminar separation bubble and this dynamic stall vortex convects along the blade with the

increase of incidence. The convection of the dynamic stall vortex delays the stall and allows the blade to produce more torque over a greater portion of the revolution. With regard to blades with the tubercle leading edges, although the turbine reduced frequency is low at relative low λ, the local unsteadiness and reduced frequency might be increased due to the tubercles which successfully enable the dynamic stall vortex to attach and convect along the blade surface which significantly improves the turbine performance at low λ.

The flow curvature effect was also recorded by the on-board pressure measurements. It is demonstrated that the increase of the turbine solidity or tip speed ratio λ will increase the flow curvature. The flow curvature will reduce the incidence angle experienced by the blade in the upwind region leading to a delayed stall and more torque generated for a greater portion of the revolution.

9.1.5 Significant and original contributions

This study has furthered the understanding of H-Darrieus wind turbine behaviour. Various turbine design parameters were studied by both experiments and simulations, and the underlying physics were properly explained. Moreover, a large number of experimental data including both turbine self-starting, time-varying results and $C_p \sim \lambda$ curves were presented in order to provide solid conclusions and guide the design of the H-Darrieus wind turbine. It must be noted that these experimental data are scarce in the literature. Special attention was paid to turbine performance at low tip speed ratios and turbine self-starting capability in order to fill the gaps in the literature.

Comprehensive and high quality aerofoil static aerodynamic databases at low Reynolds numbers were presented. The associated aerofoil behaviour under these low Reynolds numbers was explained. These databases (Appendix B and C) provide the fundamental basis for studying the H-Darrieus wind turbine by using blade element momentum (BEM) models. Furthermore, these databases can also be widely used for many other relevant studies at similar Reynolds numbers.

The on-board, time-accurate pressure measurement was employed for the first time to study the H-Darrieus wind turbine. It is demonstrated that this system is able to capture the blade behaviour even at the very fast rotational speeds. The instantaneous blade pressure distribution and its variation were accurately recorded by the on-board pressure measurement system, which is extremely difficult to measure using more traditional methods. This study provides new unsteady data to increase knowledge and understanding of the complicated aerodynamics of the H-Darrieus wind turbine.

Bio-inspired blades with tubercle leading edges were tested on the H-Darrieus wind turbine for the first time. It is demonstrated that blades with tubercle leading edges can significantly improve turbine self-starting capability.

9.2 Future work

9.2.1 CFD model improvement

Although the 2-D CFD model implemented in this study successfully captured the overall turbine performance in terms of $C_p \sim \lambda$ curve, ignoring the blade tip loss resulted in significant discrepancies at high tip speed ratios compared with experimental results. Therefore, a key improvement in accurate predicting of turbine performance might be achieved by employing a 3-D CFD model.

9.2.2 Aerofoil/blade aerodynamic database

More aerofoil static wind tunnel measurements should be performed at low Reynolds numbers in order to provide the fundamental data to study the H-Darrieus machine by using BEM methods. The database should be extensive, high quality and over the full incidence range.

9.2.3 Blades with tubercle leading edges

Blades with tubercle leading edges significantly improve the turbine performance at low tip speed ratios. One reasonable explanation for the improvement is that the local unsteadiness and local reduced frequency are increased by the tubercles resulting in the convection of the vortex (formed at the blade leading edge) along the blade surface. The vortex convection delays the blade stall and enables the blade to produce more torque in a greater portion of the revolution. However, more direct studies about blades with tubercle leading edges should be performed to provide solid conclusions about the blade behaviour. Alternative passive methods that modify the blade sudden stall behaviour to a more gradual stall could be explored in the future.

9.2.4 On-board pressure measurement

The quality of the on-board pressure measurement system employed in this study was mainly limited by the number of channels of the pressure scanner. Improvements could be achieved by applying pressure scanners with more channels in order to display the pressure variation in more details.

9.2.5 Particle Image Velocimetry (PIV) study

The Particle Image Velocimetry technique could be employed together with the on-board pressure measurement system in the future to provide synchronised pictures and flow structure data.

References

1. Johansson, T.B., Kelly, H., Reddy, A.K.N., Williams, R.H., *1993, Renewable Energy: sources for fuels and electricity.* Island Press, Washington D.C.

2. Leventhall, G., *2005, Wind Turbine Noise: Perspective for Control.* DEWI Magazin Nr. 27: p. 60-61.

3. Union, E., *2010, Directive 2010/31/EU of the European parliament and of the council on the energy performance of buildings* Official Journal of the European Union.

4. MacDonald, M., *2003, The Carbon Trust & DTI Renewable Energy Network Impact Study Annex 1:Capacity Mapping & Market Scenarios for 2010 and 2020.* The Carbon Trust & DTI.

5. Bertenyi, T., Wickins, C., and Mcintosh, S.C., *2010, Enhanced Energy Capture Through Gust-Tracking in the Urban Wind Environment.* 48th AIAA Aerospace Sciences Meeting Including the New Horizons Forum and Aerospace Exposition, Paper No. AIAA 2010–1376, 4 - 7 January, Orlando, Florida.

6. Edwards, J.M., Danao, L.A., and Howell, R.J., *2012, Novel Experimental Power Curve Determination and Computational Methods for the Performance Analysis of Vertical Axis Wind Turbines.* Journal of Solar Energy Engineering. **134**(3).

7. Worasinchai, S., *2012, Small Wind Turbine Starting Behaviour.* PhD Thesis, School of Engineering and Computing Science, University of Durham.

8. Bos, R., *2012, Self-starting of a small urban Darrieus rotor.* Master of Science Thesis, Delft University of Technology.

9. Kentfield, J.A.C., *1996, The Fundamentals of Wind-driven Water Pumpers.* 1st ed., Taylor and Francis, London, ISBN 2884492399.

10. Baker, J.R., *1983, Features to Aid or Enable Self Starting of Fixed Pitch Low Solidity Vertical Axis Wind Turbines.* Journal of Wind Engineering and Industrial Aerodynamics. **15**(1-3): p. 369-380.

11. Hill, N., Dominy, R.G., Ingram, G., and Dominy, J., *2008, Darrieus Turbines: the Physics of Self-starting.* Proceedings of the Institution of Mechanical Engineers, Part A: Journal of Power and Energy. **223**: p. 21-29.

12. Dominy, R.G., Lunt, P., Bickerdyke, A., and Dominy, J., *2007, Self-Starting Capability of a Darrieus Turbine.* Proceedings of the Institution of Mechanical Engineers, Part A: Journal of Power and Energy. **221**(1): p. 111–120.

13. Mays, I., and Musgrove, P.J., *1979, Performance of the Variable Geometry Vertical Axis Wind Turbine at High and Low Solidities.* Multi-Science Publishing Co., Ltd., London: p. 48-56.

14. Worasinchai, S., Ingram,G.L., and Dominy, R.G., *2012, The physics of H-Darrieus turbine self-starting capability: flapping-wing perspective* Proceedings of ASME Turbo Expo, Copenhagen, Denmark, June 11-15, Paper No. GT2012-69075, pp. 869-878.

15. Sheldahl, R.E., Klimas, P.C., and Feltz, L.V., *1980, Aerodynamic Performance of a 5-metre Diameter Darrieus Turbine With Extruded NACA-0015 Blades.* Technical Report No. SAND80-0179, Sandia National Laboratories, USA.

16. Strickland, J.H., *1975, The Darrieus Turbine: A Performance Prediction Model Using Multiple Streamtubes.* Sandia Laboratories, USA. **75**(431).

17. Templin, R.J., *1974, Aerodynamic Performance Theory for the NRC Vertical-Axis Wind Turbine.* National Research Council of Canada, Ottawa.

18. Rangi, R.S., South, P., and Templin, R.J., *1978, NRC's wind energy program.* Renewable Alternatives; Proceedings of the Fourth Annual Conference, London, Ontario, Canada, Vol. 1, 15.

19. Templin, R.J., *1985, The NRC Double Multiple Stream Tube Theory for Vertical Axis Wind Turbines.* NRC Wind Energy Technical Memorandum TM-WE-023.

20. Dodd, H.H., Ashwill, T.D., Berg, D.E., Ralph, M.E., Stevenson, W.A., and Veers, P.S., *1989, Test Results and Status of the DOE/Sandia 34m Test Bed.* The Canadian Wind Energy Association Conference.

21. Wilson, R.E., and Lissaman, P.B.S., *1974, Applied Aerodynamics of Wind Power Machine.* Oregon state university

22. Gouriérès, D.L., *1982, Wind Power Plants Theory and Design.* Headington Hill Hall: Pergamon Press Ltd.

23. Kirke, B.K., *1998, Evaluation of Self-Starting Vertical Axis Wind Turbines for Stand-Alone Applications.* Ph.D. Thesis, School of Engineering, Griffith University, Australia.

24. Mertens, S., Van Kuik, G., and Van Bussel, G., *2003, Performance of an HDarrieus in the Skewed Flow on a Roof.* Journal of Solar Energy Engineering. **125**(4): p. 433-440.

25. El-Samanuody, M., Ghorab, A. A. E., Youssef, Sh. Z, *2010, Effects of some design parameters on the performance of a Giromill vertical axis wind turbine.* Ain Shams Engineering Journal. **1**: p. 85-95.

26. Dabiri, J.O., *2011, Potential order-of-magnitude enhancement of wind farm power density via counter-rotating vertical-axis wind turbine arrays.* Journal of Renewable and Sustainable Energy. **3**.

27. Kinzel, M., Mulligan, Q., and Dabiri, J.O., *2012, Energy exchange in an array of vertical-axis wind turbines.* Journal of Turbulence. **13**(38): p. 1-13.

28. Greaves, P.R., *2013, Fatigue Analysis and Testing of Wind Turbine Blades.* Ph.D. Thesis, School of Engineering and computing science, University of Durham.

29. Ebert, P.R., and Wood, D.H., *1997, Observations of the starting behaviour of a small horizontal-axis wind turbine.* Renewable Energy. **12**(3): p. 245-257.

30. Lunt, P.A.V., *2005, An aerodynamic model for a vertical-axis wind turbine.* MEng Project Report, School of Engineering, University of Durham, UK.

31. Worasinchai, S., *2012, Small Wind Turbine Starting Behaviour.* Ph.D. Thesis, School of Engineering and computing science, University of Durham.

32. Chua, K.L., *2002, Darrieus: Windturbine-analysis.* The original website was http://windturbine-analysis.com. However, this website is no longer avaiable, the original data can now be found in the Ph.D. Thesis of 'Small Wind Turbine Starting Behaviour' from Supakit Worasinchai. .

33. Dumitrescu, H., Dumitrache, A., Popescu, C.L., Popescu, M.O., Frunzulica, F., and Craciunescu, A., *2014, Wind Tunnel Experiments on Vertical-Axis Wind Turbines with Straight Blades.* International Conference on Renewable Energies and Power Quality, 8th to 10th April, Cordoba, Spain.

34. Mays, I., and Holmes, B.A. , *1979, Commercial development of the variable geomentry vertical axis windmill International power generation.* Sueewy, UK.

35. Consul, C.A., Willden, R.H.J., Ferrer, E., and McCulloch, M.D., *2009, Influence of Solidity on the Performance of a Cross-Flow Turbine.* Proceedings of the 8th European Wave and Tidal Energy Conference. Uppsala, Sweden.

36. Blackwell, B.F., Sheldahl, R.E., and Feltz, L.V., *1977, Wind Tunnel Performance Data for the Darrieus Wind Turbine with NACA0012 Blades.* Sandia Laboratories, SAND76-0130, United States.

37. Worstell, M.H., *1982, Aerodynamic Performance of the 17-m-Diameter Darrieus Wind Turbine in the Three-Bladed ConVguration: An Addendum.* Sandia Laboratories, SAND-79-1753, United States.

38. Vassberg, J.C., Gopinath, A.K., and Jameson, A., *2005, Revisiting the Vertical-Axis Wind Turbine Design Using Advanced Computational Fluid Dynamics.* 43rd AIAA Aerospace Sciences Meeting and Exhibit.

39. Howell, R., Qin, N., Edwards, J., and Durrani, N., *2010, Wind Tunnel and Numerical Study of a Small Vertical Axis Wind Turbine.* Journal of Renewable Energy. **35**(2): p. 412-422.

40. Castelli, M.R., Betta, S.D., and Benini, E., *2012, Effect of Blade Number on a Straight-Bladed Vertical-Axis Darreius Wind Turbine.* World Academy of Science, Engineering and Technology, January **61**: p. 305-311.

41. Musgrove, P.J., and Mays, I.D., *1978, Development of the Variable Geometry Vertical Axis Windmill.* International Symposium on Wind Energy Systems, 2nd, Amsterdam, Netherlands, October 3-6.

42. Simhan, K., *1984, A Review of Calculation Methods for the Determination of Performance Characteristics of Vertical Axis Wind Energy Converters with Special Reference to the Influence of Solidity and Starting Characteristics.* Bremen Univiversity. Fachberichte Physik. Report, No. 12.

43. Kirke, B.K., and Lazauskas, L., *1991, Enhancing the Performance of a Vertical Axis Wind Turbine Using a Simple Variable Pitch System.* Journal of Wind Engineering. **15**(4): p. 187-195.

44. Mohamed, M.H., *2012, Performance Investigation of H-Rotor Darrieus Turbine With New Airfoil Shapes.* Journal of Energy. **47**(1): p. 522-530.

45. Eboibi, O., Danao, L.A., Howell, R., and Edwards, J.M., *2013, Numerical Study of the Influence of Blade profile and Solidity on the Performance of Vertical Axis Wind Turbines.* 51st AIAA Aerospace Sciences Meeting including the New Horizons Forum and Aerospace Exposition, AIAA 2013-1095, 07-10 January.

46. Storer, R.G., *1981, Vertical axis wind turbine.* Canberra : National Energy Research, Development and Demonstration Program.

47. Corporation, F., *1996, Final Project Report: High-Energy Rotor Development Test and Evaluation.* Sandia Laboratories, SAND96-2205, United States.

48. Mcintosh, S.C., *2009, Wind Energy for the Built Environment.* Ph.D. thesis, Cambridge University, UK.

49. Migliore, P.G., and Fritschen, J.R., *1982, Darrieus Wind Turbine Airfoil Configurations.* A subcontract report, Solar Energy Research Institute, SERU/TR-11045-1.

50. Berg, D.E., *1990, Customised Airfoils and Their Impact on VAWT Cost of Energy.* Sandia Laboratories, SAND90-1148C, United States.

51. Klimas, P.C., *1992, Tailored Airfoils for Vertical Axis Wind Turbines.* Sandia Laboratories, SAND84-1062, United States.

52. Masson, C., Leclerc, C., and Paraschivoiu, I., *1998, Appropriate Dynamic-Stall Models for Performance Predictions of VAWTs with NLF Blades.* International Journal of Rotating Machinery. **4**(2): p. 129-139.

53. Healy, J.V., *1978, The Infuence of Blade Camber on the Output of Vertical-Axis Wind Turbines.* Wind Engineering. **2**(3): p. 146-155.

54. Islam, M., Ting, D.S.K., and Fartaj, A., *2007, Desirable Airfoil Features for Smaller Capacity Straight Bladed VAWT.* Wind Engineering. **31**(3): p. 165-196.

55. Bianchini. A., F., L., and Magnani, S., *2011, Start-Up Behavior of a Three-Bladed H-Darrieus VAWT: Experimental and Numerical Analysis.* ASME 2011 Turbo Expo: Turbine Technical Conference and Exposition, GT2011-45882, Vancouver, British Columbia, Canada, June 6–10.

56. Angell, R.K., Musgrove, P.J., and Galbraith, R.A.McD., *1988, Unsteady wind tunnel testing of thick section aerofoils for use on large scale veritcal axis wind*

turbine. Wind energy Conversion, Proceeding of 10th BWEA conferecne, Mar. 22-24, London, UK: p. 195-203.

57. Claessens, M., *2006, The Design and Testing of Airfoils for Application in Small Vertical Axis Wind Turbines.* Master's thesis, Faculty of Aerospace Engineering, Delft University of Technology, Netherlands.

58. Carmichael, B.H., *1981, Low Reynolds Number Airfoil Survey.* Technical Report No. NASA-CR-165803-VOL-1, Langley Research Center, USA.

59. Mueller, T.J., and DeLaurier, J.D., *2003, Aerodynamics of small vehicles.* Annual Review of Fluid Mechanics. **35**: p. 89-111.

60. Yarusevych, S., Sullivan, P. E., and Kawall, J. G., *2009, On vortex shedding from an airfoil in low-Reynolds-number flows.* Journal of Fluid Mechanics. **632**: p. 245-271.

61. Selig, M.S., Guglielmo, J.J., Broeren, A.P., and Giguere, P., *1995, Summary of Low-Speed Airfoil Data, Vol. 1.* SoarTech Publications, Virginia Beach, VA.

62. Sheldahl, R.E., and Klimas, P.C., *1981, Aerodynamic Characteristics of Seven Symmetrical Airfoil Sections through 180-degree Angle of Attack for Use in Aerodynamic Analysis of Vertical Axis Wind Turbines.* Technical Report No. SAND80-2114, Sandia National Laboratories, USA.

63. McGowan, R., Raghav, V.S., and Komerath, N.M., *2012, Optimization of a Vertical Axis Micro Wind Turbine for Low Tip Speed Ratio Operation.* Proceedings of the AIAA IECEC Conference, Atlanta, GA.

64. Rossetti, A., and Pavesi, G., *2013, Comparison of Different Numerical Approaches to the Study of the H-Darrieus Turbines Start-Up.* Journal of Renewable Energy. **50**(0): p. 7-19.

65. Zhou, Y., Alam Mahbub, Md., Yang, H.X., Guo, H., and Wood, D.H., *2011, Fluid forces on a very low Reynolds number airfoil and their prediction.* International Journal of Heat and Fluid Flow. **32**(1): p. 329-339.

66. Timmer, W.A., *2001, Aerodynamic Characteristics of Wind Turbine Blade Airfoils at High Angles-of-Attack.* In the Proceedings of Conference Torque 2010, The Science of Making Torque from the Wind, June 28-30, Crete, Greece.

67. Critzos, C.C., Heyson, H.H., and Boswinkle, R.W. , *1955, Aerodynamic Characteristics of NACA 0012 Airfoil Section at Angles of Attack From 0 deg to 180 deg.* National Advisory Committee for Aeronautics, NACA-TN-3361.

68. Mallon, K.J., *1992, The NACA0018-64 Aerofoil at Low Reynolds Numbers with Application to Vertical Axis Wind Turbins - Including Turbulence Stimulation.* 11th Australasian Fluid Mechanics Conference, rUniversity of Tasmania, Hobart, Australia, 14-18 Decembe.

69. Ostowari, C., and Naik, D., *1984, Post-stall Studies of Untwisted Varying Aspect Ratio Blades with an NACA 4415 Airfoil Section - Part I.* Wind Engineering. **8**(3): p. 176-194.

70. Worasinchai, S., Ingram,G.L., and Dominy, R.G., *2011, A low-Reynolds-number, high-angle-of-attack investigation of wind turbine aerofoils.* Proceedings of the Institution of Mechanical Engineers, Part A: J. Power and Energy. **226**(6): p. 748-763.

71. Migliore, P.G., Wolfe, W.P., and Fanucci, J.B., *1980, Flow Curvature Effects on Darrieus Turbine Blade Aerodynamics.* Journal of Energy. **4**(2): p. 49-55.

72. Sharpe, D.J., *1984, Refinements and developments of the multiple streamtube theory for the aerodynamic performance of vertical axis wind turbines.* In Proceedings of the BWEA Wind Energy Conference: p. 146-159.

73. Paraschivoiu, I., and Delclaux, F., *1983, Double-Multiple Streamtube Model With Recent Improvements.* AIAA Journal of Energy. **7**: p. 250-255.

74. Paraschivoiu, I., Fraunie, P., and Beguier, C., *1985, Streamtube Expansion Effects on The Darrieus Wind Turbine.* AIAA Journal of Propulsion and Power. **1**(2): p. 150-155.

75. Paraschivoiu, I., *1981, Double-Multiple Streamtube Model for Darrieus Wind Turbines.* Second DOE/NASA Wind Turbines Dynamics Workshop, NASA CP-2186, Cleveland, OH, February p. 19-25.

76. Soraghan, C.E., Leithead, W.E., Feuchtwang, J., and Yue, H., *2013, Double Multiple Streamtube Model for Variable Pitch Vertical Axis Wind Turbines.* 31st AIAA Applied Aerodynamics Conference.

77. Goude, A., *2012, Fluid Mechanics of Vertical Axis Turbines.* Ph.D. thesis, Uppsala University, Sweden.

78. Ashwill, T.D., *1992, Measured Data for the Sandia 34m Vertical Axis Wind Turbine.* Sandia Laboratories, SAND91-2228, United States.

79. Edwards, J.M., *2012, The Infuence of Aerodynamic Stall on the Performance of Vertical Axis Wind Turbines.* Ph.D. thesis, Sheffield University, UK.

80. Selig, M.S., and McGranahan, B.D., *2004, Wind tunnel aerodynamic tests of six airfoils for use on small wind turbines.* Jornal of Solar Energy Engineering. **126**: p. 986-1001.

81. Jones, R., and William, D.H., *1936, The effect of surface roughness of the characteristics of the aerofoils NACA 0012 and RAF 34.* British ARC, R&M No. 1708.

82. Gregory, N., and O'Reilly, C.L., *1973, Low-Speed Aerodynamic Characteristics of NACA 0012 Aerofoil Section, including the Effects of Upper-Surface Roughness Simulating Hoar Frost.* British ARC, R&M No. 3726.

83. Gerakopulos, R., Boutilier, M.S.H., and Yarusevych, S., *2010, Aerodynamic Characterization of a NACA 0018 Airfoil at Low Reynolds Numbers.* Paper No. AIAA-2010-4629, 40th Fluid Dynamics Conference and Exhibit, 28 June - 01 July, Chicago, Illinois.

84. Timmer, W.A., *2008, Two-Dimensional Low-Reynolds Number Wind Tunnel Results for Airfoil NACA 0018.* Wind Engineering. **32**: p. 525-537.

85. Danao, L.A., Eboibi, O., and Howell, R., *2013, An experimental investigation into the influence of unsteady wind on the performance of a vertical axis wind turbine.* Journal of Applied Energy. **107**: p. 403-411.

86. Staelens, Y., Saeed, F., and Paraschivoiu, I., *2003, A straight-bladed variable-pitch VAWT concept for improved power generation.* ASME 2003 Wind Energy Symposium, Paper No. WIND2003-524, January 6–9, Reno, Nevada, USA: p. 146-154.

87. Bossanyi, E.A., *2003, Wind turbine control for load reduction.* Wind Energy. **6**(3): p. 229-244.

88. Grylls, W., Dale, B., and Sarre, P.E., *1978, A theoretical and experimental investigation into the variable pitch vertical axis wind turbine.* proceedings 2nd international symposium on wind energy systems, Amsterdam, Oct. 3-6: p. 101-118.

89. Gosselin, R., Dumas, G., and Boudreau, M., *2013, Parametric study of H-Darrieus vertical-axis turbines using uRANS simulations.* Paper CFDSC-2013 #178, Session 13–6 - Rotating Machine I, 21st Annual Conference of the CFD Society of Canada, May 6-9, Sherbrooke, Canada.

90. Kosaku, T., Sano, M., and Nakatani, K., *2002, Optimum pitch control for variable-pitch vertical-axis wind turbines by a single stage model on the momentum theory.* Systems, Man and Cybernetics, 2002 IEEE International Conference, 6-9 Oct. **5**.

91. Vandenberghe, D., and Dick, E., *1987, Optimum pitch control for vertical axis wind turbines.* Wind Engineering. **11**: p. 237-247.

92. Chougule, P., and Nielsen, S., *2014, Overview and Design of self-acting pitch control mechanism for vertical axis wind turbine using multi body simulation approach.* Journal of Physics: Conference Series 524.

93. Pearson, C., *2013, Vertical Axis Wind Turbine Acoustics.* Ph.D. thesis, Cambridge University, UK.

94. Klimas, P.C., and Worstell, M., *1981, Effects of blade preset pitch/offset on curved-blade Darrieus vertical axis wind turbine performance.* Sandia Laboratories, SAND81-1762, United States.

95. Leishman, J.G., and Beddoes, T.S., *1989, A Semi-Empirical Model for Dynamic Stall.* Journal of the American Helicopter Society. **34**(3): p. 3-17.

96. Massé, B., *1981, Description de deux programmes d'ordinateur pour le calcul des performances et des charges aérodynamiques pour des éoliennes à axe vertical.* Technical Report IREQ 2379.

97. Allet, A., and Paraschivoiu, I., *1995, Viscous Flow and Dynamic Stall EUects on Vertical-Axis Wind Turbines.* International Journal of Rotating Machinery. **2**(1): p. 1-14.

98. Leishman, J.G., *2002, Principles of Helicopter Aerodynamics.* Cambridge University Press.

99. McCroskey, W.J., McAlister, K. W., Carr, L. W., and Pucci, S. L., *1982, An experimental study on dynamic stall on advanced airfoil sections.* NASA Technical Memorandum 84245.

100. Carr, L.W., McAlister, K. W., and McCroskey, W. J., *1977, Analysis of the development of dynamic stall based on oscillating airfoil measurements.* NASA TN D-8382.

101. Simao Ferreira, C.J., Bijl, H., van Bussel, G., and van Kuik, G., *2007, Simulating dynamic stall in a 2d vawt: Modeling strategy, verification and validation with particle image velocimetry data.* Journal of Physics: Conference Series 75.

102. Tsang, K.K.Y., So, R.M.C., Leung, R.C.K., and Wang, X.Q., *2008, Dynamic stall behavior from unsteady force measurements.* Journal of Fluids and Structures. **24**: p. 129-150.

103. Wang, S., Ingham, D.B., Ma, L., Pourkashanian, M., and Tao, Z., *2010, Numerical Investigations on Dynamic Stall of Low Reynolds Number Flow Around Oscillating Airfoils.* Journal of Computers and Fluids. **39**(9): p. 1529-1541.

104. Fujisawa, N., and Shibuya, S., *2001, Observations of dynamic stall on Darrieus wind turbine blades.* Journal of Wind Engineering and Industrial Aerodynamics. **89**: p. 201-214.

105. Paraschivoiu, I., *2002, Wind turbine design: with emphasis on darrieus concept.* Montreal, Polytechnic International Press.

106. Muraca, R.J., Stephens, M.V., and Dagenhart, J.R., *1975, Theoretical performance of cross-wind axis turbines with results for a catenary vertical axis configuration.* NASA TMX-72662, USA.

107. Sharpe, D.J., *1977, A theoretical and experimental study of the darrieus vertical axis wind turbine.* School of Mechanical, Aeronautical & Production Engineering. Kingston Polytechnic. Research report.

108. Read, S., and Sharpe, D.J., *1980, An extended multiple streamtube theory for vertical axis wind turbines.* 2nd BWEA workshop, April, Cranfield, UK: p. 65-72.

109. Paraschivoiu, I., Delclaux, F., Fraunie, P., and Beguier, C., *1983, Aerodynamic analysis of the darrieus rotor including secondary effects.* Journal of Energy. **7**(5): p. 416-421.

110. Islam, M., Ting, D.S.K., and Fartaj, A., *2008, Aerodynamic models for Darrieus-type straight-bladed vertical axis wind turbines.* Renewable & sustainable energy reviews. **12**(4): p. 1087-1109.

111. Larsen, H.C., *1975, Summary of a vortex theory for the cyclogyro.* Proceedings of the second US national conferences on wind engineering research, Colorado state university. **8**: p. 1-3.

112. Fanucci, J.B., and Walter, R.E., *1976, Innovative wind machines: the theoretical performance of a vertical-axis wind turbine.* Proceedings of the vertical-axis wind turbine technology workshop, Sandia laboratories, SAND76-5586, iii-61-95, USA.

113. Holme, O.A., *1976, Contribution to the aerodynamic theory of the vertical axis wind turbine.* International symposium, on wind energy systems, September 7th–9th, Cambridge, England: p. 55-71.

114. Wilson, R.E., *1980, Wind-turbine aerodynamics.* Journal of Wind Engineering and Industrial Aerodynamics: p. 357-372.

115. Strickland, J.H., Webster, B.T., and Nguyen, T., *1979, A Vortex model of the darrieus turbine: an analytical and experimental study.* Journal of Fluids Engineering. **101**(4): p. 500-505.

116. Strickland, J.H., Webster, B.T., and Nguyen, T., *1981, A Vortex Model of the Darrieus Turbine: An Analytical and Experimental Study.* Sandia Laboratories, SAND81-7017, United States.

117. Cardona, J.L., *1984, Flow curvature and dynamic stall simulated with an aerodynamic freevortex model for VAWT.* Wind Engineering. **8**: p. 135-143.

118. Scheurich, F., Fletcher, T.M., and Brown, R.E., *2010, Simulating the aerodynamic performance and wake dynamics of Vertical Axis Wind Turbine.* Wind Energy. **14**(2): p. 159-177.

119. Brown, R.E., *2000, Rotor wake modelling for flight dynamic simulation of helicopters.* AIAA Journal. **38**(1): p. 57-63.

120. Pawsey, N.C.K., *2002, Development and Evaluation of Passive Variable-Pitch Vertical Axis Wind Turbines.* PhD Thesis, School of Mechanical and Manufacturing Engineering, The University of New South Wales, Australia.

121. Hirsch, H., and Mandal, A.C., *1987, A cascade theory for the aerodynamic performance of darrieus wind turbines.* Wind Engineering. **11**(3): p. 164-175.

122. Mandal, A.C., and Burton, J.D., *1994, The effects of dynamic stall and flow curvature on the aerodynamics of darrieus turbines applying the Cascade model.* Wind Engineering. **18**(6): p. 267-282.

123. Castelli, M.R., Englaro, A., and Benini, E., *2011, The Darrieus Wind Turbine: Proposal for a New Performance Prediction Model Based on CFD.* Jornal of Energy. **36**(8): p. 4919-4934.

124. Castelli, M.R., Ardizzon, G., Battisti, L., Benini, E., and Pavesi, G., *2010, Modelling Strategy and Numerical Validation for a Darrieus Vertical Axis Micro-Wind Turbine.* Paper No. IMECE2010-39548, ASME 2010 International Mechanical Engineering Congress and Exposition, Vancouver, British Columbia, Canada, November 12–18: p. 409-418.

125. Eboibi, O., *2013, The Influence of Blade Chord on the Aerodynamics and Performance of Vertical Axis Wind Turbines* Ph.D. thesis, Sheffield University, UK.

126. Lee, T., and Gerontakos, P., *2004, Investigation of flow over an oscillating airfoil.* Journal of Fluid Mechanics. **512**: p. 313-341.

127. Amet, E., Maître, T., Pellone, C., Achard, J. L., *2009, 2D Numerical Simulations of Blade-Vortex Interaction in a Darrieus Turbine.* Journal of Fluids Engineering. **131**(11).

128. Danao, L.A., Qin, N., Howell, R., *2012, A numerical study of blade thickness and camber effects on vertical axis wind turbines.* Proceedings of the Institution of Mechanical Engineers, Part A: Journal of Power and Energy. **226**(7): p. 867-881.

129. McLaren, K., Tullis, S., Ziada, S., *2012, Computational fluid dynamics simulation of the aerodynamics of a high solidity, small-scale vertical axis wind turbine.* Wind Energy. **15**(3): p. 349-361.

130. Danao, L.A., Edwards, J., Eboibi, O., and Howell, R., *2014, A numerical investigation into the influence of unsteady wind on the performance and aerodynamics of a vertical axis wind turbine.* Applied Energy. **116**: p. 111-124.

131. Laneville, A., and Vittecoq, P., *1986, Dynamic Stall: The Case of the Vertical Axis Wind Turbine.* Journal of Solar Energy Engineering. **108**(2): p. 140-145.

132. Untaroiu, A., Wood, H. G., Allaire, P. E., and Ribando, R. J., *2011, Investigation of Self-Starting Capability of Vertical Axis Wind Turbines Using a Computational Fluid Dynamics Approach.* Journal of Solar Energy Engineering. **133**(4): p. 041010-8.

133. Eleni, D.C., Athanasios, T.I., and Dionissios, M.P., *2012, Evaluation of the Turbulence Models for the Simulation of the Flow Over a National Advisory Committee for Aeronautics (NACA) 0012 Airfoil.* Journal of Mechanical Engineering Research. **4**(3): p. 100-111.

134. Shelton, A., Abras, J., Jurenko, R., and Smith, M.J., *2005, Improving the CFD Predictions of Airfoils in Stall.* Paper No. AIAA-2005-1227, AIAA 43rd Aerospace Sciences Meeting and Exhibit, 10-13 January, Reno, Nevada.

135. Lian, Y., and Shyy, W., *2007, Aerodynamics of Low Reynolds Number Plunging Airfoil under Gusty Environment.* AIAA-2007-71, 45th AIAA Aerospace Sciences Meeting and Exhibit, 8 - 11 January, Reno, Nevada.

136. Patankar, S.V., and Spalding, D.B., *1972, A Calculation Procedure for Heat, Mass and Momentum Transfer in Three-Dimensional Parabolic Flows.* International Journal of Heat and Mass Transfer. **15**: p. 1787-1806.

137. Shyy, W., *1997, Computational Modeling for Fluid Flow and Interfacial Transport.* corrected printing. Amsterdam: Elsevier.

138. Anderson, J.M., Streitlien, K., Barrett, D.S., and Triantafyllou, M.S., *1998, Oscillating Foils of High Propulsive Efficiency.* Journal of Fluid Mechanics. . **360**: p. 41-72.

139. Young, J., and Lai, J.C.S., *2004, Oscillation Frequency and Amplitude Effects on the Wake of Plunging Airfoil.* AIAA Journal. **42**.

140. Lai, J.C.S., and Platzer, M.F., *1999, Jet Characteristics of a Plunging Airfoil.* AIAA Journal. **37**: p. 1529-1537.

141. *ANSYS FLUENT User's Guide, Release 14.0, 2011.* Ansys Inc.

142. O'Meara, M.M., and Mueller, T.J., *1987, Laminar separation bubble characteristics on an airfoil at low Reynolds numbers.* AIAA Journal. **25**(8): p. 1033-1041.

143. Bedon, G., Castelli, M.R., and Benini, E., *2012, Evaluation of the Effect of Rotor Solidity on the Performance of a H-Darrieus Turbine Adopting a Blade Element-Momentum Algorithm.* World Academy of Science, Engineering and Technology. **6**.

144. Mohamed, M.H., *2013, Impacts of solidity and hybrid system for a small wind turbine performance.* Journal of Energy. **57**(8): p. 495-504.

145. Prandtl, L., and Betz, A., *1927, Vier abhandlungen zur Hydrodynamik and Aerodynamik.* Göttingen Nachr. : Göttingen: p. 88-92.

146. Sheng, W., Galbraith, R.A., and Coton, F.N., *2008, A Modified Dynamic Stall Model for Low Mach Numbers.* Journal of Solar Energy Engineering. **130**(3).

147. Chantharasenawong, C., *2007, Nonlinear Aeroelastic Behaviour of Aerofoils Under Dynamic Stall.* Ph.D. thesis, University of London.

148. Pendharkar, A., McGowan, R., Morillas, K., and Pinder, M., *2012, Optimization of a Vertical Axis Micro Wind Turbine for Low Tip Speed Ratio Operation.* Paper No. AIAA-2012-4244, 10th International Energy Conversion Engineering Conference, 30 July - 01 August, Atlanta, Georgia.

149. Du, L., Berson, A., and Dominy, R.G., *2014, Aerofoil behaviour at high angles of attack and at Reynolds numbers appropriate for small wind turbines.* Proceedings of the Institution of Mechanical Engineers, Part C: Journal of Mechanical Engineering Science **229**(11): p. 2007-2022.

150. Glauert, H., *1926, A general theory of the autogyro.* Technical Report No. 1111, Aeronautical Research Council, R & M, UK.

151. Lewis, K.W., *1984, The cumulative effects of roughness and Reynolds number on NACA 0015 airfoil section characteristics* Master of Science Thesis, Texas Technology University

152. Worasinchai, S., Ingram,G.L., and Dominy, R.G., *2012, Effects of Wind Turbine Starting Capability on Energy Yield.* ASME Journal of Engineering for Gas Turbines and Power. **134**(4).

153. Mankowski, O.A., *2013, The Wind Tunnel Simulation and Effect of Turbulent Air flow on Automotive Aerodynamics.* Ph.D. thesis, Durham University, UK.

154. Sims-Williams, D.B., and Dominy, R.G., *2002, The Design of an Open-Jet Wind Tunnel for Model Testing.* SAE Technical Paper 2002-01-3340.

155. Fuglsang, P., Antoniou, I., Sørensen, N.N., and Madsen, H., *1998, Validation of a Wind Tunnel Testing Facility for Blade Surface Pressure Measurements.* Risø-R-981(EN), Risø National Laboratory, Denmark.

156. Dominy, R.G., and Hodson, H.P., *1995, An investigation of factors influencing the calibration of 5-hole probes for 3-D flow measurements.* ASME Journal of Turbomachinery. **115**: p. 513-519.

157. Ingram, G., and Gregory-Smith, D., *2006, An automated instrumentation system for flow and loss measurements in a cascade.* Flow Measurement and Instrumentation. **17**(1): p. 23-28.

158. *http://optekinc.com/datasheets/opb703-705_70a-70d-b.pdf.* [Accessed: 02 Nov. 2015].

159. Wyant, J.C., *2002, White Light Interferometry* In Conference on Holography, Proceedings of SPIE. **4737**.

160. Beatty, M.F., *1986, Principles of Engineering Mechanics. Vol. 1. Kinematics: The Geometry of Motion. .* Plenum Publishing Corp.,New York.

161. *http://marmatek.com/wp-content/uploads/2014/03/Meas_ESP-HD_Manual.pdf.* [Accessed: 02 Nov. 2015].

162. Sims-Williams, D.B., and Luck, D.A., *2007, Transfer function characterization of pressure signal tubes for the measurement of large amplitude pressure fluctuations.* Proceedings of the Institution of Mechanical Engineers, Part C: Journal of Mechanical Engineering Science **221**(6): p. 707-713.

163. Sims-Williams, D.B., *2001, Self-excited Aerodynamic Unsteadiness Associated with Passenger Cars.* Ph.D. Thesis, School of Engineering and computing science, University of Durham.

164. Young, J., *2005, Numerical simulation of the unsteady aerodynamics of flapping airfoils* ph.D. thesis, The University of New South Wales, Australia

165. Abbott, I.H., and Von Doenhoff, A.E., *1959, Theory of Wing Sections: Including a Summary of Airfoil Data.* Dover Publications, New York.

166. Swalwell, K.E., Sheridan, J., and Melbourne, W.H., *2001, The Effect of Turbulence Intensity on Stall of the NACA 0021 Aerofoil.* 14th Australasian Fluid Mechanics Conference Adelaide University, Adelaide, Australia.

167. Garner, H.C., Rogers, E.W.E., Acum, W.E.A., and Maskell, E.C., *1966, Subsonic wind tunnel wall corrections.* AGARDograph 109.

168. Ewald, B.F.R.E., *1988, Wind tunnel wall correction.* AGARDograph 336.

169. Maeder, P.F., and Wood, A.D., *1956, Transonic wind tunnel test sections.* J. Zeitschrift für angewandte Mathematik und Physik ZAMP. **7**(3): p. 177-212.

170. Maskell, E.C., *1963, A theory of the blockage effects on bluff bodies and stalled wings in a closed wind tunnel.* ARC RM 3400.

171. Mangler, W., *1938, The Lift Distribution of Wings with End Plates.* NACA Technical Memorandum No. 856, Washington.

172. Hansen, K.L., Kelso, R.M., and Dally, B.B., *2011, Performance Variations of Leading-Edge Tubercles for Distinct Airfoil Profiles.* AIAA Journal. **49**(1): p. 185-194.

173. Woodward, B.L., Winn, J.P., and Fish, F.E., *2006, Morphological Specializations of Baleen Whales Associated With Hydrodynamic Performance and Ecological Niche.* Journal of morphology **267**: p. 1284-1294.

174. Friedlaender, A.S., Hazen, E.L., Nowacek, D.P., Halpin, P.N., Ware, C., Weinrich, M.T., Hurst, T., and Wiley, D., *2009, Diel changes in humpback whale Megaptera novaeangliae feeding behavior in response to sand lance Ammodytes spp. behavior and distribution.* Marine ecology progress series **395**(91-100).

175. Fish, F.E., Weber, P.W., Murray, M.M., and Howle, L.E., *2011, The Tubercles on Humpback Whales' Flippers: Application of Bio-Inspired Technology.* Integrative and Comparative Biology. **51**(1): p. 203-213.

176. Fish, F.E., and Battle, J.M., *1995, Hydrodynamic Design of the Humpback Whale Flipper.* Journal of Morphology. **225**: p. 51-60.

177. Miklosovic, D.S., Murray, M.M., Howle, L.E., and Fish, F.E., *2004, Leading Edge Tubercles Delay Stall on Humpback Whale Flippers.* Physics of Fluids. **16**(5): p. L39-L42.

178. Pedro, H.T.C., and Kobayashi, M.H., *2008, Numerical Study of Stall Delay on Humpback Whale Flippers.* 46th AIAA Aerospace Sciences Meeting and Exhibit, Reno, NV, 7- 10 Jan. AIAA Paper 2008-0584.

179. van Nierop, E., Alben, S., and Brenner, M. P., *2008, How Bumps on Whale Flippers Delay Stall: an Aerodynamic Model.* Physical Review Letters. **100**.

180. Custodio, D., *2007, The Effect of Humpback Whale-Like Leading Edge Protuberances on Hydrofoil Performance.* Master Thesis, Worcester Polytechnic Institute, Worcester, USA.

181. *https://www.gov.uk/search-for-patent* [Accessed: 02 Nov. 2015].

Appendix A Positions of the pressure tappings for static wind tunnel measurements

Suction surface		Pressure surface	
x/c	y/c	x/c	y/c
0.0231	0.0000	0.0469	0.0231
0.0469	0.0231	0.0769	0.0385
0.0769	0.0385	0.1171	0.0498
0.1171	0.0498	0.1592	0.0575
0.1592	0.0575	0.2021	0.0623
0.2021	0.0623	0.2456	0.0651
0.2456	0.0651	0.2894	0.0662
0.2894	0.0662	0.3333	0.0658
0.3333	0.0658	0.3773	0.0643
0.3773	0.0643	0.4214	0.0618
0.4214	0.0618	0.4655	0.0585
0.4655	0.0585	0.5095	0.0546
0.5095	0.0546	0.5535	0.0499
0.5535	0.0499	0.5976	0.0447
0.5976	0.0447	0.6416	0.0391
0.6416	0.0391	0.6856	0.0330
0.6856	0.0330	0.7295	0.0265
0.7295	0.0265	0.7734	0.0195
0.7734	0.0195	0.8172	0.0169
0.8172	0.0169	0.8538	0.0138
0.8538	0.0138		
0.8923	0.0000		
0.9231	0.0000		

Table A. 1 NACA0018 aerofoil pressure tapping location

Appendix B Uncorrected lift and drag coefficients

NACA0018 $Re = 60,000$

Closed-jet			Open-jet			Reference tunnel		
AOA	Cl	Cd	AOA	Cl	Cd	AOA	Cl	Cd
0	0.0148	0.0202	0	-0.0082	0.0192	0	-0.0053	0.0295
2	0.3293	0.0382	2	0.2034	0.0343	2	0.2267	0.0312
4	0.5361	0.0366	4	0.3634	0.0392	4	0.4712	0.0387
6	0.6526	0.0392	6	0.4735	0.0529	6	0.6096	0.0643
8	0.7397	0.0522	8	0.5490	0.0633	8	0.7357	0.0663
10	0.8127	0.0631	10	0.6283	0.0754	10	0.7938	0.0821
11	0.8338	0.0712	12	0.7007	0.0779	11	0.8015	0.0975
12	0.3506	0.1466	14	0.7143	0.1071	11.5	0.8155	0.1078
14	0.4224	0.1918	15	0.2726	0.1651	12	0.7440	0.1305
16	0.4508	0.2269	16	0.2795	0.1754	12.5	0.5744	0.1333
18	0.4862	0.2466	18	0.2816	0.1858	13	0.4066	0.1636
20	0.5367	0.2852	20	0.3038	0.2104	14	0.3538	0.1814
25	0.6781	0.4067	22	0.3417	0.2350	16	0.3960	0.2149
30	0.8087	0.5642	24	0.3665	0.2608	18	0.4815	0.2459
35	0.9694	0.7562	26	0.3935	0.2906	20	0.5226	0.2844
40	1.1445	1.0520	28	0.4252	0.3232	22	0.5652	0.3256
45	1.2752	1.3568	30	0.4585	0.3612	24	0.5945	0.3766
50	1.3128	1.6271	32	0.4816	0.4025	26	0.6303	0.4146
55	1.3336	1.9371	34	0.5022	0.4453	28	0.6809	0.4686
60	1.3045	2.2338	36	0.5228	0.4961	30	0.7340	0.5353
65	1.1935	2.4527	38	0.5591	0.5491	32	0.7727	0.5989
70	1.0478	2.6663	40	0.5851	0.6050	34	0.8009	0.6515
75	0.8388	2.8144	42	0.6159	0.6504	36	0.8411	0.7123
80	0.6375	2.8714	44	0.6431	0.7234	37	0.8475	0.7377
85	0.4059	2.9237	46	0.6476	0.7866	38	0.8587	0.7703
90	0.1708	2.9638	48	0.6327	0.8374	39	0.5011	0.4943
95	-0.0642	2.9453	50	0.3723	0.5214	40	0.5299	0.5362
100	-0.2733	2.8620	52	0.3619	0.5406	42	0.5382	0.5908
105	-0.4848	2.7235	54	0.3544	0.5606	44	0.5486	0.5964
110	-0.6803	2.5104	56	0.3431	0.5806	46	0.5494	0.6350
115	-0.8547	2.3770	58	0.3267	0.6006	48	0.5496	0.6738
120	-0.9712	2.1391	60	0.3237	0.6206	50	0.5510	0.7072
125	-1.0493	1.8876	62	0.3099	0.6406	52	0.5307	0.7370
130	-1.1116	1.6462	64	0.2985	0.6606	54	0.5285	0.7607
135	-1.1084	1.3752	66	0.2782	0.6806	56	0.5178	0.8014
140	-1.0448	1.1016	68	0.2665	0.6950	58	0.5067	0.8384
145	-0.9402	0.8483	70	0.2569	0.7171	60	0.4943	0.8583
150	-0.7329	0.5600	72	0.2391	0.7306	62	0.4826	0.9061

155	-0.6474	0.4157	74	0.2209	0.7416	64	0.4528	0.9113
160	-0.5476	0.2866	76	0.1974	0.7546	66	0.4365	0.9512
164	-0.5611	0.2227	78	0.1817	0.7706	68	0.4109	0.9685
166	-0.5887	0.1876	80	0.1597	0.7850	70	0.3896	0.9956
168	-0.6362	0.1408	82	0.1392	0.8000	72	0.3603	1.0194
170	-0.6436	0.0779	84	0.1091	0.8061	74	0.3313	1.0363
172	-0.5745	0.0449	86	0.0892	0.8191	76	0.3000	1.0449
174	-0.4564	0.0375	88	0.0697	0.8251	78	0.2719	1.0604
176	-0.2854	0.0473	90	0.0551	0.8261	80	0.2360	1.0651
178	-0.0863	0.0669	92	0.0263	0.8229	82	0.2117	1.0772
180	-0.0221	0.0673	94	0.0012	0.8164	84	0.1822	1.0791
			96	-0.0250	0.8160	86	0.1419	1.0808
			98	-0.0477	0.8043	88	0.1078	1.0937
			100	-0.0688	0.7952	90	0.0660	1.0951
			102	-0.0894	0.7884	92	0.0398	1.0957
			104	-0.1154	0.7761	94	-0.0002	1.0754
			106	-0.1397	0.7684	96	-0.0317	1.0711
			108	-0.1596	0.7540	98	-0.0678	1.0620
			110	-0.1863	0.7324	100	-0.0977	1.0505
			112	-0.2116	0.7254	102	-0.1321	1.0258
			114	-0.2223	0.7022	104	-0.1648	1.0200
			116	-0.2432	0.6857	106	-0.1940	1.0044
			118	-0.2596	0.6592	108	-0.2236	0.9826
			120	-0.2739	0.6351	110	-0.2533	0.9584
			122	-0.2803	0.6186	112	-0.2788	0.9376
			124	-0.3084	0.5965	114	-0.3062	0.9241
			126	-0.3165	0.5731	116	-0.3207	0.8873
			128	-0.3314	0.5535	118	-0.3438	0.8470
			130	-0.3531	0.5464	120	-0.3654	0.8266
			132	-0.5996	0.8372	122	-0.3878	0.8013
			134	-0.6151	0.8132	124	-0.3977	0.7603
			136	-0.6363	0.7709	126	-0.4105	0.7342
			138	-0.6399	0.7314	128	-0.4235	0.6974
			140	-0.6420	0.6723	130	-0.4327	0.6607
			142	-0.6263	0.6226	132	-0.4564	0.6548
			144	-0.6131	0.5674	134	-0.4557	0.6138
			146	-0.5838	0.5136	136	-0.4572	0.5651
			148	-0.5318	0.4496	138	-0.4564	0.5408
			150	-0.4969	0.3894	140	-0.4273	0.4808
			152	-0.4464	0.3234	141	-0.8344	0.8487
			154	-0.4155	0.2798	142	-0.8360	0.8180
			156	-0.3879	0.2451	144	-0.8086	0.7691
			158	-0.3702	0.2139	146	-0.7767	0.6900
			160	-0.3839	0.1958	148	-0.7450	0.6166
			162	-0.4091	0.1840	150	-0.6805	0.5262
			164	-0.4683	0.1624	152	-0.5988	0.4294

				166	-0.5516	0.1278	154	-0.5723	0.3671
				168	-0.5721	0.0858	156	-0.5475	0.3479
				170	-0.4982	0.0613	158	-0.5352	0.3022
				172	-0.3897	0.0519	160	-0.5151	0.2627
				174	-0.2650	0.0533	162	-0.5220	0.2573
				176	-0.1621	0.0565	164	-0.5810	0.2327
				178	-0.0829	0.0592	166	-0.6403	0.1939
				180	-0.0269	0.0544	168	-0.6894	0.1242
							170	-0.6241	0.0776
							172	-0.5249	0.0624
							174	-0.3939	0.0557
							176	-0.1671	0.0727
							178	-0.0587	0.0800
							180	0.0112	0.0685

NACA0018 $Re = 100,000$

Closed-jet			Open-jet			Reference tunnel		
AOA	**Cl**	**Cd**	**AOA**	**Cl**	**Cd**	**AOA**	**Cl**	**Cd**
0	0.0409	0.0203	0	0.0074	0.0202	0	0.0067	0.0273
2	0.1988	0.0293	2	0.1275	0.0201	2	0.1814	0.0238
4	0.4422	0.0276	4	0.2614	0.0201	4	0.4001	0.0266
6	0.6491	0.0421	6	0.4150	0.0286	6	0.5989	0.0393
8	0.7795	0.0530	8	0.5647	0.0454	8	0.7489	0.0557
10	0.8784	0.0632	10	0.6917	0.0612	10	0.8477	0.0760
12	0.9538	0.0847	12	0.7964	0.0804	12	0.9335	0.0938
14	1.0019	0.1109	14	0.8655	0.0994	13	0.9603	0.1003
15	0.3698	0.2008	16	0.9165	0.1229	13.5	0.9736	0.1070
16	0.4280	0.2317	17	0.9367	0.1308	14	0.9808	0.1177
18	0.4655	0.2608	18	0.3206	0.2000	14.5	0.3995	0.1976
20	0.5521	0.2828	20	0.3384	0.2222	15	0.4146	0.2076
25	0.6952	0.3965	22	0.3697	0.2515	16	0.4117	0.2194
30	0.8417	0.5591	24	0.3987	0.2794	18	0.4852	0.2770
35	1.0072	0.8047	26	0.4278	0.3132	20	0.5300	0.3245
40	1.1955	1.0996	28	0.4646	0.3540	22	0.5884	0.3642
45	1.3288	1.3841	30	0.4991	0.3956	24	0.6338	0.3956
50	1.3649	1.6509	32	0.5415	0.4458	26	0.6699	0.4346
55	1.3543	1.9554	34	0.5872	0.5052	28	0.7227	0.4919
60	1.3022	2.2291	36	0.6308	0.5642	30	0.7781	0.5561
65	1.2088	2.4911	38	0.6726	0.6305	32	0.8145	0.6153
70	1.0814	2.7437	40	0.7099	0.6982	34	0.8549	0.6770
75	0.8837	2.8900	42	0.7212	0.7478	36	0.8735	0.7319
80	0.6636	3.0548	44	0.7399	0.8116	38	0.8853	0.7785
85	0.4337	3.1516	46	0.7465	0.8700	39	0.7276	0.6598
90	0.1855	3.1884	48	0.7502	0.9197	40	0.5675	0.5269
95	-0.0712	3.1806	50	0.3999	0.5472	42	0.5665	0.5667

100	-0.3213	3.0769	52	0.3877	0.5652	44	0.5607	0.6116
105	-0.5500	2.9683	54	0.3834	0.5902	46	0.5595	0.6439
110	-0.7590	2.7800	56	0.3725	0.6100	48	0.5571	0.6758
115	-0.9265	2.5459	58	0.3609	0.6279	50	0.5541	0.7232
120	-1.0536	2.2925	60	0.3504	0.6506	52	0.5475	0.7608
125	-1.1414	2.0339	62	0.3437	0.6774	54	0.5438	0.7994
130	-1.2081	1.7844	64	0.3289	0.7007	56	0.5227	0.8214
135	-1.1901	1.4838	66	0.3120	0.7101	58	0.5116	0.8546
140	-1.1329	1.2009	68	0.3052	0.7487	60	0.4982	0.8807
145	-0.9972	0.9042	70	0.2850	0.7539	62	0.4772	0.9057
150	-0.8078	0.6202	72	0.2642	0.7724	64	0.4570	0.9310
155	-0.5939	0.3901	74	0.2437	0.7847	66	0.4362	0.9582
160	-0.5147	0.2776	76	0.2250	0.8049	68	0.4131	0.9851
164	-0.5063	0.2221	78	0.2034	0.8211	70	0.3862	1.0010
166	-0.5698	0.2005	80	0.1793	0.8329	72	0.3632	1.0273
168	-0.6595	0.1591	82	0.1549	0.8426	74	0.3357	1.0486
170	-0.7224	0.1004	84	0.1314	0.8543	76	0.3067	1.0657
172	-0.6569	0.0551	86	0.1049	0.8587	78	0.2765	1.0730
174	-0.5340	0.0424	88	0.0798	0.8629	80	0.2387	1.0802
176	-0.3893	0.0494	90	0.0533	0.8670	82	0.2088	1.0872
178	-0.1919	0.0558	92	0.0258	0.8594	84	0.1741	1.0937
180	-0.0120	0.0688	94	0.0027	0.8417	86	0.1394	1.0921
			96	-0.0235	0.8345	88	0.1058	1.0975
			98	-0.0479	0.8270	90	0.0699	1.0951
			100	-0.0749	0.8215	92	0.0369	1.0915
			102	-0.0978	0.8114	94	-0.0023	1.0885
			104	-0.1268	0.8058	96	-0.0364	1.0790
			106	-0.1485	0.7951	98	-0.0669	1.0706
			108	-0.1744	0.7806	100	-0.1011	1.0641
			110	-0.1893	0.7618	102	-0.1311	1.0561
			112	-0.2121	0.7426	104	-0.1604	1.0298
			114	-0.2334	0.7282	106	-0.1917	1.0127
			116	-0.2515	0.7107	108	-0.2217	0.9943
			118	-0.2616	0.6821	110	-0.2496	0.9796
			120	-0.2786	0.6538	112	-0.2707	0.9326
			122	-0.2895	0.6255	114	-0.2980	0.9151
			124	-0.2999	0.5981	116	-0.3199	0.8991
			126	-0.3128	0.5752	118	-0.3462	0.8682
			128	-0.3293	0.5593	120	-0.3673	0.8423
			130	-0.3502	0.5411	122	-0.3836	0.8082
			132	-0.3609	0.5273	124	-0.3958	0.7706
			134	-0.6366	0.8460	126	-0.4071	0.7312
			136	-0.6669	0.8253	128	-0.4221	0.7044
			138	-0.6748	0.7746	130	-0.4326	0.6738
			140	-0.6783	0.7416	132	-0.4427	0.6447
			142	-0.6591	0.6701	134	-0.4488	0.6127

				144	-0.6287	0.6026	136	-0.4488	0.5698
				146	-0.5859	0.5260	138	-0.4477	0.5207
				148	-0.5403	0.4591	140	-0.4393	0.4926
				150	-0.5185	0.4074	141	-0.8354	0.8734
				152	-0.4785	0.3575	142	-0.8673	0.8646
				154	-0.4407	0.3085	144	-0.8677	0.8123
				156	-0.4208	0.2724	146	-0.8220	0.7299
				158	-0.4041	0.2409	148	-0.7766	0.6413
				160	-0.4022	0.2198	150	-0.7028	0.5445
				162	-0.4269	0.2070	152	-0.6377	0.4608
				164	-0.5323	0.1936	154	-0.5950	0.4011
				166	-0.6035	0.1529	156	-0.5513	0.3278
				168	-0.6237	0.0986	158	-0.5388	0.2818
				170	-0.5664	0.0728	160	-0.5244	0.2630
				172	-0.4711	0.0622	162	-0.5235	0.2497
				174	-0.3671	0.0600	164	-0.5852	0.2306
				176	-0.2698	0.0667	166	-0.6656	0.1982
				178	-0.0854	0.0714	168	-0.7452	0.1279
				180	-0.0218	0.0675	170	-0.6982	0.0785
							172	-0.5911	0.0604
							174	-0.4621	0.0573
							176	-0.3446	0.0730
							178	-0.1022	0.0780
							180	0.0126	0.0794

NACA0018 $Re = 140,000$

Closed-jet			Open-jet			Reference tunnel		
AOA	**Cl**	**Cd**	**AOA**	**Cl**	**Cd**	**AOA**	**Cl**	**Cd**
0	0.0137	0.0222	0	0.0074	0.0202	0	0.0227	0.0248
2	0.1859	0.0235	2	0.1275	0.0201	2	0.1619	0.0229
4	0.4023	0.0233	4	0.2614	0.0201	4	0.3585	0.0267
6	0.6575	0.0369	6	0.4150	0.0286	6	0.5624	0.0411
8	0.8460	0.0476	8	0.5647	0.0454	8	0.7675	0.0550
10	0.9341	0.0606	10	0.6917	0.0612	10	0.8825	0.0697
12	1.0076	0.0775	12	0.7964	0.0804	12	0.9443	0.0876
14	1.0556	0.1058	14	0.8655	0.0994	14	1.0030	0.1110
15	0.3904	0.2044	16	0.9165	0.1229	14.5	1.0144	0.1160
16	0.4427	0.2239	17	0.9367	0.1308	15	1.0245	0.1273
18	0.4933	0.2610	18	0.3206	0.2000	15.5	0.8050	0.1961
20	0.5626	0.3012	20	0.3384	0.2222	16	0.4259	0.2232
25	0.7456	0.4305	22	0.3697	0.2515	18	0.4951	0.2752
30	0.9369	0.5956	24	0.3987	0.2794	20	0.5704	0.3182
35	1.1473	0.8935	26	0.4278	0.3132	22	0.6093	0.3572
40	1.3445	1.2088	28	0.4646	0.3540	24	0.6445	0.3996
45	1.4435	1.4542	30	0.4991	0.3956	26	0.6780	0.4358

50	1.5086	1.7201	32	0.5415	0.4458	28	0.7278	0.4858
55	1.4719	2.0541	34	0.5872	0.5052	30	0.7718	0.5539
60	1.4308	2.3938	36	0.6308	0.5642	32	0.8208	0.6175
65	1.3414	2.6912	38	0.6726	0.6305	34	0.8575	0.6879
70	1.2014	2.9831	40	0.7099	0.6982	36	0.8676	0.7332
75	0.9923	3.1456	42	0.7212	0.7478	37	0.8785	0.7597
80	0.7624	3.2912	44	0.7399	0.8116	38	0.8758	0.7838
85	0.5063	3.3865	46	0.7465	0.8700	39	0.8331	0.7535
90	0.2307	3.4219	48	0.7502	0.9197	40	0.5473	0.5432
95	-0.0444	3.3854	50	0.3999	0.5472	42	0.5625	0.5877
100	-0.3123	3.2914	52	0.3877	0.5652	44	0.5585	0.6212
105	-0.5346	3.1315	54	0.3834	0.5902	46	0.5563	0.6533
110	-0.7741	2.9672	56	0.3725	0.6100	48	0.5532	0.6903
115	-0.9697	2.7345	58	0.3609	0.6279	50	0.5495	0.7315
120	-1.1054	2.4585	60	0.3504	0.6506	52	0.5464	0.7599
125	-1.1927	2.1576	62	0.3437	0.6774	54	0.5361	0.7918
130	-1.2378	1.8631	64	0.3289	0.7007	56	0.5275	0.8278
135	-1.2207	1.5435	66	0.3120	0.7101	58	0.5150	0.8576
140	-1.1547	1.2431	68	0.3052	0.7487	60	0.4996	0.8871
145	-1.0230	0.9459	70	0.2850	0.7539	62	0.4799	0.9126
150	-0.8198	0.6371	72	0.2642	0.7724	64	0.4602	0.9411
155	-0.6716	0.4444	74	0.2437	0.7847	66	0.4374	0.9639
160	-0.5864	0.3210	76	0.2250	0.8049	68	0.4140	0.9878
164	-0.5935	0.2488	78	0.2034	0.8211	70	0.3873	1.0039
166	-0.6637	0.2303	80	0.1793	0.8329	72	0.3617	1.0257
168	-0.7533	0.1910	82	0.1549	0.8426	74	0.3220	1.0405
170	-0.7848	0.1330	84	0.1314	0.8543	76	0.3035	1.0608
172	-0.7372	0.0868	86	0.1049	0.8587	78	0.2729	1.0705
174	-0.6151	0.0660	88	0.0798	0.8629	80	0.2405	1.0731
176	-0.4475	0.0576	90	0.0533	0.8670	82	0.2053	1.0800
178	-0.2885	0.0551	92	0.0278	0.8667	84	0.1720	1.0857
180	0.0354	0.0607	94	0.0023	0.8628	86	0.1362	1.0897
			96	-0.0249	0.8580	88	0.1040	1.0925
			98	-0.0491	0.8487	90	0.0709	1.0978
			100	-0.0754	0.8407	92	0.0362	1.0908
			102	-0.1005	0.8307	94	0.0000	1.0857
			104	-0.1240	0.8174	96	-0.0324	1.0797
			106	-0.1473	0.8001	98	-0.0635	1.0665
			108	-0.1710	0.7823	100	-0.0988	1.0577
			110	-0.1918	0.7655	102	-0.1296	1.0420
			112	-0.2126	0.7459	104	-0.1595	1.0282
			114	-0.2320	0.7280	106	-0.1889	1.0147
			116	-0.2473	0.7019	108	-0.2150	0.9952
			118	-0.2736	0.6808	110	-0.2460	0.9699
			120	-0.2827	0.6608	112	-0.2720	0.9451
			122	-0.2936	0.6343	114	-0.2979	0.9244

124	-0.3140	0.6196	116	-0.3214	0.8919
126	-0.3250	0.5940	118	-0.3500	0.8803
128	-0.3453	0.5806	120	-0.3647	0.8406
130	-0.3570	0.5606	122	-0.3819	0.8067
132	-0.3632	0.5340	124	-0.3948	0.7606
134	-0.4745	0.5833	126	-0.4084	0.7393
136	-0.7036	0.8625	128	-0.4254	0.7119
138	-0.7187	0.8205	130	-0.4364	0.6807
140	-0.7236	0.7782	132	-0.4393	0.6397
142	-0.6945	0.7037	134	-0.4447	0.6048
144	-0.6668	0.6368	136	-0.4506	0.5738
146	-0.6199	0.5606	138	-0.4554	0.5406
148	-0.5801	0.4876	139	-0.4577	0.5263
150	-0.5480	0.4282	140	-0.6035	0.6211
152	-0.5054	0.3712	141	-0.8598	0.8874
154	-0.4591	0.3185	142	-0.8551	0.8361
156	-0.4304	0.2789	144	-0.8528	0.8056
158	-0.4119	0.2464	146	-0.8350	0.7331
160	-0.4097	0.2227	148	-0.7880	0.6475
162	-0.4242	0.2058	150	-0.7257	0.5623
164	-0.5103	0.1948	152	-0.6568	0.4723
166	-0.6406	0.1565	154	-0.5944	0.3969
168	-0.6645	0.1043	156	-0.5630	0.3563
170	-0.5965	0.0741	158	-0.5360	0.3158
172	-0.4998	0.0626	160	-0.5355	0.2984
174	-0.3984	0.0614	162	-0.5320	0.2755
176	-0.3090	0.0661	164	-0.6027	0.2582
178	-0.1110	0.0744	166	-0.6611	0.1900
180	-0.0112	0.0715	168	-0.7289	0.1358
			170	-0.7367	0.0835
			172	-0.6253	0.0661
			174	-0.5001	0.0594
			176	-0.3772	0.0692
			178	-0.1913	0.0800
			180	0.0221	0.0714

Appendix C Corrected lift and drag coefficients

NACA0018 $Re = 60,000$

Closed-jet			Open-jet		
AOA	Cl	Cd	AOA	Cl	Cd
0.00	0.0144	0.0198	0.00	-0.0085	0.0191
2.04	0.3181	0.0373	1.21	0.2101	0.0315
4.07	0.5182	0.0357	2.58	0.3753	0.0302
6.08	0.6303	0.0382	4.15	0.4891	0.0376
8.10	0.7121	0.0507	5.85	0.5670	0.0428
10.11	0.7801	0.0611	7.54	0.6490	0.0484
11.11	0.7988	0.0689	9.26	0.7237	0.0445
12.05	0.3296	0.1391	11.21	0.7378	0.0723
14.06	0.3927	0.1799	13.93	0.2816	0.1600
16.06	0.4155	0.2111	14.91	0.2882	0.1697
18.06	0.4460	0.2283	16.90	0.2909	0.1804
20.07	0.4878	0.2616	18.81	0.3138	0.2041
25.09	0.5990	0.3625	20.66	0.3530	0.2271
30.11	0.6890	0.4851	22.57	0.3785	0.2517
35.13	0.7918	0.6233	24.46	0.4065	0.2800
40.15	0.8789	0.8152	26.34	0.4392	0.3109
45.17	0.9224	0.9903	28.21	0.4736	0.3469
50.17	0.9031	1.1295	30.12	0.4974	0.3867
55.18	0.8685	1.2731	32.04	0.5187	0.4281
60.17	0.8084	1.3970	33.96	0.5400	0.4774
65.16	0.7142	1.4810	35.81	0.5775	0.5277
70.14	0.6065	1.5575	37.71	0.6043	0.5816
75.11	0.4748	1.6077	39.59	0.6361	0.6245
80.08	0.3578	1.6264	41.49	0.6643	0.6952
85.05	0.2261	1.6433	43.47	0.6689	0.7580
90.02	0.0946	1.6561	45.53	0.6534	0.8101
94.99	-0.0357	1.6503	48.55	0.3845	0.5120
99.96	-0.1536	1.6234	50.59	0.3737	0.5316
104.94	-0.2782	1.5771	52.62	0.3660	0.5520
109.91	-0.4034	1.5021	54.66	0.3543	0.5725
114.89	-0.5176	1.4526	56.72	0.3374	0.5933
119.87	-0.6114	1.3588	58.73	0.3343	0.6134
124.86	-0.6892	1.2512	60.79	0.3201	0.6340
129.85	-0.7620	1.1388	62.83	0.3083	0.6545
134.85	-0.7989	1.0003	64.91	0.2873	0.6753
139.86	-0.7943	0.8452	66.96	0.2753	0.6902
144.88	-0.7530	0.6856	69.00	0.2653	0.7126
149.90	-0.6251	0.4819	71.07	0.2470	0.7267

154.91	-0.5706	0.3698
159.93	-0.4975	0.2628
163.93	-0.5177	0.2074
165.92	-0.5479	0.1762
167.92	-0.5990	0.1337
169.91	-0.6155	0.0752
171.92	-0.5541	0.0437
173.94	-0.4410	0.0366
175.96	-0.2750	0.0460
177.99	-0.0828	0.0648
180.00	-0.0212	0.0651

73.14	0.2281	0.7382
75.23	0.2039	0.7519
77.29	0.1876	0.7683
79.38	0.1650	0.7833
81.46	0.1438	0.7987
83.57	0.1127	0.8053
85.65	0.0921	0.8186
87.73	0.0719	0.8248
89.78	0.0569	0.8259
91.90	0.0272	0.8229
94.00	0.0013	0.8164
96.10	-0.0259	0.8160
98.19	-0.0493	0.8042
100.27	-0.0711	0.7948
102.35	-0.0924	0.7878
104.45	-0.1192	0.7752
106.55	-0.1443	0.7671
108.62	-0.1648	0.7523
110.73	-0.1925	0.7300
112.83	-0.2186	0.7224
114.87	-0.2296	0.6989
116.95	-0.2512	0.6817
119.01	-0.2681	0.6546
121.07	-0.2829	0.6300
123.10	-0.2895	0.6132
125.21	-0.3186	0.5901
127.24	-0.3269	0.5663
129.30	-0.3423	0.5460
131.38	-0.3647	0.5379
134.34	-0.6193	0.8126
136.40	-0.6353	0.7874
138.49	-0.6572	0.7433
140.50	-0.6609	0.7034
142.51	-0.6631	0.6442
144.45	-0.6468	0.5959
146.40	-0.6333	0.5418
148.28	-0.6030	0.4904
150.08	-0.5492	0.4303
151.94	-0.5132	0.3726
153.74	-0.4611	0.3098
155.62	-0.4292	0.2680
157.52	-0.4006	0.2348
159.45	-0.3823	0.2045
161.50	-0.3965	0.1857
163.60	-0.4225	0.1726
165.83	-0.4837	0.1474

168.16	-0.5697	0.1070
170.24	-0.5909	0.0635
171.95	-0.5145	0.0444
173.52	-0.4025	0.0415
175.04	-0.2737	0.0485
176.63	-0.1674	0.0547
178.32	-0.0856	0.0587
180.11	-0.0278	0.0544

NACA0018 $Re = 100,000$

Closed-jet			Open-jet		
AOA	**Cl**	**Cd**	**AOA**	**Cl**	**Cd**
0.00	0.0397	0.0287	0.00	-0.0011	0.0195
2.03	0.1924	0.0269	1.40	0.1573	0.0190
4.06	0.4284	0.0410	2.95	0.2779	0.0191
6.09	0.6264	0.0515	4.35	0.4361	0.0253
8.10	0.7503	0.0612	5.72	0.6018	0.0343
10.11	0.8432	0.0816	7.31	0.7113	0.0380
12.13	0.9106	0.1061	8.97	0.8014	0.0426
14.13	0.9503	0.1879	10.80	0.8450	0.0514
15.05	0.3430	0.2152	12.64	0.8876	0.0751
16.06	0.3940	0.2406	13.58	0.9052	0.0837
18.06	0.4256	0.2595	16.81	0.3149	0.1870
20.06	0.5021	0.3542	18.75	0.3297	0.2073
25.08	0.6154	0.4812	20.65	0.3573	0.2329
30.10	0.7179	0.6564	22.52	0.3913	0.2623
35.13	0.8141	0.8440	24.39	0.4258	0.2943
40.16	0.9093	1.0050	26.26	0.4588	0.3275
45.18	0.9561	1.1410	28.15	0.4902	0.3632
50.18	0.9348	1.2810	30.00	0.5289	0.4061
55.18	0.8792	1.3950	31.89	0.5585	0.4403
60.17	0.8076	1.4950	33.72	0.6025	0.4970
65.16	0.7189	1.5839	35.55	0.6470	0.5573
70.14	0.6186	1.6323	37.36	0.6990	0.6304
75.12	0.4946	1.6845	39.24	0.7285	0.6891
80.09	0.3626	1.7139	41.18	0.7451	0.7438
85.06	0.2337	1.7249	43.19	0.7420	0.7847
90.02	0.0995	1.7226	45.21	0.7382	0.8386
94.99	-0.0382	1.6913	48.47	0.4038	0.5252
99.96	-0.1750	1.6574	50.50	0.3957	0.5439
104.93	-0.3043	1.5961	52.53	0.3881	0.5663
109.90	-0.4318	1.5148	54.57	0.3770	0.5864
114.88	-0.5463	1.4200	56.62	0.3647	0.6051
119.86	-0.6467	1.3148	58.66	0.3531	0.6253
124.85	-0.7312	1.2042	60.70	0.3434	0.6489

129.84	-0.8079	1.0574
134.84	-0.8404	0.9033
139.85	-0.8445	0.7222
144.87	-0.7893	0.5266
149.89	-0.6797	0.3490
154.92	-0.5265	0.2551
159.93	-0.4686	0.2068
163.93	-0.4672	0.1877
165.92	-0.5286	0.1505
167.91	-0.6180	0.0963
169.90	-0.6870	0.0535
171.91	-0.6319	0.0413
173.93	-0.5153	0.0480
175.95	-0.3750	0.0541
177.97	-0.1846	0.0666
180.00	-0.0115	0.0666

62.73	0.3345	0.6737
64.80	0.3175	0.6930
66.87	0.2994	0.7096
68.92	0.2852	0.7296
70.99	0.2658	0.7499
73.08	0.2436	0.7606
75.15	0.2241	0.7786
77.23	0.2030	0.7934
79.32	0.1795	0.8042
81.41	0.1550	0.8121
83.50	0.1317	0.8245
85.60	0.1066	0.8371
87.70	0.0792	0.8435
89.80	0.0536	0.8440
91.90	0.0267	0.8393
93.99	0.0028	0.8417
96.09	-0.0243	0.8345
98.19	-0.0495	0.8269
100.29	-0.0774	0.8211
102.38	-0.1010	0.8108
104.50	-0.1310	0.8047
106.58	-0.1534	0.7936
108.68	-0.1801	0.7785
110.74	-0.1955	0.7593
112.83	-0.2191	0.7396
114.91	-0.2411	0.7245
116.98	-0.2598	0.7064
119.02	-0.2702	0.6775
121.09	-0.2877	0.6485
123.13	-0.2990	0.6197
125.17	-0.3097	0.5920
127.22	-0.3231	0.5685
129.29	-0.3401	0.5519
131.37	-0.3617	0.5327
133.41	-0.3728	0.5184
136.49	-0.6575	0.8184
138.61	-0.6888	0.7950
140.64	-0.6970	0.7435
142.65	-0.7006	0.7102
144.58	-0.6808	0.6405
146.46	-0.6493	0.5756
148.29	-0.6052	0.5025
150.11	-0.5581	0.4391
152.03	-0.5355	0.3891
153.87	-0.4943	0.3419
155.72	-0.4552	0.2953

157.64	-0.4347	0.2603
159.58	-0.4174	0.2297
161.57	-0.4154	0.2087
163.67	-0.4409	0.1946
166.08	-0.5498	0.1743
168.36	-0.6233	0.1280
170.44	-0.6442	0.0721
172.21	-0.5851	0.0509
173.84	-0.4866	0.0470
175.43	-0.3791	0.0508
177.05	-0.2787	0.0617
178.33	-0.0882	0.0709
180.09	-0.0225	0.0674

NACA0018 $Re = 140,000$

Closed-jet			Open-jet		
AOA	**Cl**	**Cd**	**AOA**	**Cl**	**Cd**
0.00	0.0133	0.0217	0.00	0.0076	0.0202
2.02	0.1802	0.0230	1.50	0.1317	0.0190
4.05	0.3901	0.0228	2.98	0.2700	0.0155
6.09	0.6354	0.0360	4.38	0.4287	0.0169
8.11	0.8153	0.0463	5.79	0.5833	0.0236
10.12	0.8973	0.0588	7.30	0.7145	0.0286
12.13	0.9638	0.0748	8.89	0.8226	0.0371
14.14	1.0024	0.1014	10.62	0.8940	0.0483
15.05	0.3618	0.1912	12.42	0.9467	0.0657
16.06	0.4084	0.2084	13.34	0.9675	0.0710
18.07	0.4510	0.2407	16.75	0.3312	0.1930
20.07	0.5094	0.2752	18.68	0.3496	0.2144
25.09	0.6549	0.3815	20.56	0.3819	0.2422
30.11	0.7926	0.5085	22.44	0.4118	0.2685
35.15	0.9101	0.7152	24.33	0.4418	0.3007
40.18	1.0005	0.9078	26.18	0.4799	0.3393
45.19	1.0249	1.0419	28.05	0.5155	0.3786
50.20	1.0203	1.1740	29.88	0.5593	0.4258
55.20	0.9396	1.3232	31.71	0.6065	0.4816
60.19	0.8639	1.4587	33.53	0.6516	0.5370
65.18	0.7733	1.5658	35.37	0.6948	0.5997
70.16	0.6632	1.6619	37.23	0.7332	0.6639
75.13	0.5352	1.7119	39.18	0.7450	0.7123
80.10	0.4028	1.7548	41.11	0.7643	0.7742
85.07	0.2640	1.7820	43.08	0.7710	0.8320
90.03	0.1197	1.7919	45.07	0.7749	0.8813
94.99	-0.0231	1.7817	48.44	0.4131	0.5363
99.96	-0.1650	1.7549	50.48	0.4005	0.5549

104.93	-0.2889	1.7076
109.90	-0.4283	1.6568
114.87	-0.5554	1.5805
119.85	-0.6607	1.4828
124.84	-0.7483	1.3661
129.84	-0.8164	1.2400
134.84	-0.8525	1.0877
139.85	-0.8536	0.9273
144.86	-0.8027	0.7490
149.89	-0.6871	0.5389
154.91	-0.5879	0.3926
159.92	-0.5284	0.2919
163.92	-0.5442	0.2302
165.91	-0.6112	0.2140
167.90	-0.7004	0.1792
169.90	-0.7402	0.1266
171.90	-0.7035	0.0836
173.92	-0.5900	0.0639
175.94	-0.4302	0.0558
177.96	-0.2775	0.0535
180.00	0.0340	0.0588

52.50	0.3960	0.5801
54.54	0.3848	0.6005
56.59	0.3728	0.6190
58.63	0.3620	0.6422
60.66	0.3550	0.6693
62.71	0.3397	0.6933
64.78	0.3222	0.7034
66.81	0.3152	0.7424
68.89	0.2943	0.7483
70.97	0.2729	0.7677
73.05	0.2517	0.7807
75.12	0.2324	0.8014
77.21	0.2101	0.8183
79.30	0.1852	0.8307
81.39	0.1600	0.8410
83.49	0.1357	0.8532
85.59	0.1083	0.8580
87.69	0.0825	0.8625
89.79	0.0550	0.8668
91.89	0.0288	0.8667
93.99	0.0024	0.8628
96.10	-0.0257	0.8580
98.19	-0.0507	0.8485
100.29	-0.0779	0.8404
102.39	-0.1038	0.8301
104.48	-0.1281	0.8163
106.58	-0.1521	0.7986
108.67	-0.1766	0.7803
110.75	-0.1982	0.7630
112.83	-0.2196	0.7428
114.91	-0.2396	0.7243
116.97	-0.2554	0.6977
119.07	-0.2826	0.6757
121.10	-0.2920	0.6554
123.15	-0.3033	0.6284
125.23	-0.3243	0.6128
127.27	-0.3357	0.5868
129.35	-0.3567	0.5725
131.40	-0.3688	0.5519
133.42	-0.3752	0.5250
135.85	-0.4901	0.5680
138.75	-0.7268	0.8287
140.81	-0.7424	0.7853
142.83	-0.7474	0.7425
144.71	-0.7174	0.6708
146.61	-0.6887	0.6065

	148.42	-0.6403	0.5344
	150.27	-0.5992	0.4647
	152.14	-0.5661	0.4078
	153.98	-0.5220	0.3537
	155.79	-0.4742	0.3042
	157.68	-0.4446	0.2663
	159.61	-0.4254	0.2349
	161.60	-0.4232	0.2113
	163.66	-0.4381	0.1935
	165.99	-0.5271	0.1770
	168.50	-0.6617	0.1285
	170.60	-0.6863	0.0742
	172.33	-0.6161	0.0499
	173.95	-0.5163	0.0455
	175.56	-0.4115	0.0506
	177.21	-0.3192	0.0596
	178.43	-0.1146	0.0735
	180.04	-0.0115	0.0715

Appendix D Microcontroller datalogger technical details

The data logger hardware is built from a commercial microcontroller board, the Olimex "Olimexino" board, a commercial Bluetooth adaptor card and a custom designed interface board.

The microcontroller board includes an STM32F103 Cortex M3 32 bit ARM microcontroller running at $72MHz$. Amongst other things, the microcontroller includes $20KB$ RAM and $128KB$ flash memory, a 12 bit analogue to digital converter (ADC), general purpose digital inputs and outputs GPIO) and SPI and UART serial ports. The board includes a micro SD card holder and a LIPO battery charger.

In use, the battery provides the power required by all the electronics in the logger system. Acquired data from the pressure sensor and associated timing information is recorded on the SD card. The data can be downloaded remotely from the card using the Bluetooth connection, or alternatively the card can be removed and the data files read directly into a PC using a card reader.

The Bluetooth adaptor used is based on an NXP BGP203 Bluetooth module, which is controlled by the microcontroller using one of its UART serial ports. In use, the module is programmed to implement the Bluetooth Serial Port Profile (SPP) so that the logger can be controller remotely using any Bluetooth enabled device (e.g. a laptop) running a simple terminal emulator program (e.g. PUTTY or Teraterm).

The custom interface board plugs into the Olimexino microcontroller board. It provides signal conditioning to convert the bipolar analogue signal from the pressure sensor to the unipolar range accepted by the microcontroller's ADC. In addition, interfacing is provided to drive the pressure sensor's $12V$ CMOS level digital channel selection inputs from the microcontroller's $3.3V$ logic GPIO lines. The board also provides interfacing to a Honeywell HOA1404 optical reflective sensor (for detection of completed revolutions). Finally, it generates the required $+5V$, $+12V$ and $-12V$ supplies required by the pressure sensor from the microcontroller's $3.3V$ supply.

The logger software is written in C++, compiled using gcc and makes partial use of the LeafLabs libmaple and SdFat libraries (http://leaflabs.com/docs/libmaple.html). The general principle of operation is that a pressure sensor channel is first selected, and then ADC readings are taken at regular time intervals. These intervals are synchronised to the optical sensor input so that at constant rotational speed they will occur at the same rotational angle. A time stamp with microsecond resolution is also

recorded at every new revolution so that the actual rotation speed can, if desired, be calculated. Data collection is interrupt driven from one of the microcontroller's on-board general purpose timers, programmed for automatic reload to eliminate software delays. From the interrupt service routine data is stored in an in-memory circular buffer list whilst a background program frees those buffers after writing the data to the SD card. The required sensor channel list, the number of revolutions for which to continue sampling a channel and the anticipated revolution speed are all user configurable using the Bluetooth interface. From experimentation it was found that the data logging system could sample at a rate of at least $1{,}440$ samples per revolution at a revolution speed of $8Hz$, equating to one sample for each $1/4$ degree of rotation.

Microcontroller datalogger circuit diagram